UNIVERSITAT DE BARCELONA

Active tectonics in Northern Africa: The Nubia-Eurasia boundary in Tunisia

Miquel Camafort Blanco

Active tectonics in Northern Africa: The Nubia-Eurasia boundary in Tunisia

Memòria de tesis doctoral presentada per

Miquel Camafort Blanco

Per optar al Grau de Doctor per la Universitat de Barcelona

Aquesta memòria s'ha dut a terme dins del Programa de Doctorat de Ciències de la Terra de la Universitat de Barcelona sota la direcció del Dr. César Rodríguez Ranero i la Dra. Eulàlia Gràcia i Mont i ha estat tutelada pel Dr. Raimon Pallàs i Serra.

Barcelona, Març de 2019

Explorant l'inexplorat...

Agraïments / Acknowledgements

En primer lloc vull agrair als meus directors de tesi, el César i la Laia, haver confiat en mi des del primer moment, primer per a treballar en el projecte Geomargen-2 i després per a oferir-me i animar-me a seguir la feina feta amb aquesta tesi doctoral. Moltes gràcies també per animar-me, guiar-me, ajudar-me i en definitiva per tota la dedicació que heu dipositat en mi durant aquest viatge.

En especial vull agrair-li també al Sergio l'ajuda que des del primer dia m'ha donat en tot el que ha calgut, primer com a company i ara com a amic. Moltes gràcies pels grans moments que hem passat i pels que vindran.

A Vicen y a Billy por acogerme en mis estancias en Granada y por acompañarme en el trabajo de campo en Túnez. A Vicen en concreto por todos los conocimientos que me ha transmitido de GIS, por su buen rollo y por su ayuda en tirar el paper hacia adelante. A Billy por todo lo que aprendí con él de geología de campo, por su aportación también en el paper y por los buenos momentos que pasamos en Túnez. A los compañeros doctorandos de Granada por haberme acogido y haberme hecho disfrutar aun más de mis estancias en esa maravillosa ciudad.

No em vull oblidar de les persones que en els inicis de la meva carrera com a geòleg em van ajudar a arribar fins aquí. En especial i en primer lloc a la Marta González de l'Institut Geològic de Catalunya, per tota l'ajuda i l'energia dipositades en mi durant els tres anys com a becari a l'Institut, per fer-me créixer com a geòleg, per introduir-me al món del GIS que tant m'apassiona *y por ser una tía tan genial, ¡muchas gracias Marta!* Al Jordi Pinyol per tutoritzar-me també durant la beca a l'IGC, a tots els companys del Departament d'Enginyeria Geològica i Riscos Geològics de l'institut per encomanar-me la seva passió pels riscos geològics, i a tots els companys becaris, en especial al Calabria, el Míguel i la Esther. Al Jaume Calvet, el Raimon Pallàs, el Joan-Manuel Vilaplana, i a tot el Departament de Geodinàmica i Geofísica de la Universitat de Barcelona per haver-me ajudat sempre en tot el que ha calgut, per haver confiat en mi i per d'alguna manera haver contribuït en que hagi acabat fent aquesta tesi.

A la Blanca Payàs per haver confiat en mi, haver-me donat flexibilitat per poder acabar aquesta tesi i per donar-me la oportunitat de formar part d'aquesta nova aventura que m'omple i em motiva tant.

A Claudio por el curro que nos pegamos el primer año mano a mano en los informes de Repsol, por haberme ayudado en todo lo que he necesitado y por haber estado siempre predispuesto a ayudar en lo que hiciera falta y siempre con el buen rollo por delante, grazie mille!

A la Clàudia, la Marina, l'Estela, la Laura, l'Slaven i el Dani que van començar sent companys de despatx i campanyes i han acabat sent companys de sopars, festes, riures, fatigues, cafès i en definitiva amics. Al Manel per les sortides en bici al començament de la tesi, per la seva energia positiva i per acollir-me a Dublín i a Viena. A la nova fornada de doctorands amb els que també hem passat molt bons moments i m'han recolzat en aquesta última etapa, la Cris, el Davide, la Irene, la Marta i el Will. I en general a tots els companys de l'ICM que d'alguna manera o altra han fet aquest camí més fàcil, gràcies!

Als *Rather* per haver estat sempre allà i continuar-hi sent, per tot el que hem gaudit, tota l'ajuda que m'heu donat durant aquest camí i per haver "aguantat" estoicament les meves absències durant les campanyes. I als *Deceles* pels riures i els assajos revitalitzadors en aquesta última etapa. Al David, la Clara, el Gerins, l'Uli i el Jus per sempre ser-hi i pels bons moments que sempre passem junts. Al Gerins (Gerard Casadevall Bach) també per haver-me dissenyat la portada de la tesi. A l'Alejo i el Marsuel, perquè tot i no coincidir molt, sempre hi sou. I al Ritxi, per ser-hi, per escoltar-me, per aconsellar-me, per ajudar-me i per ser aquell amic que tothom voldria tenir.

Als meus pares per ajudar-me sempre en tot moment i de forma incondicional i per fer-me ser qui sóc avui, us ho dec tot. A la meva germana per les converses, l'ajuda, els consells, el seu suport incondicional i per confiar en mi a l'hora de tirar aquesta tesi endavant i al Rob per l'interès que sempre ha mostrat en la meva feina i per juntament amb ma germana haver-me fet tiet en aquest últim tram. A la meva àvia que sempre m'ajudava en el que fes falta. I a la meva família postissa dels Medina que m'han acollit des d'un primer moment, m'han cuidat i s'han preocupat de mi perquè pogués acabar aquesta tesi.

Finalment a la Paula, companya en tot aquest viatge i que ha patit més que ningú els "danys colaterals" d'aquesta tesi, per haver-me recolzat sempre que ho he necessitat, per donar-ho tot perquè jo pogués tirar endavant la tesi, per animar-me en els moments més difícils i en definitiva per sempre ser-hi.

A tots, moltes gràcies.

Funding

The author of this thesis has been supported by the project Geomargen-2 funded by Repsol and EU project EMODnet-HRSM. Additional funding has been obtained on the framework of SHAKE (CGL2011-30005-C02-02) and INSIGHT (CTM2015-70155-R) projects. This work was carried out within the Grup de Recerca Consolidat de la Generalitat de Catalunya *Barcelona Centre for Subsurface Imaging (B-CSI)* (2017SGR1662).

Contents

Part V: CONCLUSIONS & FORWARD LOOK

Summary

This PhD thesis presents a geological and geophysical study that characterizes the Quaternary stratigraphy, geomorphology, recent tectonics, and discusses their implications to understand the geodynamic evolution of North Tunisia, including the emerged land and continental margin. The study area spans much of the region containing the boundary between the African and Eurasian tectonic plates in this sector. The onshore main structural pattern strikes in a NE-SW trend that extends offshore, into the North Tunisian continental margin plateau that is part of the same recent deformation system. I have carried out specific analyses of these two onshore and offshore regions where present-day tectonics has been previously poorly studied. Although some limited active-tectonic studies had been carried out onshore, the offshore area was scarcely studied to date, and never explored in the detail presented in this work, let alone studied in an onshore-offshore integrative study. To carry out the joint study of the two regions we have had to take different methodological approaches.

Onshore Northern Tunisia we applied a morphometric relief analysis of digital elevation models based in drainage network metrics to characterize active tectonics and its influence into the drainage evolution of the area. This analysis was ground-truthed with a field campaign in March 2015 to examine the several morphometric anomalies obtained with the relief analysis carried out before. Our analysis indicates that recent river captures have been the main factor driving the fluvial network reorganization in Northern Tunisia. Morphometric indices evidence fluvial network reorganization that indicates that the catchment area of the Medjerda River has increased through time by capturing adjacent axial valleys to the east of its previous drainage divide. These captures are probably driven by the gradual uplift of adjacent axial valleys by reverse/oblique slip faults like El Alia-Teboursouk and Dkhila faults or associated folding. Our fieldwork discovered that these faults cut Pleistocene sediments and possible associated coseismic structures were identified, further supporting recent fault activity with estimated maximum magnitudes (M_w) of 6.7 and 6.5 respectively for each fault.

To study the offshore North Tunisian continental margin we have integrated a comprehensive dataset of about 12,000 km of 2D parametric echosounder profiles (acquired with the Innomar SES-2000 Compact and the TOPAS PS 18 sub-bottom profilers) and about 15,600 km^2 of high-resolution bathymetry and back-scatter mosaics (acquired using the ELAC Seabeam 1050D and the

Kongsberg EM710 multibeam echosounders) on cruises with RV "García del Cid" and RV "Ángeles Alvariño" respectively. This dataset has been acquired in two cruises of our group during 2013 (Geomargen-2 and Geomargen-2AA) within the frame of the Geomargen-2 project funded by REPSOL. Additionally to the geophysical dataset, we integrated available age data from a giant piston core collected by the R/V Marion Dufresne in 1995 during the MAST II PALAEOFLUX Program (Dinarès-Turell et al., 2002), which provides the calibration of horizons mapped with TOPAS profiles. This large dataset acquired in offshore Northern Tunisia permitted a detailed analysis of the offshore Tunisian plateau for the first time.

The geomorphologic and morpho-structural study of the offshore North Tunisian margin has revealed a complex seafloor topography. The coexistence of a wide range of geomorphic features, such as contourites, moats, Cold-Water Coral Mounds (CWCMs), fold ridges, fault scarps, pockmarks and collapse pockmarks, basement highs, slide scars and mass transport deposits (MTD), the Bizerte Canyon and a rough shelf coupled with active gas release represent a complex scenario, where sedimentary, erosive and tectonic processes interplay to shape the seafloor and shallow strata structure. This first high-resolution study of the offshore area has been key to understand the complex shallow structure of the area and subsequently identify and characterize active faulting and related structures.

The seismo-stratigraphic analysis of deposits supports that individual Quaternary basins develop syn-tectonic to faulting, i.e. active tectonics clearly influence recent sedimentation patterns. This analysis found a change in Sediment Accumulation Rates (SAR) coeval to a change in the strata geometry of the units next to faults at 402 ± 5 ky (mid Middle Pleistocene) supporting a change in active faulting intensity caused by enhanced contractional tectonics. This change may relate to the NW-SE convergence between Nubia and Eurasia, and probably marks the end of the Tyrrhenian back-arc extension and of subduction trench migration in the Ionian Sea. Such a geodynamic change also supports a change in driving mechanism, so that kinematics are possibly driven by lithospheric collision between Nubia and Eurasia, as the main force governing tectonics in the central Mediterranean.

The structural analysis of the offshore North Tunisian continental margin has revealed a series of active faults mapped for the first time in the region with a general transpressional to compressional regime. Most active faults occur within the north-eastern sector of the mapped area and possibly represent the current reactivation of previous structures with different kinematics and inverted in compression by the present-day NW-SE trending convergence between the Nubia and

Eurasian plates. Most of them are possibly pre-existing faults formed during the opening of the Tyrrhenian Sea that started at ~10-8 Ma. Some fewer faults possibly related to the fold-and-thrust belt system associated to the opening of the Algero-Balearic basin (formed at around 17-14 Ma (Late Burdigalian – Langhian)) have also been identified, and some are reactivated displaying different fault components. These results support that part of the current NW-SE convergence is being accommodated by shortening in our study region. Here, the newly identified Hayat fault is a major structure possibly accommodating a significant component of the convergence. In the offshore study area, estimated maximum earthquake magnitudes range from M_w 6.25 to 7.54.

In summary, active faults with a main transpressive to compressive component have been identified and mapped in the whole area onshore-offshore. Active faults re-activate two groups of faults originally created during the early-middle Miocene opening of the Algero-balearic basin that formed the North African fold-and-thrust belt, and the opening during end Tortonian to Messinian age of the Tyrrhenian basin, that tectonically extended the northern sector of the offshore study area. The distribution of active faults corresponds to a sparse seismicity band that expands further south than in neighbouring regions. The broad area of deformation is probably related to the geometry and dynamics of the slab underlying Tunisia, and to the collision of the North African lithosphere with relatively thick continental lithosphere of the Sardinia-Corsica. Regions of continental lithosphere in collision with young thinner oceanic lithosphere, as the nearby oceanic plates north of Algeria and north of Sicily, display narrower deformation zones. The results of this thesis show that the sparse and diffuse seismicity of Northern Tunisia is associated to tectonics in both onshore and offshore regions that differ in kinematics and distribution from the neighbouring regions and provide information to improve the regional seismic hazard assessment model for Northern Tunisia and nearby regions.

Part I

INTRODUCTION

CHAPTER 1

Objectives and scientific approach

In this first chapter we present the motivation of this work, the main goal of this thesis together with other specific objectives, and a general scientific approach to the basic concepts involved in this work.

1.1. Motivation

The main motivation of this study is to advance our understanding of active tectonics in Northern Tunisia and to integrate it in the current geodynamic context of this sector, particularly complex and currently poorly defined due to the scarcity of studies of the plate boundary between the Nubia and Eurasian plates in the region.

The North Tunisian geological structure including areas onshore and offshore, was formed during a yet not fully understood geodynamic evolution. Since the Palaeogene, the evolution of the North Tunisian margin is associated to the northward subduction of the Nubian plate under the Eurasian plate, accommodating an imprecise amount of shortening between the plates (Wortel and Spakman, 2000; Faccenna et al., 2005; Booth-Rea et al., 2007; van Hinsbergen et al., 2014). The geodynamic evolution of North Tunisia shares common geological features with the mountain belts that surround other western Mediterranean Basins (Rosenbaum et al., 2002; Gelabert et al., 2002; Platt et al., 2003; Facenna et al., 2004; Spakman and Wortel, 2004). Moreover, mantle tomography of teleseismic earthquakes shows that the subducted Tethyan mantle lithosphere is distributed in different slabs lying under the Betics and Rif, and Calabria (Wortel and Spakmann, 2000) and possibly Algerian Tell and Tunisia (Fichtner and Villaseñor, 2015). These recent findings suggested

a complex and segmented geodynamic evolution along the plate boundary, with specific and unique tectonic characteristics for each mountain belt.

This area is characterized by a wide, but poorly defined, deformation zone accommodating a slow NW-SE trending convergence rate of ~5 mm/yr (e.g. DeMets et al., 1994; Sella et al., 2002; Calais et al., 2003; McClusky et al., 2003; D'agostino and Selvaggi, 2004; Serpelloni et al, 2007; Noquet, 2012). In addition to its complex evolution, the present-day north Tunisian Margin is also characterized by a sparse and scarce instrumental seismicity in contrast to neighbouring areas along the margin of north Morocco, north Algeria and north Sicily. While these other areas display a comparatively narrower and denser seismicity (e.g. Serpelloni et al., 2007; Beghoul et al., 2009; Meghraoui and Pondrelli, 2012; Nocquet, 2012), the North Tunisian margin is characterized by a diffuse distribution pattern with low to moderate magnitude seismic events (Gueddiche et al., 1998; Bahrouni et al., 2014; Ksentini and Romhdane, 2014). However, historical records that describe the destruction of Roman and Arabic settlements in Tunisia support that large magnitude seismic events have occurred during the past millennia (e.g. Ambraseys, 1962; Bahrouni et al., 2014; Ksentini and Romhdane, 2014). While magnitudes of instrumental earthquakes range from M_w 2 to M_w 5.5 (e.g. Ksentini and Romhdane, 2014), previous historical major events have epicentral intensities of VIII to X on the MSK scale (Ksentini and Romhdane, 2011; 2014) demonstrating that this area has a moderate to high seismic hazard. Regarding the recurrence interval (R.I.) of past earthquakes, the slow plate convergence and R.I. values of other areas along the plate boundary suggests an average value of <1000 years for the North Tunisian region (Gràcia et al., 2010; Serpelloni et al., 2007; Babonneau et al., 2017). Thus, active tectonic processes are occurring in this region, despite recent deformation are poorly constrained, so that further study is key to understand its current geodynamic setting and the potential seismic hazard.

The link between the onshore and offshore structures in Northern Tunisia has been long suggested, as the onshore structural pattern (e.g. Castany, 1954; Rouvier, 1977; El Euchi et al., 2004; Melki et al., 2012) follows a NE-SW trend that continues into the offshore North Tunisian plateau. This is the reason why to investigate active tectonic structures of the Nubia-Eurasia boundary in Northern Tunisia we use multi-disciplinary approaches and multi-scale datasets from a large region that includes onshore Northern Tunisia and the offshore Tunisian plateau comprised between Sicily and Sardinia. Onshore, we carried out a field campaign in March 2015, with the main goal of ground-truthing the results obtained from a previous quantitative morphometric relief analysis. This analysis is based on the application of different geomorphic indexes to characterize

recent/ongoing tectonic activity and its influence into the drainage evolution of the onshore Northern Tunisia.

Offshore, two marine surveys were carried out during year 2013. The first survey referred to as Geomargen-2, took place between April and May 2013. The main goal of this survey was to map the seafloor morphology of the Tunisian margin offshore and to explore the shallow subsurface geological structures within the first 50-80 meters below the seafloor. To accomplish this goal, an extensive high-resolution bathymetric dataset was acquired together with high-resolution parametric echosounder profiles and backscatter data. The second marine survey, Geomargen-2AA, took place from November to December 2013. Additional high-resolution bathymetric data and TOPAS profiles were acquired to further characterize the regional tectonic framework and to enlarge the dataset to the north-east within the Italian EEZ waters. The acoustic dataset together with the sedimentological data (i.e. our >100 ~4-m-long gravity cores, and a ~25-m-long piston core from Dinarès-Turell et al., 2002) and seismological data (i.e. earthquake and focal mechanism solutions from different repositories, such as ISC-GEM, ISC, Global CMT and the European-Mediterranean RCMT catalogue) were used to characterize the current tectonics of the Nubia-Eurasia boundary in Northern Tunisia.

The results obtained from the analysis of these extensive datasets provide new information into the active tectonics and the current geodynamic setting of the Nubia-Eurasia boundary in Northern Tunisia.

1.2. Objectives

The main goal of this Thesis is to characterize the current tectonic activity in northern Tunisia (onshore and offshore) and to integrate the results obtained within the Nubia-Eurasia plate boundary context. With this aim, we performed a multiscale and multidisciplinary approach with geological, geomorphological and geophysical observations on both offshore and onshore areas. This approach was designed to better analyse the active tectonic processes occurring in the region, and to characterize the current geodynamic setting underwent in this sector of the boundary between Nubia and Eurasia plates.

In order to achieve the main joint objective, onshore and offshore studies were carried out in parallel. Specific onshore objectives consist in:

i) To determine the active tectonic structures on land that form the Nubia-Eurasia boundary in this complex region, where present-day tectonic researches have been scarcely carried out.

Specific offshore objectives consist in:

i) To characterize the seafloor morphology and morphostructure of the explored area focusing on the influence of sedimentary, erosive and tectonic processes occurring on the seafloor.
ii) To define the Quaternary seismic stratigraphy in order to characterize the recent tectono-sedimentary evolution of the explored area.
iii) To identify and characterize the main and secondary active tectonic structures of the North Tunisian continental margin.

The final objective of this work is to integrate onshore and offshore results to provide active tectonic data across both areas. This integration will provide the first comprehensive "big picture" of the present-day tectonic activity within this sector of the Nubia-Eurasia plate boundary in Northern Tunisia.

1.3. Basic concepts

In this section we introduce a few basic concepts essential to understand the geological setting of this work. We mainly focus on general concepts regarding plate tectonics, subduction zones, active tectonics, seismicity, seismic hazard and marine geomorphology.

1.3.1. Fundamentals of plate tectonics

Plate tectonics describes the large-scale motion of seven large plates and the movements of a larger number of smaller plates of the Earth's lithosphere. The model builds on the concept of continental drift, an idea developed during the first decades of the 20th century (Wegener, 1915). The geoscientific community accepted plate-tectonic theory after seafloor spreading was validated in the late 1950s and early 1960 (e.g. Hess, 1962; Vine and Matthews, 1963; Morgan, 1968; Le Pichon, 1968) and subduction was introduced (Isacks et al., 1968). **Plate tectonics** explains that the **lithosphere**, the outermost rigid layer of the Earth composed by the crust and the uppermost solid mantle (Figure 1.1), is divided into small number of nearly rigid plates that move relative to one another over the **asthenosphere**, the weaker, viscous, hotter and deeper part of the upper mantle

(Figure 1.1) due to the large-scale convection of the mantle including ridges and subduction zones (e.g. Cox and Hart, 1986; Hamblin, 1992). Furthermore, affirms that most of the deformation that results from the motion of tectonic plates is accommodated along the edges of the plates or plate boundaries. In fact, global seismicity distribution depicts these plate boundaries with most of the earthquakes and volcanism occurring along them (Fowler, 1990) (Figure 1.2).

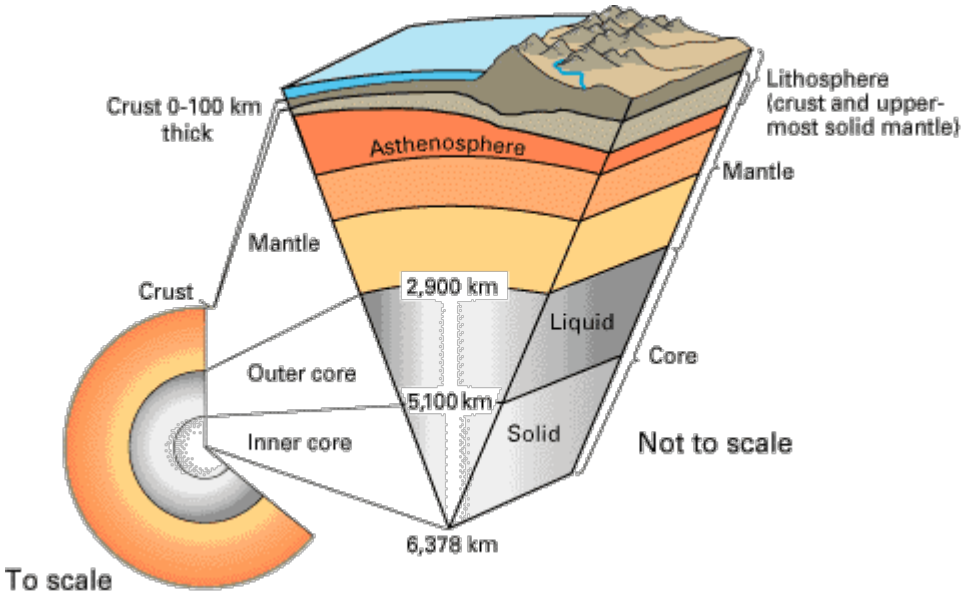

Figure 1.1. *Cutaway views of the internal structure of the Earth showing its three main layers (crust, mantle and core). Extracted from USGS, 2018a.*

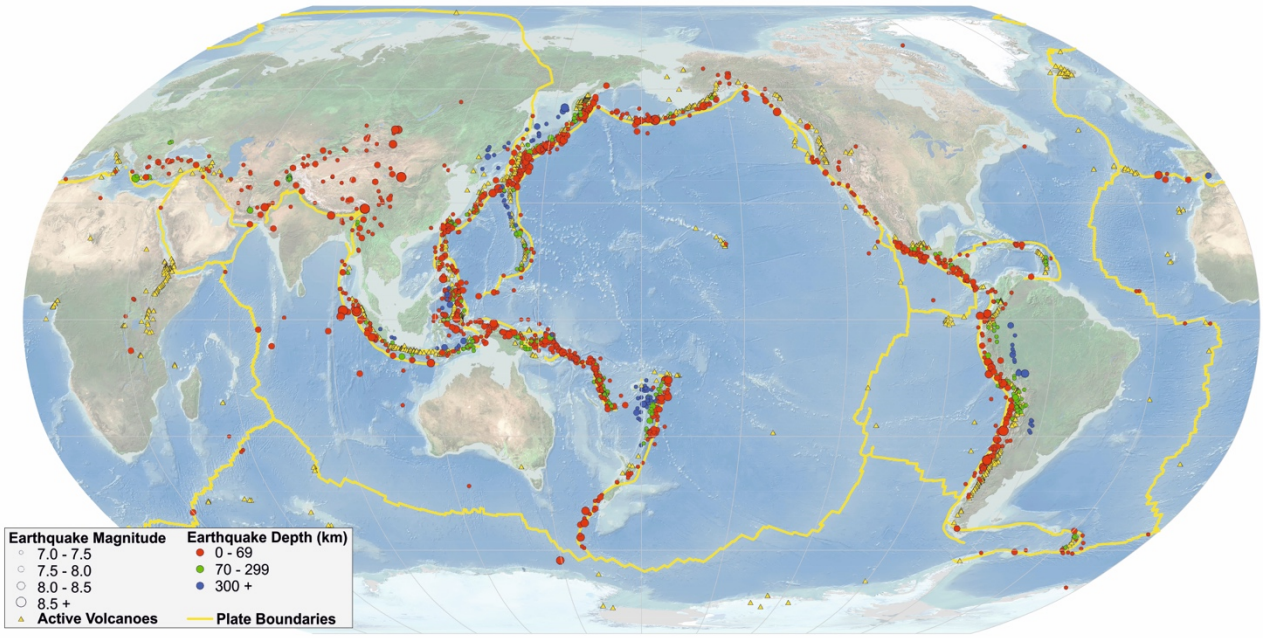

Figure 1.2. *Worldwide seismicity map from years 1900 to 2013. Modified from USGS, 2018b.*

There are three types of plate boundaries (e.g. Hamblin, 1992; Kearey et al., 2009) (Figure 1.3):

i) **Transform or conservative:** Where lithospheric plates move laterally relative to each other with the resulting generation of strike-slip motion fault systems. In this case, the lithosphere is neither created nor destroyed.

ii) **Divergent or constructive:** Where plates move away from each other with the resulting thinning of the lithosphere and the generation of new oceanic lithosphere. The boundaries are represented by mid-ocean ridges and continental rifts.

iii) **Convergent or destructive:** Where plates approach to each other. When two plates have different density, the convergence results in the plunging of the denser plate (typically oceanic) beneath the other, deepening into the mantle. On the other hand, when plates have the same density, the collision results in the formation of a mountain range.

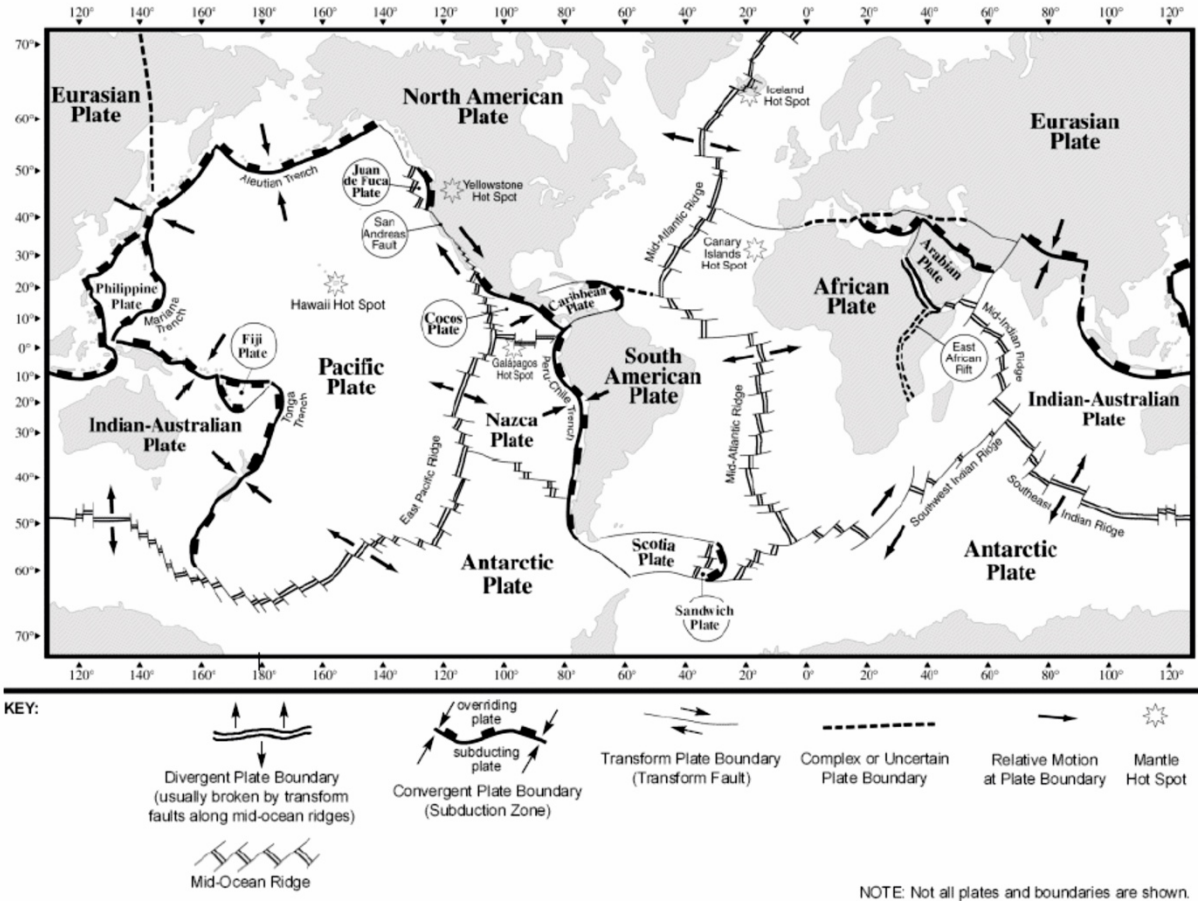

Figure 1.3. *Worldwide map showing the major tectonic plates and the different types of plate boundaries. Extracted from Fowler, 1990.*

1.3.2. Basic concepts of subduction zones

Subduction processes in convergent boundaries occur when two colliding plates have different densities and the denser moves under the other one, sinking into the mantle (Figure 1.4). The denser plate is usually an oceanic plate (i.e. oceanic lithosphere formed at mid-ocean ridges) that cools, thickens and becomes denser as it moves away from the spreading ridge. This denser oceanic lithosphere becomes gravitationally unstable with respect to the hotter asthenospheric mantle rocks below and bends downward sinking into the mantle when both plates collide (known as slab; Figure 1.4). The less dense plate remains at the surface and could become a continental plate or a young less dense oceanic plate (e.g. Fowler, 1990; Turcotte and Schubert, 2002; Kearey et al., 2009).

The downgoing lithosphere becomes negatively buoyant due to its greater density respect to the asthenospheric mantle. This negative buoyancy exerts a downward body force that is transferred to the surface section of the lithosphere since the lithosphere has an elastic nature. This force, known as **slab pull**, is considered to be the major driving force of plate tectonics. At depths of about 500 to 600 km, the increased viscosity and density of the mantle hinders the penetration of all slabs deeper in the mantle (e.g. Fowler, 1990; Turcotte and Schubert, 2002; Kearey et al., 2009). However, some slabs penetrate the 660 km discontinuity and dive to reach the core-mantle boundary (Fukao et al., 2001; Fukao and Obayashi, 2013).

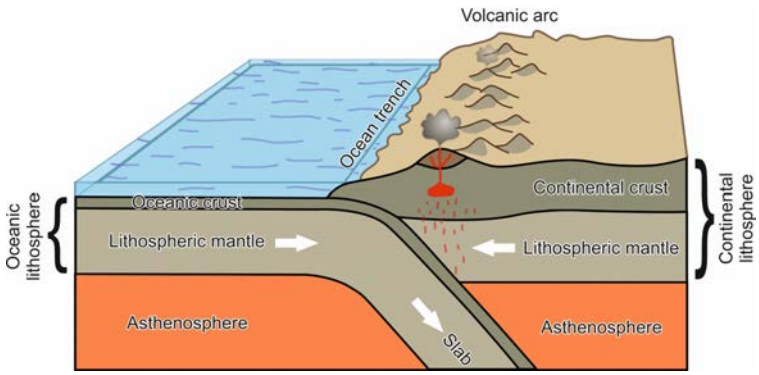

Figure 1.4. *Schematic cross-section of a subduction zone. Modified from USGS, 2018c.*

As explained in Section 1.3.1, plate boundaries hold most of the seismicity and volcanism around the globe. In particular, most great earthquakes (Mw > 8.0) tend to occur on or near subduction plate boundaries (Figure 1.5) and the greatest occur in these type of convergent boundaries (Lay, 2016). The five greatest earthquakes ever recorded are: the 1960 Chile earthquake (Mw ~ 9.5), the great Alaska earthquake in 1964 (Mw ~ 9.2), the 2004 Sumatra earthquake (Mw ~ 9.2), the recent 2011 Tohoku earthquake in Japan (Mw ~ 9.0) and the 1952 Kamchatka earthquake in Russia (Mw ~ 9.0) (Lay, 2016) (Figure 1.5).

Most **great subduction earthquakes** are shallow thrust-fault earthquakes (also referred as mega-thrust earthquakes) caused by the interaction between the downgoing and overriding plates. These shallow thrust-faulting earthquakes can only rupture within the brittle deformation zone, thus from the surface down to the onset of ductile deformation, which is referred as the seismogenic zone (e.g. Sibson, 1984; Scholz, 1988, 2002). The maximum seismogenic depth on most of subduction zones ranges between 40-60 km depth. Although most of the great earthquakes are classified as shallow (0-70 km deep), subduction zones are characterized by seismicity from the surface to almost 700 km depth. This intermediate and deep seismicity is intra-slab, i.e. does not occur at the contact between plates but inside the sinking plate. The intra-slab seismicity is caused by different mechanisms and define the Wadati-Benioff zone that marks the location and geometry of the descending slab (Roberts and Bally, 2012).

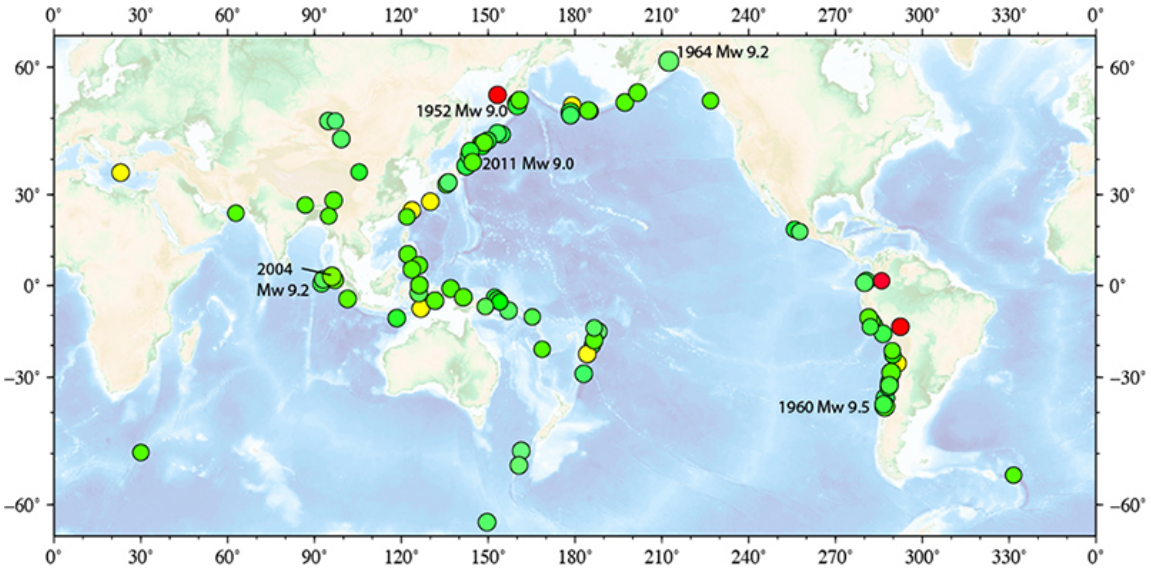

Figure 1.5. *Global distribution of 96 great earthquakes (M ≥ 8.0) occurred from 1900 to 2015. Green dots indicate shallow seismic events (depths ≤ 70 km); yellow dots indicate intermediate depth seismic events (70 to 400 km); red dots indicate deep seismic events (depths ≥ 400 km). Events are obtained from USGS catalogues. Note that most of the shallow great events are on the circum-Pacific margins where subduction zones are located, and how intermediate and deep earthquake events occur within subducted oceanic slabs. Extracted from Lay, 2016.*

As a result of the subduction process, hydrated minerals from the subducted lithosphere are introduced in the mantle. Heating of these minerals induces dehydration of the slab by releasing of water content that in turn, hydrates the adjacent mantle of the overlaying plate and overriding asthenosphere (so-called mantle wedge). This mechanism decreases the potential melting temperature of the adjacent asthenospheric mantle, generating magmatism that rises through the mantle until forming a **volcanic arc** or contributes to a back-arc spreading centre (e.g. Turcotte and Schubert, 2002; Kearey et al., 2009) (Figure 1.4).

1.3.3. Essential concepts of active tectonics and faults

The term **tectonics** refers to the processes, structures and landforms associated with the deformation of the Earth's lithosphere (i.e. refers to the evolution of these structures and landforms over time) (Keller and Pinter, 2002). This way, tectonics include from the origin of continents and ocean basins (at a global scale) to the slip of a single small fault (at a local scale). When the term **active tectonics** is used, it refers to those tectonic processes that produce deformation of the Earth's crust on a time scale of significance to human society (Wallace, 1986; Keller and Pinter, 2002). Although active tectonics would include slow deformations of the Earth's crust with weak damages to human structures, it is also broadly used for processes capable of producing catastrophes. A **catastrophe** or **natural disaster** is defined as any situation in which the damage to people, property, or society in general is sufficiently severe that recovery, rehabilitation, or both, are a long, involved process (Keller and Pinter, 2002). In particular, an earthquake is an active tectonic process likely to produce a catastrophe or a seismic disaster.

A **fault** is defined as a fracture or fracture system along which rocks have been displaced and are classified in three major types (Yeats et al., 1997):

i) **Normal faults:** The hanging wall moves down with respect to the footwall. The maximum principal compressive stress (σ_1) is vertical.

ii) **Reverse faults:** The hanging wall moves up with respect to the footwall. The minimum principal compressive stress (σ_3) is vertical.

iii) **Strike-slip faults:** The relative displacement between blocks is horizontal, in the direction of the strike. The intermediate principal compressive stress (σ_2) is vertical.

However, if none of the principal stresses is vertical, faults move by oblique slips. Moreover, it is noteworthy that faults almost never occur as a single trace but they form **fault zones** (groups of related faults that are subparallel in map view and often overlap in en-echelon or braided patterns). Also, large faults are **segmented**, with each segment displaying individual style and history. Fault rupture during earthquakes may stop at the segments boundaries, although great earthquakes can involve several ones (Keller and Pinter, 2002).

The term **active fault** has different definitions depending on the seismic region where it is located. Generally, there is an agreement to consider a fault to be **active** if it has moved during the Holocene Epoch (past 11.7 ky according to ICS (2018)) (Keller and Pinter, 2002). Nevertheless, in low to moderate seismic regions, such as the SW Iberian margin, a fault is considered to be active

if it has moved during the Quaternary epoch. Due to Northern Tunisia is a low to moderate seismic area, in this thesis we consider a fault as active if it has moved during the Quaternary Period, past 2.58 Ma according to ICS (2018)) (Keller and Pinter, 2002).

1.3.4. General concepts of seismicity

Processes involved in plate tectonics produce **stress** (force per unit area on a specified plane) and build up **strain** (deformation or rupture resulting from stress) in the rocks. When this stress exceeds the strength of the rocks, a rupture occurs (faulting) with the consequent releasing of energy in the form of an earthquake in the brittle domain.

An **earthquake** is a sudden motion or trembling in the Earth caused by the abrupt release of strain on a fault, with the consequent generation of seismic waves that cause the ground to vibrate (Yeats et al., 1997; Keller and Pinter, 2002). Although earthquakes are usually resulting from faulting, they can also be caused by explosions, volcanic activity or landslides.

Earthquakes can range in size from weak (that can not be felt by humans) to extremely violent (capable of generate large destruction and casualties). The **magnitude of an earthquake** is the number that characterizes this size (or strength) of an earthquake and it is determined from measurements on seismograms (measuring the energy released at the source of the earthquake). Different magnitude scales are defined and represent different ways of deriving magnitudes from the different information recorded on seismograms. Some of these scales are the local or Richter magnitude (ML), surface-wave magnitude (Ms), short and long period body-wave magnitude (mb and mB respectively) and moment magnitude (Mw). **Moment magnitude** is the most recent and commonly used scale and it is based on the earthquake's seismic moment (M_0), a measure of how much work an earthquake does to overcome the friction force (Kanamori, 1977; Hanks and Kanamori, 1979). The seismic moment measures the size of an earthquake considering the amount of slip, the fault rupture area and a factor for the strain encountered. Moment magnitude is commonly used worldwide for moderate to large earthquakes because (i) it can be easily estimated with modern instrumentation, (ii) it is directly linked to physical parameters, (iii) it can be independently calculated by geologic, geodetic and seismographic methods, and (iiii) it is the only magnitude scale that properly estimates the size of very large earthquakes (Yeats et al., 1997).

The **seismicity** (or seismic activity) of a given geographical location is the type, frequency and size of earthquakes experienced over a period of time (Keller and Pinter, 2002).

1.3.5. General concepts of seismic hazard

Faults are considered **seismic sources**, and the identification of seismic sources is the first step in evaluating the seismic risk. **Seismic risk** is the probability of damages and loses of exposed elements (people, property, or society) due to the occurrence of an earthquake or its effects and can be summarized with the further equation (Reiter, 1991):

Seismic risk = Seismic hazard * Seismic vulnerability (Figure 1.6).

Seismic hazard is the physical phenomenon itself and refers to the potential of earthquake-related natural phenomena and its expected periodicity. These phenomena can be the primary effects of violent ground-shaking motion that can be accompanied by surface rupture and permanent displacement but also liquefaction, landslading, tsunami generation or even fire (Yeats et al., 1997; Keller and Pinter, 2002) (Figure 1.6).

Seismic vulnerability has been used in different ways over time but it is a commonplace meaning: "being prone to or susceptible to damage or injury" (Wisner et al., 2003). Nevertheless, Wisner et al. (2003) propose a refine meaning in relation to natural hazards: "the characteristics of a person or group and their situation that influence their capacity to anticipate, cope with, resist and recover from the impact of a natural hazard" (Figure 1.6).

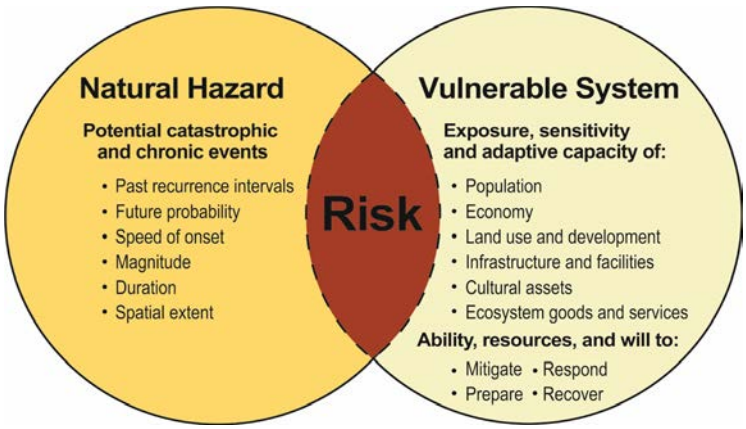

Figure 1.6. *Diagram representing the risk equation of natural hazards. Extracted from Wood, 2011.*

1.3.6. Geomorphology of continental margins

In this section we describe the general physiography of continental margins and the different marine geomorphological features that are found in the offshore North Tunisian continental margin. These include the following elements: Submarine canyons, Contourites and moats, Cold-water coral mounds, Pockmarks and Collapse pockmarks and Submarine landslides.

a) General physiography

Continental margins form the transition between oceans and continents and constitute one of the main domains of the oceanic floors together with deep-ocean basins and mid-ocean ridges. They cover about 28% of the oceans and can be defined in three different physiographic domains: the continental shelf, the continental slope and the continental rise which links with the abyssal plain (Figure 1.7) (e.g. Kennett, 1982). Nevertheless, the explored area of the North Tunisian continental margin differs from the typical scheme illustrated in Figure 1.7 and shows an extended continental margin with two main domains: the continental shelf and an extended plateau-slope system covering most of the whole explored region.

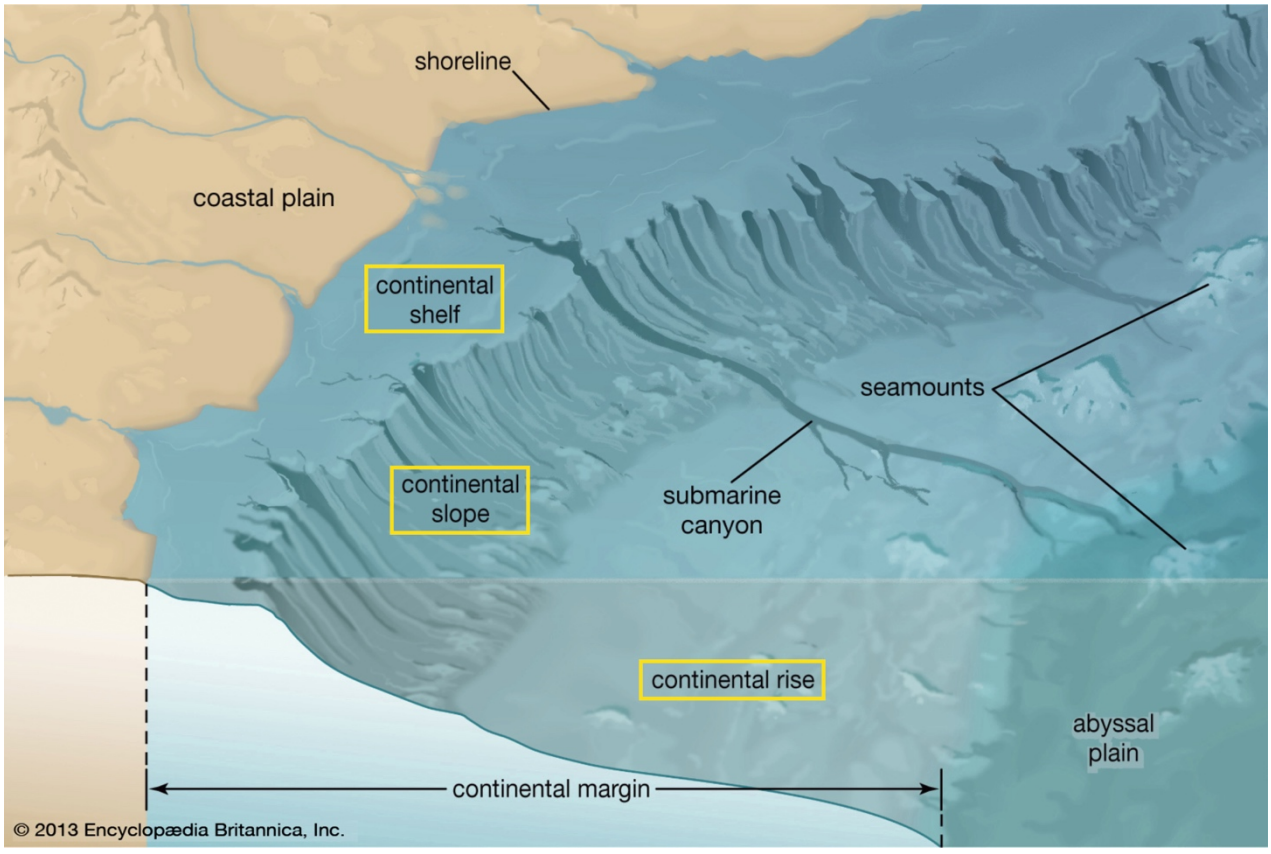

Figure 1.7. *Physiographic domains of continental margins (modified from Encyclopaedia Britanica, 2018).*

The three different physiographic domains of the continental margins are described below:

i) The **continental shelf** is the physiographic domain closer to the shoreline characterized by being submerged under relatively shallow waters typically extending from the coast to depths of about 100 to 200 m. It is also characterized by being inclined seawards with gentle gradients on the order of 0.5º. It varies considerably in width from almost being non-existent to about 1,500 km, corresponding to the Siberian shelf in the Arctic Ocean

(with a world average of about 80 km). Generally, it ends at its seaward border with an abrupt drop known as the shelf-break or shelf-edge. The present shelf-edges were formed about 18,000 years ago when sea-level stood at that level coinciding with the maximum extent of the ice sheets during the last glacial period (Gross and Grant, 1972; Kennett, 1982; Pinet, 2003).

ii) The **continental slope** is "the deepening seafloor out from the shelf-edge to the upper limit of the continental rise, or the point where there is a general decrease in steepness" (IHO, 2008). It dips into the ocean basins at average slopes of 2-4º although it can reach much steeper gradients locally. In fact, continental slopes can drop from the shelf-edge (at around 200 m) to depths typically of around 3000-4000 m over a distance of 100 km (Kennett, 1982). Another particular feature is that they are commonly indented by submarine canyons that act as transfer conduits of water and sediments.

iii) The **continental rise** is found between the continental slope and the abyssal plain and represents the final domain in the boundary between the continent and the deep ocean basins. It is formed by thick sediment accumulations coming from the continents and deposited at the base of the continental slope. It is marked by a gentle seaward slope that gradually decreases to that of the abyssal plain (Kennett, 1982). Continental rises are most commonly present in passive margins covering more than 27.1 million km^2 of them (while less than 2.3 million km^2 are found adjacent to active margins) (Harris et al., 2014).

b) Marine geomorphological features

Submarine canyons

Submarine canyons act as major transfer conduits of water and terrigenous sediments from the continents to the deep ocean basins (Figure 1.7). Most of them commonly commence at the mouth of large rivers, and branch out towards the shoreline. In other cases, submarine canyons are strongly controlled by tectonics and can be deflected along structural boundaries, thus adopting irregular pathways. They are one of the most studied and easily recognisable features of the continental margins and are characterised by steep walls, V- and/or U-shaped cross sections, straight to sinuous valleys and considerably irregular floors. Most canyons end to the base of the continental slope and extend seaward as channels into fan systems (Kennett, 1982). They can vary considerably in length with an estimated average length of 41.1 km. The largest submarine canyons are located in polar areas and use to twice the size of those in non-polar regions. The four largest canyons of

the Earth are located on polar slopes due to the influence of sediments derived from glaciated catchments during the Quaternary. The largest one is the Bering-Bristol-Pribylov Canyon complex that has an area of about 33,340 km^2 (Harris et al., 2014).

Contourites and moats

Contourites are "sediments deposited or substantially reworked by the persistent action of bottom-currents" (Figure 1.8) (Stow et al., 2002). Their geomorphology is mainly influenced by three factors: intensity of regional bottom-currents, sediment supply and seafloor topography (Faugères et al., 1993). Bottom currents are capable to construct large accumulations of sediments, known as contourite drifts. These contourite drifts usually develop elongated geometries parallel to the bottom-current flows and they can reach hundreds of kilometres long, be more than 100 km wide, up to 2 km thick and acquire reliefs up to 1,500 m above the surrounding seafloor. Lithology of contourite drifts does not differ much with respect to the pelagic and hemipelagic surrounding sediments. Regarding to the grain size, it is commonly fine size (silt and sand) but may be also gravel size. These deposits are also characterised by the occurrence of sedimentary structures related to bottom-current reworked sediments as traction structures including cross laminae and ripples. Contourite drifts are usually bounded on one or both sides by moats that are "channels parallel to the slope and originated by non-deposition and localised erosion beneath the core of the bottom current, accentuated by the Coriolis force" (Rebesco et al., 2014).

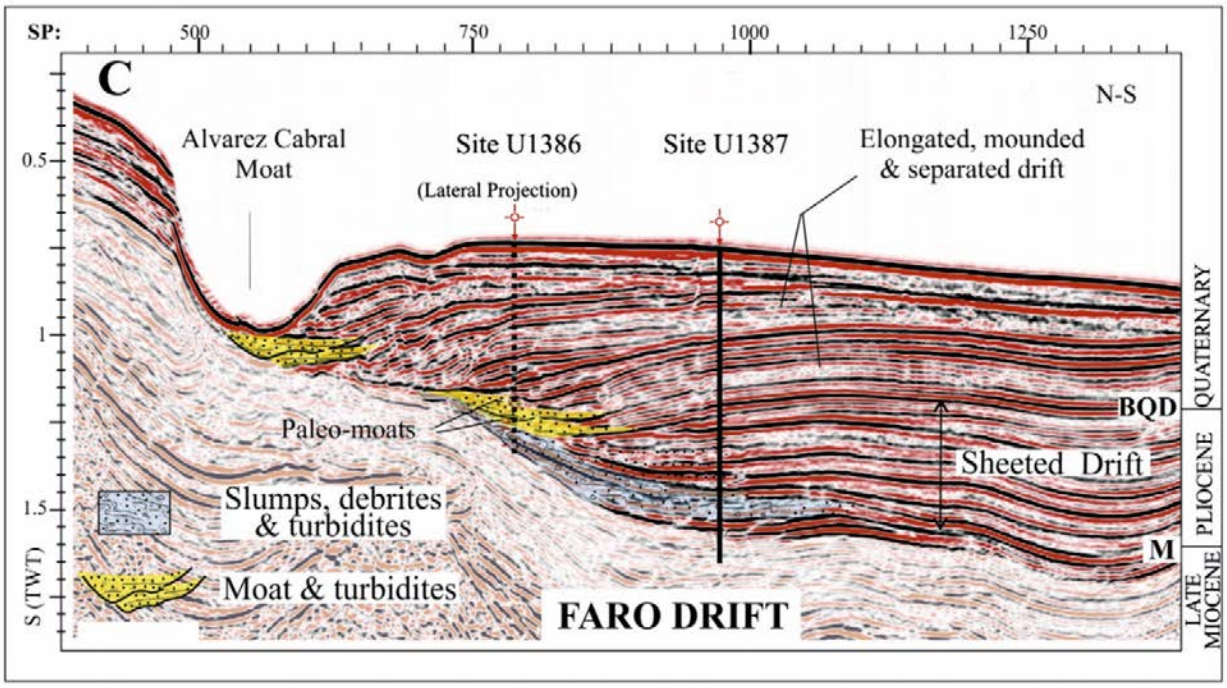

***Figure 1.8**. Example of a large contourite drift (seismic profile of the Faro drift in the Gulf of Cádiz margin). Extracted from Alonso et al. (2016).*

Cold-water coral mounds

Cold-water coral mounds (CWCM) are (bio)morphological features, from few to tens of meters high and up to few kilometres in length, formed through complex interactions between biological and geological processes under cyclic suitable hydrodynamic and oceanographic conditions (Figure 1.9). Their main composition typically consists of frameworks of reef forming cold-water corals (Madrepora oculata and Lophelia pertusa) supported by a matrix of biodetrital carbonate sediments (Wheeler et al., 2007; Roberts et al. 2009; Brooke et al., 2013; Nauman et al., 2014).

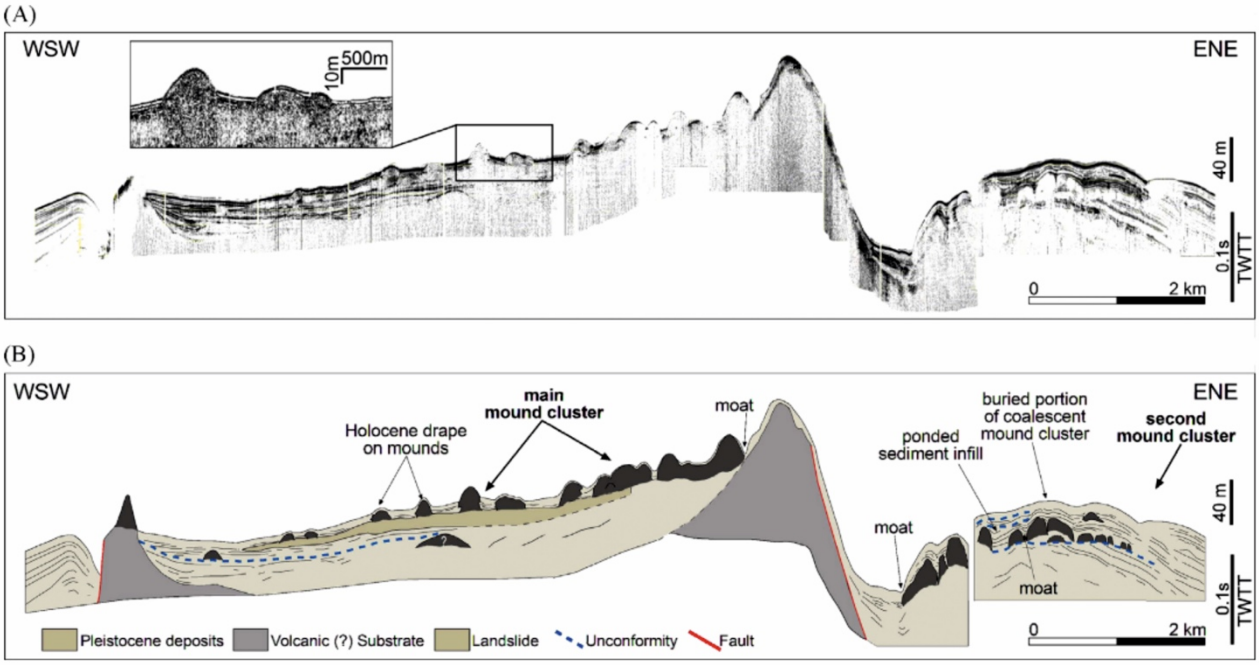

Figure 1.9. *Example of a cold-water coral mound field. A) Multiparametric seismic record of the West Melilla mounds; B) line drawing interpretation of the profile. Extracted from Lo Iacono et al., (2014).*

A CWCM is the geologic result of different periods and generations of reef development, sedimentation and erosion (e.g. Squires, 1964; Wilson, 1979; Roberts et al., 2009; Douarin et al., 2009). Mounds typically contain stratified sequences of reef deposits separated by fine to coarse sediments, which generally correspond to unsuitable environmental condition for coral growth, in some case corresponding to a contemporary increase of sedimentation rates (Lo Iacono et al., 2018). The cyclicity of reef growth stages operates on tens of thousands years, alternating to longer geological mound growth phases, operating at scales of few thousands up to hundreds of thousands (sometimes million) years (Monty et al., 1995 ; Hebbeln and Samankassou, 2015). After an initiation phase of small scale incipient mounds, there is a following rapid vertical mound growth, with cyclical reef development, providing the environments and processes to build larger mounds

(Squires, 1964; Wilson, 1979; Kano et al., 2007; Roberts et al., 2009; Huvenne et al., 2009; Douarin et al., 2014; Lo Iacono et al., 2018). On their tops CWCM may actually support contemporary reefs, coral graveyards or fine sediments draping and burying old coral frameworks (Guinan et al., 2000).

Pockmarks and Collapse pockmarks

Pockmarks are gas escape-related features corresponding to circular or sub-circular cone-shaped depressions, typically associated with sub-surface gas in fine-grained substrates along gas chimneys (Figure 1.10) (King and MacLean, 1970; Hovland and Judd, 1988; Judd and Hovland, 2007). They form when pockets of local over-pressured fluids erupt through the seafloor surface sediments and can represent relict morphologies related to past gas expulsion processes or can be active features, maintained by overpressured shallow fluids migration (Cathles et al., 2010; Moss et al., 2012). Pockmarks display a wide range of dimension, varying from tens of meters to few kilometers wide (giant pockmarks) and few meters to tens of meters deep. Their dimensions are generally related to the sediment texture: the finer the sediment the larger the size of the pockmark (Judd and Hovland, 2007).

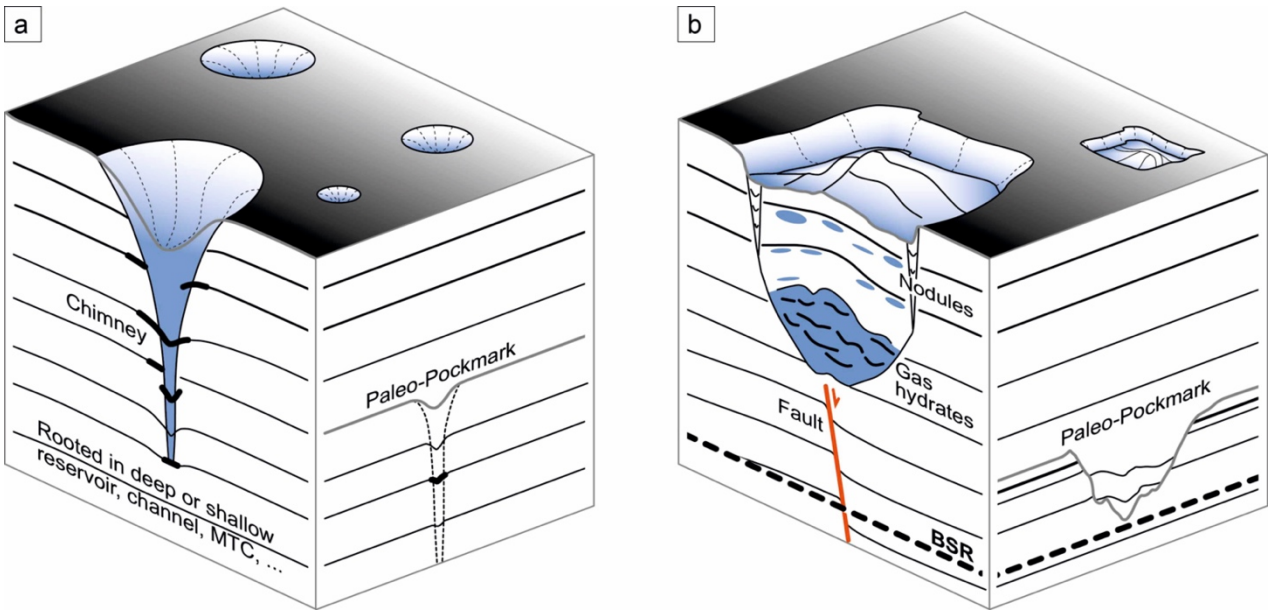

Figure 1.10. *Sketch showing geometrical characteristics of Pockmarks and Collapse pockmarks. a) pockmarks describing circular depressions associated to gas chimney; b: collapse pockmarks describing irregular and distorted depression and associated in this case to the presence of gas hydrates. Extracted from Riboulot et al. (2016).*

The control of tectonic activity on pockmark distribution has been suggested in several studies, with pockmarks aligned and coalescing along tectonic features representing preferential pathways for fluid expulsion (Pilcher and Argent., 2007). Linear pockmark trains have been observed in

correspondence of faults, with small pockmarks joining and coalescing in giant pockmarks (Pilcher and Argent, 2007), either can be randomly distributed, not showing any specific spatial pattern in their distribution (Pilcher and Argent, 2007, Ribolout et al., 2013). Nonetheless, pockmarks occurrence can also be related to different sub-seafloor features, such as buried channels, mud volcanoes, mud diapirs, glaciogenic deposits and landslides (e.g. Eichhubl et al., 2000; Pilcher and Argent, 2007; Andresen et al., 2011; Ribolout et al., 2013).

Other circular geological features have been identified in offshore Northern Tunisia and have been grouped within the term "**collapse pockmarks**". These collapse pockmarks are sub-circular to irregular shape depressions with a flat and/or irregular seafloor morphology and rimmed by an abrupt edge. Unlike the typical pockmarks, these pockmark-like features have been associated to several different collapse phenomena, such as the decomposition of gas hydrates of underlying sedimentary layers (e.g. Sultan et al., 2010; 2014), the dissolution of underlying rocks (e.g. Lofi et al., 2012; Bertoni et Cartwright, 2005), the evolution of pockmarks to more mature stages (e.g. Betzler et al., 2011), and the occurrence of pull-apart basins (e.g. Stewart, 1999) among others. Moreover, a particular feature of these kind of pockmarks is that usually show slid sediments coming from the rim.

Submarine landslides

Submarine landslides (or simply "submarine slides") are major methods of sediment transport down the continental slopes (Kennett, 1982). They deliver massive quantities of sediments to the continental rises and abyssal plains and constitute important phenomena in the shaping of continental margins (Bloom, 1978). A submarine landslide (as well as a subaerial landslide) occurs when the downwards driving stress (mainly gravity) exceeds the shear strength of the slope-forming material. Landslides have two main features, a failure surface and a displaced mass of sediments or rocks (Figure 1.11). The upper part of the failure surface is named headwall scarp (or slide scar) and it is an easily identifiable feature on the seafloor (Figure 1.11). A clear difference between subaerial and submarine landslides is the enormous size that the lasts can get. In fact, submarine landslides can have a significant hazard when generate a tsunami (Hampton et al., 1996).

Submarine landslides are triggered by different causes but rapid accumulations of thick sedimentary deposits, the slope of the seafloor, and high environmental stresses are the most common ones. These conditions tend to be located in certain environments, and therefore, submarine slides are common there: fjords, active river deltas, submarine canyon-fan systems, the open continental slope and volcanic islands and ridges. From all the different causes, earthquakes

are the main triggering factor of most submarine landslides (Hampton et al., 1996). In fact, in the Mediterranean Sea has been found that tectonically active margins present numerous but smaller landslides, while passive margins tend to display larger but fewer slides (Urgeles and Camerlenghi, 2013).

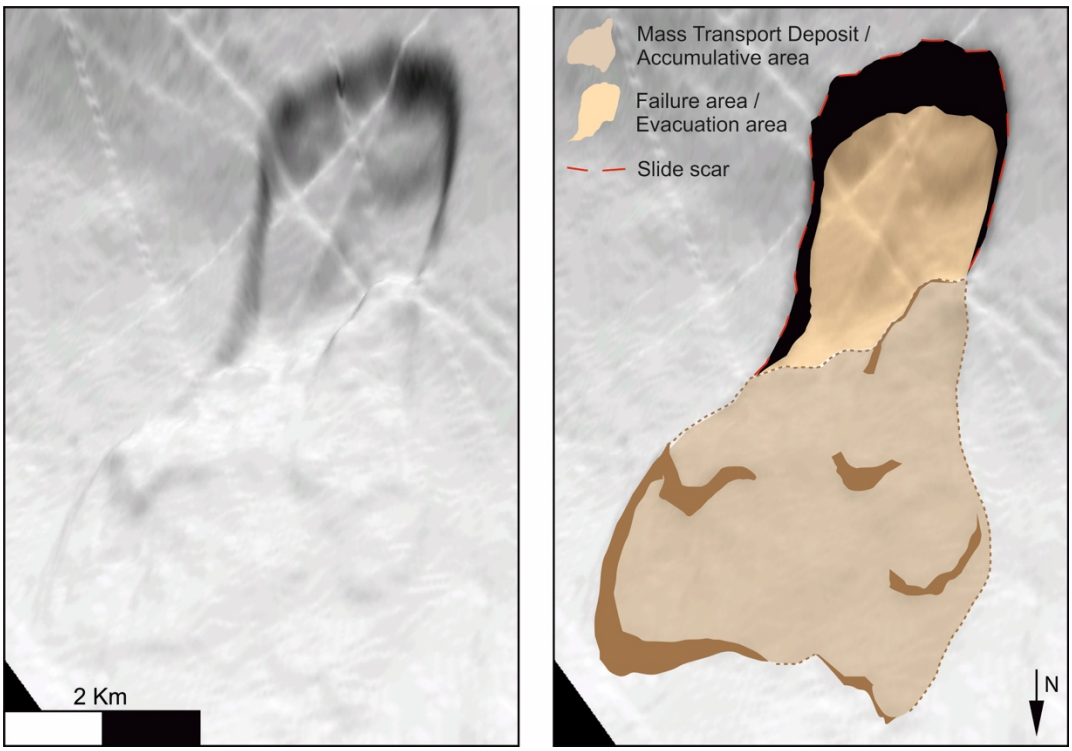

Figure 1.11. *Example of a submarine landslide. a) shaded relief map; b) interpretation highlighting different morphometric parameters. Modified from Rodriguez et al. (2017).*

CHAPTER 2

Geodynamic and geological setting

The study area of this PhD Thesis corresponds to the region extending across areas of the onshore and offshore Northern Tunisia including the continental margin (i.e. white polygons in Figure 2.1). This region extends from 7º30'W to 11ºE and from 35º30'N to 38º30'N, and it is located at the eastern sector of the Western Mediterranean. In the frame of the Mediterranean Sea context, the study area is located between the Algero-Balearic basin to the west, the Tyrrhenian Sea to the north, and the Sicily channel to the south-east, which further east connects to the Ionian Basin. Along the study area and surrounding regions runs the poorly defined boundary between the Nubia and Eurasian plates. The current plate boundary in Tunisia accommodates the NW-SE convergence between Nubia and Eurasia (~0.5 cm/yr) with deformation distributed in several tectonic structures extending across a large zone (e.g. DeMets et al., 1994; Sella et al., 2002; Calais et al., 2003; McClusky et al., 2003; D'agostino and Selvaggi, 2004; Serpelloni et al., 2007; Noquet, 2012).

2.1. Geodynamic setting

The geodynamic evolution of the North Tunisian Margin is associated to the complex development of the Western Mediterranean region, which is characterized by the opening of back-arc basins caused by slab rollback mechanisms with the consequent formation of mountain belts along subduction fronts (e.g. Rosenbaum et al., 2002; Spakman and Wortel, 2004; Schettino and Turco, 2011; Faccenna et al., 2014a). The evolution of the Western Mediterranean Sea as well as the geodynamic evolution and seismicity of Northern Tunisia within the Mediterranean context are explained below.

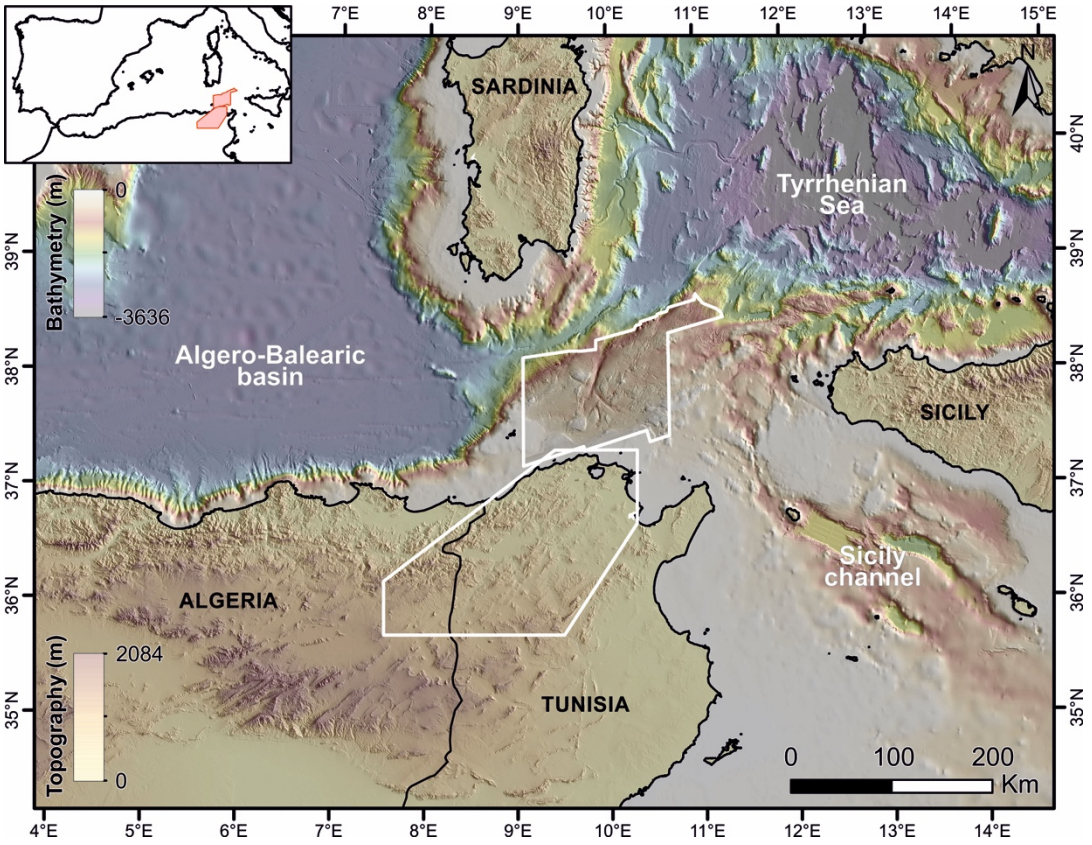

Figure 2.1. *Shaded bathymetric and topographic map of the central Mediterranean region. In white are represented the polygons corresponding to the two study areas of this work, offshore and onshore. Bathymetric data at 30 m grid-size has been acquired by our group during two cruises in 2013 and has been complemented by the EMODnet-HRSM compilation(EMODnet, 2018). Topographic data is from SRTM 30m grid-size from the National Aeronautics and Space Administration (NASA) and the National Geospatial-Intelligence Agency (NGA). Inset: Location of the two study areas represented by red polygons.*

2.1.1. Geodynamic evolution of the Western Mediterranean

The evolution of the Western Mediterranean has been debated since the 1980's when the first kinematic reconstructions were proposed (e.g. Rehault et al., 1984; Dewey et al., 1989). The models proposed were based on land geological field data, magnetic anomaly mapping studies, palaeomagnetism, volcanic geochemistry, seismic reflection and wide-angle data (Rehault et al., 1984; Dewey et al., 1989; Lonergan and White, 1997; Gueguen et al., 1998; Gelabert et al., 2002; Rosenbaum et al., 2002; Frizon de Lamotte et al., 2011; Faccenna et al., 2014a). The generally accepted evolutionary model to explain the opening of the Western Mediterranean basins since the Paleogene considers slab rollback as the main driving mechanism (e.g. Rehault et al., 1984; Schettino and Turco, 2006; Jolivet et al., 2009; Carminati et al., 2012; Faccenna et al., 2014a). Seismic tomography studies allowed to unveil the mantle structure of the imaged subducted slabs that have been included into existing geodynamic models (Wortel and Spakman, 2000; Spakman

and Wortel, 2004; Fichtner and Villaseñor, 2015; Mancilla et al., 2015; Villaseñor et al., 2015). These studies introduced fundamental concepts within the Western Mediterranean evolution: (i) slab detachment and lithosphere tearing, and (ii) fragmented slabs instead of a continuous one as opposed to early models. Although the models differ in some aspects and timing, the most accepted reconstruction of the Cenozoic evolution of the Western Mediterranean is summarized below (e.g. Faccenna et al., 2014a and references therein).

A compressional regime caused by the northward subduction of the Nubian plate under Eurasia led to the formation of mountain belts such as the Apennines, the Dinarides or the Betic-Rif orogens (Figure 2.2.a), but during subduction, slab rollback initiated and caused a change in the regional tectonic regime. This tectonic change occurred around 30-35 Ma (Figures 2.2.b and 2.2.c), and extension took over after compression in all the back-arc areas. Trenches started to retreat at cm/yr rates and previously thickened orogenic wedges collapsed . This new extensional regime led to the exhumation of high-temperature metamorphic rocks in extensional shear zones. In subduction zones, a high pressure-low temperature regime still prevailed. In the Western Mediterranean, this first stage of migrating trench zones towards the east caused the rotation of Sardinia, Corsica, the Balearic Islands and the Kabylies, which consequently opened the Valencia, Liguro-Provençal, Algerian and Alboran basins. In northern Africa, the opening of these basins was followed by the emplacement of the Kabylies block and thrust system onto the north African margin (Faccenna et al., 2014a and references therein).

The subsequent stage occurred after the Miocene (Figures 2.2.d, 2.2.e and 2.2.f), where trench retreat was associated to a progressive arching and bending of the arcs due to the reduced lateral dimension of the remaining retreating slabs. Moreover, in regions such as the Tyrrhenian or the Alboran basins, the lateral tearing of the slab led to the detachment of the subducting lithosphere from the continental plate, which triggered an acceleration of the trench retreat and rise of anorogenic volcanism. In the Western Mediterranean, this second stage was fundamental for the formation of the Alboran and Tyrrhenian basins. The Alboran basin was formed by the westward rollback of the subducting Alpine-Tethys oceanic lithosphere while the Tyrrhenian Sea opened by the east-southeastward rollback migration of the Apennines-Calabrian subduction front (Faccenna et al., 2014a and references therein).

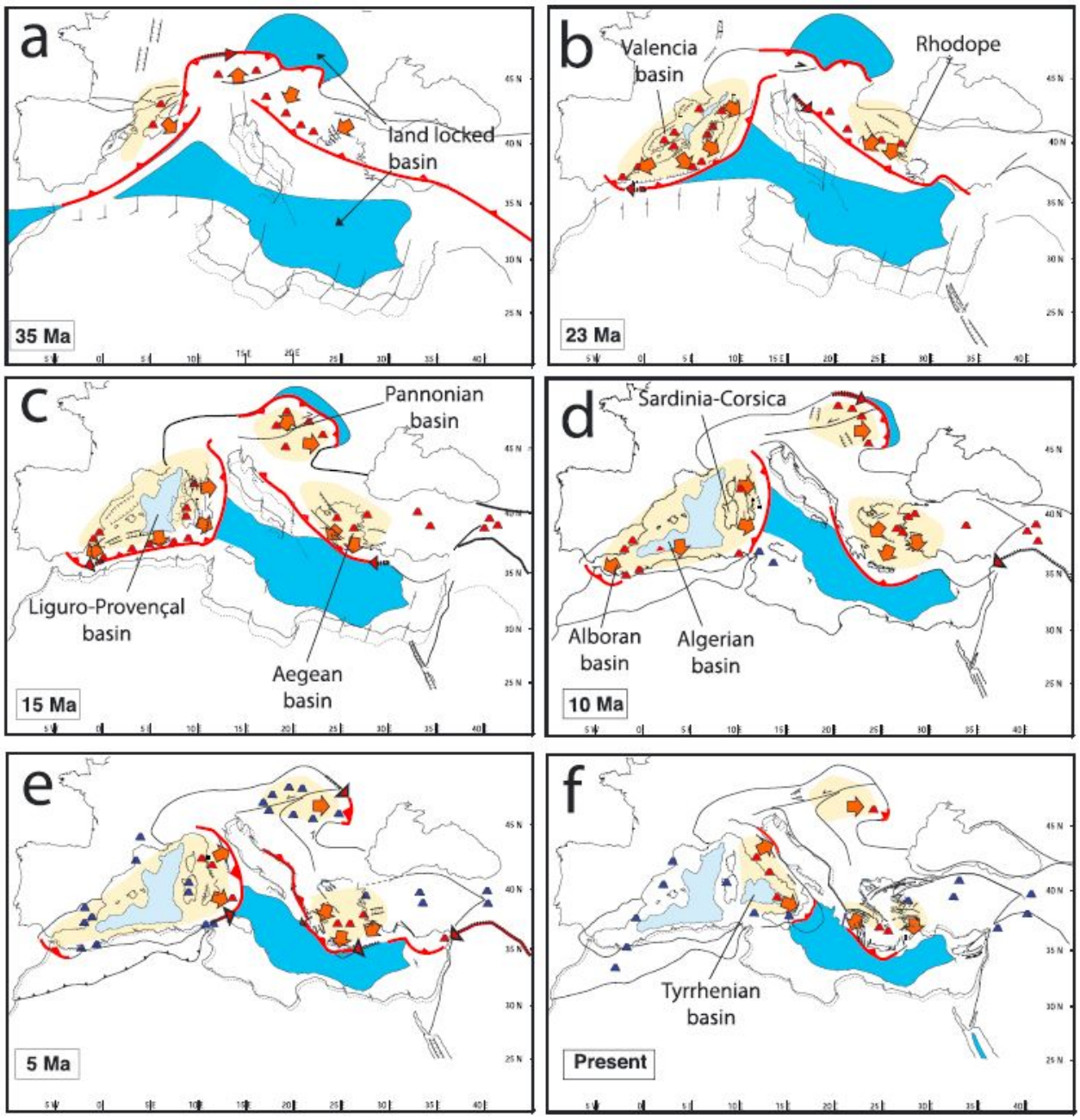

Figure 2.2. *Evolution of the Mediterranean region. Red lines indicate active subduction fronts. Red and blue triangles indicate calc-alkaline and anorogenic volcanoes, respectively. Pale yellow areas indicate areas of extension and orange arrows show the stretching directions (Faccenna et al., 2014a).*

2.1.2. The Northern Tunisian margin in the frame of the Western Mediterranean

The tectonic evolution of northern Tunisia shares common features with the mountain belts surrounding the Western Mediterranean, which since the Paleogene accommodated the shortening related to the northward subduction of the Nubian plate under the Eurasian plate (Wortel and Spakman, 2000; Faccenna et al., 2004; Booth-Rea et al., 2007; van Hinsbergen et al., 2014).

However, mantle tomography shows that the subducted Tethys lithosphere is segmented in the mantle in different slabs that lie under the Betics and Rif (Alboran slab), the Algerian Tell (west segment of the African slab), Tunisia (east segment of the African slab), and Calabria (Fichtner and Villaseñor, 2015) (Figure 2.3). Thus, each one of these belts is associated to particular tectonic features, having undergone an independent tectonic evolution at some stage, mainly caused by the development of Subduction Transform Edge Propagator faults (STEP faults) (Govers and Wortel, 2005), such as the Nekor and Crevillente faults in the Gibraltar arc (Mancilla et al., 2015) and structures to the south of the Tyrrehnian sea, such as the Malta escarpment in the Calabrian arc (e.g. Argnani and Bonazzi, 2005; Soumaya et al., 2015).

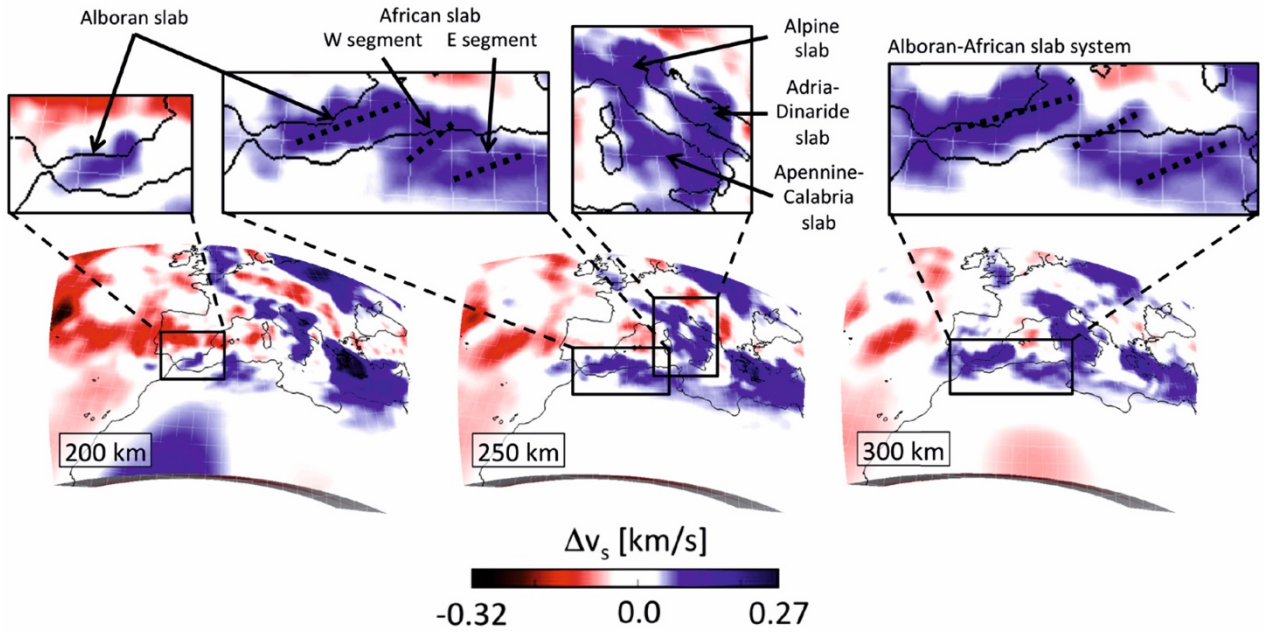

Figure 2.3. *Tomographic images of horizontal slices through the absolute variations of isotropic S velocity from 200 to 300 km depth. Up to three slabs can be identified along the North African margin, which are marked with dashed lines (Fichtner and Villaseñor, 2015).*

The tomographic images of the slabs under Algeria and Tunisia (Figure 2.4) indicate that they are detached from the base of the overlying lithosphere at ~150 km depth (Fichtner and Villaseñor, 2015). However, under SE Tunisia the slab may extend to shallower regions and be connected to the Nubia plate as suggested by the presence of a high-velocity reflector imaged by wide-angle refraction seismics in the mantle at 87 km depth, located under central Tunisia and slightly north of the southern Atlas deformation front (Research Group for Lithospheric Structure in Tunisia, 1992).

In Algeria, the slab rupture occurred during the Middle Miocene producing a post-collisional K-rich calc-alkaline magmatism dated at 17 Ma (Abbassene et al., 2016). Meanwhile, in Tunisia the rupture of the Calabrian slab, and the possible concomitant delamination of the African

continental mantle lithosphere (Roure et al., 2012) is constrained by calc-alkaline rhyolites dated between 14-8 Ma in Nefza and Galite islands and post-orogenic alkali basalts extruded at 8-6 Ma (Savelli, 2002; Decrée et al., 2014). After slab rupture, shortening continued in the region with the NW-SE convergence between Nubia and Eurasia, producing a southward propagation of the Tunisian Atlas belt, with an important component of left-lateral transpression (Melki et al., 2011) that continues at the present day (Soumaya et al., 2015). Furthermore, this late shortening produced the tectonic inversion of numerous extensional structures developed by slab rollback or slab rupture dynamics, including the Algero-balearic and Tyrrhenian basins (e.g. Kherroubi et al., 2009; Billi et al., 2011; Giaconia et al., 2015).

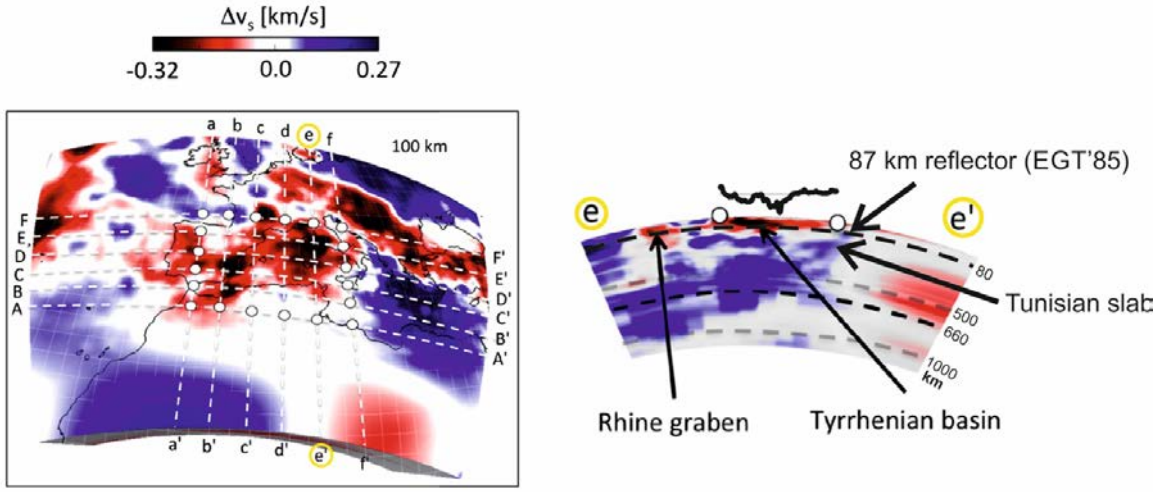

Figure 2.4. *Left: Tomographic model of the Atlantic-Mediterranean region. Right: N-S cross-section (e-e') across North Africa, Tunisia and Western Tyrrhenian basin showing the Tunisian slab and the location of the 87 km depth intra-mantle reflector detected by the EGT'85 seismic refraction experiment (Fichtner and Villaseñor, 2015; Research group for lithospheric structure in Tunisia, 1992).*

2.1.3. Seismicity and kinematics of Northern Tunisia

The distribution of shallow (<30 km deep) tele-seismic seismicity in the western Mediterranean defines different regions with variable recorded earthquake activity. This seismicity represents crustal zones that apparently accommodate the Nubia-Eurasia convergence on faults with diverse amount of deformation (Figure 2.5) (Ambraseys, 1962; Serpelloni et al., 2007; Nocquet, 2012; Soumaya et al., 2015). In western Mediterranean, such in the Gibraltar Arc, there is a sparse seismicity following the arc geometry between Africa and Iberia, with earthquakes of low to moderate magnitude that do not define a clear pattern of lineaments (Figure 2.5). In fact, a diffuse deformation zone is interpreted across a suite of faults characterized by dominant strike-slip focal mechanisms.

To the east, in the Algerian Margin, seismicity is grouped along a narrow belt that spans across the continental slope within a ~150-km-wide band parallel to the coast (e.g. Serpelloni et al., 2007; Beghoul et al., 2009; Meghraoui and Pondrelli, 2012; Nocquet, 2012) (Figure 2.5). In this region, thrust-fault mechanisms prevail with nodal planes roughly parallel to the main topographic reliefs (Figure 2.6). In northern Algeria, earthquake magnitudes are the highest along the north Africa mountain belt, reaching > M_w 7 in the areas between El Asnam and Algiers, with a recent offshore earthquake of M_w 6.8 in Boumerdès in 2003 (Ambraseys, 1981; Ouyed, 1981; Meghraoui et al., 1996; Bouhadad et al., 2004; Braunmiller and Bernardi, 2005; Déverchère et al., 2005; Kherroubi et al., 2009; Yelles-Chaouche et al., 2017). Eastwards, in eastern Algeria, seismicity covers a wider region although it is mainly grouped along the southern Tunisian Atlas, mostly dominated by strike-slip focal mechanisms (Figure 2.6).

The transition from north Africa to the north Sicily well-defined band of thrust focal mechanisms occurs across Tunisia. However, in Tunisia, instrumental seismicity is scarce and with mainly low-magnitude teleseismic earthquakes, so that few focal mechanisms have been determined for our study region (Gueddiche et al., 1998; Pondrelli et al., 2006; Bahrouni et al., 2014; Ksentini and Romhdane, 2014; Ousadou et al., 2014; Soumaya et al., 2015). Offshore, the northern continental platform extending from Tunisia has little instrumental seismicity recorded, and only towards eastern Tunisia (in the Gulf of Hammamet) and southern Sicily (in the Pelagian block) some few focal mechanisms have been computed (with prevailing thrust and strike-slip mechanisms respectively) (Soumaya et al., 2015) (Figure 2.6).

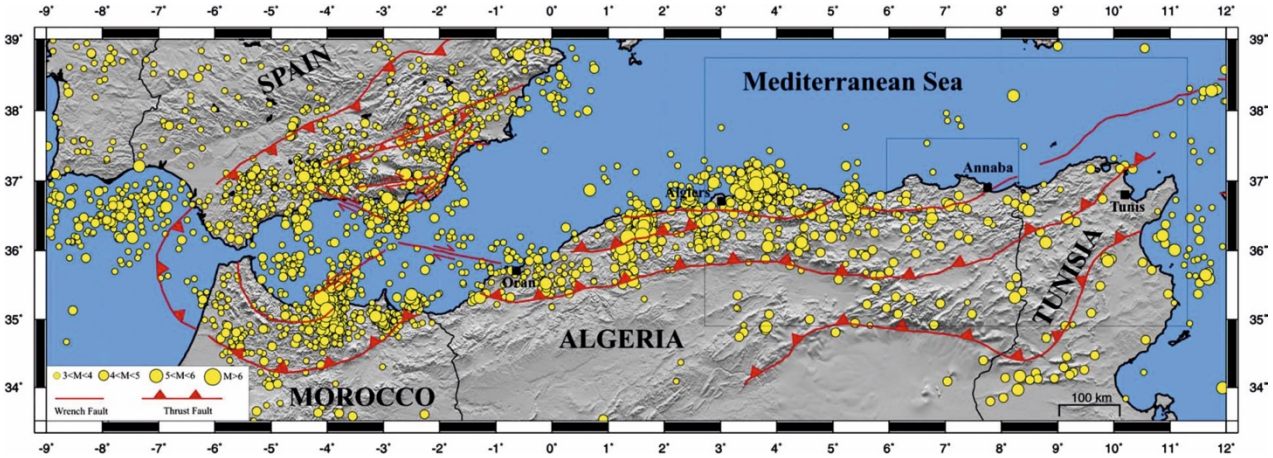

Figure 2.5. *Instrumental seismicity distribution (yellow dots) of the Ibero-Maghrebian region within the Nubia-Eurasia plate boundary. Magnitudes range from M_w 3 to M_w > 6 obtained from the NEIC catalogue (The National Earthquake Information Center - USGS). The main faults and mountain belts are depicted in red. Modified from Kherroubi et al. (2009).*

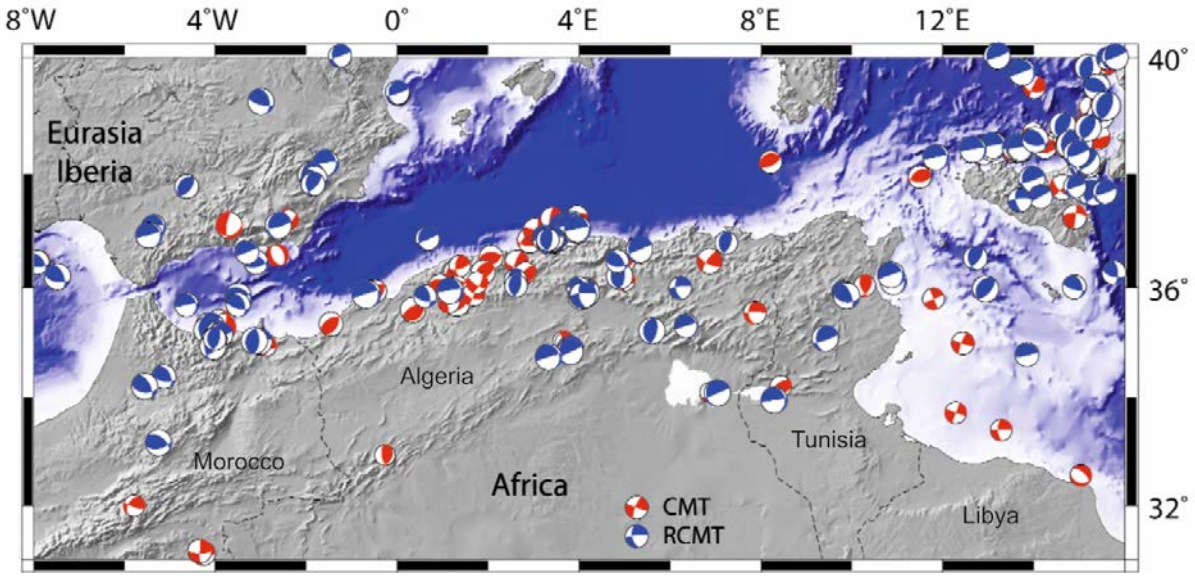

Figure 2.6. *Topographic and bathymetric map of the Western Mediterranean area, at the boundary between Eurasia and Africa with the focal mechanisms distribution on the Ibero-Maghrebian region. Moment tensor solutions in red are from the Global CMT (Global CMT, 2015) and in blue are from the RCMT (RCMT, 2015). Modified from Meghraoui and Pondrelli (2012).*

According to different geological and geodetical works, the Nubia-Eurasia convergence has a main NW-SE orientation with the displacement vectors adopting more E-W trends towards the Atlantic Ocean (e.g. DeMets et al., 1994; Sella et al., 2002; Calais et al., 2003; McClusky et al., 2013; D'agostino and Selvaggi, 2004; Serpelloni et al, 2007; Noquet, 2012) (Figure 2.7). Furthermore, there is little variation in convergence rates along the boundary ranging from 4.7 ± 1 mm/yr in the Gibraltar arc to 5.5 ± 1 mm/yr in NW Sicily (Serpelloni et al., 2007). The slow NW-SE convergence rate in Tunisia, of ~0.5 cm/yr, (e.g. Serpelloni et al, 2007) (Figure 2.7), results in low to moderate magnitude seismicity (Gueddiche et al., 1998). Instrumental seismicity in the period from 1920 to 2010 recorded magnitudes ranging from M_w 2 to M_w 5.5 (Ksentini and Romhdane, 2014) (Figure 2.5) with mainly strike-slip and thrust moment tensor solutions for the Northern Tunisian region (Soumaya et al., 2015). However, historical records describing the destruction of Roman and Arabic settlements support higher magnitude seismic events from which intensities of VIII to X on the MSK scale have been estimated (e.g. Ambraseys, 1962; Vogt, 1993; Mejri et al., 2010; Bahrouni et al., 2014; Ksentini and Romhdane, 2014) (Figure 2.8). The most relevant occurred i) in Utica in 412 A.D. with coseismic ground fractures and aftershocks that lasted for one week; ii) in Kairowan (North Tunisia) in 854 A.D. with thirteen villages destroyed; iii) in Tunis in 856 A.D. with ~45.000 casualties and with an estimated moment magnitude (M_w) of 6.8; and iv) in Tunis in 1758 A.D., with numerous houses destroyed and thousands of victims (Ksentini and Romhdane, 2011; 2014).

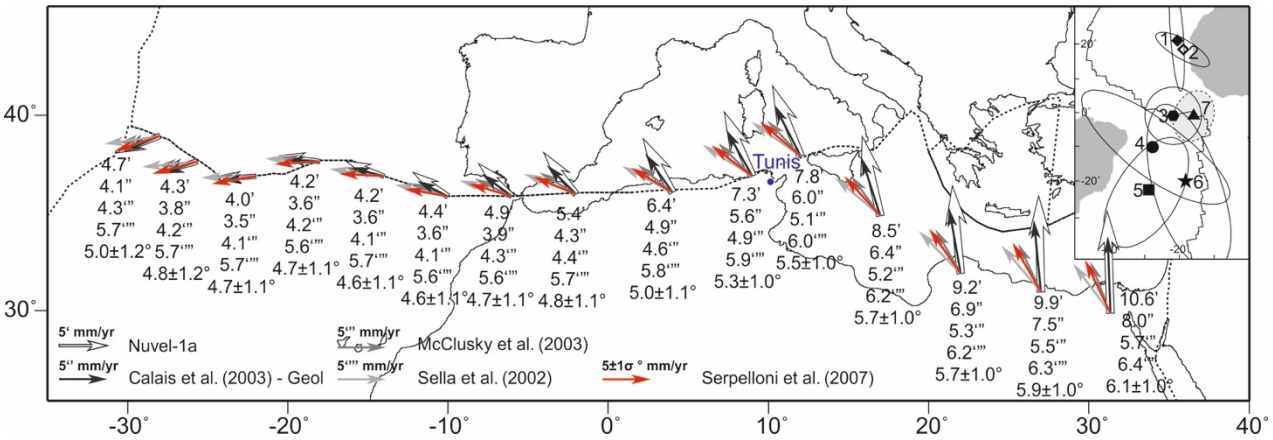

Figure 2.7. *Africa-Eurasia kinematic boundary conditions predicted by geological and geodetical data derived relative to Euler poles, along a simplified plate boundary (dashed line). Arrows and numbers show the displacement vectors and rates (in mm yr^{-1}) of the African plate with respect to the Eurasian plate. Inset: Location and error ellipses (at 95% confidence level) of Africa (Nubia)-Eurasia rotation poles from: (1) Nuvel-1A (DeMets et al. 1994); (2) Calais et al. (2003), geological model; (3) McClusky et al. (2003); (4) Calais et al. (2003), geodetic model; (5) D'Agostino and Selvaggi (2004); (6) REVEL (Sella et al. 2002), and (7) Serpelloni et al. (2007). Modified from Serpelloni et al. (2007).*

Figure 2.8. *Examples of historical Roman and Arabic ruins deformations and diagram of stress tensors in Tunisia. Affected Roman constructions (A: Bella Rugia, B: Enfidha, C: Monastir); Roman–Arab constructions (D1, D2 Cherichira aqueduct). Modified from Bahrouni et al. (2014).*

2.2. Geological setting of Northern Tunisia

Northern Tunisia corresponds to the easternmost part of the Maghrebian chain that in turn belongs to the southern belt of the Peri-Mediterranean Alpine System, which records a complex Cenozoic evolution (i.e. the Maghrebides Chain extends from the Strait of Gibraltar to Tunisia). Offshore, this fold-and-thrust belt extends and links towards the Sicilian-Apenninic chain (Tricart et al., 1994; Catalano et al., 2000; Sulli, 2000; Euchi et al., 2004; Mauffret, 2007; Belayouni et al., 2010, 2012; Melki et al., 2012; Roure et al., 2012). Next, the geological setting of both onshore and offshore Northern Tunisia is described.

2.2.1. Geological setting onshore

Geologically, onshore Northern Tunisia can be broadly divided in two main areas: the Tellian and the Atlas domains (Figure 2.9). The Tellian domain crops out to the northwest and is characterized by the Flysch sediments of the Tethyan oceanic crust (the Numidian Flysch nappes) overthrusting the allochtonous nappes of the north-Mahgrebian Mesozoic to Early Miocene passive margin (the Tellian external nappes), following a NE-SW trend (Figure 2.9). The underlying Atlas domain corresponds to the foreland thrust belt, which deforms the sedimentary cover of the north Maghrebian Triassic to Neogene passive margin (Figure 2.9) (Rouvier, 1977; Khomsi et al., 2009; Melki et al., 2010; 2011). Aside from these main domains, some authors also define a central domain characterized by the location of Triassic salt domes (Triassic dome zone; Figure 2.9). This domain corresponds to the northernmost sector of the Tunisian Atlas foreland following a NE-SW trend narrow region, which parallels the front of the Tellian external nappes (Piqué et al., 2002; Khomsi et al., 2009; Belayouni et al., 2012). Furthermore, the Tunisian Atlas domain is also bounded by the stable Saharan Platform (Saharan Platform zone) to the south that represents the undeformed African foreland (Bouaziz et al., 2002; Belayouni et al., 2012). The Internal Nappe (Internal Zone in Figure 2.9.b) is absent in the onshore Northern Tunisia but occurs offshore (see Section 2.2.2). The tectonostratigraphic units cropping out onshore Northern Tunisia are described below, from west to east:

i) The Tellian domain: Numidian Flysch Nappes

The Numidian Flysch Nappes occur at the north-westernmost region and are made of eastward-verging folded and thrusted units composed of Oligocene to Burdigalian rocks. This formation is characterized by allochthonous siliciclastic turbidite deposits, derived from the Tethyan oceanic crust, and composed of Numidian sandstones and related clayey successions (as also occurs along

the Maghrebian Chain) (Belayouni et al., 2012, 2013; Riahi et al., 2015; Booth-Rea et al., 2018) (Figure 2.9.b).

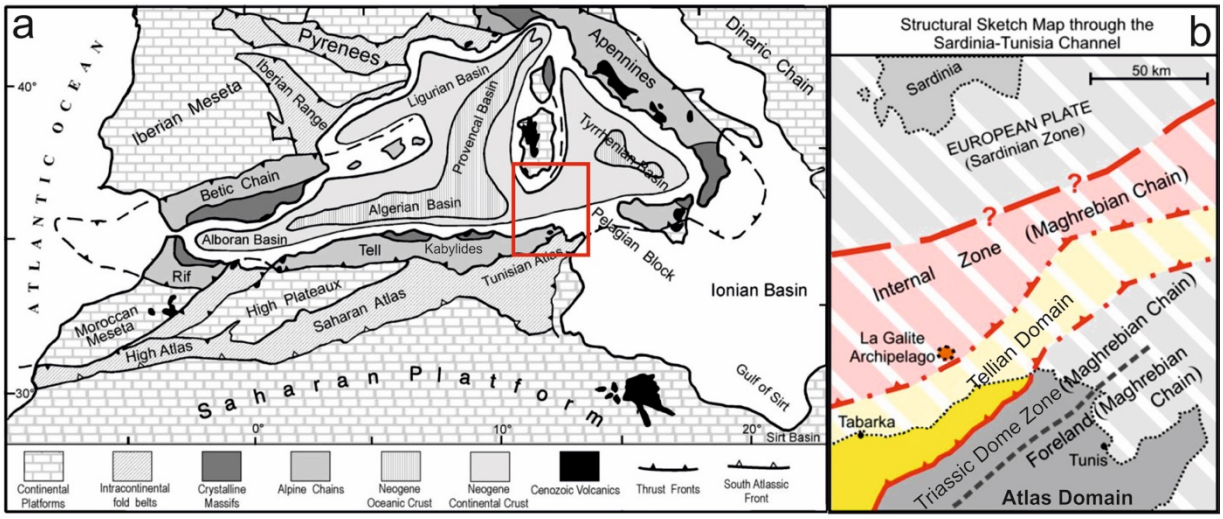

Figure 2.9. *a) Tectonic pattern of the western Mediterranean showing the main platforms, fold belts, crystalline massifs, alpine chains, Neogene oceanic and continental crusts, and Cenozoic volcanism. b) Structural sketch map of onshore and offshore Northern Tunisia and Sardinia areas (location in Figure in 2.8a). Modified from Bouaziz et al. (2002) and Belayouni et al. (2010).*

ii) The Tellian domain: Tellian external Nappes

The Tellian external Nappes (para-autochtonous nappes) are tectonically sandwiched between the allochthonous Numidian Flysch Nappes and the autochtonous Atlas sediments. These units include a complex sedimentary sequence ranging Triassic to Langhian in age, characterized by important omissions and variations in lateral thickness. The competent materials within these units are Eocene and Cretaceous limestones occurring discontinuously and embedded between an underlying Triassic gypsum-dolostone detachment and overlaid by Palaeocene and late Eocene clays (Belayouni et al., 2012, 2013; Booth-Rea et al., 2018) (Figure 2.9.b).

iii) The Atlas domain

These units correspond to the autochthonous Tunisian paleomargin sediments from the Atlassic foreland, which spans from Triassic to Langhian ages. At the western sector of this domain, elongated Triassic outcrops dominate NE-SW gentle folded structures. This western zone is commonly known as “Triassic dome zone” or “Tunisian trough”, and its southern boundary is marked by the Teboursouk-Fej el Hadoum alignment (ETF alignment in Figure 2.10). Towards the east, the Atlas domain is mainly composed by gentle folds and few thrusts with a base often injected

by Triassic evaporites (i.e. gypsum, slates, carbonates and multicolour sandstones) (Piqué et al., 2002; Khomsi et al., 2009; Belayouni et al., 2012; Booth-Rea et al., 2018) (Figures 2.9.a and 2.9.b).

a) Stratigraphy

Sediment units spanning from Mesozoic until present occur in northern Tunisia (Figure 2.10) (Melki et al., 2012). Gypsum, clays, carbonates and multicolor sandy facies with chaotical structures characterise **Triassic** units. These units often act as a detachment level of the thrust faults and present tectonic contacts with other formations in northern Tunisia. **Jurassic** sedimentary units are characterized by calcareous facies with some marly intercalations typical of deep-sea environments. **Cretaceous** sediments crop out mainly in northern Tunisia and consist of fossiliferous marls and clays with micritic limestone intercalations and sandy and quartzitic recurrences. These sediments were deposited in a subsiding marine environment.

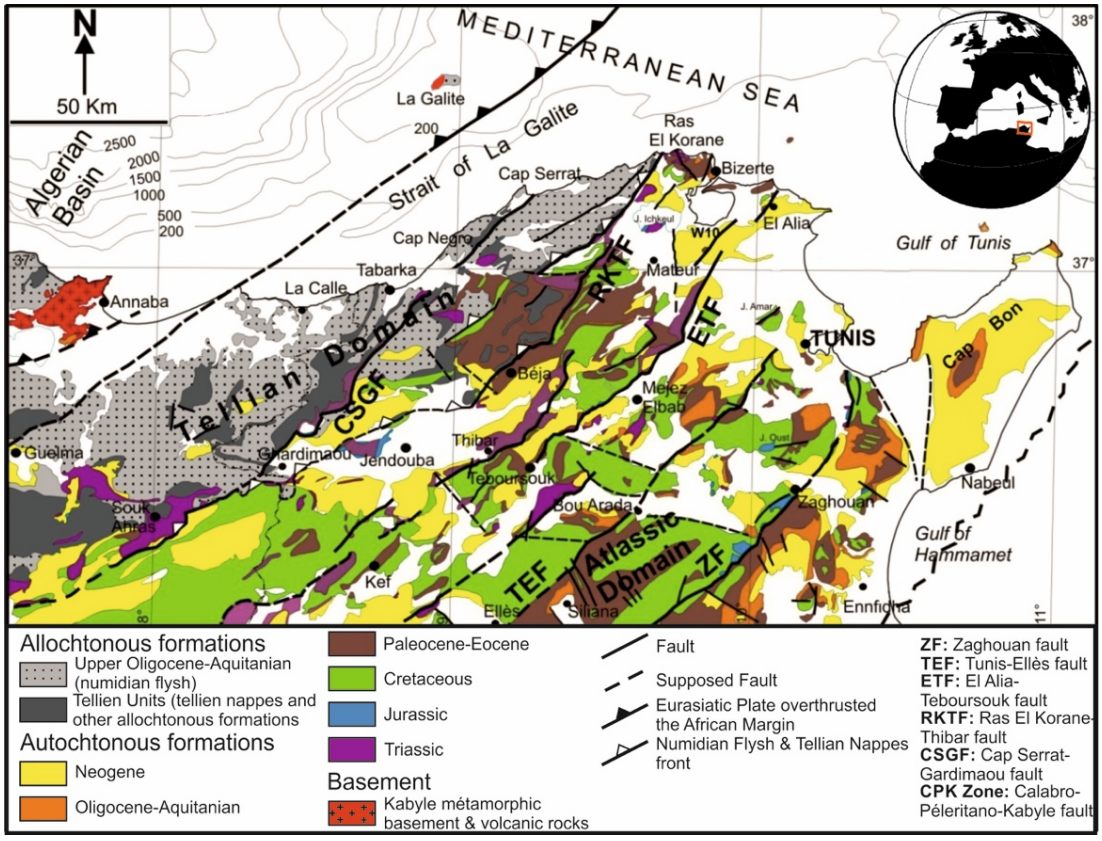

Figure 2.10. *Geological map of northern Tunisia, including the allochthonous and autochthonous formations, the basement and the main fault systems (modified from Melki et al., 2012).*

Paleocene-Eocene sediments crop out in northern Tunisia and are represented by a monotonous brown argillaceous package. These argillaceous deposits present a lithological succession with marls and limestone intercalations. Eocene sediments are formed by carbonate series of early Eocene age that produce positive reliefs above other softer units. Oligocene-

Aquitanian rocks form the north-western succession of the Numidian Flysch. This formation is characterized by allochthonous turbidites that include clays at the base and sandstones and shales at the top. The south-eastern basins of northern Tunisia contain sandy, clayey and carbonated facies indicating a shallow marine to fluvial environment.

During the **Miocene**, limestone bars were deposited above conglomerate facies in the Gulf of Tunis, indicating the beginning of a transgression period. Following strata are composed of clays, silts and occasionally of sandy limestones at the base and marls and salts at the top. Deep-marine green clays rich in microfauna were deposited in eastern Tunisia during the late Miocene, capped by regressive continental series at the top. Coastal and offshore areas are represented by thick series composed of clays, sandstones and lignite alternations characterizing an internal shelf depositional environment.

During the **Pliocene**, marine sediments were deposited along the eastern coast of Tunisia with argillaceous and sandy-fossiliferous series. On the other hand, early Pliocene continental clays and sandstones occur towards the west. The late Pliocene is essentially represented by sandy series.

Quaternary sediments mostly occur along current valleys of northern Tunisia and are fluvial terraces, alluvial fans or colluvial covers together with lacustrine sediments in some particular regions (Figure 2.10). Some of the Plio-Quaternary fluvial terraces are found abandoned and raised from their original location and usually show rounded pebbles with poor cementation. Bannour and Bonvallot (1988) proposed that Quaternary diapiric dynamics deformed and raised up some alluvial terraces of the Medjerda River, nevertheless, the geometry and distribution of folds occurs strongly controlled by pre-existing structures what suggest that Quaternary contractional deformations does not promote diapirism (Masrouhi et al., 2014). These Quaternary deposits are represented by continental facies composed of gravels, clays, sands and silts. Marine and aeolian deposits crop out also along the northern and north-eastern littoral of Tunisia.

b) Structural setting

The main structures in northern Tunisia are large sinistral to reverse NE-SW faults and their associated folds (Figure 2.11). These faults use the Triassic evaporites as detachment level and produce positive reliefs following the general NE-SW regional topographic trend. Deformation in both the Tellian and Atlas domains shows a transpressive component with the development of large NE-SW sinistral-reverse strike-slip structures, like the Cap Serrat-Gardimaou, Ras El Korane-Thibar, El Alia-Teboursouk, Tunis-Ellès and Zaghouan faults (Figure 2.11) (Melki et al., 2012).

Moreover, there are also conjugate dextral and normal NW-SE to WNW-ESE trending faults (Zargouni, 1978; Melki et al., 2010; Zouaghi et al., 2011).

The phase of present-day active deformation in northern Tunisia started around the Upper Pliocene, related to the north-westward motion of Nubia relative to Eurasia. This process caused the uplift of the Atlas and reactivated pre-existing faults (McClusky et al., 2003; Serpelloni et al., 2007). WNW-ESE trending faults were reactivated by a reverse dextral motion, while the NE-SW trending ones were reactivated with pure to oblique reverse motion. This reactivation generated new folds with NE-SW trending axes (Mejri, 2010; Alyahyaoui and Zouari, 2014). Moreover, the south-western boundary of the Tunisian Atlas is delineated by large NW-SE trending dextral structures, like the Gafsa and Tozeur-Negrine faults (Zargouni and Ruhland, 1981; Ben Hassen et al., 2014).

Concerning the large-scale crustal structure of Tunisia, the Moho discontinuity deepens towards the south, from depths of approximately 21 km near the north coastline to a maximum depths of 37 km near the southern deformation front. However, in NE-SW direction the Moho discontinuity depth is uniform (Research Group for Lithospheric Structure in Tunisia; 1992).

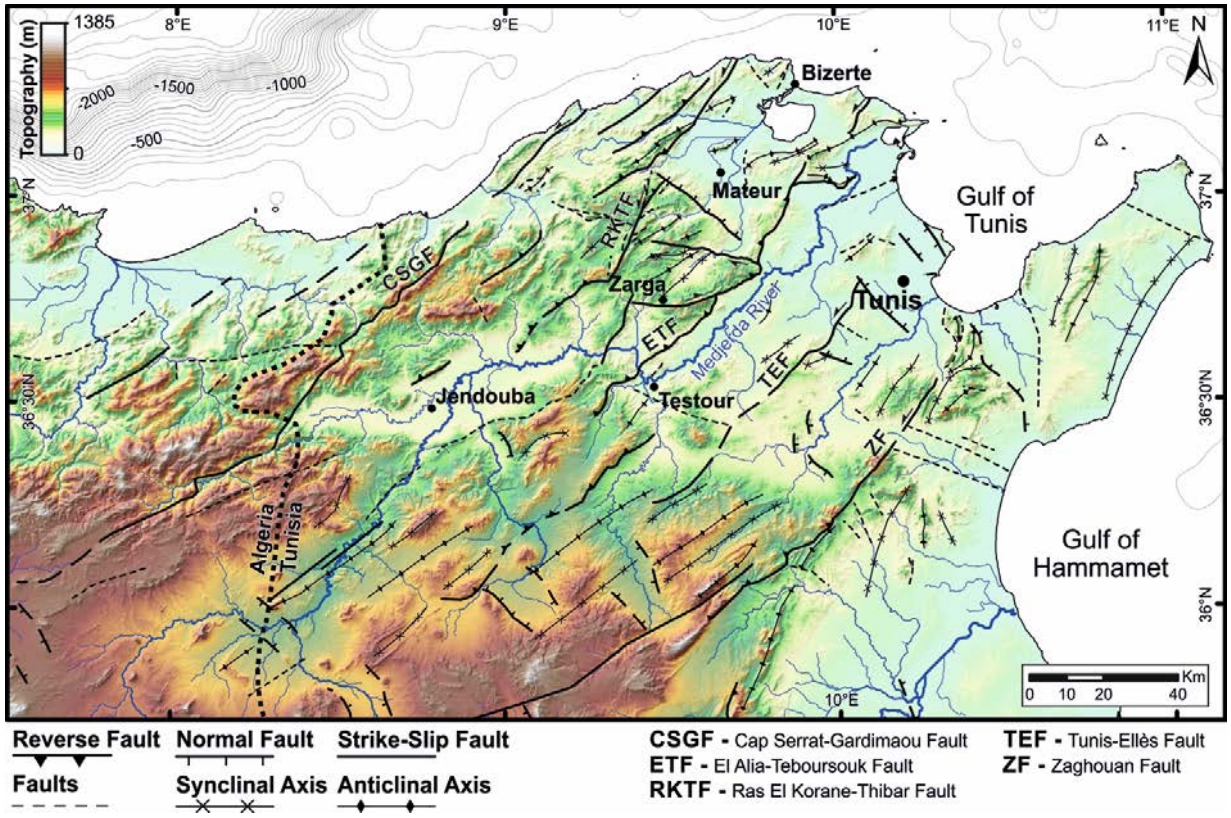

Figure 2.11. *Topography of northern Tunisia with the main tectonic structures (i.e. reverse, normal and strike-slip faults) and the drainage system. The main trunk corresponds to the Medjerda River. Tectonic structures include data from Melki et al. (2012), Bahrouni et al. (2014) and Rabaute and Chamot-Rooke (2015) as well as our own data.*

c) Geomorphological setting

The main geomorphological features of northern Tunisia are NE-SW oriented ranges with their respective associated valleys (Figure 2.11). In some locations, the drainage network shows rectangular patterns and river deflections that may reflect major lithological or tectonic boundaries. The Medjerda River is the largest catchment of Tunisia and drains an area of ~23,340 km^2. It runs as an axial valley 400 km from eastern Algeria to the Gulf of Tunis in a SW-NE direction, parallel to the main faults and folds of northern Tunisia. The source of the Medjerda River lies in Algeria at 1300 m in a semi-arid region of the Atlas system (Delile et al., 2015). According to Faust et al. (2004), the current climate corresponds to the Mediterranean subtropics (with a transition from Mediterranean semiarid, corresponding to the southern Algerian region, to semihumid conditions, corresponding to the northern Tunisian region). Furthermore, although morphodynamic changes through the floodplain sediments of the Medjerda have been described (and have been related to North Atlantic Bond events), the Quaternary sedimentation of the river seems to have taken place under rather stable circumstances allowing to develop well-stratified layer sequences (Faust et al., 2004; Zielhofer and Faust, 2008). The tributaries of the Medjerda River drain areas ranging from 54 to 2,564 km^2 and running from 8.5 to 163 km long, and show two preferential orthogonal flow directions, NE-SW and NW-SE. Clearly and entirely transverse catchments to the main geological grain are short and only developed across the present deformation front, draining to the Gulf of Hammamet (Figure 2.11).

The topography of Tunisia is relatively smooth with heights below 1,385 m and gentle slopes of about 6º. The highest elevations in the region occur at the Medjerda headwaters in eastern Algeria with heights up to 1770 m. The landscapes are mainly fluvial, with rivers with meandering shapes and locally incised reaches. Large lacustrine zones mostly occur towards the east and an east-west line at the northern edge of the Saharan platform where the lowest point in Tunisia (-17 m) occurs coinciding with the salt lake of Shatt al Gharsah.

2.2.2. Geological setting offshore

The explored region in the offshore Northern Tunisian continental margin is part of the north Africa collisional fold-thrust belt system and represents the offshore link between the Maghrebian and the Sicilian-Apenninic chains (e.g. Mascle et al. 2001; 2004; Belayouni et al., 2010). It shows NE-SW trending structures made up of a stack of SE-verging thrust sheets, which are an extension of the structures observed in onshore northern Algeria and Tunisia (e.g. Catalano et al., 2000; Tricart

et al., 1994). In fact, the internal nappe derived from the collision between the microplate detached from Pangea during Late Jurassic to Early Cretaceous (the "Mesomediterranean Microplate" or "Alkapeca", an acronym from the initial letters of Alboran Domain and the main internal massifs of the Kabylian in Algeria, Peloritain in Sicily and Calabria), and the Meso-Cenozoic north Africa paleomargin is absent in Northern Tunisia and it is found submerged offshore. La Galite archipelago (Figure 2.12.c) has been considered to be above crystalline basement belonging to the Alkapeca internal zone (Tricart et al., 1994; Bouillin et al., 1998). This internal domain laterally crops out in northern Algeria (Kabylides units) and in the Calabria-Peloritain Arc (Belayouni et al., 2010; 2012; Decrée et al; 2014).

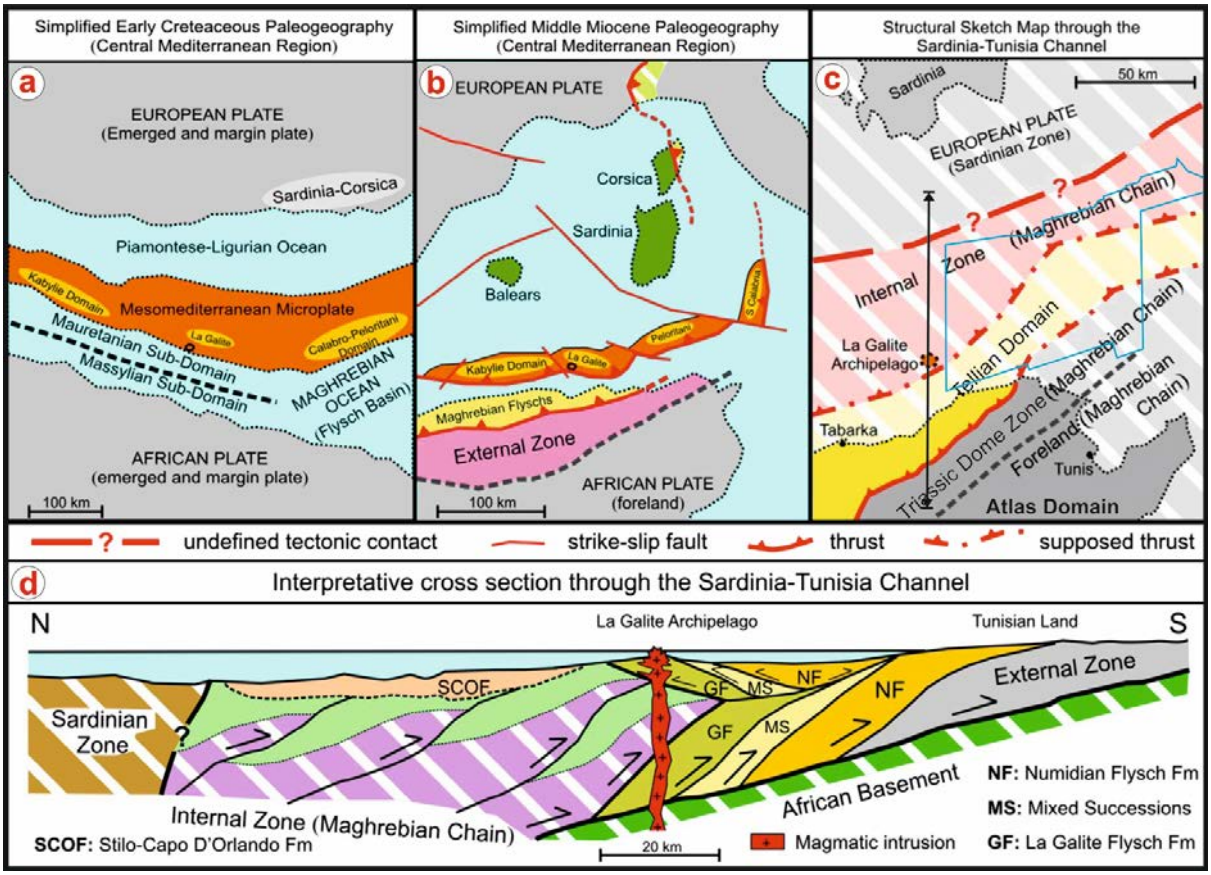

Figure 2.12. *Geodynamic evolution of the central-western Mediterranean (a and b), present-day structural map with the location of the offshore study area outlined by a blue polygon (c), and an interpretative cross section through the Sardinia-Tunisia Channel (d). Location of the cross section is shown in (c) with a black thin line. Figure modified from Belayouni et al. (2010).*

The Kabylian Equivalent Unit in El Euchi et al. (2004) represents the eastern equivalent of the north Algeria Kabylian crystalline units, and it is composed by Hercynian basement intruded by late Hercynian granitoids (Tricart et al., 1994). This Kabylian equivalent Unit occurs at the western and northern sectors of our study zone (Internal zone in Figure 2.12.c and CPK zone (Calabria-Peloritan-Kabilian zone) in Figure 2.13). In fact, Mascle et al. (2004) ground-truthed Kabylian

equivalent rocks at the Tunisian slope east of the Bizerte canyon (Figure 2.14). Although there are no previous works with a detailed geological mapping offshore Northern Tunisia, the link between the onshore and offshore structures in Northern Tunisia is evident, as the NE-SW onshore structural pattern continues into the offshore North Tunisian plateau (e.g. Castany, 1954; Rouvier, 1977; El Euchi et al., 2004; Melki et al., 2012). Therefore, the geological main domains cropping out onshore Northern Tunisia, and explained above (Section 2.2.1), continue offshore. The domains east of the Kabylian Equivalent Unit are the allochthonous Tellian domain and the autochthonous Atlas domain (Figure 2.12.c). In fact, as displayed in the MCS line-drawing profile by Tricart et al. (1994) (Figure 2.13), the boundary between the Kabylian Equivalent Unit and the Tellian domain is located somewhere close to Bizerte Canyon (also referred as La Galite Channel in Figures 2.13 and 2.14). In the same MCS profile it is noted that at the western sector of our study zone the Kabylian Equivalent Unit is overlain by up to 2 km thick Early Miocene arkose turbidites layer (Tricart et al., 1994). According to the main NE-SW structural trend of onshore Northern Tunisia, the Tellian domain would be placed in a central position running parallel to the Kabylian Equivalent Unit from the SW to the NE of the explored region (Figure 2.12.c). The Triassic dome zone included in the Atlas domain (Section 2.2.1) would be covering the south-easternmost sector of the explored region (Figure 2.12.c). The Triassic dome zone is also displayed in the MCS interpreted profile of Tricart et al. (1994) (Figure 2.13). In the easternmost sector of the profile and coinciding with the Skerki bank (Figure 2.13), overthrusted units with Triassic evaporite bodies in between occur and correspond to the Triassic dome zone.

Above these units, a thin Plio-Quaternary sedimentary succession overlay, filling up ancient depressions and partly covering structural highs (e.g. Auzende et al., 1974; Gennesseaux and Stanley, 1983; Tricart et al., 1994). Regarding to the crustal structure, Pierce and Barton (1992) note that the crust beneath the Sardinian and Tunisian coasts is probably continental. However, at the centre of the Sardinia Channel crustal thickness is neither typically oceanic nor continental, suggesting a considerably thinned continental crust.

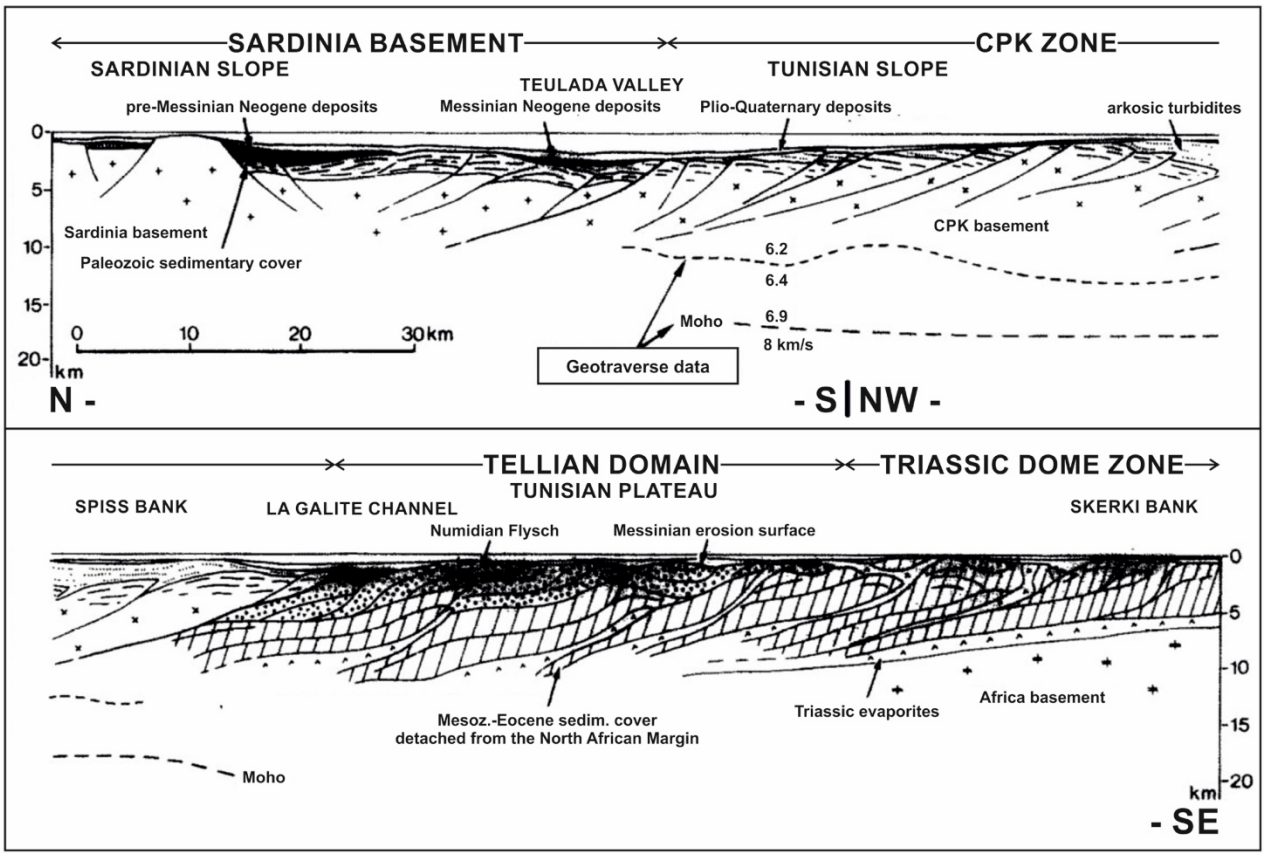

Figure 2.13. *Line-drawing interpretation of a MCS profile running from the southern Sardinian margin to the Tunisian plateau (modified from Tricart et al. (1994)). DSC: Deep Sardinia Channel; CPK: Calabro-Peloritani-Kabylian Zone. This profile is located in Figure 2.14 with a blue dashed line.*

a) Structural setting

Offshore North Tunisia shows the same main NE-SW structural trend as occurs in onshore Tunisia. Several positive relief features occur within the offshore study area, and represent the surface expression of well-cemented series, particularly sandstones and limestones, forming anticline south-verging folds of the NE-SW trending fold-and-thrust belt system (Gennesseaux and Stanley, 1983; Tricart et al., 1994; Belayouni et al., 2010) (Figure 2.12.d). Nevertheless, Gennesseaux and Stanley (1983) already noted another NNE-SSW trend on the south-eastern Sardinia margin controlling large structures (as the Carbonara Valley or the Ichnusa seamount; Figure 2.14), coinciding with the NNE-SSW trend of the Bizerte Canyon in the Tunisian plateau (Figure 2.14). Because of this similar orientation, Gennesseaux and Stanley, 1983 assume that the NNE-SSW structures of both the Sardinia margin and the Tunisian plateau had the same extensional origin related to vertical movements along the Tyrrhenian Sea margin. Moreover, Maldonado and Stanley (1976) already noted a fault displacement below the Bizerte canyon suggesting a tectonic origin for this valley.

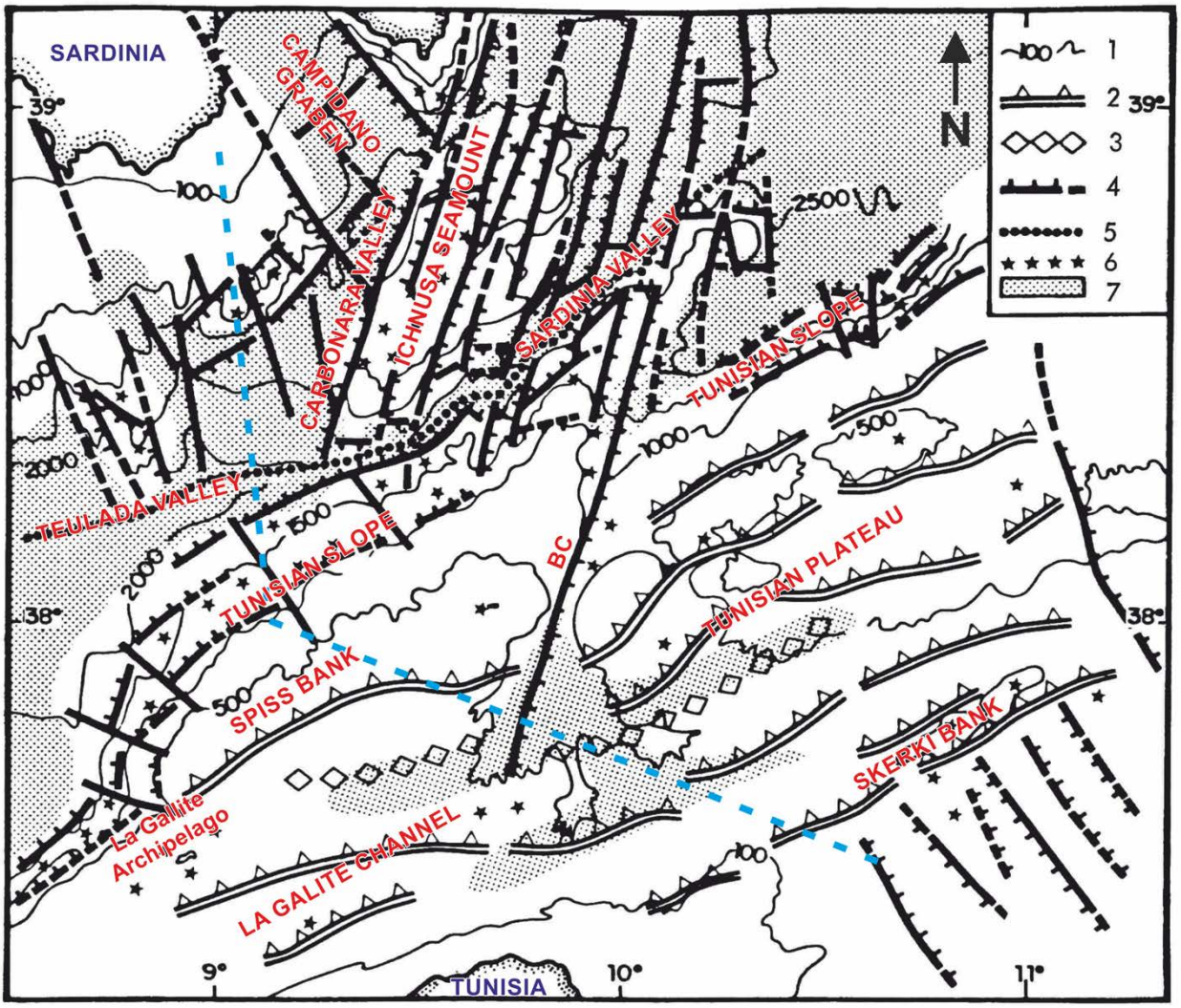

Figure 2.14. *Simplified bathymetric map of the Tunisia-Sardinia offshore area. Major structural features are named and drown. Legend: 1) Bathymetric contours; 2) Reverse faults; 3) Low surface relief features; 4) Effect of extension as recorded by NW-SE grabens near the Strait of Sicily, by normal faults (oriented NNE-SSW) on the Sardinian margin and forming the Bizerte canyon (BC) on the Tunisian plateau, by normal faults on the Tunisian and Sardinian slopes and by the Campidano Graben; 5) Axes of the Teulada and Sardinia Valleys, displaying the main boundary between the Tunisian and Sardinian margins; 6) Acoustic basement; 7) Pliocene-Quaternary sedimentary sequences shown as thin (<300 m; in white) and thick (>300 m; dot pattern) accumulations. Dashed light blue line shows the location of the seismic profile in Figure 2.13. Modified from Gennesseaux and Stanley, 1983.*

Part II

METHODOLOGY

CHAPTER 3

Methods and datasets

In this PhD Thesis has been used a multidisciplinary methodological approach that integrates analyses of new data collected both onshore and offshore. Although our research approach shares some methods on both domains, i.e. methodology, data type and analysis tools, the onshore and offshore areas also require some specific methods due to the differences intrinsic to the data sets available or collected in both areas.

Onshore, we aimed to study active tectonics in Northern Tunisia by applying a morphometric relief analysis based on the study of digital elevation models widely used in works from other regions (e.g. Keller and Pinter, 2002; Molin et al., 2004; Pedrera et al., 2009; Pérez-Peña et al., 2010; Azañón et al., 2012). The results obtained by the morphometric analysis were later ground-truthed during a field campaign. With this work we identified and mapped active tectonic structures for the Northern Tunisian region that allowed us to better understand the current tectonics in this sector in the frame of the Nubia-Eurasia boundary.

Offshore, with the same main research goal, we acquired and analysed high-resolution swath-bathymetry and backscatter mosaics, and parametric echosounder profiles. These datasets were used for detailed geomorphological and seismo-stratigraphic analyses to study the current tectonic activity in the North Tunisian continental margin. In addition to the geophysical dataset, we integrated age data from a giant piston core collected by the R/V Marion Dufresne in 1995 during the MAST II PALAEOFLUX Program (Dinarès-Turell et al., 2002), which provided calibration of horizons mapped with the sub-bottom (i.e. TOPAS) profiles. Similar high-resolution datasets have been used for exploring active tectonics in submarine areas, such as the southern California margin

(Marlow et al., 2000), the Marmara Sea (Polonia et al., 2002) or the Alboran Sea (Gràcia et al., 2006; Martínez-García et al., 2011).

Finally, some methods and dataset type have been common for both onshore and offshore areas, as earthquake magnitude estimation methods and seismicity datasets, among others. Although the methods used for this thesis are described within this chapter, specific descriptions of some methods and datasets are included within the results chapters.

3.1. Data Acquisition

3.1.1. Offshore Northern Tunisian Margin

a) Geomargen-2 cruise (RV "García del Cid")

From April to May 2013 the first high-resolution bathymetric map of the Northern Tunisian seafloor was acquired during the Geomargen-2 cruise, carried out in the framework of the Geomargen-2 project funded by Repsol Exploración S.A. (Succursale en Tunisie S.A.). Simultaneously to bathymetric data, acoustic backscatter and high-resolution parametric echosounder profiles were also acquired with the R/V "García del Cid" from the "Consejo Superior de Investigaciones Científicas" (CSIC). The area mapped represents about 13,000 km^2 and the parametric echosounder profiles sums a total length of 8,445 km (Figure 3.1).

The main goals of the survey were:

i) To characterize the morphology of the offshore North Tunisian margin (i.e. the outer shelf, plateau and slope system) to analyse geomorphic features and discover those potentially related to active fluid escape processes.

ii) To explore the subsurface within the shallowest tens of meters of the sub-seafloor geological features, and relate them to corresponding seafloor relief.

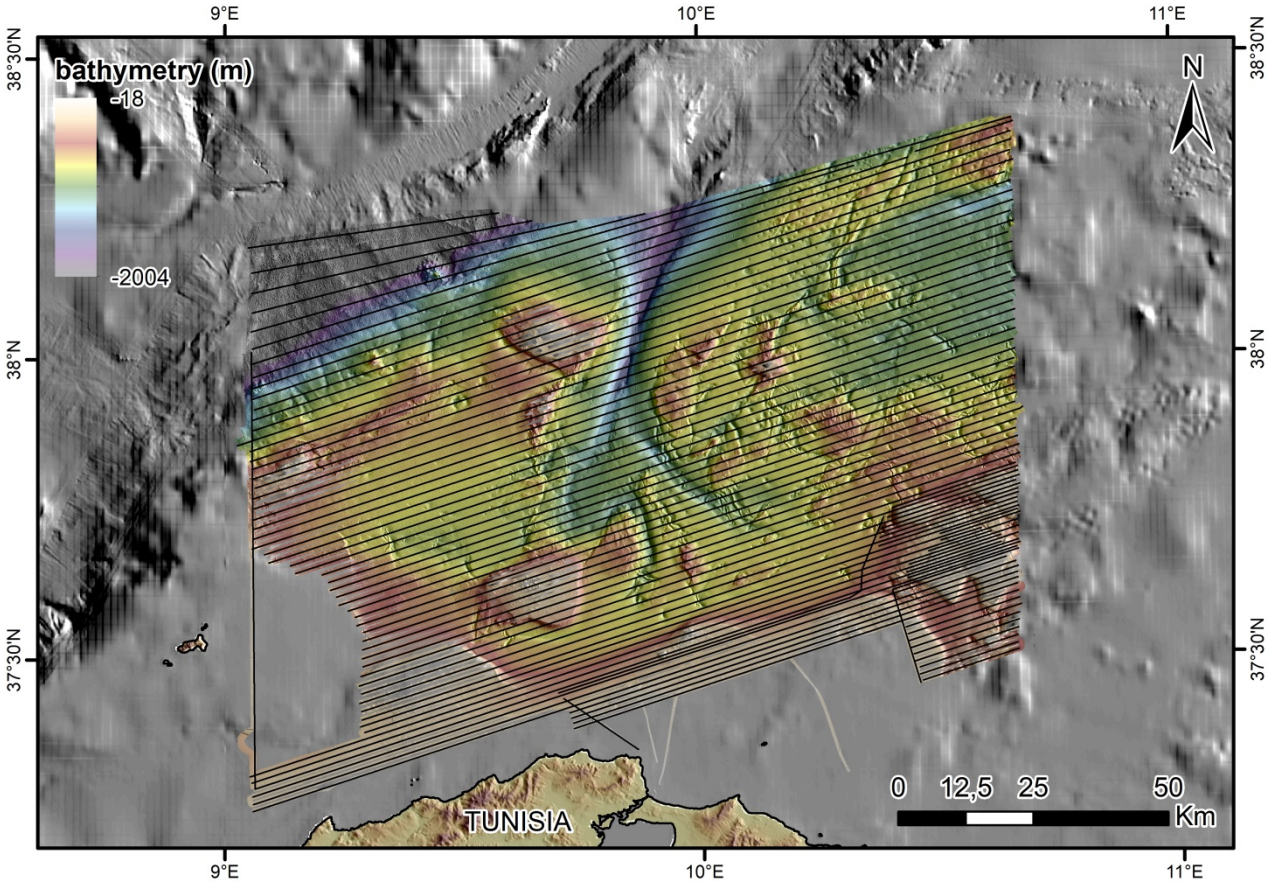

Figure 3.1. *New high-resolution bathymetric map obtained during the Geomargen-2 cruise. Black lines correspond to the location of the parametric echosounder profiles acquired and used in this work.*

b) Geomargen-2AA cruise (RV "Ángeles Alvariño")

From November to December 2013 an extensive campaign of sediment core sampling was carried out in the offshore Northern Tunisian margin during the Geomargen-2AA cruise in the frame of the Geomargen-2 project. During the Geomargen-2AA survey, complementary data were also acquired and used for this thesis, such as a high-resolution bathymetric mosaic and high-resolution TOPAS profiles. This survey was carried out onboard the Spanish R/V "Ángeles Alvariño" belonging to the "Instituto Español de Oceanografia" (IEO).

The sediment core program was designed to evaluate recent/ongoing fluid-flow sites in the North Tunisian continental margin. A total of 135 gravity cores were recovered, as well as several dredges and seafloor camera observations, although this is not included in detail as part of this work. Aside from the coring program, the marine geophysical data acquisition plan was divided into two areas with different goals:

i) An area matching with the Geomargen-2 surveyed map (i.e. within the Tunisian territorial waters), where the data was acquired perpendicular to the main tectonic structures in order to better study the regional tectonic framework.

ii) An area located north-east of the Geomargen-2 surveyed map (i.e. within the Italian territorial waters), in order to connect the bathymetric dataset available for the Tyrrhenian Sea (EMODnet mosaic) with our high-resolution bathymetric map obtained during the Geomargen-2 cruise.

In Figure 3.2 are displayed the data acquired during the Geomargen-2AA cruise that is used in this work. In particular, the dataset analyzed in this PhD Thesis work consists of a bathymetric map covering an area of about 6,434 km^2 and 3,500 km of TOPAS profiles covering an extensive region of the North Tunisian continental margin (Figure 3.2).

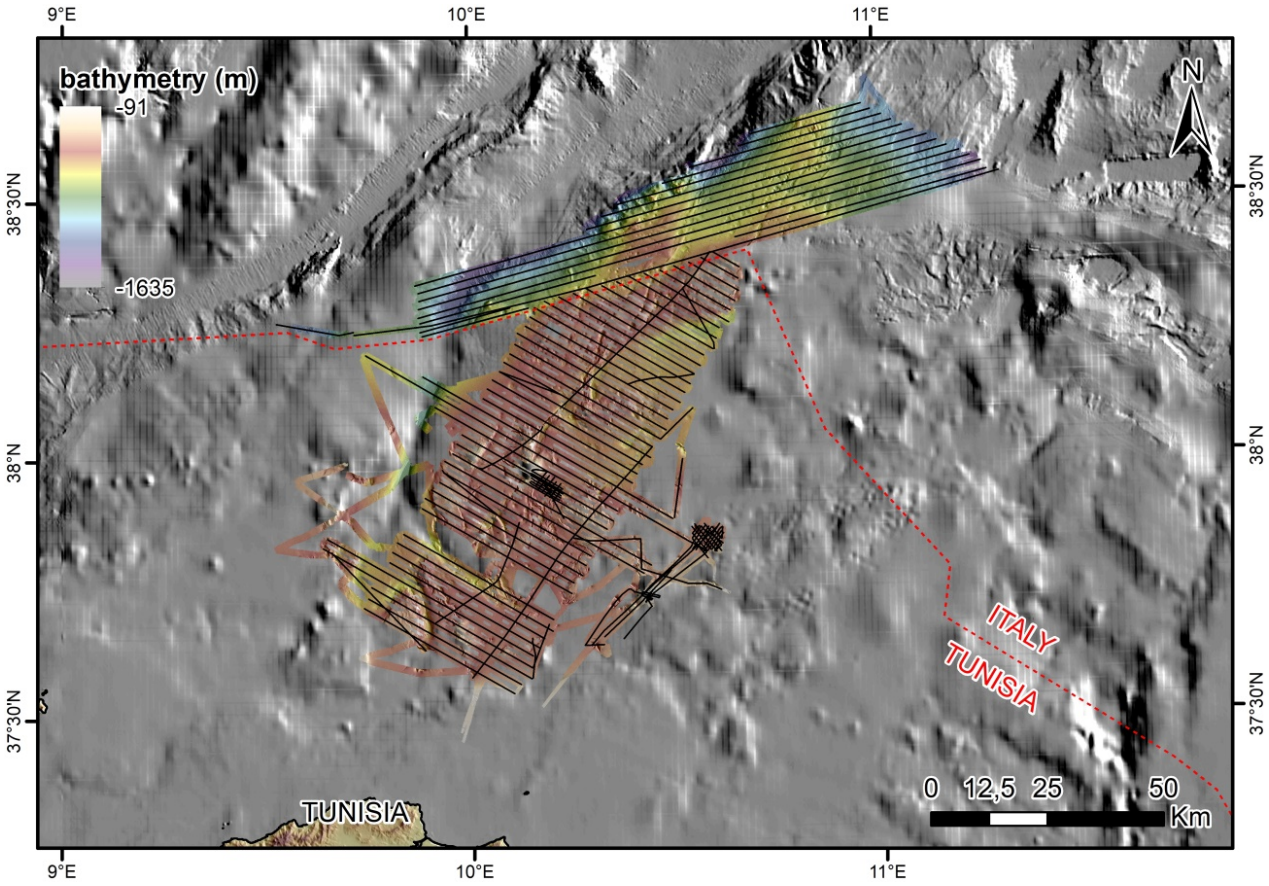

Figure 3.2. *New bathymetric map acquired during the Geomargen 2-AA cruise. Black lines show the location of the TOPAS profiles acquired and used in this work. The boundary between Tunisian and Italian waters are depicted by a dashed red line. Color palette of this figure differs from previous Figure 3.1.*

3.1.2. Onshore Northern Tunisian Margin

During March 2015 a field campaign was planned onshore Northern Tunisia in order to ground-truth the results obtained from the quantitative analysis of digital elevation models previously carried out in the frame of my MSc project presented at the University of Barcelona in 2015. The fieldwork was carried out to investigate and determine the possible relationship between morphometric anomalies obtained from the relief analyses and active tectonic structures or fluvial captures detected on the field. With this aim, we analysed specific faults (e.g. measured striae and dips, studied its kinematics, etc.), investigated Pleistocene river terraces close to the faults, identified abandoned terraces in wind gaps (gap through which a waterway once flowed), and looked for paleo-seismological evidences such as co-seismic rupture structures including open cracks in the terrain.

3.2. Offshore geological and geophysical methods

In the offshore area we used a compilation of geological and geophysical data acquired in the North Tunisian continental margin. The dataset comprises high-resolution swath-bathymetry, acoustic backscatter mosaics and parametric echosounder profiles acquired during the Geomargen-2 and Geomargen-2AA cruises (Section 3.1.1). The region surveyed during both surveys covers an area between longitude 9°3.6'E and 11º16.6'E, and latitude 37°14.7'N and 38°41.2'N. The total area covered extends for around 15,600 km^2 in a range of 18 to 2221 m depth (Figure 3.3). A final bathymetric map has been produced merging the bathymetric datasets from the two oceanographic cruises in a single mosaic (Figure 3.3).

In addition, we use the 23.66 m long LC07 piston core (Figure 3.3) acquired in the frame of the MAST II PALAEOFLUX Program. This long sediment core was collected by the giant piston coring "CALYPSO" by the French R/V "Marion Dufresne" in 1995 within our study area (Rothwell, 1995; Dinarès-Turell et al., 2002). This sediment core allowed dating seismic horizons mapped during the seismostratigraphic analysis.

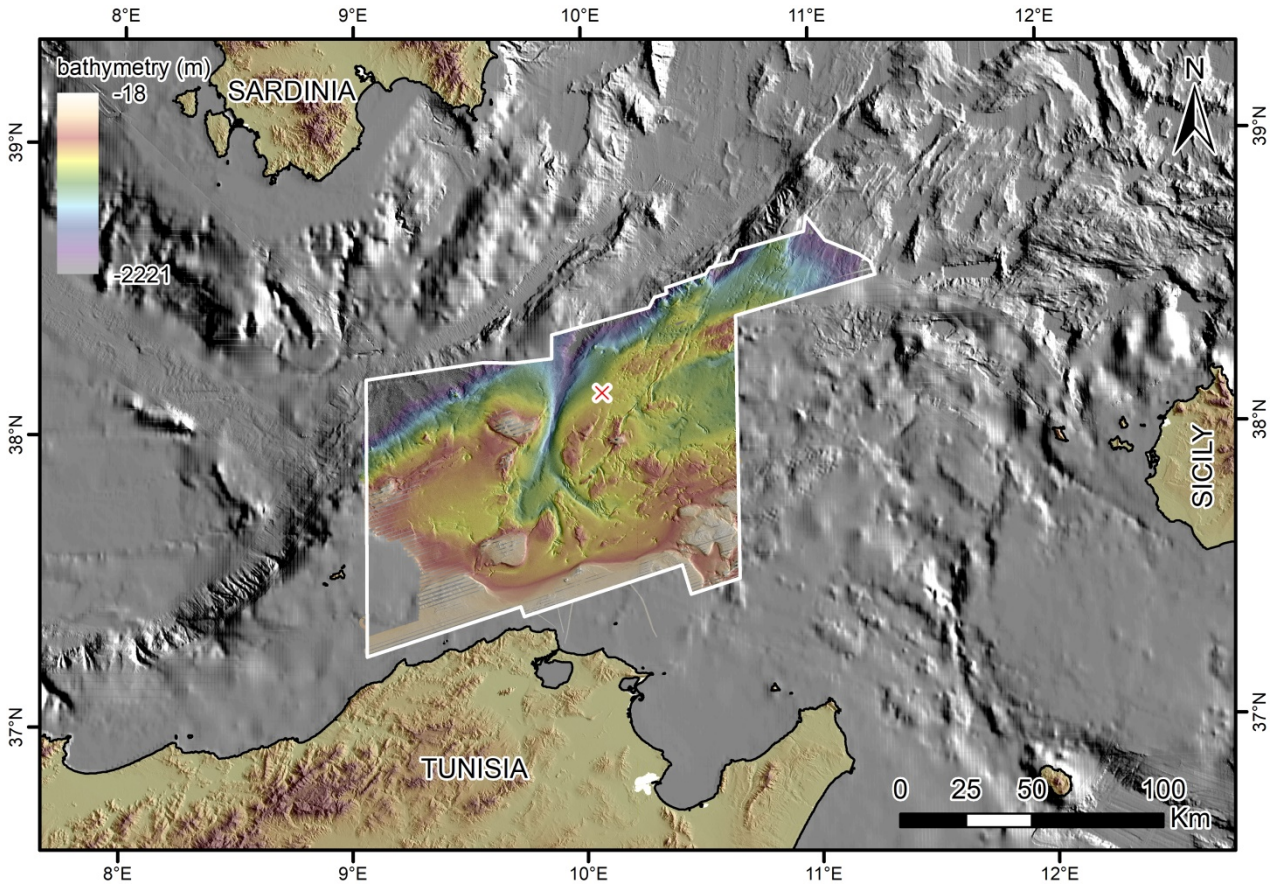

Figure 3.3. *Location of our study area offshore (white polygon) in the shelf-slope system of the northern Tunisian Margin (Central Mediterranean). The red cross shows the location of the LC07 sediment core (Dinarès-Turell et al., 2002).*

3.2.1. High-resolution swath-bathymetry and acoustic backscatter imagery

Multibeam echosounders provide essential information that helped us to understand the relief and nature of the seafloor by sending a high-frequency acoustic signal that is reflected on the seafloor and recovered back by transducers on the keel of the vessel (Figure 3.4). The recovered signal provides both elevation (bathymetry in m) and acoustic backscatter strength of the acoustic signal returned by the seafloor (acoustic backscatter imagery) (e.g. Diez and Gràcia, 2005; Gràcia and Diez, 2005).

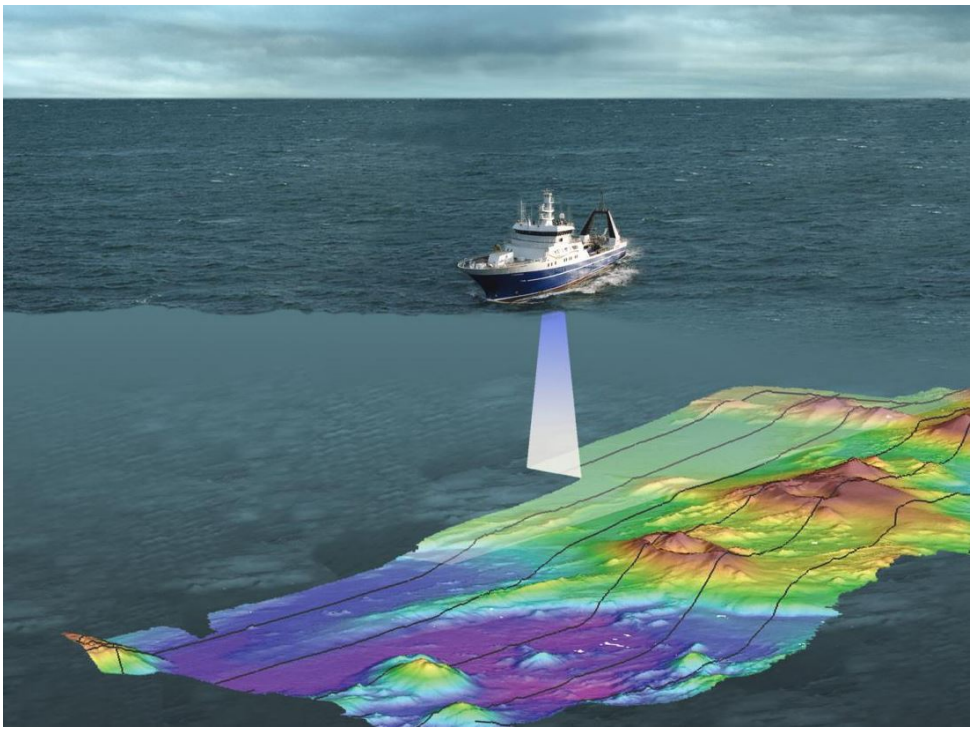

Figure 3.4. *Picture showing a research vessel surveying a seafloor area with a multibeam echosounder (NIWA, 2018).*

a) High-resolution swath-bathymetry

Bathymetric maps are Digital Elevation Models (DEM) of the seafloor and are acquired by multibeam echosounders usually mounted on the hull of vessels (although they can also be mounted in other vehicles, such as Autonomous Underwater Vehicles (AUV)) (Figures 3.4 and 3.5). The principle of multibeam echosounders is based on measuring the time taken by an acoustic wave to propagate through the water to the seafloor and back to the transducers (Diez and Gràcia, 2005; Gràcia and Diez, 2005). In the offshore North Tunisian margin, swath-bathymetry allowed us to map the study area in great detail with a high spatial resolution (cell size for the entire region of 30x30 m), which allows us to recognize different geomorphic features and to obtain information about the sedimentary, erosive and tectonic processes shaping the area (Figure 3.5).

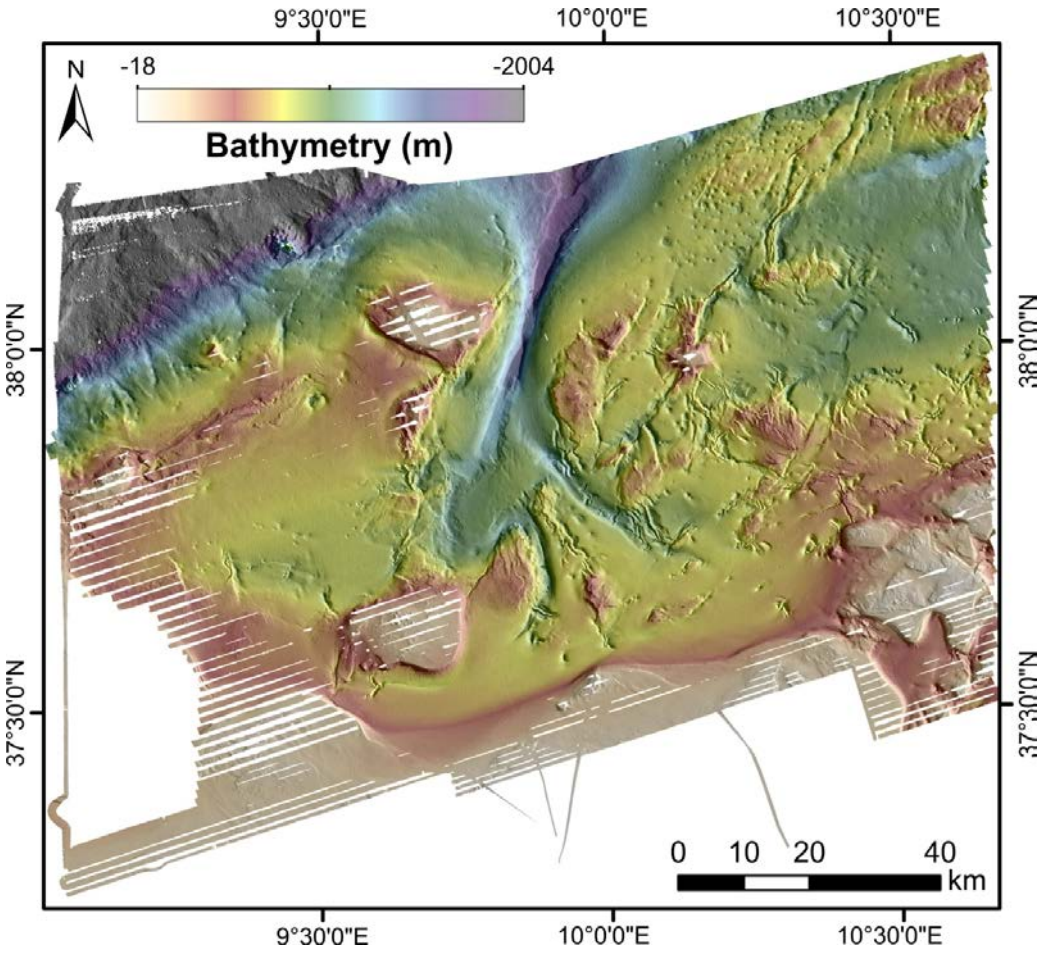

Figure 3.5. *Swath bathymetric mosaic acquired during the Geomargen-2 survey, and displayed above the shaded relief map (with an illumination azimuth of 72º and an altitude of 45º).*

The high-resolution swath-bathymetry data was acquired using the ELAC Seabeam 1050D multibeam echosounder installed on board the RV "García del Cid" (Geomargen-2 cruise) (Figure 3.5) and the Kongsberg EM710 multibeam echosounder installed onboard the RV "Ángeles Alvariño" (Geomargen-2AA cruise):

i) The ELAC Seabeam 1050D echosounder is a multibeam system for shallow to medium water depth range, covering the range of the surveyed area (from ~20 to ~2000 m). The Elac Seabeam 1050D system corresponds to a dual multibeam sonar, characterized by a main frequency of 50 kHz and emitting 126 individual beams for a swath width of 153º. It provides 1.5º resolution, exceeding IHO (International Hidrographic Organization) standards (ELAC Nautik, 2011). The multibeam swath coverage is proportional to the water depth, which explains the restrained coverage above topographic highs and near the shelf (Figure 3.5). Average survey speed during the Geomargen-2 cruise acquisition was 6 knots and nominal overlap between adjacent swaths was of 15%.

ii) The EM710 multibeam echosounder is a high to very high resolution seafloor mapping system. The acquisition depth is from less than 3 m to 2000 m below the transducers. Swath width is up to 5.5 times water depth, to a maximum of more than 2000 m (Kongsberg, 2018a). The EM710 echosounder operates at frequencies in the range of 70 to 100 KHz with a maximum ping rate of more than 30 per second.

Previous to data processing, an exhaustive quality control was carried out onboard during both cruises using the software CARIS HIPS and SIPS. The quality control focused on: i) positioning, i.e. checking the navigation values to verify that data geo-reference was correct; ii) depth, i.e. checking that depth values were within the expected ranges; it implies to check for the vessel altitude, sound velocity profiles, and presence of data artefacts; and iii) coverage, i.e. checking that the seafloor was fully covered through generation of Digital Elevation Models (DEMs) during the acquisition.

Post-processing and data analysis

Post-processing of the large bathymetric dataset was performed by the Marine Technology Unit (UTM-CSIC) using the HIPS system, a comprehensive submarine mapping software developed by CARIS. After the calibration, filtering and cleaning of bathymetric data, final Digital Elevation Models (DEM) were computed. During this work, the final DEMs were analysed with the ESRI ArcGIS software to produce different maps, such as false colour shaded-relief maps, and the extraction of different morphometric information. In this work, bathymetric shaded relief maps are often displayed with predominant illumination azimuth of 72º and an altitude of 45º in order to follow the main acquisition direction of the ship and thus, avoiding most of the related artefacts.

In addition to these map displays, we furthered the bathymetric data analysis out two modern processing approaches: i) a high-pass filtering of the topography (after Howell et al., 2015) and ii) the Red Relief Image Map (RRIM) after Chiba et al. (2008). Both methods are useful in identifying seafloor fault-related features and are particularly good for highlighting subtle seafloor morphologies, enhancing seafloor lineaments. Moreover, two morphometric analyses were computed for the offshore area in order to carry out a quantitative analysis of the seafloor relief. Although these analyses are typically applied onshore and based in drainage network metrics (see Section 3.3.1 of this Chapter), the high quality of our bathymetry data permitted the use of similar approaches to seafloor relief data. We used two methods applied spatially and independently of drainage systems: i) a spatial auto-correlation technique for the hypsometric integral, and ii) the swath profiles.

High-pass filtering of the topography

This high-pass filtering of the topography is a method where a high-pass filtering is applied in order to take out the short-wavelengths of the bathymetric data (Howell et al. 2015). Thus, this method highlights the high frequency information of the data and highlights subtle changes in the topography often masked by high amplitude low frequency features. It has been particularly useful to identify surface fault traces along the offshore margin. To obtain this short-wavelengths map (filtered topography map, Figure 3.6.c) we first filter the original bathymetry (Figure 3.6.a) to obtain a long-wavelength map (Figure 3.6.b), which we later subtract from the original one (Figure 3.6.a). In our case, all calculations for obtaining the different maps were done using ArcGIS software. After some testing, to calculate the long-wavelengths map (Figure 3.6.b) we filtered the original bathymetry (Figure 3.6.a) with the *focal statistics tool* (e.g. from the Spatial Analyst toolbox of ArcGIS) using a 600 m circle search radius and applying a mean filtering. Finally, to obtain the filtered topography map (high-pass filtered map, Figure 3.6.c), we subtracted the long-wavelength map from the original bathymetry by using the *raster calculator tool* (from the Spatial Analyst toolbox of ArcGIS).

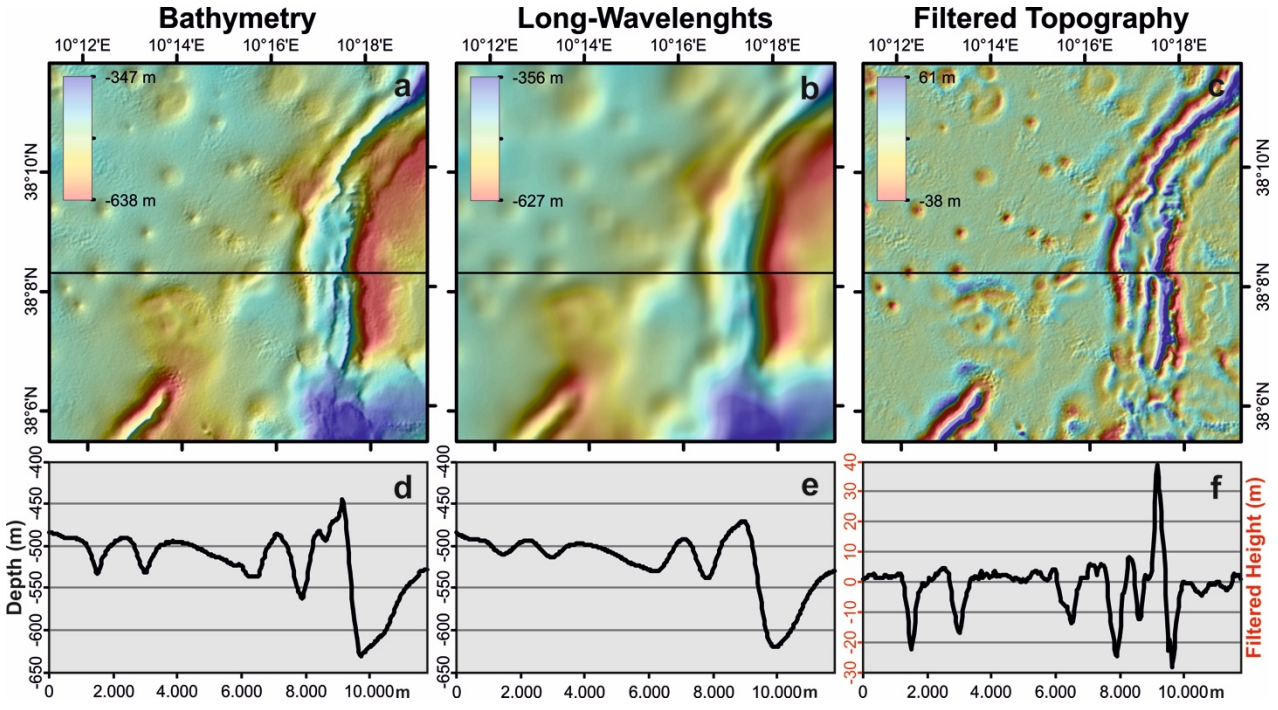

Figure 3.6. *Examples of shaded relief maps that explain the high pass filtering of the topography method. a) Bathymetric map; b) Bathymetric map where the long-wavelengths have been filtered; c) High pass filtered map obtained by subtracting the long-wavelengths map from the original bathymetric map; d) Depth profile; e) Long-wavelength depth profile; f) High pass-filtered topography profile. Profiles are displayed by a black line in Figures* 3.6.*a,* 3.6.*b and* 3.6.*c. Location of Figures* 3.6.*a,* 3.6.*b and* 3.6.*c is shown in Figure* 3.7.

As shown in Figure 3.6.c, subtle changes in the seafloor surface are more easily identified than in the original bathymetry, and different morphologies stand out (e.g. note the clearer delineation of pockmarks). The map of our entire study area with filtered topography is shown in Figure 3.7.

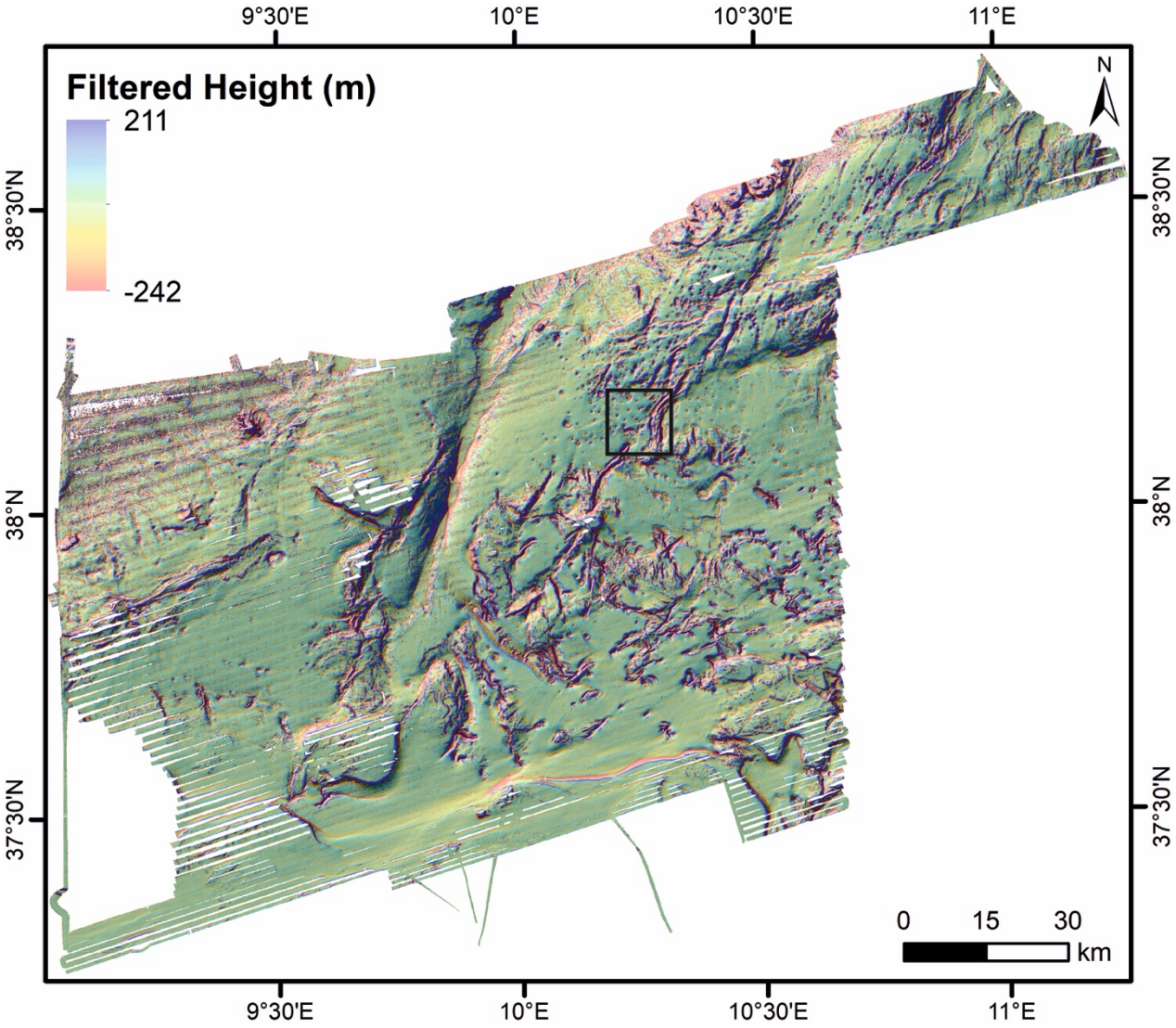

Figure 3.7. *Filtered topography map of our study area in the offshore North Tunisian margin. The filtered topography is shown above the original bathymetry shaded relief map in order to better display the different morphologies of the seafloor. The black box shows the location of Figures* 3.6.*a,* 3.6.*b and* 3.6.*c.*

Red Relief Image Map (RRIM)

The Red Relief Image Map (RRIM) is a visualization method of the topography that allows to visualize the topographic slope, concavities and convexities at the same time Chiba et al. (2008). We calculated the RRIM for our data using the ArcGIS software tools. As shown in Figure 3.8, the RRIM visualization method (Figure 3.8.c) is based in the following method:

i) An overlapping slope map in a white to red palette depicting gentle and abrupt slopes respectively (Figure 3.8.a) and,

ii) A curvature map in a black and white palette depicting convex and concave shapes respectively (Figure 3.8.b).

We calculated the slope and curvature maps with the *Slope and Curvature tools* of the Spatial Analyst toolbox from the ArcGIS software. This analysis calculates the surface curvature cell by cell, analysing each cell regarding to its eight neighbourhood cells (ArcGIS Help Library, 2017). The curvature is the second derivative of the surface or "the slope of the slope". With this kind of analyses, the edges of the structures stand out helping the visualization and interpretation. Finally, we display the maps applying a transparency to the uppermost slope map. In order to better display our data, and following Chiba and Hasi (2016), we applied a white to red palette for the slope map with a blue colour for the values between 0 and 1º (Figure 3.8.a), the ones displaying flat areas. The RRIM for our entire study area is presented in Figure 3.9.

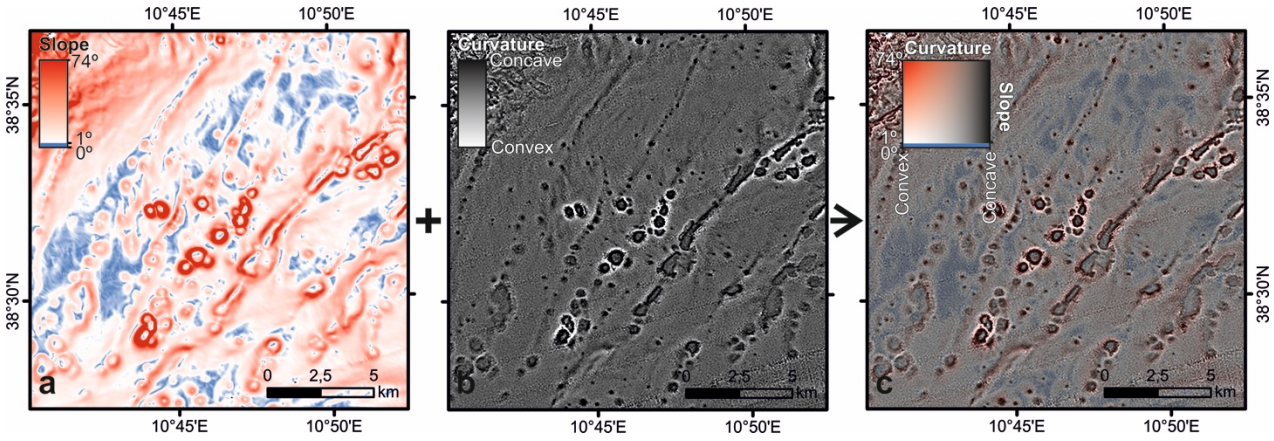

Figure 3.8. *Examples of maps explaining the different steps for the RRIM visualization method. a) Slope map; b) curvature map; c) Red Relief Image Map (RRIM). Modified from Chiba et al. (2008). Location of the Figures* 3.8.*a,* 3.8.*b and* 3.8.*c is located in Figure 3.9.*

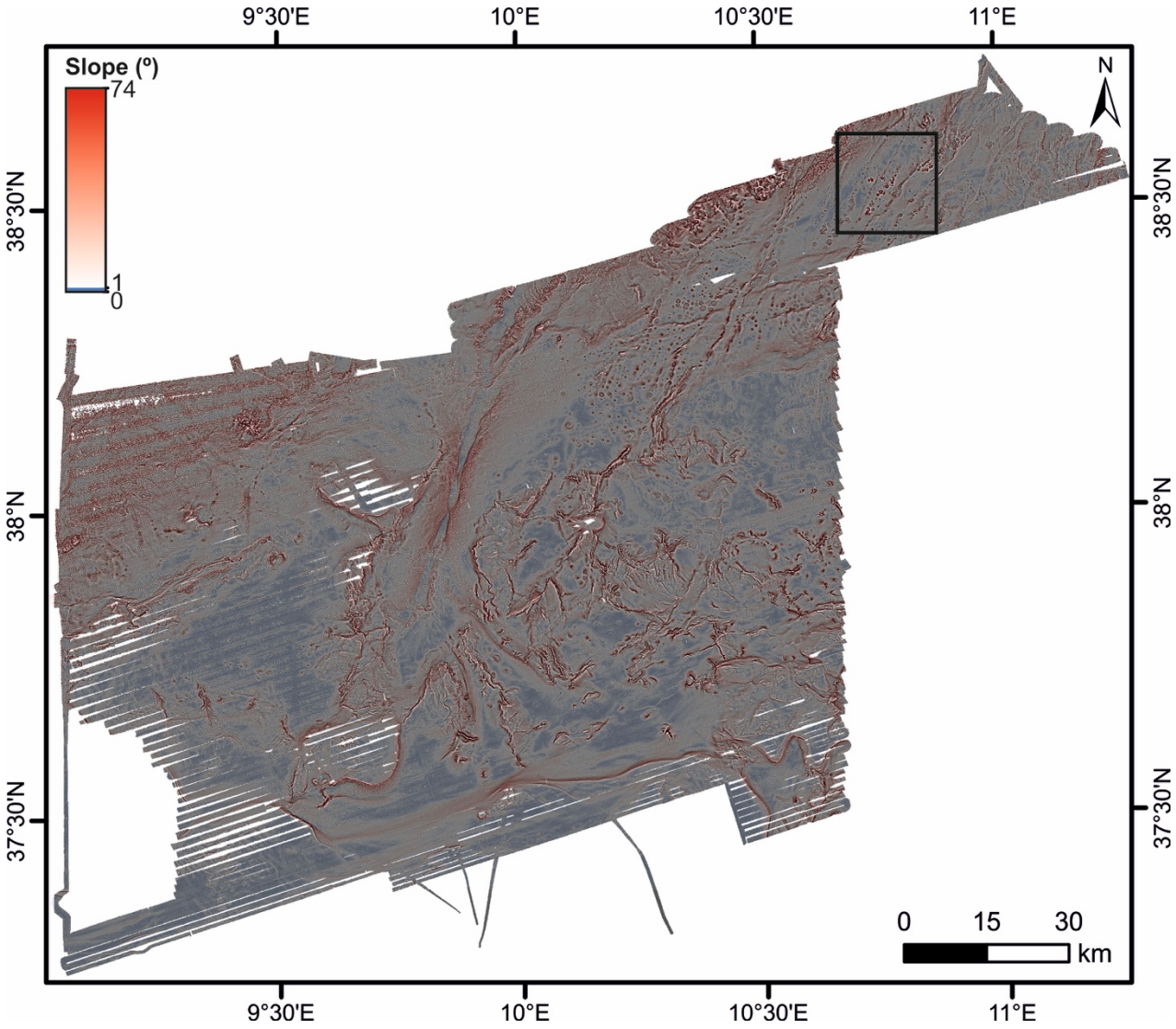

Figure 3.9. *Red Relief Image Map (RRIM) of our study area in the offshore North Tunisian margin. The black box shows the location of Figures* 3.8.*a,* 3.8.*b and* 3.8.*c.*

Spatial auto-correlation technique for the hypsometric integral

Hypsometry is one of the most useful morphometric parameters to describe and analyse the distribution of elevations within an area (usually drainage basins). Hypsometry studies the mass distribution depending on elevations (Strahler, 1952), and can be evaluated by the hypsometric curve and the hypsometric integral (Hi) (see Section 3.3.1 for further information). The hypsometric integral can be approximated by means of the following equation (Pike and Wilson, 1971; Keller and Pinter, 2002):

$$\mathrm{Hi} = \frac{\text{mean elevation} - \text{minimum elevation}}{\text{maximum elevation} - \text{minimum elevation}} \qquad \textit{Equation 3.1}$$

Hypsometry analyses used to be applied onshore in order to evaluate the stage of evolution of the landscape. The relationship between hypsometry and the degree of dissection of the landscape permits its use as an indicator of landscape's erosional stage (Keller and Pinter, 2002). Nevertheless, following the method proposed by Pérez-Peña et al. (2009c), where Hi values are computed for regular squares of an analysis grid instead of values for drainage basins, we are able to obtain Hi values offshore. However, while onshore Hi values are related with the dissection of the landscape and therefore with uplift phenomena, offshore the results show information about the elevation uniformity (or variation) of the seafloor. High values of Hi indicate that most of the relief within a square is high relative to the mean values, while low values indicate that most of the relief is low relative to the mean. In particular, in offshore Tunisia, high Hi values are usually related to pockmark fields while low values are usually related to concave-up slopes or prominent vertical features as cold-water coral mounds. As displayed in Figure 3.10 Hi values can vary considerably across neighbour squares due to cell allocation and that is why Pérez-Peña et al. (2009c) propose to apply a hot spot analysis in order to spatially identify clusters of high or low values. In particular, they propose the Getis-Ord Gi* statistic method (Ord and Getis, 1995) (Figure 3.11). All the calculations were done using the ArcGIS software. To calculate the minimum, maximum and mean values for regular squares we used the *block statistics tool* (from the Spatial Analyst toolbox) with a block size of 25 cells (25 cells x 30 m = 750 m). The Gedis-Ord analysis was applied using a 1000 m search radius with the *hot spot analysis (Getis-Ord Gi*) tool* (from the Spatial Statistics toolbox).

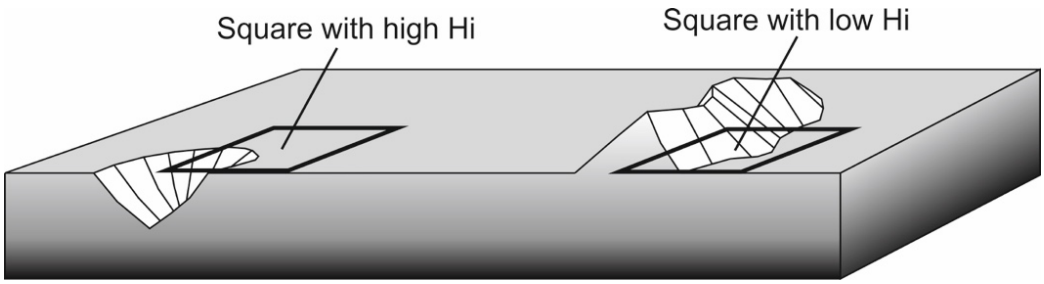

Figure 3.10. *Illustration showing how Hi (hypsometric integral) values computed for regular squares can present high variability depending on the square location (modified from Pérez-Peña et al., 2009c).*

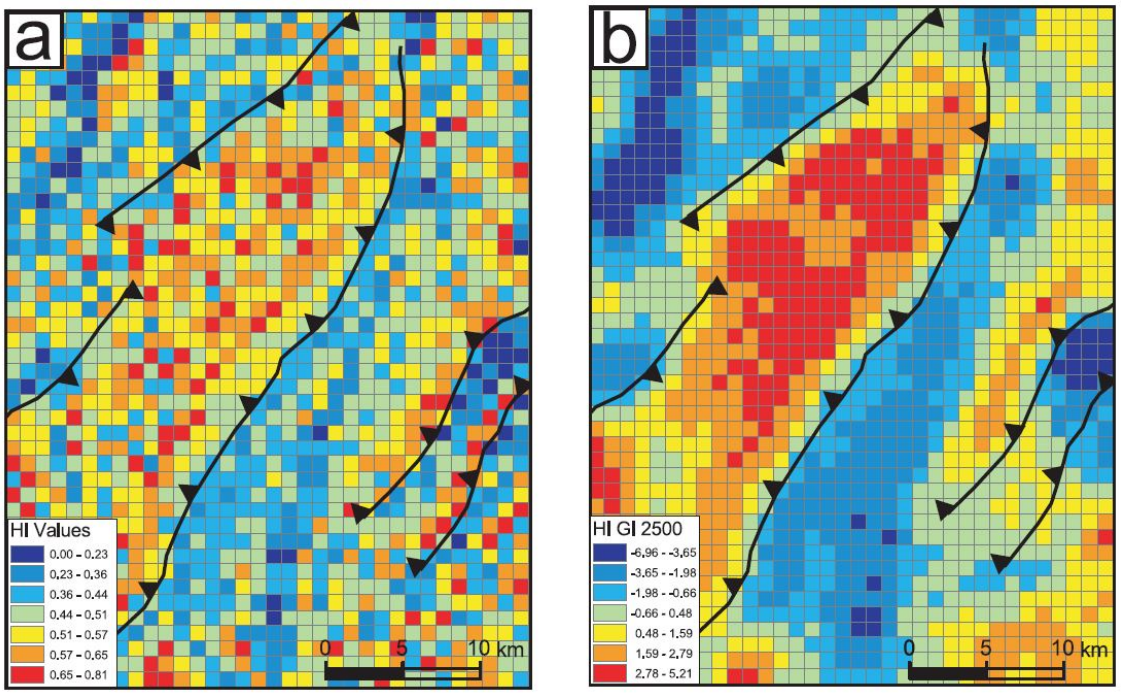

Figure 3.11. *Example of the Hot Spot analysis applied in Pérez-Peña et al. (2009). a) Hi (hypsometric integral) distributions, b) Gedis-Ord statistic estimation for the Hi values. The results of the hot spot analysis clearly display clusters of low and high values, with the later showing uplifting areas.*

Swath profiles

Swath profiles analysis is a common technique applied in morphometric studies (e.g. Molin et al., 2004; Azañón et al., 2015). They consist in stacking several parallel topographic profiles in a same diagram. In our case, we plot the different profiles and also the maximum, minimum and mean values (with the envelope of the standard deviation). The profiles extracted in order to study the regional relief were acquired in a NE-SW orientation and following the vessel track in order to avoid the noise between traces. For extracting swath profiles across the Bizerte Canyon we applied the method described in Hergarten et al. (2014), where they extract swath profiles across curved geomorphic features (Figure 3.12). In our case, all the computations have been done with the ArcGIS software.

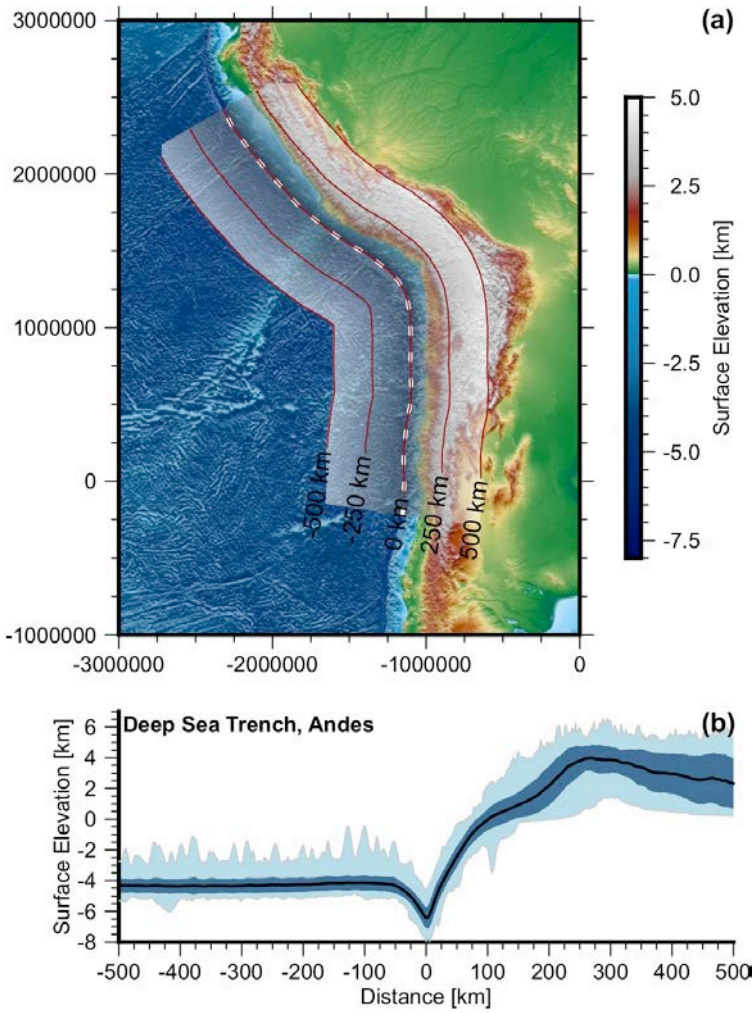

Figure 3.12. *Swath profile following the Andes Trench. a) Topographic and bathymetric map, b) Swath profile. The mean elevation is shown by the black line. Extreme values and mean values ±1 standard deviation are indicated by the light- and dark-blue areas, respectively. Extracted from Hergarten et al. (2014).*

b) Acoustic backscatter imagery

Acoustic imagery records the backscatter strength (reflectivity) of the acoustic signal returned by the seafloor (Figure 3.13). The acoustic backscatter strength varies according to the nature of the seafloor, roughness and the angle of incidence. This way, in flat areas, different values of reflectivity must be related to different seafloor facies. High reflectivity is typically related to hard rock (rock outcrop) or coarse grainsizes (e.g. gravel, sands, coral rubble), while low reflectivity is related to fine grainsizes (silt and clay). Backscatter strength and its textural organization in the corresponding acoustic images are primarily related to the geomorphology and sedimentary environments of the insonified seafloor (e.g. Diez and Gràcia, 2005; Gràcia and Diez, 2005).

In this work, acoustic backscatter data were acquired simultaneously to bathymetry by using the Seabeam 1050D and EM710 echosounders, respectively.

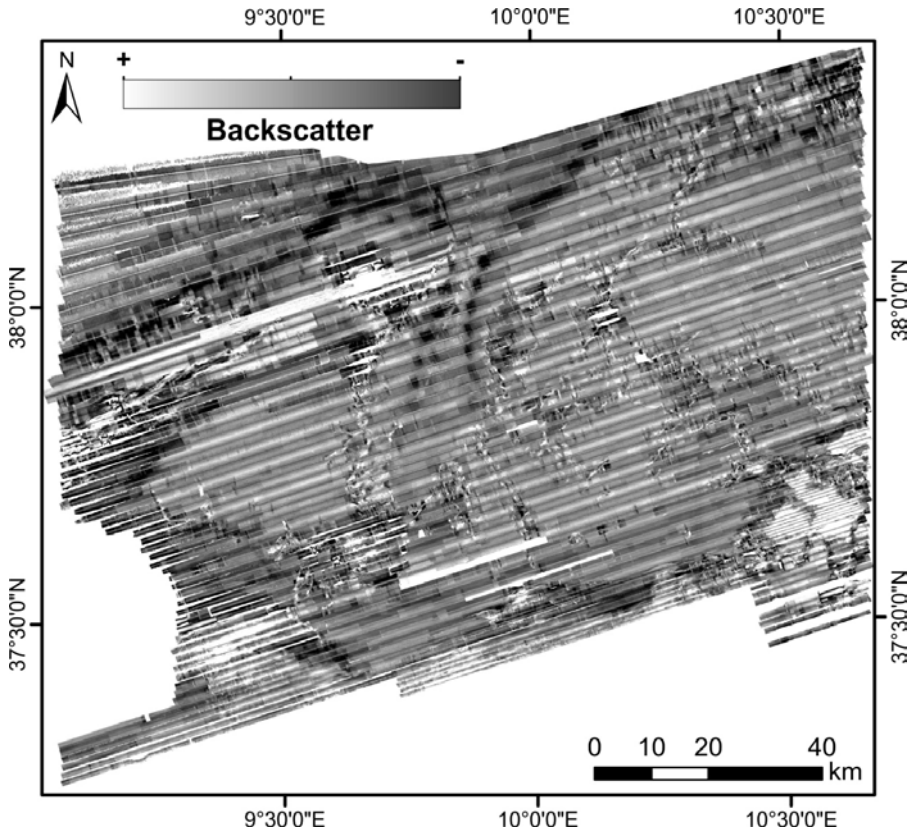

Figure 3.13. *Acoustic backscatter mosaic acquired during the Geomargen-2 survey.*

Post-processing and data analysis

SIPS processing software from CARIS was used for acoustic backscatter processing. To process the intensity of the reflected wave, a series of geometric and radiometric corrections were made to the raw data. Finally, the acoustic backscatter mosaic was obtained by the UTM-CSIC acoustic team at the most adequate resolution, taken into account the data quality and average water depth. Later analyses through the ESRI ArcGIS software were carried out during this work.

3.2.2. High-resolution sub-bottom profiler

Parametric echosounder profiles were acquired using the portable Innomar SES-2000 Compact sub-bottom profiler installed on a steel pole on the starboard side of the RV "García del Cid", thus enabling quick retraction for transits at higher speed, and the Kongsberg TOPAS PS 18 sub-bottom profiler installed onboard the RV "Ángeles Alvariño".

The Innomar SES-2000 Compact sub-bottom profiler emits primary high frequencies approximately of 100 kHz (band 85-115 kHz) and secondary low frequencies at 4, 5, 6, 8, 10, 12 and 15 kHz (band 2-22 kHz). The system works for a water depth range between 0.5 to 400 m, with a sediment penetration up to 40 m (depending on sediment type and noise) and a layer resolution

up to 5 cm (Innomar, 2018). Low-frequency records allowed to image the first meters of sub-seafloor, specifically in the shallower portion of the margin (Figure 3.14.a).

The TOPAS PS 18 sub-bottom profiler has a large operational depth range from 20 m to full ocean depth (>11,000 m). It is based on low frequency sound generation by the non-linear interaction between two high frequency signals. Primary frequencies range from 15 to 21 kHz while secondary frequencies range from 0.5 to 6 kHz. The system has a nominal penetration capability of more than 200 m and a resolution of better than 0.15 m (Kongsberg, 2018b) (Figure 3.14.b).

Post-processing and data analysis

Seismic parametric data, stored through the software SES-WIN in raw file (specific of the echosounder manufacturer) were converted in SEG-Y format through the SES-CONVERT software by the UTM-CSIC. For this work SEG-Y files were imported to the Kingdom Suite software to be analysed and interpreted.

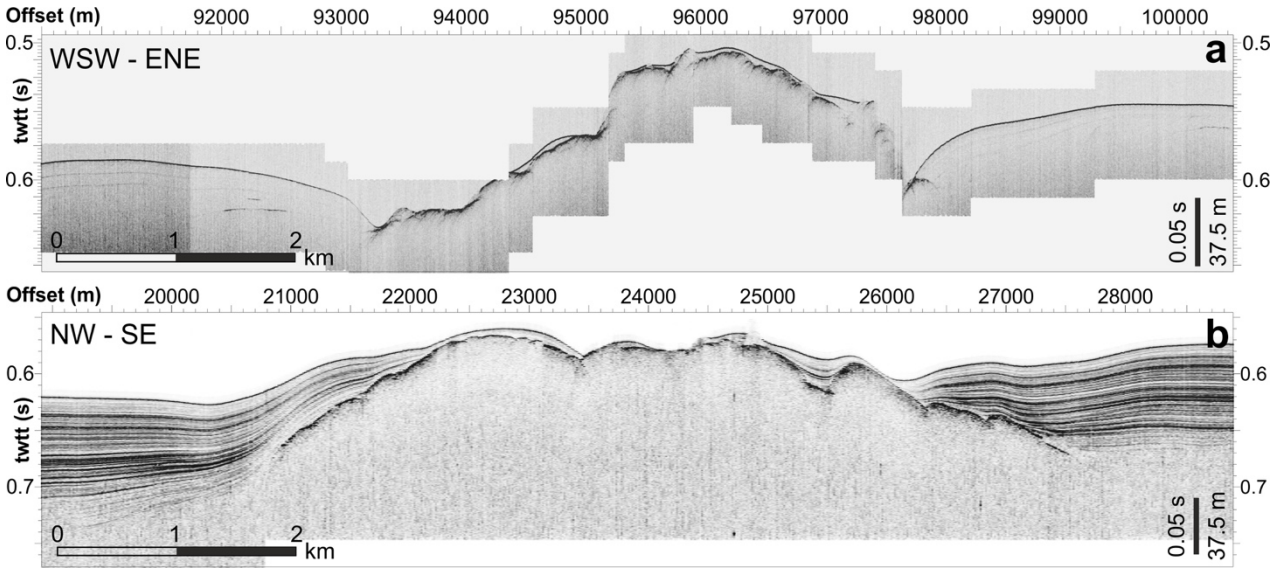

Figure 3.14. *a) Example of a profile acquired with the parametric echosounder Innomar SES-2000 in the frame of the the Geomargen-2 cruise; b) Example of a Kongsberg TOPAS parametric echosounder profile acquired during the Geomargen-2AA cruise.*

3.3. Geological and morphometric methods used onshore

Onshore we applied different morphometric analyses to characterize the recent tectonic activity of northern Tunisia. First, we extracted the drainage network from a Digital Elevation Model (DEM) of 30 m pixel resolution and selected the main basins with their trunk channels to analyse. For each basin, we computed the normalized longitudinal profile, the hypsometric curve, the area-slope

distribution and the normalized steepness index (ksn). We also studied the first-order vertical steep knickpoints within the study area. This morphometric analysis was accompanied by fieldwork to examine morphometric anomalies, wind gap locations and deformation features in Quaternary sediments to determine the possible relation between morphometry anomalies and active tectonic structures or fluvial captures.

3.3.1. Morphometric analysis

a) Drainage network extraction and selection of drainage basins

To perform the morphometric analysis, we used a DEM of the Shuttle Radar Topography Mission (SRTM) from the National Aeronautics and Space Administration (NASA) and the National Geospatial-Intelligence Agency (NGA). This DEM provides a grid of 1 arc-second of resolution (approximately 30 m), a linear vertical relative height error of less than 10 m and a circular relative geolocation error of less than 15 m (Farr et al., 2007). To extract the drainage network for the morphometric analysis we used the "D8 flow" algorithm (O'Callaghan and Mark, 1984) and delineated channels with an area threshold of 3 km^2 (Figure 3.15). Once having the main channels of Northern Tunisia rivers, we delineated its associated drainage basins by using the ArcGIS software (Figure 3.15).

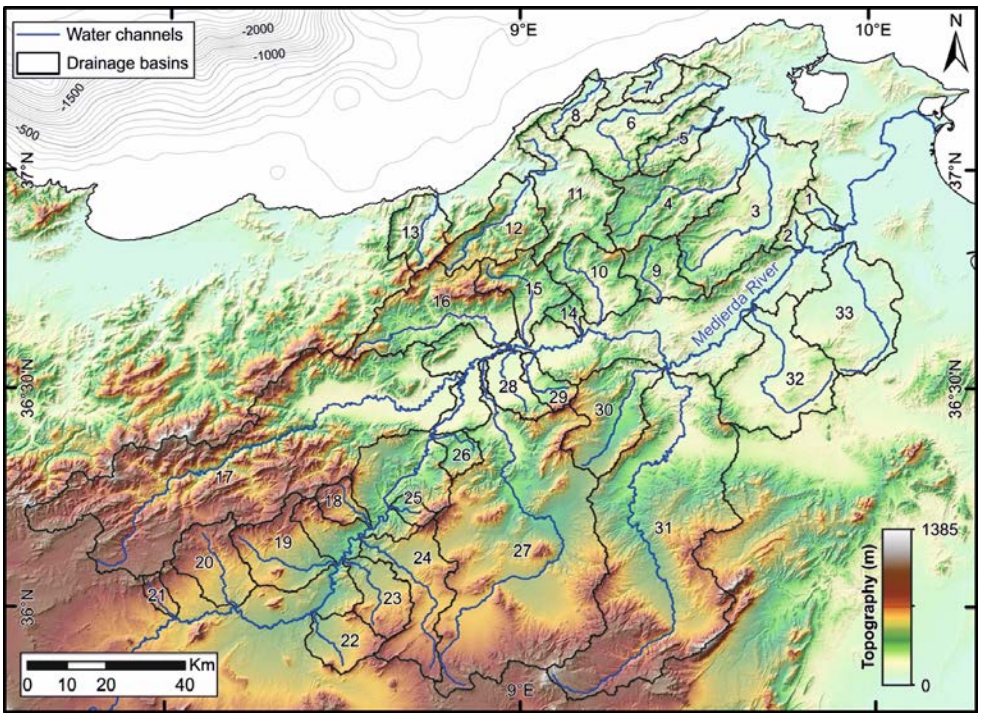

Figure 3.15. *Main Medjerda River and tributary channels of northern Tunisia. Its associated drainage basins have been used in the morphometric analysis. The numbers refer to the different catchment areas.*

b) River normalized profiles

Rivers in equilibrium condition develop a typical concave-shaped profile, with higher gradients in source areas and gentler near the mouth. This shape can be interpreted as the long-term resulting balance between internal forces that produce surface uplift and external processes that tend to erode it away. Any deviation of this equilibrium profile suggests active uplift or lithological changes of the riverbed (Brookfield, 1998; Pérez-Peña et al., 2009a; Matoš et al., 2016). Analysis of river longitudinal profiles has been used to discern the role of lithology and tectonic uplift as controlling factors (Brookfield, 1998; Pérez-Peña et al., 2009a; Kirby and Whipple, 2012; Giaconia et al., 2012a). However, the comparison of longitudinal profiles from rivers with different lengths and gradients can be intricate. Demoulin (1998) proposed the representation of river longitudinal profiles in a normalized form. These profiles show relative distances and elevations in a range from 0 to 1, by normalizing with the total length and relative elevation of each river. This representation allows comparing rivers with different lengths and gradients (Demoulin, 1998; Ruszkiczay-Rüdiger et al., 2009; Castillo et al., 2013; Matoš et al., 2016). This normalized form also allows extracting geomorphic metrics to evaluate profile concavity. The concavity factor (Cf) is defined as the percent area of the triangle between the river profile and the line connecting mouth and source (Figure 3.16). The normalized distance from head to the point where the maximum concavity (MaxC) is reached is defined as MaxL (Figure 3.16).

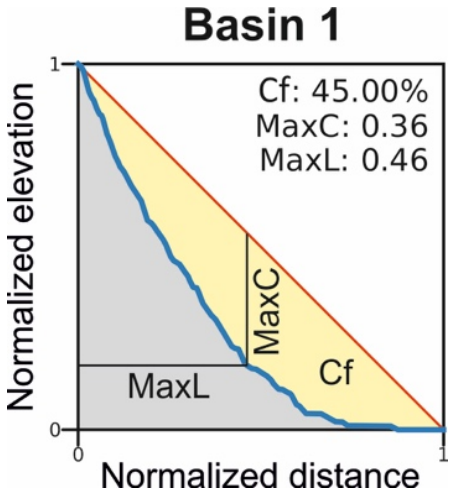

Figure 3.16. *Example of a normalized river profile from basin n° 1 (location of the profile is shown in Figure 3.15). Cf: percent concavity (area in yellow), MaxC: maximum concavity, MaxL: distance where the maximum concavity occurs.*

In this work we computed the normalized profiles with their related indexes (Cf, MaxC and MaxL) for the trunk channels of the selected drainage basins. These parameters allow analysing the equilibrium stage of selected rivers, i.e. how these rivers move closer or away from their graded

profiles. Ideally, normalized river profiles with high Cf and low MaxL (rivers with maximum concavities close to the river source) are characteristic for concave profiles that are approaching their equilibrium stages, while convex profiles with low Cf are characteristic for areas where tectonic uplift is dominant (Demoulin, 1998; Ruszkiczay-Rüdiger et al. 2009; Castillo et al., 2013; Matoš et al., 2014; 2016).

c) Channel steepness index

Bedrock rivers depict a power relation between channel slope and its discharge (approximated by up-stream area) (Equation 3.2):

$$\frac{dz}{dx} = \left(\frac{U}{K}\right)^{\frac{1}{n}} A_{(x)}^{-\frac{m}{n}} \qquad \textit{Equation 3.2}$$

Where dz/dx is the local channel slope, U is the rock uplift rate, K is an erodibility coefficient, A is drainage area, and m and n are empirical constants (Seidl and Dietrich, 1992; Howard et al., 1994; Perron and Royden, 2013). In this equation, $(U/K)^{1/n}$ refers to channel steepness (ks) and n/m to the concavity index (θ). The concavity index typically varies in a narrow range (~0.4-0.6) and it is thought to be relatively insensitive to differences in rock uplift rate and bedrock lithology (Kirby and Whipple, 2012; Whipple et al., 2013). However, the steepness index is directly related to uplift-rate (U) and soil erodibility (K), thus making this index a useful metric in landscape analysis (Whipple and Tucker, 1999; Whipple, 2004; Kirby and Whipple, 2012; Ferrater et al., 2015; Matoš et al., 2016; Andreani and Gloaguen, 2016).

One of the most popular approaches to estimate the channel steepness is through the integration of both sides of Equation 3.2, which leads to Equation 3.3 (Perron and Royden, 2013):

$$z_{(x)} = z_{(x0)} + \left(\frac{U}{KA_0^m}\right)^{\frac{1}{n}} X \qquad \textit{Equation 3.3}$$

With

$$X = \int_{x0}^{x} \left(\frac{A_0}{A_{(x)}}\right)^{\frac{m}{n}} dx \qquad \textit{Equation 3.4}$$

Equation 3.3 has a linear form that relates a new horizontal coordinate (X) (Equation 3.4) with the profile elevation (Perron and Royden, 2013; Royden and Perron, 2013), the slope of this line will be the ksn index (A_0 is normally taken as 1 m^2 to remove dimensionality).

In this work, we use the analytical solution proposed by Perron and Royden (2013) to calculate Chi values at pixel level by calculating the cumulative sum of $(A_0/A(_x))^{m/n}$ upstream for a fixed concavity (θ_{ref}), and multiplying by the distance between two neighbouring pixels. The Chi index, in spite of having units of meters, can present large-scale variations by using different θ_{ref} values. A general value of 0.45 is often used as a convenient value for large drainage basins (Willett et al., 2014; Yang et al., 2015), however a finer analysis can be achieved by using a m/n value that minimize dispersion in chi plots (Perron and Royden, 2013; Willet et al., 2014; Goren et al., 2015).

In order to select the best reference concavity for the study area, we performed a sensitivity analysis based in previous works (Perron and Royden, 2013; Willet et al., 2014; Goren et al., 2015). The slope of a chi-elevation plot is defined as $(U/K\ A_0^m)^{1/n}$, thus profiles that present changes in uplift (U) or lithology (K) along their lengths will present different slopes. This fact makes that look for a m/n that maximize individual profile linearity is not the best strategy. A different approach has been suggested in recent works, by selecting a m/n value that minimize dispersion of the data in Chi-elevation space. To account for this dispersion, we plotted all possible values of chi-elevation from Medjerda basin (i.e. all pixels belonging to the network) and computed R2 of their linear regression for different m/n values from 0 to 1 (Figure 3.17). The reference m/n value of 0.3 produces the best fit (Figure 3.17), i.e. the minimum dispersion between the different channels of the basin. To illustrate this, the Figure 3.18 depicts the chi profiles with their R2 for m/n values of 0.2, 0.3 and 0.4, showing that the chi plot with m/n = 0.3 minimizes dispersion.

Our approach estimates the ksn index along a channel by linear regressions in Chi-elevation space in two different ways: i) Local values of ksn index are calculated for all the pixels of the whole drainage network by taking linear regressions with wide windows of 15 pixels down and upstream (or more with especially noisy profiles, Figure 3.19). This approach to calculate gradients (slope and ksn), spite of slightly lowering absolute values, minimizes profile noise and retain profile knickpoints (Figure 3.19). The local ksn values have been used to derive ksn profiles for each channel and a ksn map for the whole study area. Alongside with regression slope (gradients), we also obtain R2 values, in order to remove those with low linearity (high noise). To generate the ksn map, also points with very high values due to reservoirs or DEM errors have been removed. ii) By the other hand, regional ksn trends have been derived by doing linear regressions on Chi profiles. These regressions depict mean ksn trends, and also allow locate slope break knickpoints between segment with very different regional ksn.

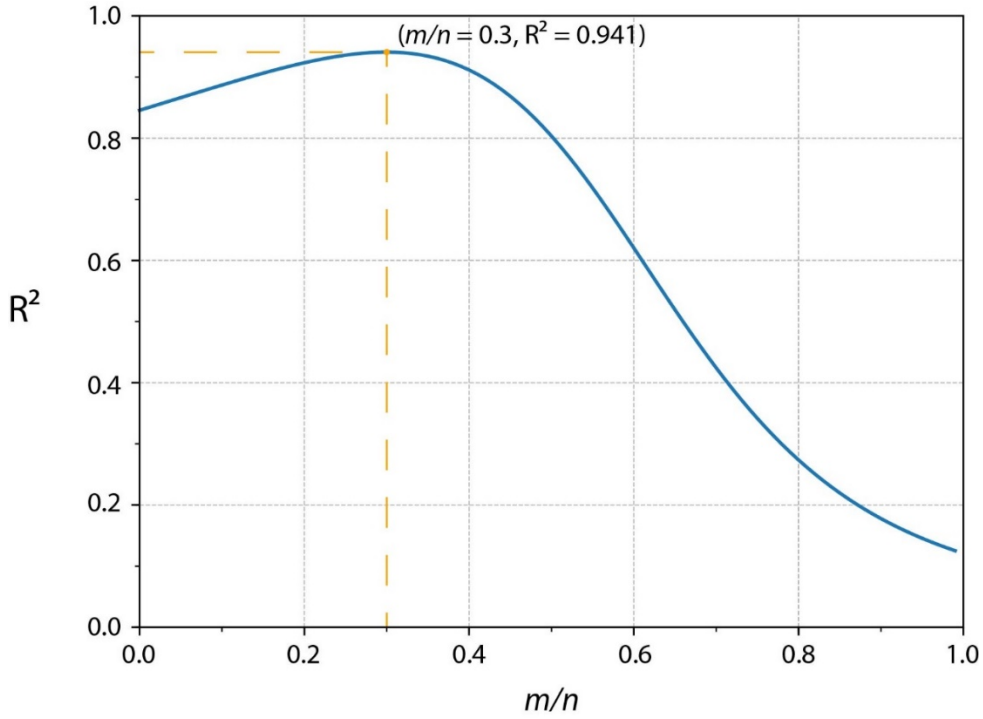

Figure 3.17. *Sensitivity analysis of m/n for the Medjerda basin. We have computed the R2 for the chi and elevation of all the points of the basin computed with different m/n values (from 0 to 1 with a step of 0.01). The reference concavity that produces the higher correlation and thus minimum dispersion is 0.3.*

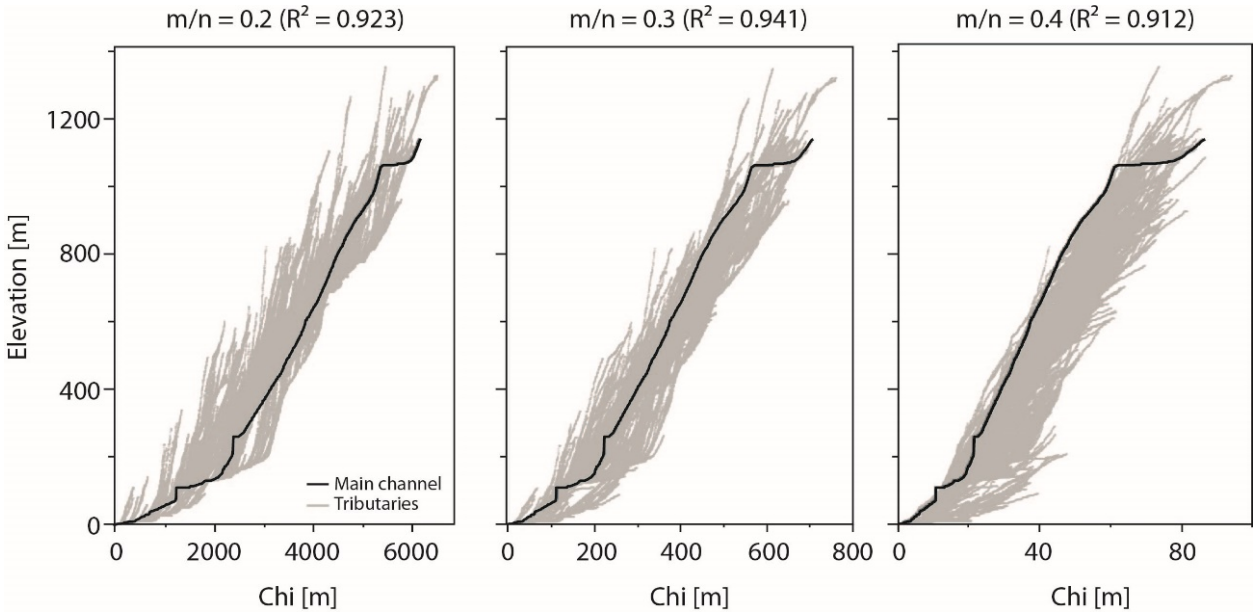

Figure 3.18. *Chi plots for all the tributaries of the Medjerda river computed with m/n values of 0.2, 0.3 and 0.4. R2 values of the sensitivity analysis are indicated.*

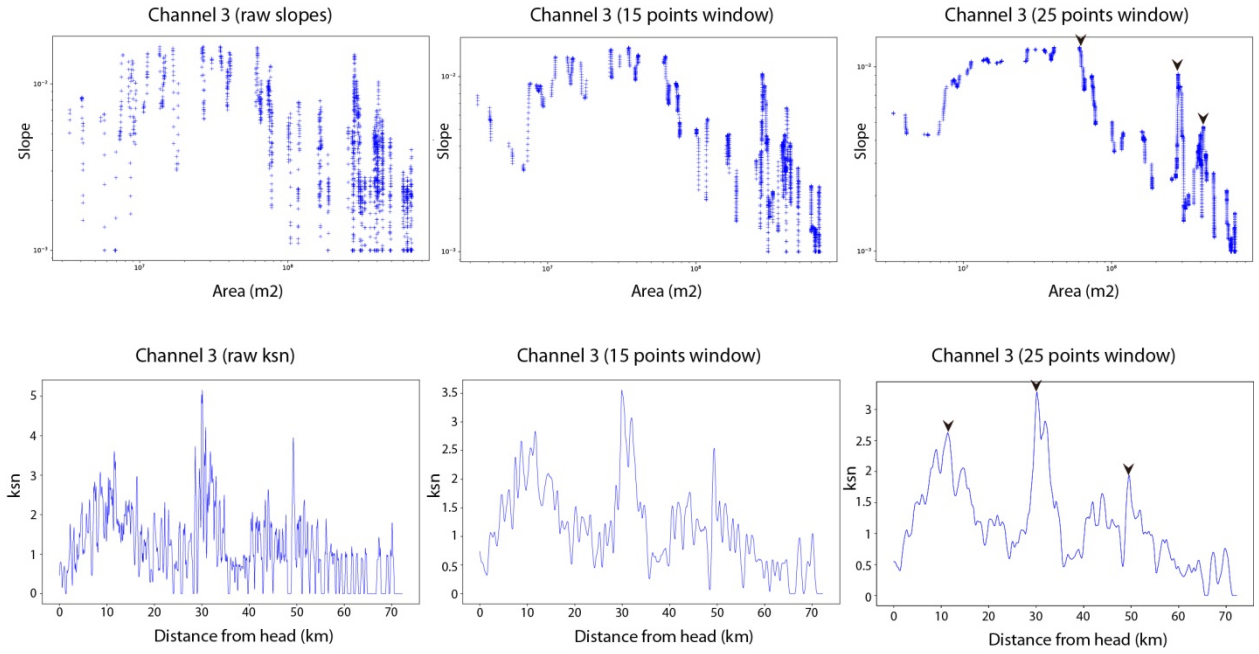

Figure 3.19. *Effect of estimating profile gradients (slope and ksn) with regression using wide windows centered in each pixel. Note that the 25 points window (up and downstream) slightly lower absolute values, but minimize noise at the same time that define knickpoints better.*

d) Knickpoint analysis

Abrupt slope changes or changes in slope trends along river longitudinal profiles are commonly known as knickpoints. They are defined as the "fluvial portion of the transient boundary between adjusting and relict topography" (Crosby and Whipple, 2006). Knickpoints in erosive systems form in response to a perturbation (tectonic activity, lithological changes, capture processes, etc.) that produces a migrating boundary that separates upstream regions that remain unaffected from downstream regions that are adjusting to the new conditions.

As we calculated the local ksn values for each pixel of the main channels, we can derive ksn plots for them (Figure 3.20). Knickpoints will be depicted in these profiles as "peaks", making also possible to record their absolute values of ksn. However, as these ksn profiles can show noise, we would combine the logarithmic area-slope plot with these new derived ksn profiles. By general rule, we won't consider any knickpoint that is not clearly depicted in area-slope logarithmic plots. In case of noisy data, we will increase the number of points to derive local ksn and slopes (Figure 3.19). In the case of segments with a high regional ksn value, the knickpoint only will be considered whether its value is clearly higher than the regional ksn of the segment to discard possible artifacts (Figure 3.20). We only will consider knickpoints with ksn values larger than 2.5 and classify them into three different classes; i) minor or local knickpoints (ksn between 2.5 and 4.5), ii) moderate knickpoints (ksn between 4.5 and 6.5), and iii) major knickpoints (ksn over 6.5).

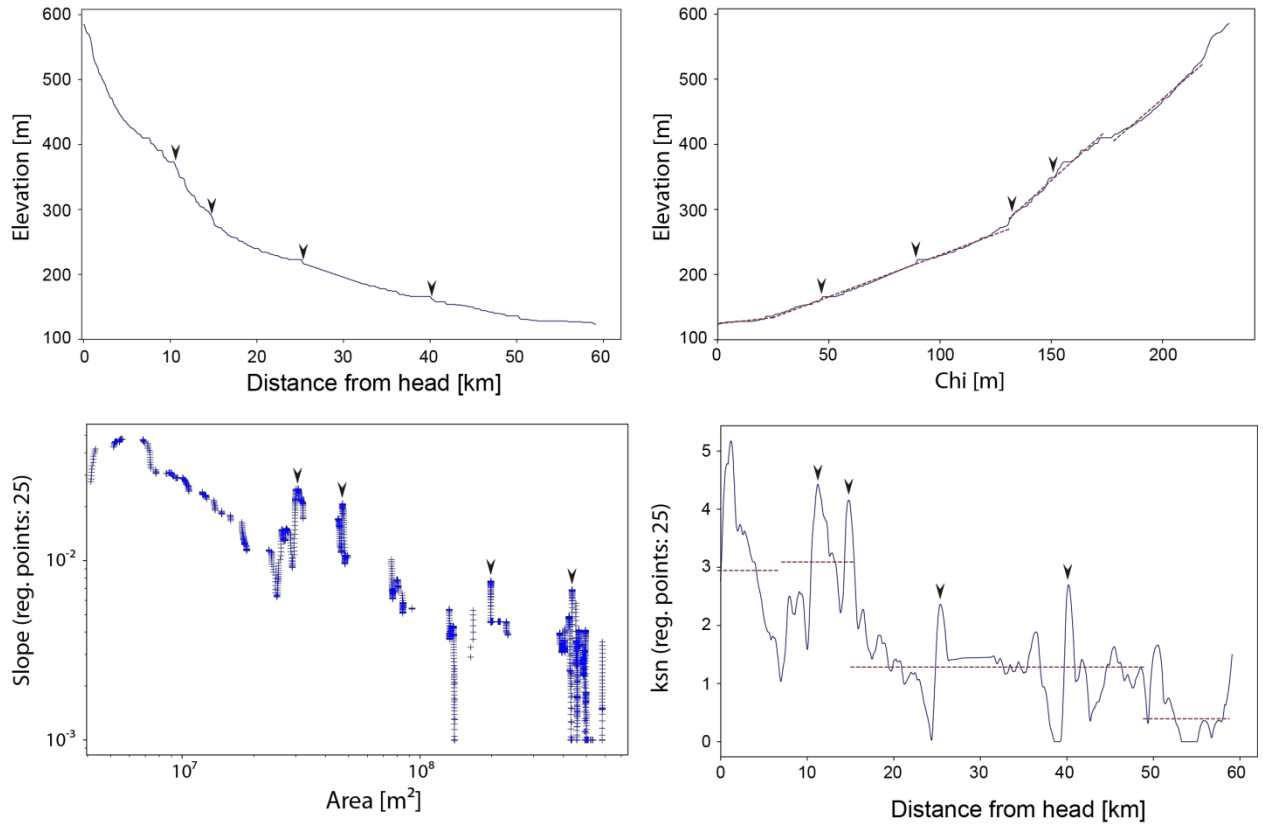

Figure 3.20. *Four different profiles used in this work; longitudinal profile, chi profile, area-slope logarithmic plot and ksn profile. Derived knickpoints are shown in the four profiles. Regresed ksn segments derived in the chi plots are also shown in the ksn profile. Only knickpoints clearly identified in the area-slope plots are defined (note the first peak in the ksn profile that is located in the colluvial part of the profile has been discarded).*

e) Hypsometric curves and integral

Hypsometry studies the mass distribution within a drainage basin in terms of area-elevation (Strahler, 1952), and can be evaluated by the hypsometric curve and the hypsometric integral (Hi). The hypsometric curve describes the distribution of cumulative relative areas (a/A) vs. relative elevations (h/H), and the Hi is a measure of the relative area below the curve (Strahler, 1952; Ohmori, 1993; Keller and Pinter, 2002) (Figure 3.21). The shape of this curve correlates with the stage of geomorphologic evolution of a particular drainage basin and, therefore, provides useful information about its erosional stage (Strahler, 1952; Ohmori, 1993; Pérez-Peña et al., 2009b). Basins in a young stage of development will depict convex-shaped curves, mature basins will yield S-shaped curves, and intensively eroded basins close to the peneplain stage will draw highly concave curves (Strahler, 1952; Ohmori, 1993; Pérez-Peña et al., 2009b). In active mountain ranges, hypsometric curves will evolve over time and will inform about the interplay between tectonic forces that tend to maintain convex curves, and erosional processes that push hypsometric curves to mature and concave shapes (Pérez-Peña et al., 2009b, Ferrater, et al., 2015; Matoš et al., 2016).

River capture processes will produce an increase of convexity from mouth to head, due to the advance of the new incision wave by headward erosion (Pérez-Peña et al., 2009b; Ferrater et al., 2015). In this work, we extracted the hypsometric curves for the selected basins with the aid of *CalHypso ArcGIS tool* and the data from the 30 m DEM explained above (Pérez-Peña et al., 2009b).

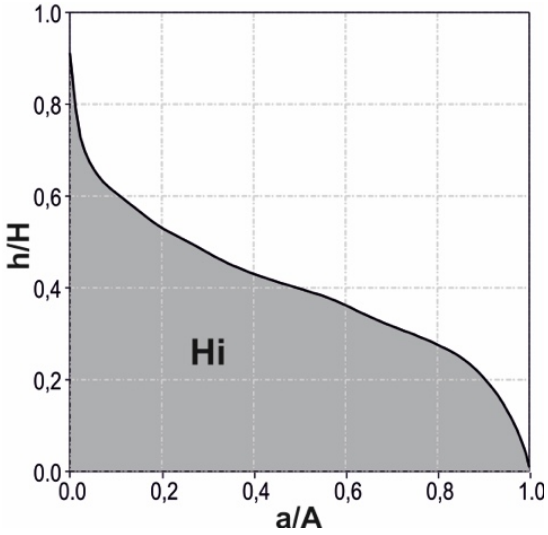

Figure 3.21. *Example of a hypsometric curve (basin n° 30). The grey area under the curve is the hypsometric integral (grey area, Hi). Total elevation (H) is the relief within the basin (maximum elevation minus minimum elevation), total area (A) is total surface area of the basin, and area (a) is the surface area within the basin above a given altitude (h).*

3.3.2. Fieldwork

The morphometric analysis (Section 3.1.1) was completed and ground-truthed with a field campaign focusing on the most interesting locations. First, we analysed some of the faults with potential activity indicated by the morphometric analysis. We studied their kinematics, measured *striae* and dips, and searched for recent sediments affected by these faults. Secondly, we studied Pliocene to Pleistocene river terraces closer to the faults, in order to evaluate their location with respect to the actual rivers. Thereby, we focused on the identification of terraces in abandoned fluvial channels, likely related to river captures. We analysed striated pebbles in these abandoned terraces by measuring dip, direction and sense of movement (when possible) of *striae*, and performed a stress analysis with the *T-Tecto* software (Figure 3.22). These structural markers preserve information on the stresses that their host rocks have undergone (Ruano and Galindo-Zaldívar, 2004). Finally, we looked for paleoseismological indicators, such as colluvial wedges, recent fault scarps, co-seismic cracks, etc. (e.g. Papanikolau et al., 2015). Due to the large extent of the field area analysed by the morphometric analysis, we restricted the fieldwork to a limited area where we ground-truthed our geomorphic interpretation.

Figure 3.22. *Fieldwork photos. a) Me and J.V. Pérez Peña (from the Universidad de Granada, Spain) measuring striae from pebbles in an abandoned terrace of the Tine River in Northern Tunisia, b) An example of a striated pebble.*

3.4. Methods for seismic hazard assessment

3.4.1. Seismicity and focal mechanism datasets

To analyse the earthquake distribution and type within the region we use seismicity datasets taken from the ISC (ISC, 2018) and the ISC-GEM (ISC-GEM, 2018) catalogues. We also use focal mechanism solutions from the Global CMT (Global CMT, 2015) and the European-Mediterranean RCMT catalogues (RCMT, 2015).

a) ISC Bulletin

The ISC (International Seismological Centre) Bulletin is the primary output of the ISC and contains data from year 1900 to present day. This bulletin is the longest, continuous and definitive summary of the seismicity of the world. Data of the bulletin is collected from over 130 seismological agencies around the world including hypocentres, phase arrival-times, focal mechanism solutions, etc. These data are automatically grouped into events and an automatic threshold process decides whether each event should be checked manually by ISC analysts and then relocated (ISC, 2018). The ISC Bulletin is available on http://www.isc.ac.uk/iscbulletin/.

b) ISC-GEM catalogue

The ISC-GEM (International Seismological Centre - Global Earthquake Model) Global Instrumental Earthquake catalogue (1904-2014) results from the aim to improve the currently existing global catalogs for large earthquakes (magnitude $M_w > 5.5$) and to serve to user groups who asses and model seismic hazard and seismic risk. This ISC-GEM catalogue presents a major

improvement compared to previously products because it contains homogeneous locations and magnitudes with uncertainty estimations using uniform techniques (where possible) (Storchak et al., 2013; ISC-GEM, 2018). The ISC–GEM catalogue is available on www.isc.ac.uk/iscgem and its last version 5.0 was publicly released on the 27 of February 2018 (Figure 3.23).

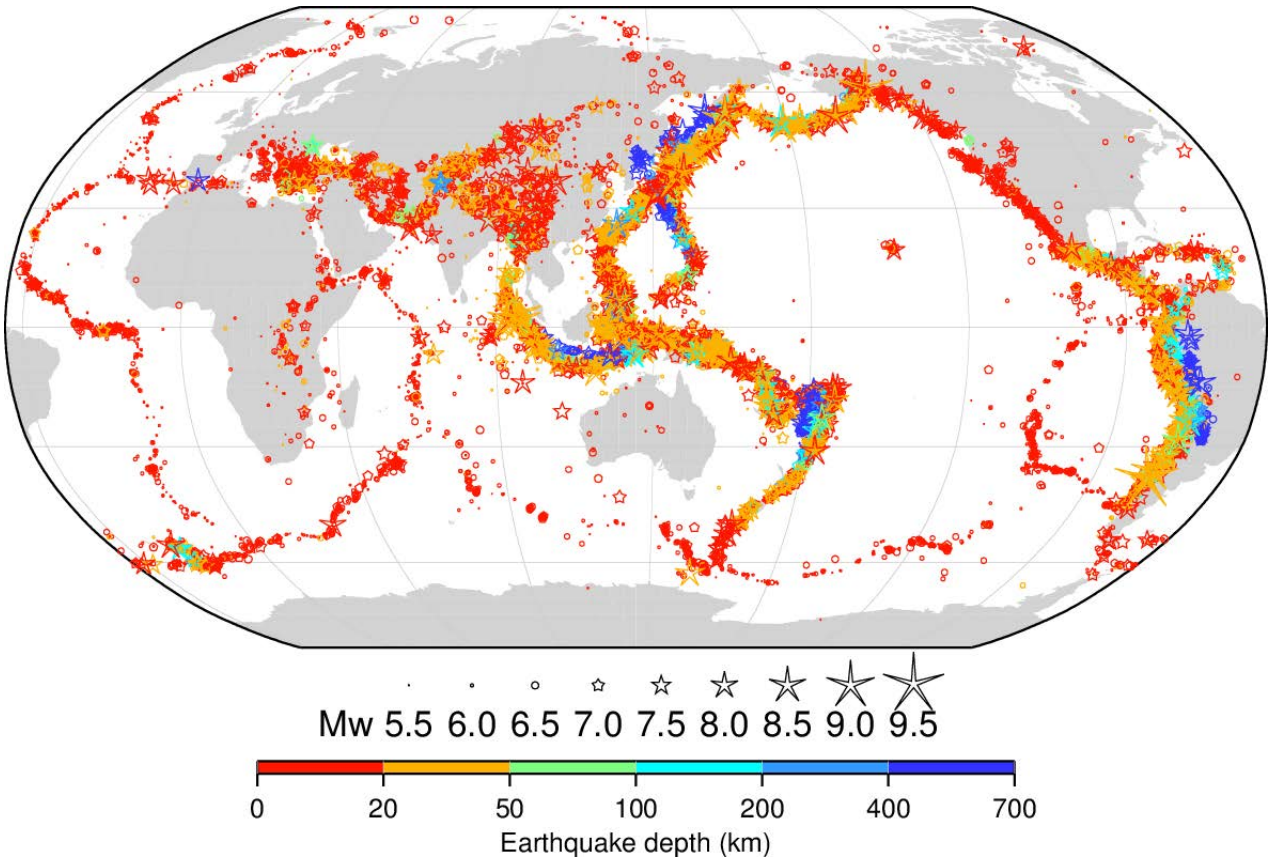

Figure 3.23. *Map of the earthquakes listed in the version 5.0 of the ISC-GEM Catalogue from year 1904 to 2014, which includes more than 28,000 events (ISC-GEM, 2018).*

c) Global CMT catalogue

The Global Centroid-Moment-Tensor (CMT) project is founded by the National Science Foundation (USA) and its catalogue contains more than 25,000 moment tensors for earthquakes since 1976 (Global CMT, 2015) (Figure 3.24). The Global CMT catalogue is available at http://www.globalcmt.org/.

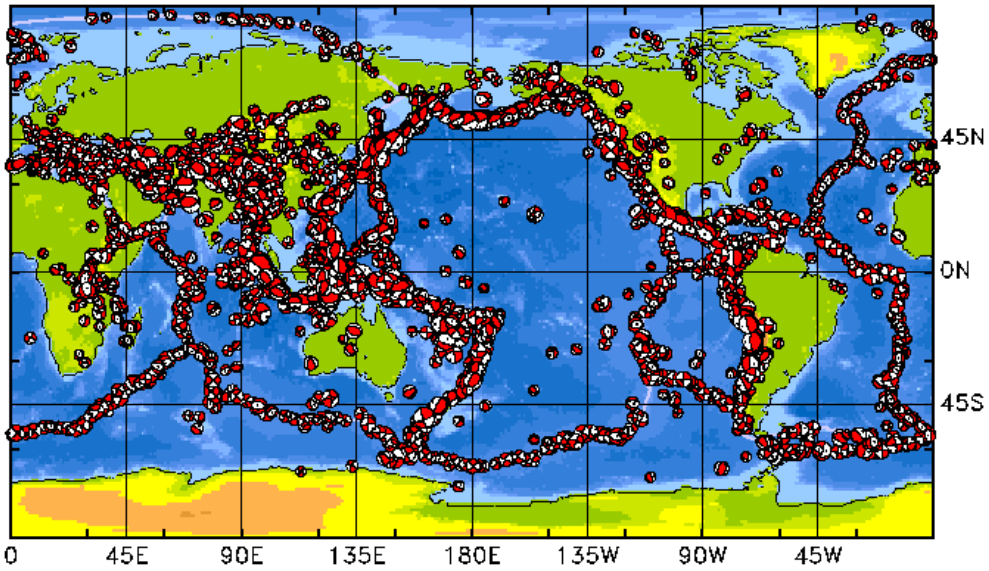

Figure 3.24. *Map of the focal mechanism or moment tensor solutions from the Global CMT catalogue displaying shallow intermediate to high magnitude earthquakes for the years 1976-2005 (Global CMT, 2015).*

d) European-Mediterranean RCMT catalogue

The European-Mediterranean RCMT (Regional Centroid-Moment Tensors) catalogue hosts information of seismic moment tensors in the European-Mediterranean area. This catalogue collected data since 1997 for intermediate magnitude earthquakes ($4.5 < M_w < 5.5$) occurring in the area. The European-Mediterranean RCMT catalogue is available at http://rcmt2.bo.ingv.it/.

3.4.2. Earthquake maximum magnitude estimation

To estimate the maximum earthquake magnitude (M_w) expected for the faults identified, we use two empirical equations that relate rupture length (R_L) and maximum magnitude (M_w). These empirical relationships can be applied in Northern Tunisia, since active faults identified are located in continental crust and seismicity within the study area is relatively shallow as constrained to the crust (Soumaya et al. 2015). On one hand, we use one of the first empirical relationships proposed for continental crust faults, the one of Wells and Coppersmith (1994), and on the other hand, we use one of the most recent equations and specifically for low rate (<10 mm/y) faults in continental crust contexts, the one of Wesnousky (2008). This equation is included in Stirling et al. (2013), one of the most updated compilations of empirical equations for earthquake magnitude estimation.

The equation proposed by Wells and Coppersmith (1994), is based on empirical parameters from 77 continental crust instrumental earthquakes, and estimates the moment magnitude (M_w) expected according to the surface rupture length of the fault (LRS) (Equation 3.5).

$$M_w = a + b * \log(LRS) \qquad \textit{Equation 3.5}$$

where a and b vary according to the fault type, as shown in Table 3.1.

Fault type	Coefficient (a)	Standard error (b)
Strike-slip	5.16 (0.13)	1.12 (0.08)
Reverse	5.00 (0.22)	1.22 (0.16)

Table 3.1. *Wells and Coppersmith (1994) coefficients for the calculation of M_w depending on rupture length.*

To obtain the strike-slip parameters, Wells and Coppersmith (1994) used earthquakes with magnitudes (M_w) ranging from 5.6 to 8.1 and surface ruptures lengths between 1.3 and 432 km, while for reverse faults, they used earthquakes with magnitudes (M_w) between 5.4 and 7.4 and longitudes ranging from 3.3 to 85 km.

The method proposed by Wesnousky (2008) presents different equations according to the fault type to be analyzed. For the present work, we use the equations for strike-slip (Equation 3.6) and reverse (Equation 3.7) faults. These equations were obtained by the empirical study on the basis of 22 strike-slip earthquakes and only 8 events of reverse faults (Wesnousky, 2008). Moreover, all of the referred earthquakes had rupture lengths greater than 15 km and were located in plate boundary settings worldwide (Wesnousky, 2008 in Stirling et al., 2013).

$$M_w = 5.56 + 0.87*\log L \text{ (strike-slip)} \qquad \textit{Equation 3.6}$$

$$M_w = 4.11 + 1.88*\log L \text{ (reverse)} \qquad \textit{Equation 3.7}$$

where L is the fault surface rupture length in kilometers (km).

Part III

RESULTS

CHAPTER 4

Active tectonics and drainage anomalies in the onshore Northern Tunisia

4.1. Introduction

Relief analysis based on drainage network metrics is an appropriate tool to detect and characterize active tectonic structures in regions of low to moderate tectonic activity (e.g. Keller and Pinter, 2002; Molin et al., 2004; Pedrera et al., 2009; Pérez-Peña et al., 2010; Azañón et al., 2012). Recent studies suggested that river network systems will need moderate to long periods (10^4-10^7 yr) to reach their final equilibrium profiles, i.e. steady-state conditions (Goren et al., 2015). However, rates of response increase exponentially from equilibrium and therefore, gross deviation from the equilibrium conditions will reflect relatively recent events (Brookfield, 1998; Pérez-Peña et al., 2009a). The combination of different morphotectonic indices allows us to differentiate uplift from subsiding regions at different scales. This approach together with a geomorphological study and field ground-truth helps to discriminate among different mechanisms that may influence topography and associated development of drainage networks (e.g. Bull and McFadden, 1977; Azor et al., 2002; Giaconia et al., 2012a; 2012b). These methodologies have been previously applied in Tunisia with the same goal, although focusing in a local scale and do not taking into account the whole northern Tunisian region (Slama et al., 2015; Mimouni et al., 2016; Rabii et al., 2016; Sadrette et al., 2016).

The main goal of this chapter is to determine the active tectonic structures that compose the Nubia-Eurasia plate boundary in the Northern Tunisia region, where present-day tectonics has been poorly studied. Thus, we applied a quantitative morphometric method to analyse the topography of northern Tunisia, accompanied by fieldwork in order to determine the evolution of the Medjerda

River fluvial network and its relationship with tectonic structures. Following this approach, we mapped some of the possibly main active faults located in the study area and surveyed potential capture sites, abandoned fluvial channels, and fluvial terraces, searching for evidences of recent deformation, such as striated pebbles in river terraces and seismogenic related structures. Finally, we estimated the seismic potential of two active seismogenic faults that we identified in the frame of this work.

4.2. Methodology

We applied morphometric analyses to characterize the recent tectonic activity and drainage evolution of the onshore North Tunisia area. This analysis has been carried out within a wide area that follows the main NE-SW tectonic trend displayed by the topographic highs and faults (see red polygon in Figure 4.1). First, we identified the drainage network from a Digital Elevation Model (DEM) of ~30 m pixel resolution. We extracted the drainage network using the D8 flow algorithm (O'Callaghan and Mark, 1984), and delineated channels within a threshold area of 3 km^2 with their respective basins. For each basin, we computed the normalized longitudinal profile with its related indexes (Cf, MaxC and MaxL) for the trunk channels, the hypsometric curve, the area-slope distribution and the normalized steepness index (ksn). We also determined the first-order vertical steep knickpoints within the study area. These morphometric analyses were accompanied by fieldwork to examine morphometric anomalies, wind gap locations, and deformation features in Quaternary sediments to reveal the possible relationship between morphometry anomalies and active tectonic structures or fluvial captures. Due to the wide extension of the study area in the morphometric analysis, we restricted the fieldwork to a limited zone where we mapped and ground-truthed our geomorphic interpretation (red box in Figure 4.1). Finally, by using empirical equations and relationships (Wells and Coppersmith, 1994; Wesnousky, 2008) we estimated the seismic potential of two large and active seismogenic faults identified during this work. For further information regarding the different methods applied see Chapter 3.

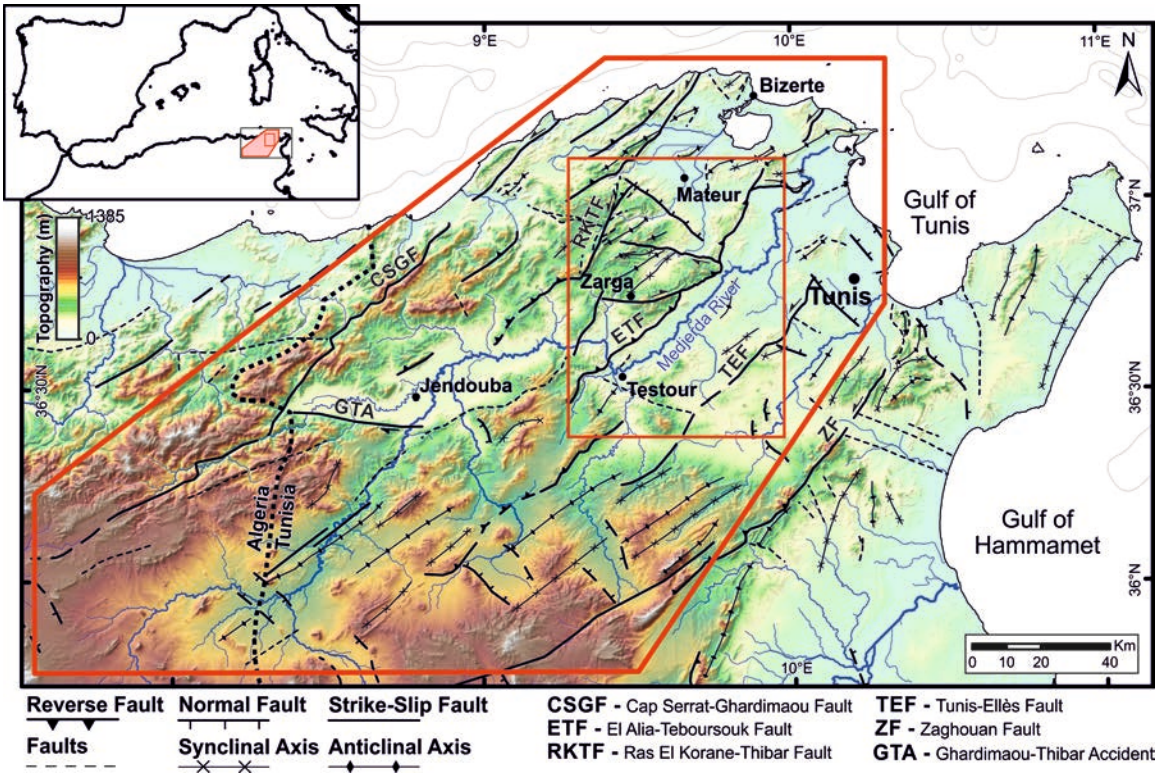

Figure 4.1. *Topographic and tectonic sketch of Northern Tunisia with the main shortening structures in the region and the drainage pattern. The thick red polygon marks the study area onshore. The thin red box shows the area surveyed in the field (Figure 4.14). The upper-left inset shows the location of this figure. Tectonic structures include data from Melki et al. (2012), Bahrouni et al. (2014) and Rabaute and Chamot-Rooke (2015), as well as our own field data.*

4.3. Results

4.3.1. River normalized profiles

We extracted the normalized longitudinal profiles for the 33 basins and the Medjerda River main channel. Due to its length and greater area, we decided to analyse the Medjerda River separately. Concavities (Cf) vary in a wide range from -2.82 % (linear-to-convex profiles) to 67.46% (very concave profiles), with an average value of 29.01% (Figure 4.2 and Table 4.1). From the 33 analysed basins, 10 basins show concavities lower than 20%, thus indicating that they are far from equilibrium conditions (Figure 4.3).

In order to analyse how convexity is distributed over the study area, we followed the approach described by Ruszkiczay-Rüdiger et al. (2009) and Matoš et al. (2014, 2016), by plotting MaxC (maximum concavity) and MaxL (the normalized distance from head to the point where MaxC is

reached) values in a scatter diagram (Figure 4.4). This diagram shows 4 different groups: Groups G1 and G2 indicate unstable young basins, group G3 includes intermediate-stage basins, and group G4 indicates basins that are in a mature stage of development. Young basins of groups G1 and G2 concentrate in tributaries of the Medjerda River south of Jendouba city (basins 18 to 27), whereas in the northern area, basins of groups G3 and G4 predominate (Figure 4.5). The Medjerda River has been classified as intermediate, however, due to its length and complexity it could not be analyzed together with the rest of the basins.

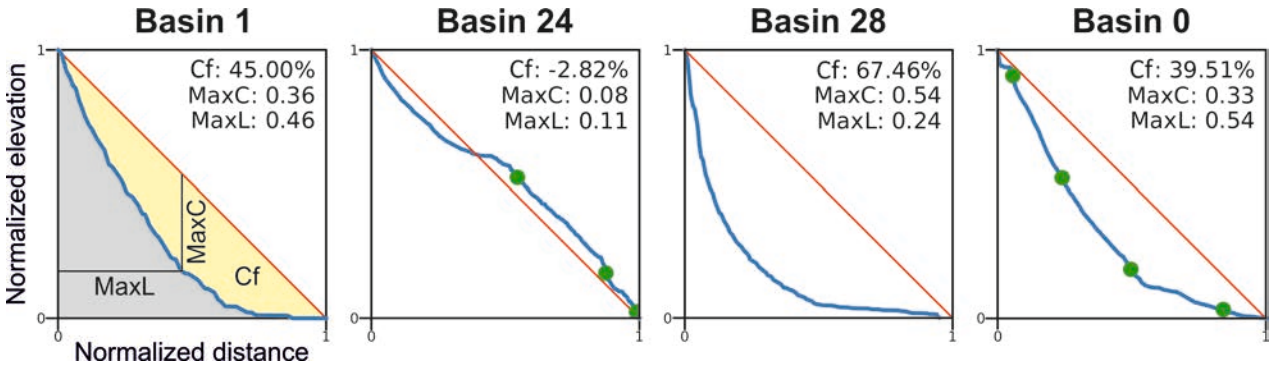

Figure 4.2. *Examples of different types of normalized profiles analysed in the Northern Tunisia study area; linear-to-convex profile (with MaxC < 0.25 and Cf < 25% or even negative in convex profiles, e.g. B24), very concave (MaxC > 0.4 and Cf > 50%, e.g. B28), and intermediate profiles (with intermediate values, e.g. B0 (Medjerda River Basin)). The first profile (Basin 1) shows how related parameters are calculate,. Cf: percent concavity (area in yellow), MaxC: maximum concavity, MaxL: distance where the maximum concavity occurs. The location of the extracted knickpoints is shown by green circles. The rest of the profiles are shown in Figure 4.3.*

ID	Hi	Cf (%)	MaxC	MaxL	Basin Area (km^2)	Channel Lenght (km)
0	0.36	39.51	0.33	0.54	23404.79	527.52
1	0.32	45.00	0.36	0.46	98.55	14.73
2	0.27	39.72	0.31	0.27	60.303	10.43
3	0.29	36.14	0.28	0.46	689.14	72.24
4	0.36	32.77	0.25	0.43	546.542	63.94
5	0.36	35.48	0.31	0.21	156.324	28.03
6	0.30	39.44	0.40	0.19	455.365	61.1
7	0.27	24.88	0.23	0.33	100.618	17.19
8	0.31	36.74	0.29	0.50	124.527	24.43
9	0.34	13.01	0.12	0.60	319.23	30.2
10	0.32	40.48	0.31	0.29	339.532	34.97
11	0.32	32.54	0.28	0.41	492.875	36.8
12	0.41	25.60	0.26	0.61	348.199	42.24
13	0.29	60.52	0.49	0.24	218.283	23.83
14	0.47	6.16	0.08	0.63	54.532	10.52
15	0.30	32.67	0.28	0.41	263.575	38.82
16	0.33	50.55	0.42	0.28	585.802	59.49
17	0.39	40.97	0.31	0.60	2573.478	168.87
18	0.48	14.65	0.14	0.34	101.873	18.84
19	0.34	24.24	0.20	0.21	342.719	35.54
20	0.35	13.80	0.13	0.42	302.171	30.12
21	0.32	27.36	0.21	0.31	55.499	13.61
22	0.26	14.99	0.11	0.70	205.079	22.08
23	0.41	8.03	0.10	0.20	231.605	33.5
24	0.45	-2.82	0.08	0.11	455.064	58.58
25	0.35	20.25	0.17	0.45	54.912	10.78
26	0.32	19.40	0.19	0.27	84.954	18.24
27	0.38	24.64	0.20	0.17	2390.379	146.31
28	0.12	67.46	0.54	0.24	167.573	29.09
29	0.27	33.87	0.25	0.45	100.416	24.37
30	0.40	-1.67	0.03	0.88	454.062	46.81
31	0.35	35.39	0.30	0.31	2219.993	167.76
32	0.21	-2.53	0.07	0.85	652.55	57.13
33	0.24	57.15	0.51	0.25	706.643	73.88

Table 4.1. *Values of geomorphic indexes for selected basins within the study area (see text for further explanation). ID = 0 corresponds to the Medjerda Basin.*

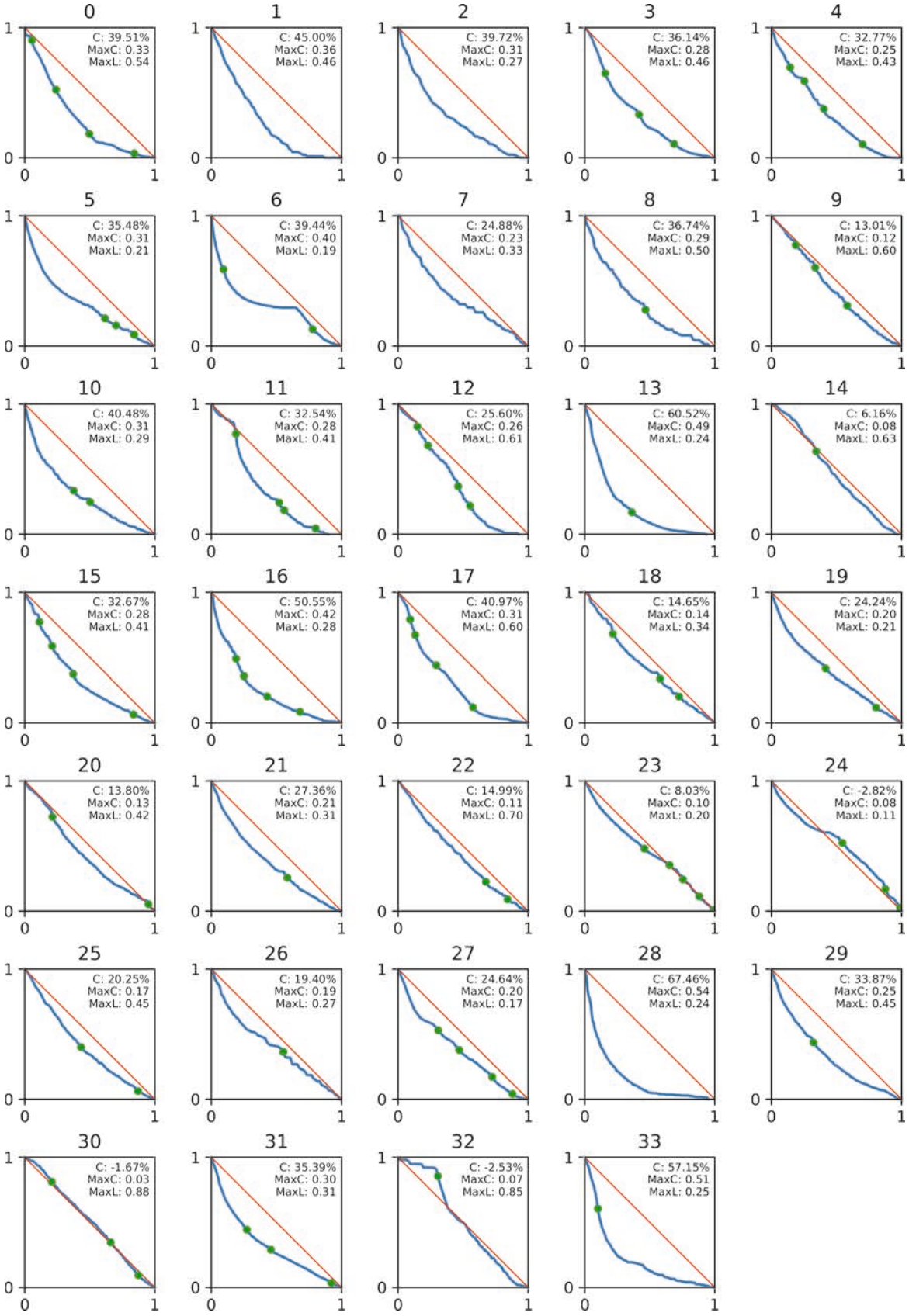

Figure 4.3. *Normalized profiles for the 33 analysed basins and for the Medjerda main basin (Basin n° 0). Knickpoints are extracted from the ksn profiles and are depicted by green dots. Values of concavity (Cf), maximum concavity (MaxC) and distance where the maximum concavity occurs (MaxL) are indicated (see text for further information).*

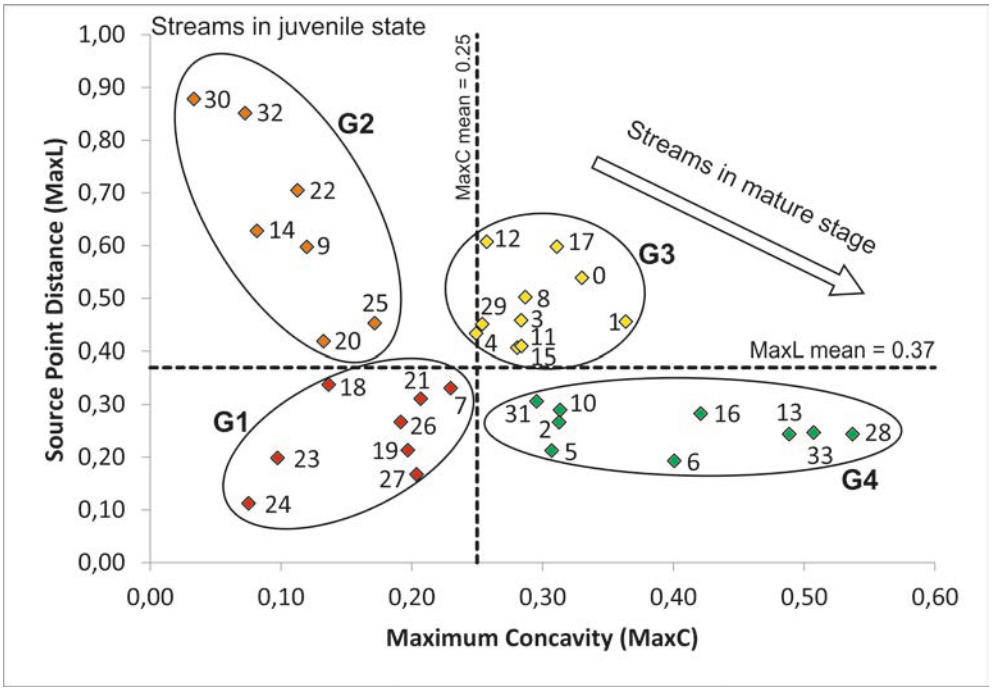

Figure 4.4. *Scatter plot of maximum concavity (MaxC) versus source point distance (MaxL). We differentiate 4 groups on this diagram: G1 and G2 indicate unstable young basins, G3 includes intermediate basins, and G4 corresponds to basins in a mature development stage.*

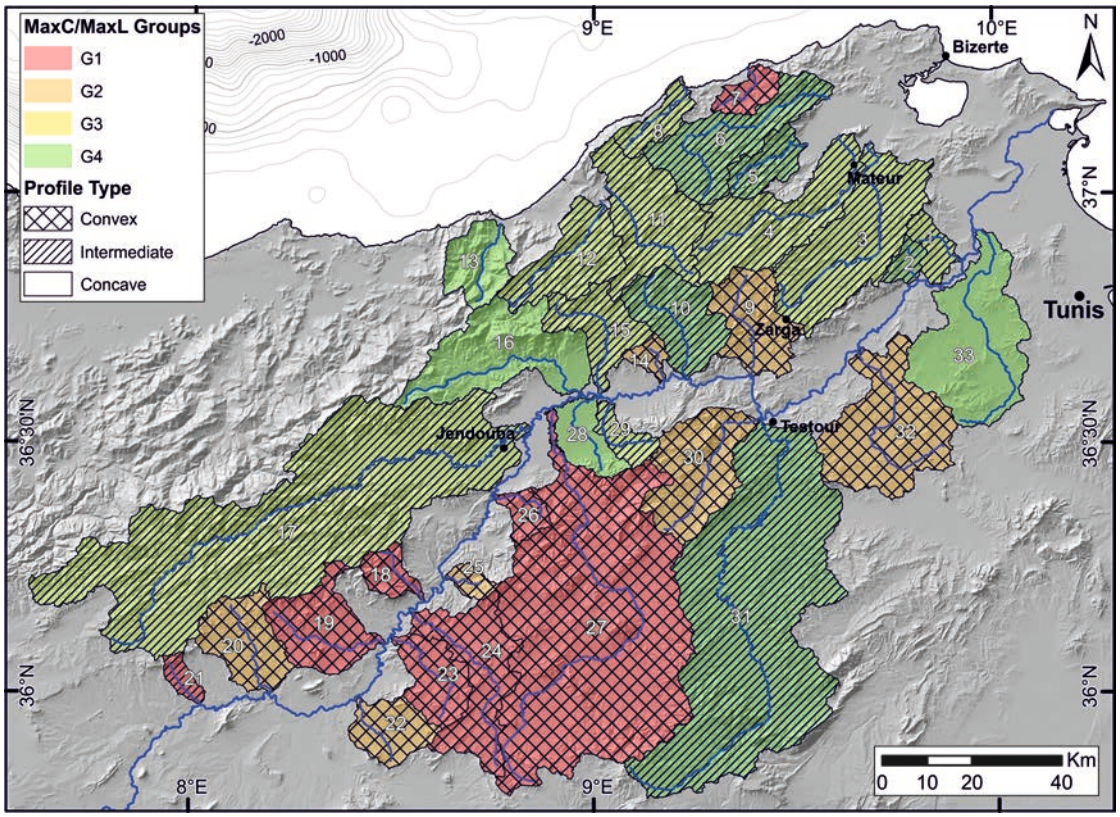

Figure 4.5. *Drainage basins depicted according to the different groups obtained through the scatter plot of MaxC vs MaxL values (Figure 4.4), as well as according to the river profile morphology (convex, intermediate or concave, Figure 4.3).*

4.3.2. Normalized steepness index

According to the sensitivity analysis especially made for the study area, Chi-elevation profiles have been obtained with an m/n coefficient of 0.3 for the whole drainage network. These channels were defined by using an area threshold of 1 km^2 to avoid possible inclusion of colluvial channels dominated by debris-flows (Stock and Dietrich, 2003; Kirby and Whipple, 2012). We used the whole drainage area of the Medjerda basin for the analysis, although here we present only the results within the study area (red polygon in Figure 4.1). In order to spatially analyse the ksn index, we performed regressions for segments of 1 km length over chi-elevation plots and removed those with low linearity (R^2 lower than 0.95). We also removed the segments that included dams or reservoirs. With the remaining ksn segments, we interpolated a surface that shows the distribution ranging from high values (red) to low values (blue) (Figure 4.6).

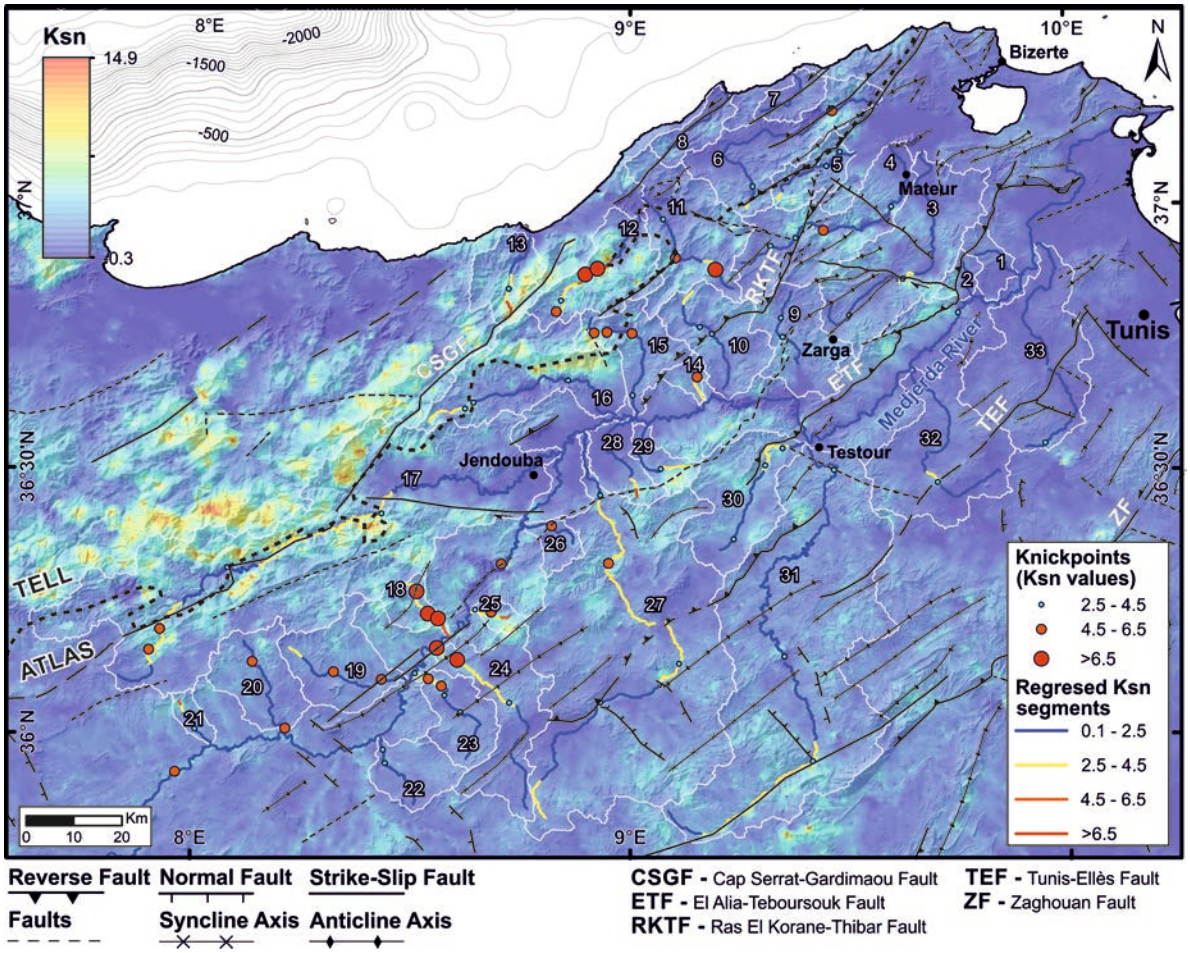

Figure 4.6. *Ksn values heat map for the whole study area and ksn regressed segments over the 33 selected basins. Ksn heat map has been obtained for 1 km length segments for the whole drainage network (channels with a threshold area of 1 km^2). Regressed segments were selected manually by visual inspection of chi-elevation plots. The main tectonic structures are depicted. Knickpoints are also displayed.*

High ksn values are predominant in the western part of the studied area, coinciding with the main division between basins draining towards Argelia and tributaries of the Medjerda River. Basins number 12, 13, 16 and 17 contain the highest values following a NE-SW trend. This cluster of high ksn values placed in the western sector could be masking other relatively high values throughout the study area; similar to the NE-SW trend located in the centre of the study area (lower parts of basins 25, 27 and 30 and upper parts of basins 28 and 29).

Together with the spatial analysis of the ksn index, we also extracted chi-elevation plots for all the trunk channels of the 33 basins analysed (Figure 4.7.a). In general, the northern basins show lower slopes than the southern ones, except those within the Tellian domain (e.g. basins 12 and 13) (Figures 4.6, 4.7.a and 4.8). The Medjerda chi profile shows an interesting slope-break on its junction with tributary number 17, near Jendouba city (Figure 4.7.b). At this point, the Medjerda trunk channel changes its orientation (from ENE to NNE) and increases its slope in the Chi profile, i.e. increases its ksn general trend. The tributary nº 17 maintains the same chi-elevation slope and orientation as the lower reach of the Medjerda River. This observation probably indicates that the tributary nº 17 was the old course of the Medjerda River prior to subsequent river captures occurred in the Medjerda River extending its main course towards the south (Figure 4.7.b).

Finally, the ksn regressed segments made on the chi profiles of the trunk channels (Figure 4.8) show lower values in the northern basins, and present maximum values in transverse channels as basins 18, 24, 25, 28 and 29 and lower part of basin 30, noting recent uplifts in this southern region and thus coinciding with the ksn map (Figure 4.6). These regressed ksn segments also depict the same feature observed in the Chi profiles; ksn values for the channel nº 17 is higher west of Jendouba, but it presents similar values than the Medjerda trunk channel on its lower part.

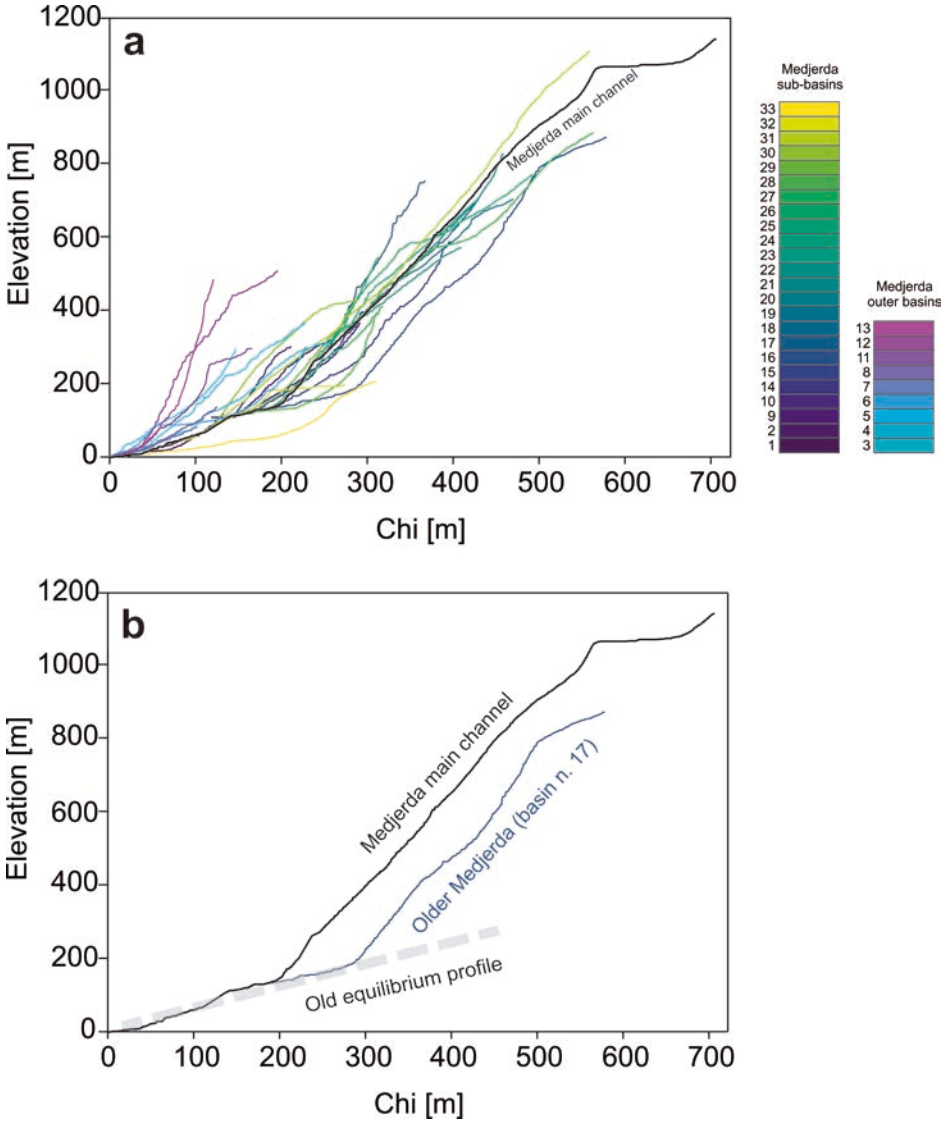

Figure 4.7. *(a) Chi-elevation plots for all the selected basins. Basins are differentiated by color and Medjerda main channel is depicted in black. Medjerda profile shows a steeper gradient than its tributaries, which indicates an increase in drainage area. (b) Chi-elevation profiles for Medjerda main channel and basin nº 17, which is interpreted as the old course of the Medjerda River. Note how the lower part of the basin nº 17 maintains the same trend as mouth of the Medjerda River (i.e. old equilibrium profile).*

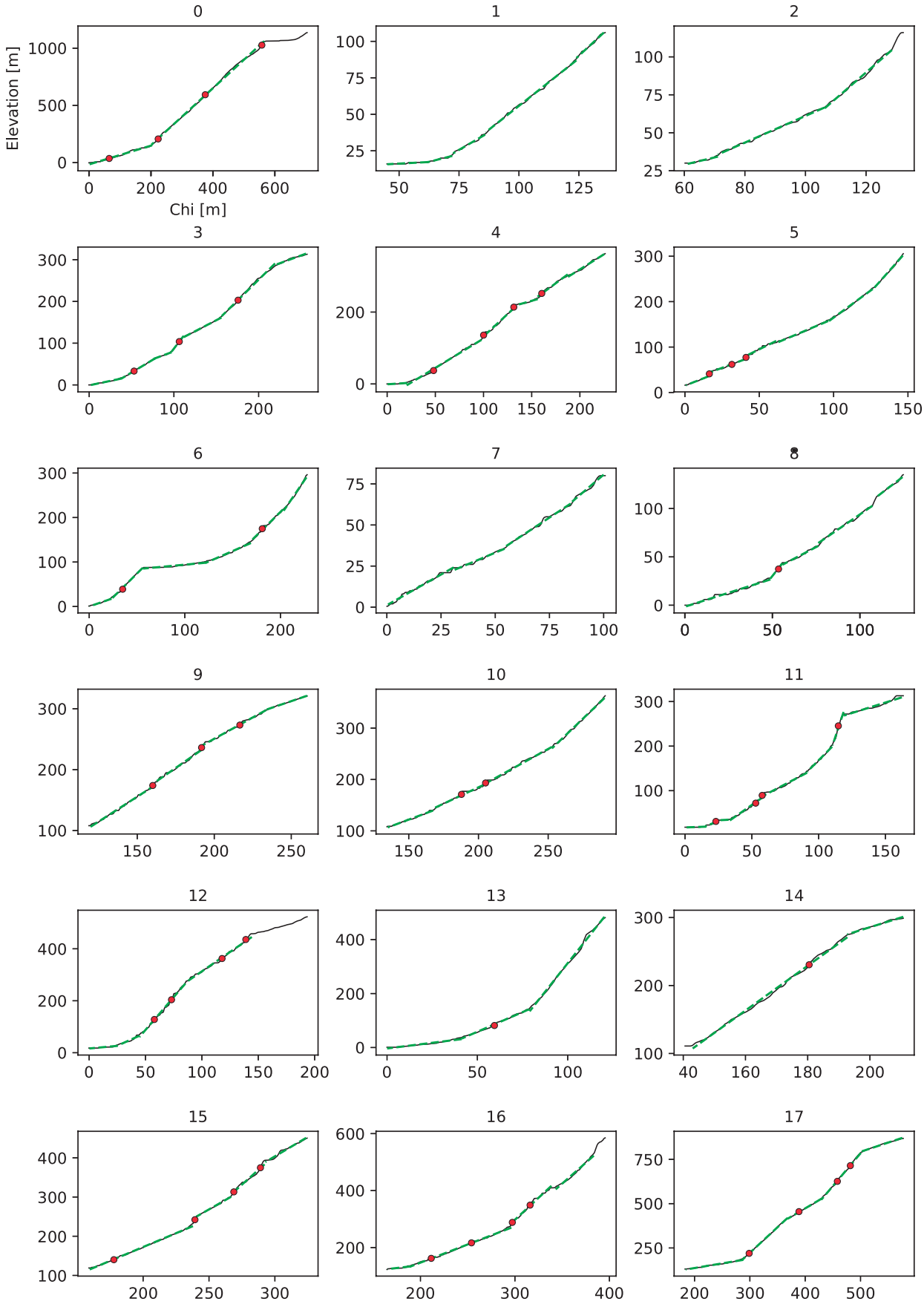
0
1
2
3
4
5
6
7
8
9
10
11
12
13
14
15
16
17
Elevation [m]
Chi [m]

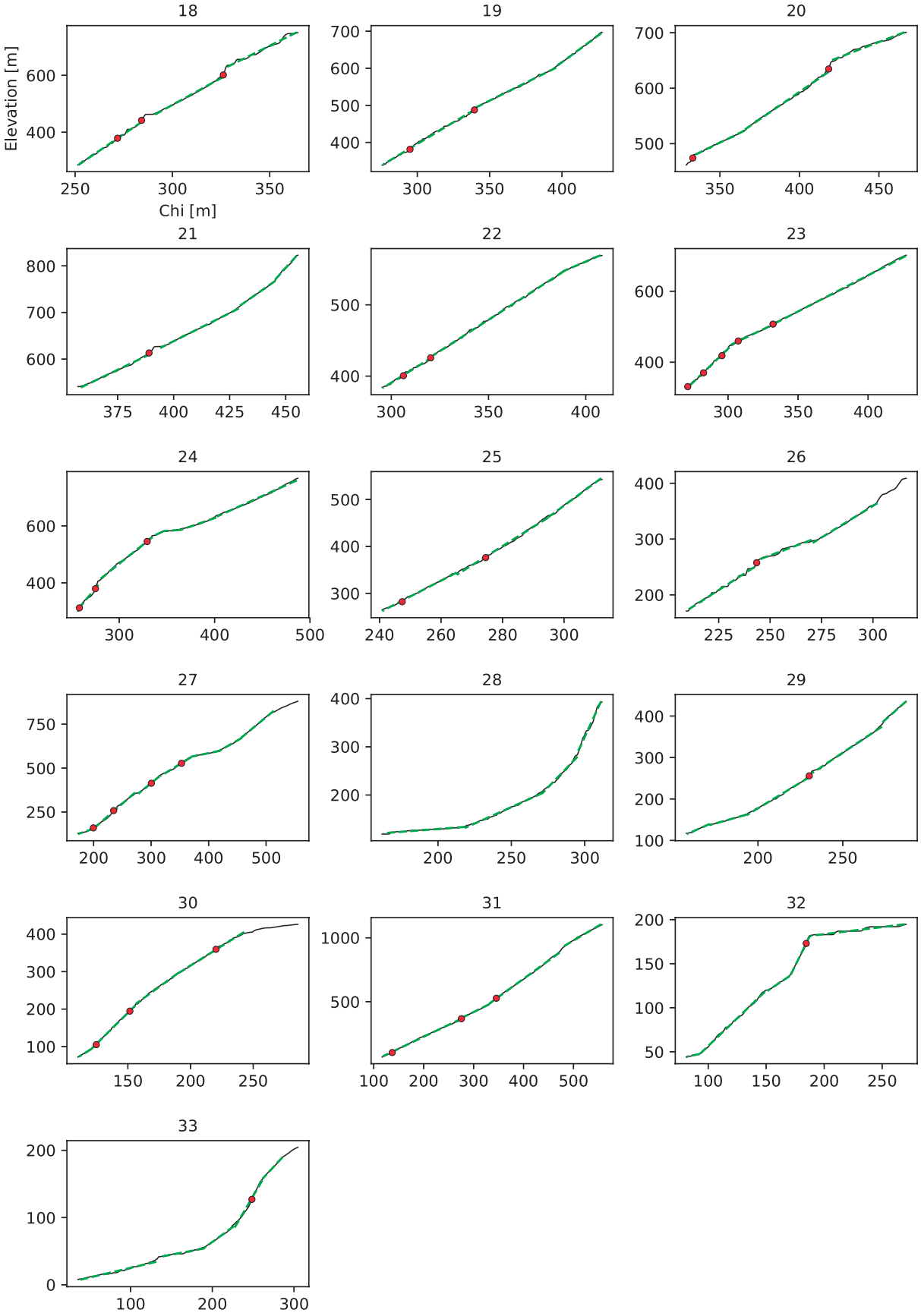

Figure 4.8. *Chi-elevation profiles for the trunk channels of the 33 analysed basins and for the Medjerda main channel (Channel number 0). Derived knickpoints are depicted as red dots.*

4.3.3. Hypsometric curves and Hi

We extracted the hypsometric curves with their respective hypsometric integrals (Hi) for all the 33 studied basins (Table 4.1 and Figure 4.9). Hi shows low values, ranging from 0.12 to 0.48 with an average value of 0.33 (Table 4.1), characteristic of mature landscapes. Most of the hypsometric curves show concave or S-shaped profiles, as expected with landscapes in a mature stage of development (Figure 4.9). However, a number of curves present clear convexities in their lower parts (basins 18, 23, 24, 26, 27 and 30), which are related to an increased river incision driven by headward erosion (Pérez-Peña et al., 2010; Giaconia et al., 2012a). In addition, some complex curves feature heterogeneous landscapes. We divided the hypsometric curves regarding to their shapes (i.e. concave, s-shaped, complex and convex mouths) and Hi values (Figure 4.10). Relatively high Hi values with convex mouths are identified in transverse basins south of Jendouba city, noting rejuvenation processes, in agreement with previous results of normalized profiles and ksn index analyses.

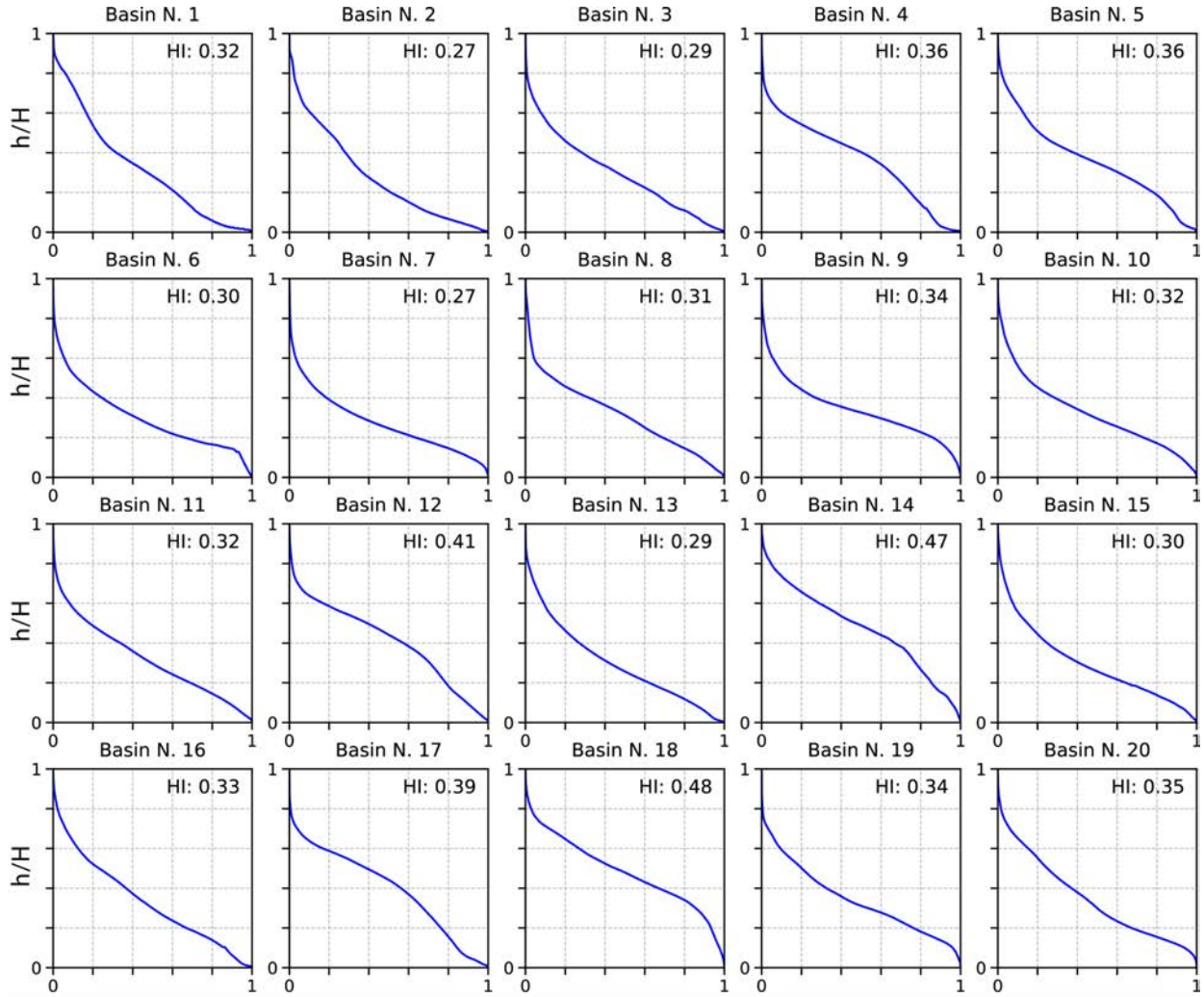

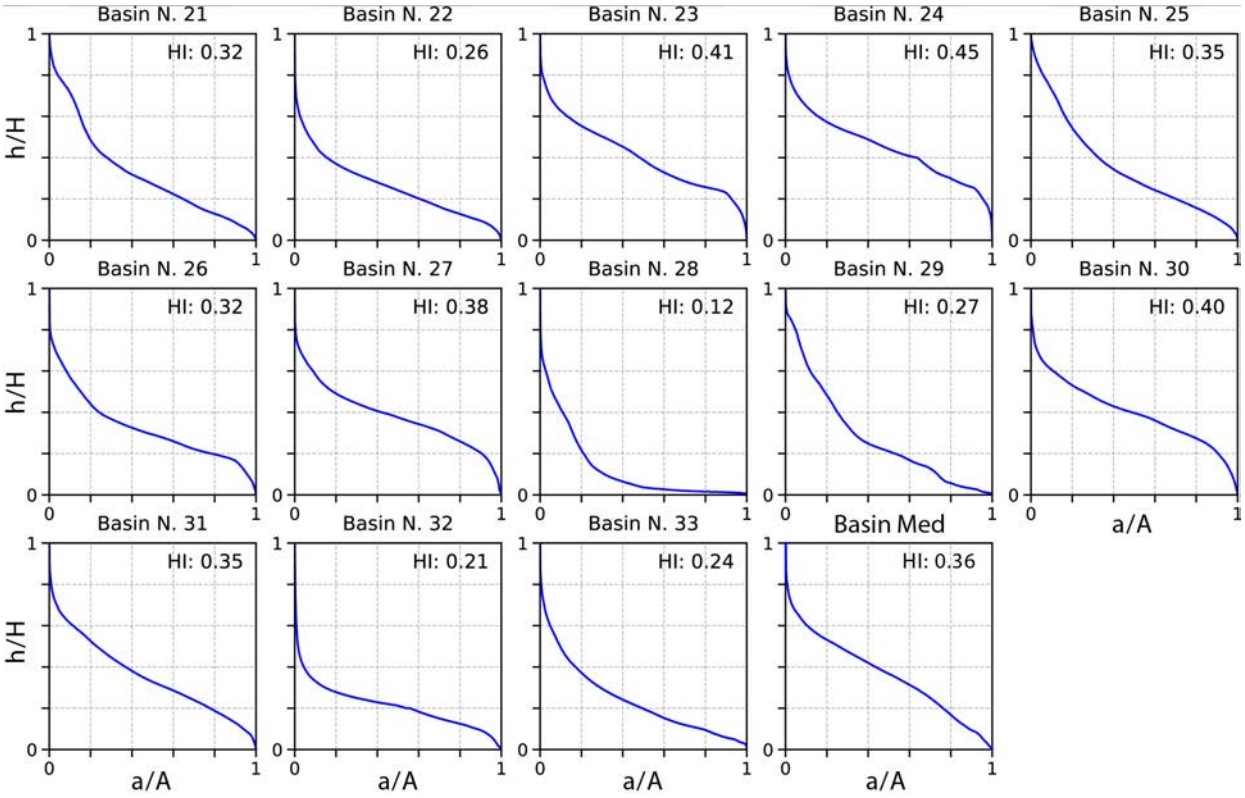

Figure 4.9. *Hypsometric curves and hypsometric integral values (HI) for the 33 analysed basins and for the Medjerda main basin (Basin Med.).*

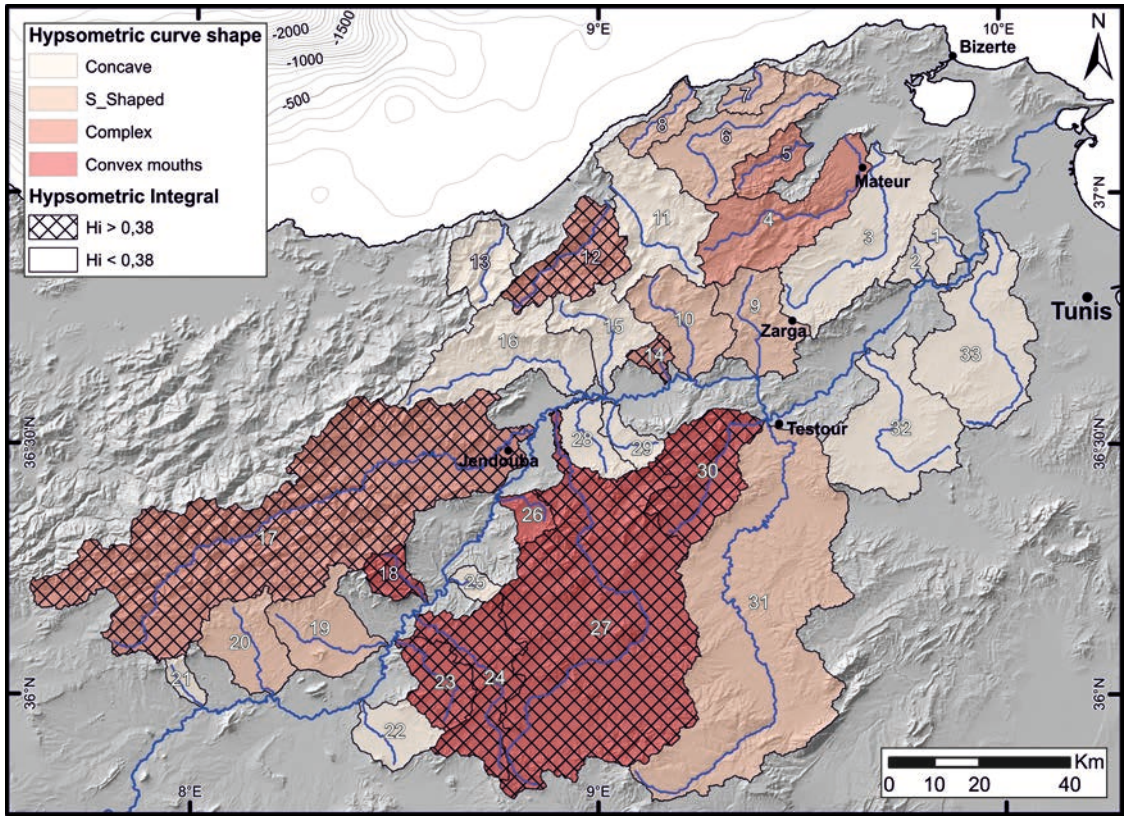

Figure 4.10. *Studied basins represented according to the hypsometric integral values (Hi) and hypsometric curve shapes (Figure 4.9).*

4.3.4. Knickpoint analysis

Through the analysis of ksn profiles and area-slope logarithmic plots we identified knickpoints on several rivers throughout the study area (Figures 4.11 and 4.12). We discarded the knickpoints with ksn values lower than 2.5, as they may be related to local processes. The knickpoints were classified in three main classes as explained in the methodology section (see Chapter 3).

Some of the identified knickpoints correspond to erodibility variations (Figure 4.13). However, sharp lithological contrasts in Northern Tunisia are restricted only to small outcrops of Eocene and Jurassic carbonates, and Oligocene sandstones of the Tellian domain. The lithological contrasts between these two domains could explain the presence of moderate knickpoints in the North (e.g. basins 12 and 15) and Southwest (basin 17), while the moderate knickpoint of basin 4 may be associated to an isolated outcrop of Eocene carbonates (Figure 4.13). The major knickpoints seem to do not have lithological influence as they occur within Neogene sediments or Cretaceous marls in the Medjerda River and basin nº 27, and over Triassic clays on basins 23 and 24 (Figures 4.13 and 4.6). The major and moderate knickpoints that concentrate in the South of the study area agree with higher ksn segments (Figure 4.6), as well as with the MaxC/MaxL groups of the normalized profiles and convex hypsometric curves (Figures 4.5 and 4.10).

Most of minor and local knickpoints fit well with tectonic structures, however, their low ksn values may indicate that the activity of such structures is probably low. Other local knickpoints that do not correlate either with lithology or tectonic structures may indicate other local processes such as landslides, local changes in drainage or even the aforementioned small outcrops of Eocene and Jurassic carbonates.

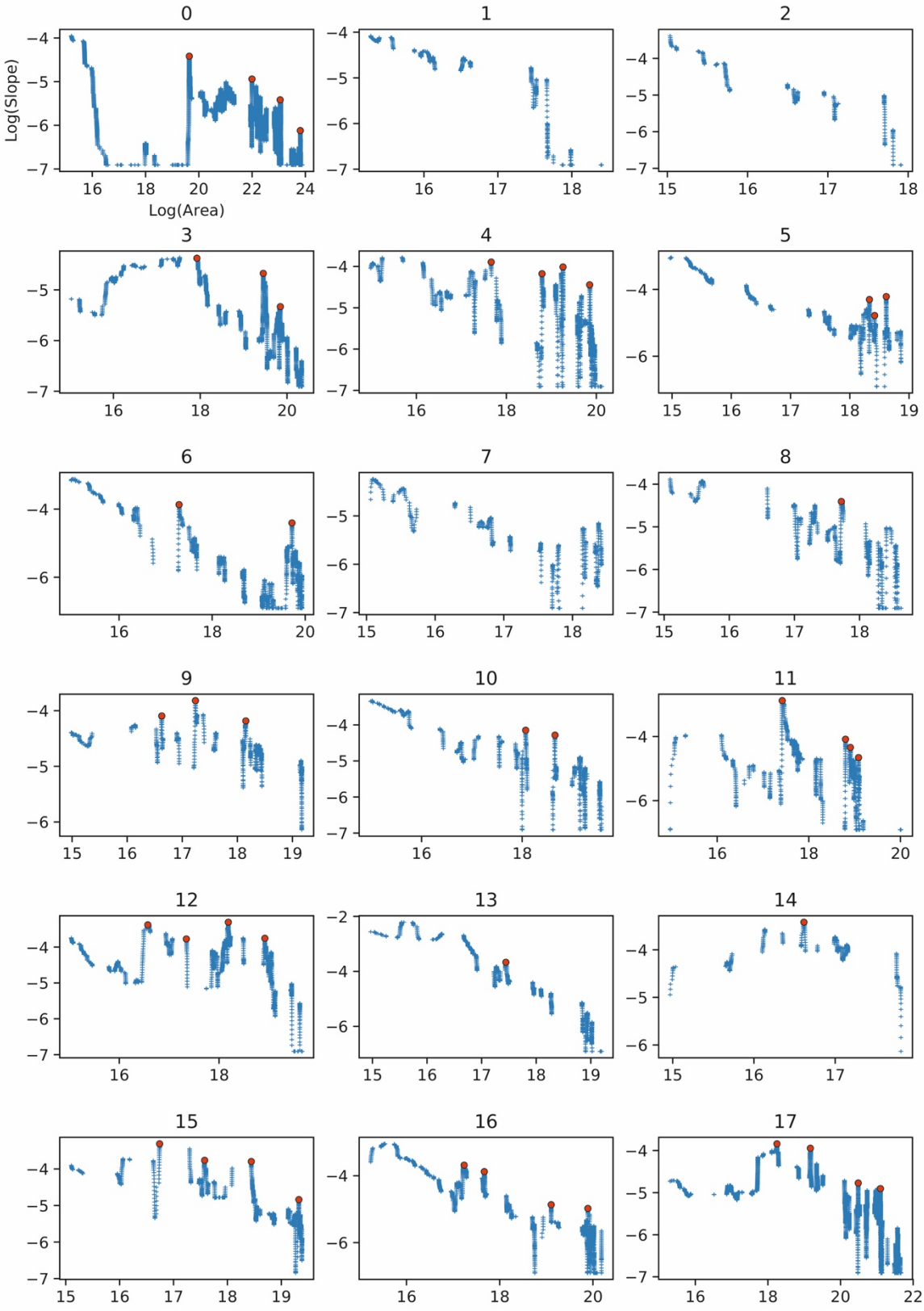
0
1
2
3
4
5
6
7
8
9
10
11
12
13
14
15
16
17
Log(Slope)
Log(Area)

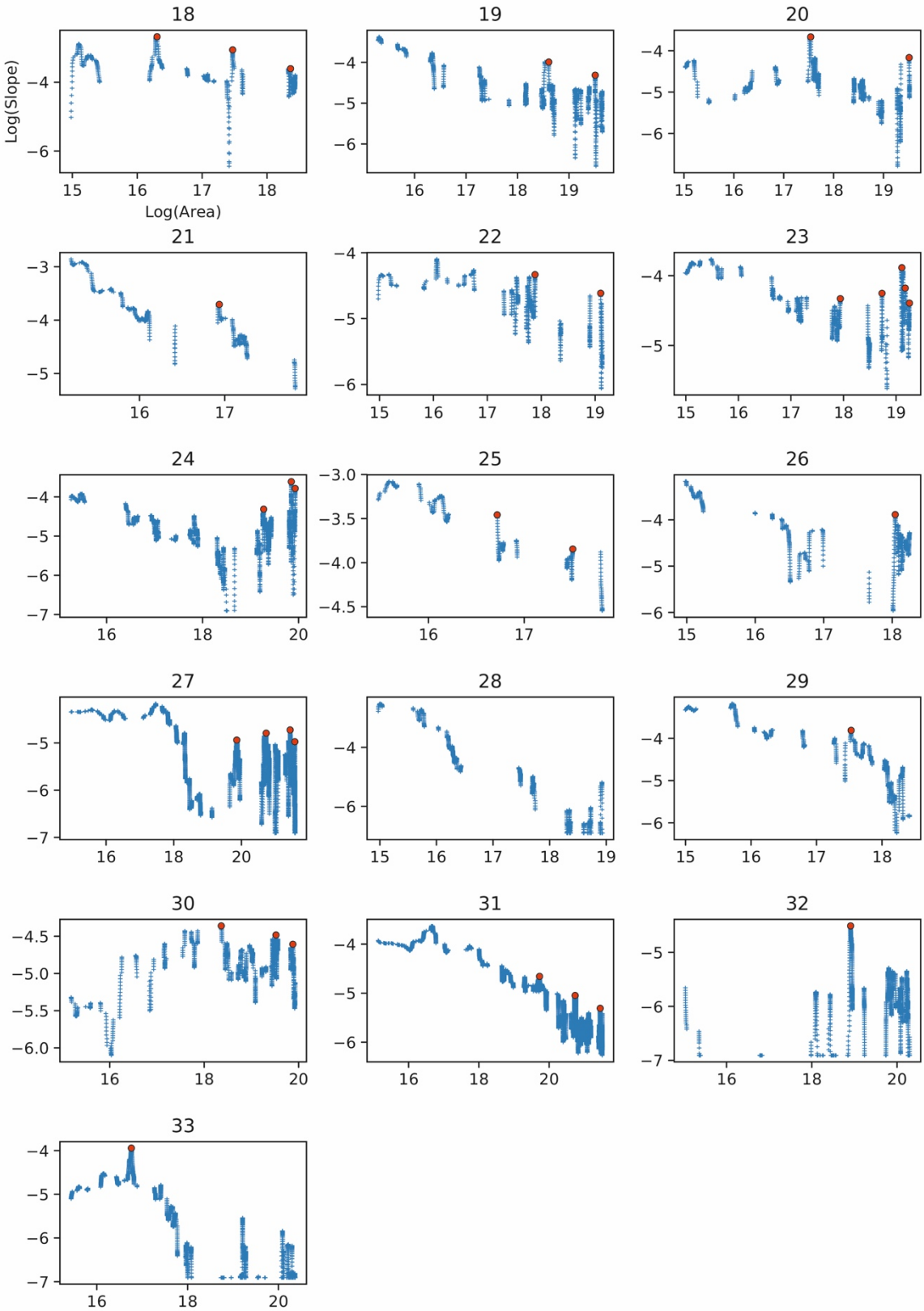

Figure 4.11. *Area-slope logarithmic plots for the trunk channels of the 33 analyzed basins and for the Medjerda main channel (profile 0). Derived knickpoints are shown as red dots.*

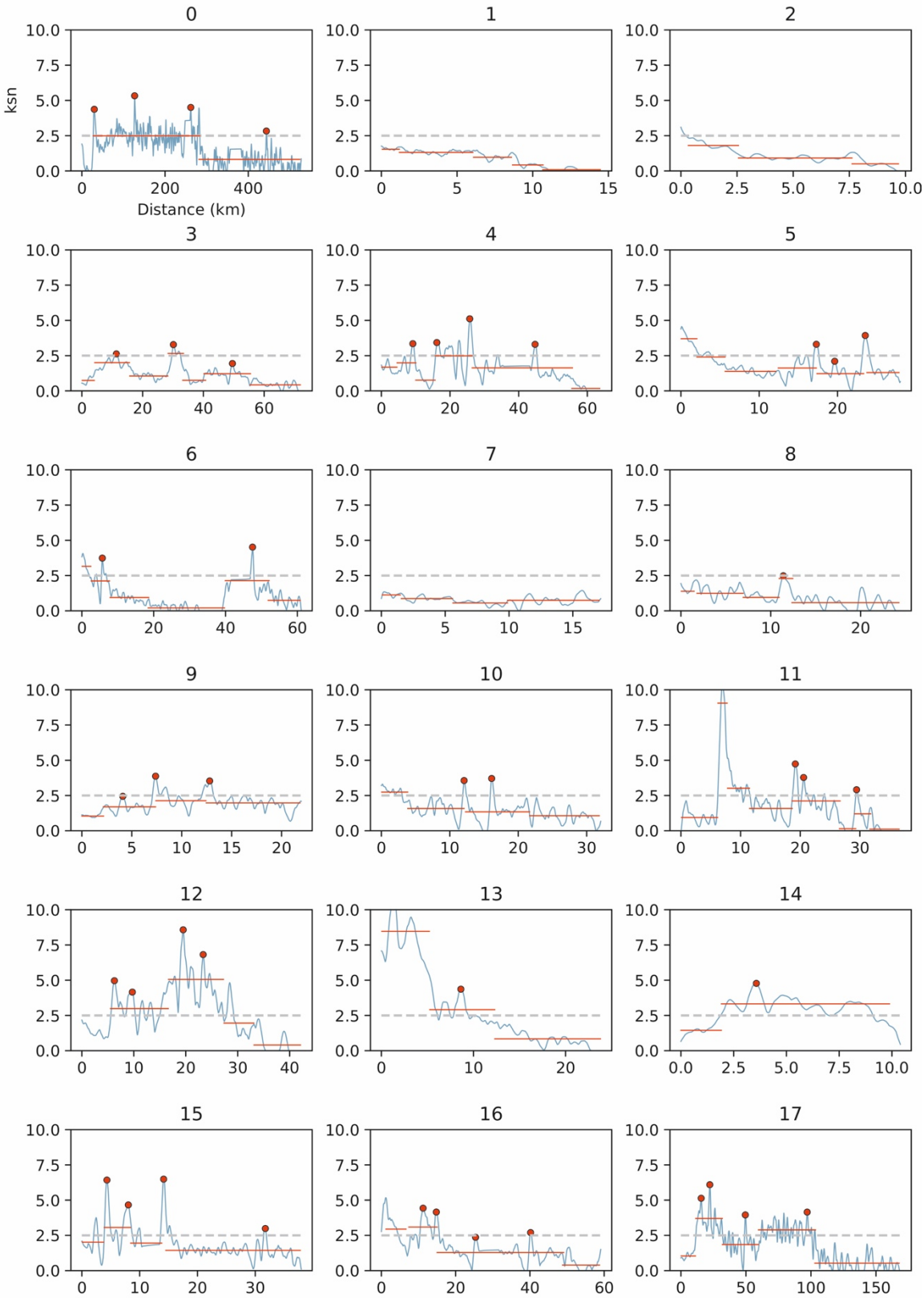
0
1
2
3
4
5
6
7
8
9
10
11
12
13
14
15
16
17
ksn
Distance (km)

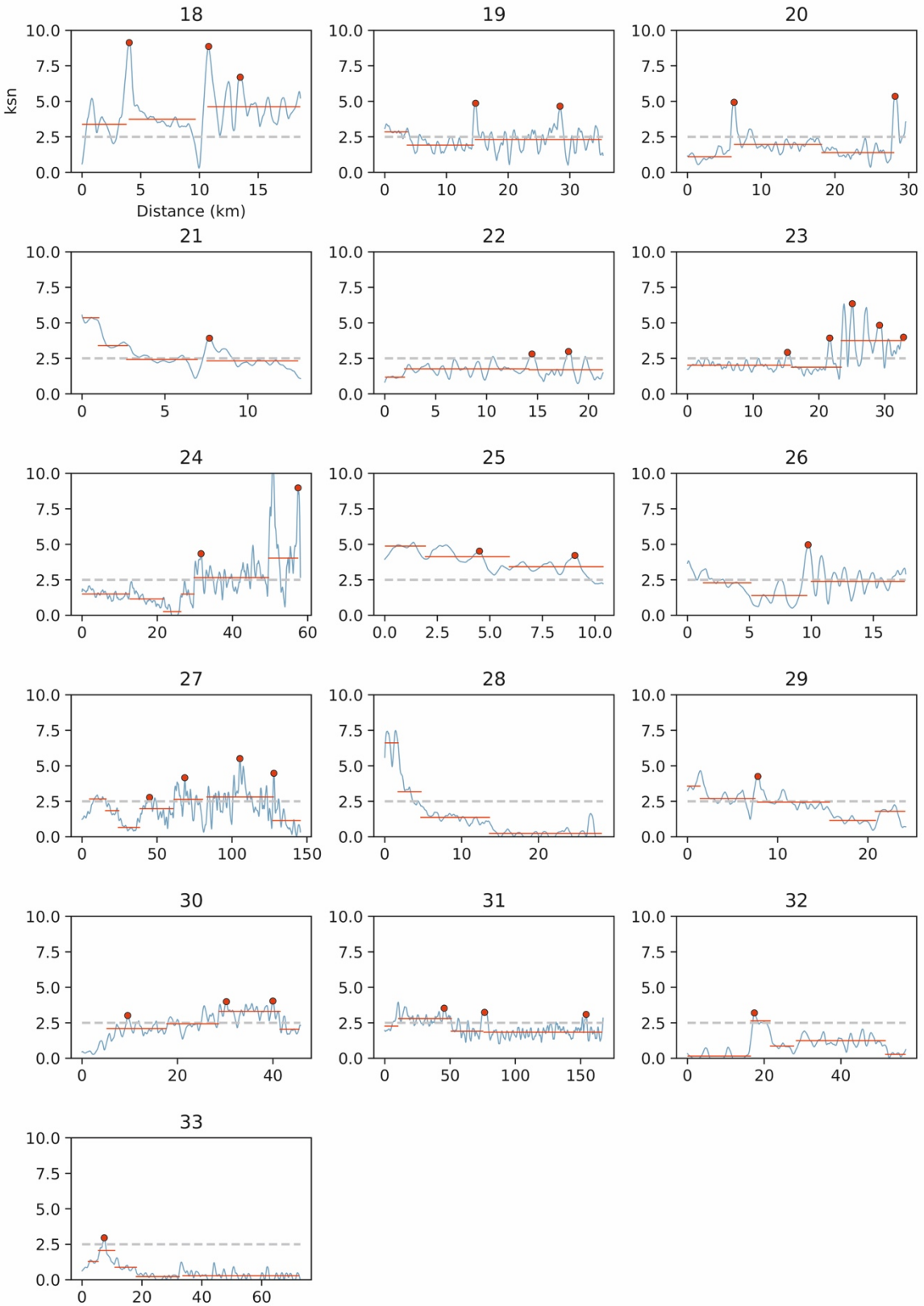

Figure 4.12. *Ksn-distance profiles for the trunk channels of the 33 analysed basins and for Medjerda main channel (profile 0). The ksn profiles have been constructed by calculating the ksn index within a mobile window of 15 pixels centred in each profile vertex. Selected knickpoints along the channels are depicted as red dots.*

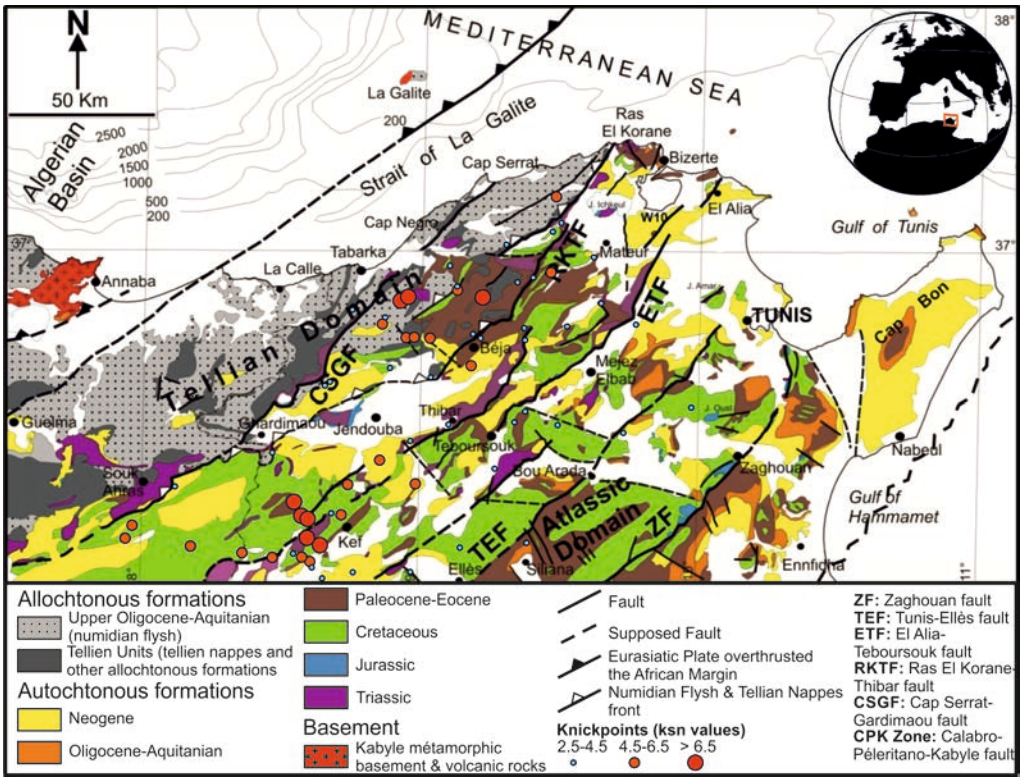

Figure 4.13. *Geological map of Northern Tunisia with the knickpoint locations (modified from Melki et al. (2012)). Knickpoints are displayed according to their ksn values.*

4.3.5. Fieldwork

Together with the morphometric analysis we undertook a short field campaign to study the region located NW of Testour (Figure 4.14). This area was selected on the light of previous morphometric results, since includes the first main deflection of the Medjerda River. The following section summarize the main findings of the field campaign.

In Zarga Village we identified an abandoned fluvial channel, confirmed by successive numerous levels of river terraces located on the watershed between Tine and Medjerda River basins (Figures 4.14 and 4.16.A), suggesting that a significant ancient river flowed across the watershed through the Tine River Valley. We systematically measured dip, direction and sense of movement of striae in pebbles (when possible), produced due to pebble displacement during faulting/folding affecting the terraces. We analysed 5 field stations corresponding with abandoned terrace levels (Figures 4.14, 4.16.E and 4.16.F). A total of 16 pebbles were measured for the stations 1.4 and 2.1, 21 for the station 2.7, and 17 for the stations 3.4 and 6.10 (Figure 4.14). Striae orientations on each point of the surface pebble should be parallel to the orientation of maximum shear-stress (Ruano and Galindo-Zaldívar, 2004). Following that assumption, a stress ellipsoid can be determined by fault-slip data inversion. We used the Gauss Method implemented in the software T-Tecto (Zalohar,

2009) to obtain P and T dihedral solutions. The results of the stress-inversion suggested a stress pattern with a maximum compressive stress oriented N-S to NW-SE (Figure 4.14), thus agreeing with the motion of the ETF, Zarga and Dkhila faults.

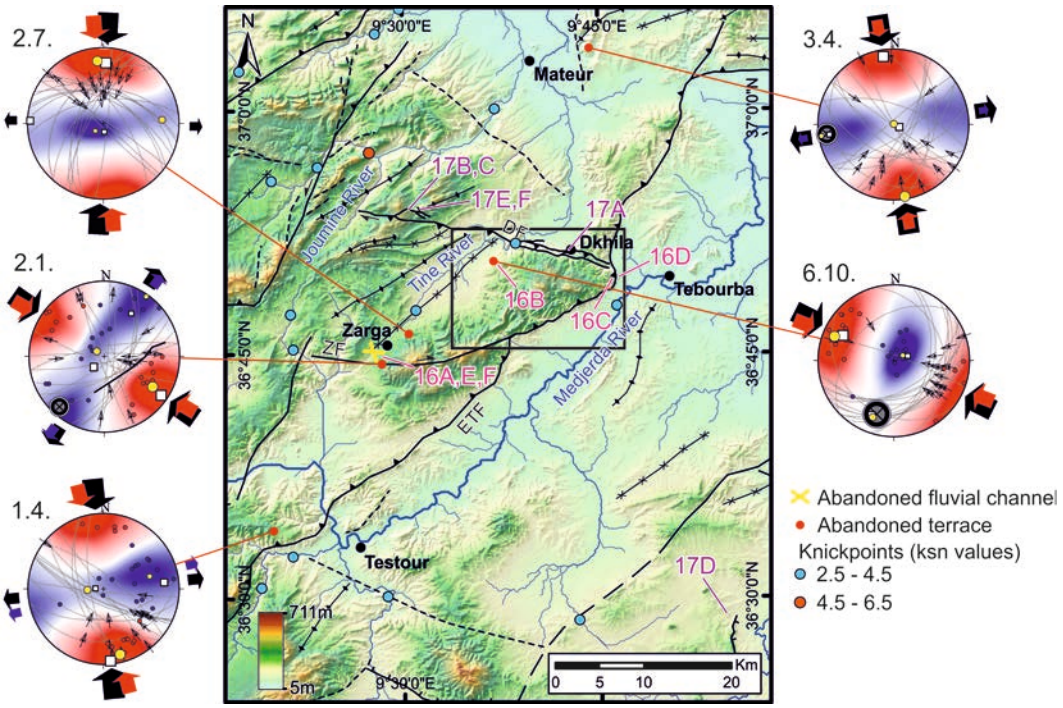

Figure 4.14. *Map with the structural data and observations surveyed in the field (location of the area is displayed by a red box in Figure 4.1). Stereoplots with stress tensor results for striated pebbles. Black box shows the location of Figure 4.15. Knickpoints are displayed (according to their ksn values).*

The Quaternary sediment filling of the Tine River valley located above the hanging-wall of the ETF thrust is strongly asymmetric. We identified four terrace levels being the youngest ones in the centre of the valley while the oldest ones occur above and in the southern side (Figure 4.15). The higher the terraces, the older and more folded they are, reaching dips up to 50º towards the NW in the oldest level (Figures 4.15 and 4.16.B). In these terraces, Pleistocene conglomerates show conspicuous striated pebbles that indicate a horizontal NW-SE main stress axis agreeing with the current Nubia-Eurasia convergence (Figure 4.14). These observations suggested that river terraces step up the hanging-wall flat of the ETF thrust, attesting for both tectonic uplift and horizontal displacement. These findings may evidence a capture of part of the Tine basin by the Medjerda River and being the capture point close to the Zarga village, due to the continued uplift of a block likely constrained by the joint activity of the ETF, Zarga and Dkhila faults (Figure 4.14). The absence of a moderate or major knickpoint associated to this capture, indicates that it should have occurred long time ago, giving the Medjerda trunk channel to attain an equilibrium condition (Figure 4.14).

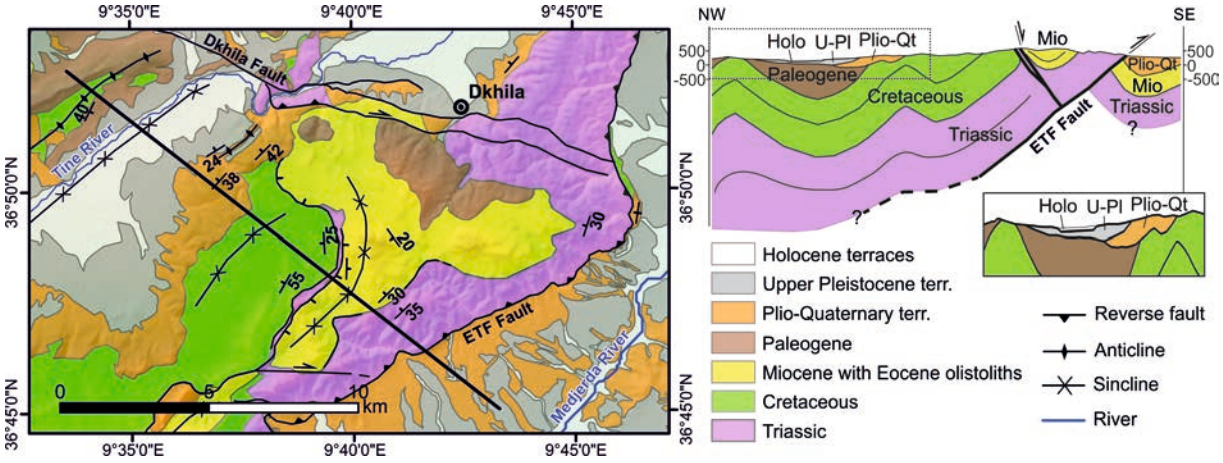

Figure 4.15. *Left: Detailed geological map located in Figure 4.14 (black rectangle). Right: NW-SE cross section of the block formed by the Dkhila and ETF faults. In the cross section we can see how ETF cuts the Plio-Quaternary terraces. The small inset under the cross section shows a zoom and vertically exaggerated section, displaying an asymmetric disposition of the terraces within the Tine River valley.*

To the West of Tebourba we observed that the El Alia-Teboursouk fault zone (ETF) is defined by several decametres of gypsum mylonites and breccias that affect Triassic red beds and gypsum, which dip between 35º and 50º towards the NW (Figures 4.14, 4.15 and 4.16.C). Asymmetric tails in porphyroclasts and gypsum slickenfibers indicate hanging-wall transport towards the SE. The hanging-wall Triassic sediments show a flat geometry, sub-parallel to the fault zone. On the footwall of the ETF fault, we found Plio-Quaternary fluvial sediments verticalized by the thrust activity (Figures 4.14 and 4.16.D). All of these observations suggested a fault-propagation-fold associated to a reverse fault that detaches on a Triassic gypsum unit. Furthermore, the apparent absence of a hanging-wall ramp suggested a large displacement along the thrust.

Near the Dkhila village, we observed an unnamed 86ºN fault dipping 74º towards the south that we name Dkhila fault (DF). The Tine River shows a local knickpoint when crossing through that fault, probably accounting for its activity (Figure 4.14). North of Dkhila fault, Plio-Quaternary terraces are folded and verticalized (Figures 4.14 and 4.17.A). We found that the fault motion put Triassic material above terrace sediments. The trace of this fault remains visible until the Joumine River valley, where different segments conform a horsetail configuration. In these segments we identified 122ºN striae in competent lower Eocene limestone blocks, showing a dextral strike-slip motion (Figures 4.14, 4.17.B and 4.17.C). These blocks break in 50ºN reverse faults dipping 60º (Figures 4.14 and 4.17.C). In one of these limestone blocks with anticlinal disposition, we observed meter to decametre open cracks with associated striae, possibly indicating co-seismic deformation that suggest recent tectonic activity (Figures 4.14, 4.17.E and 4.17.F). The orientation of cracks,

parallel and perpendicular to the main fault (130ºN and 45ºN, respectively) with sinistral movements for the parallel ones and normal for the perpendicular ones (i.e. with contrary kinematics to the main faults), support this interpretation (Philip and Meghraoui, 1983; Branellec et al., 2015). Although with a probable co-seismic origin, most of the opening cracks are possibly due to a landslide affecting part of the anticline's northern flank. A similar case of lateral landslide spreading has also been described in the Pyrenees (e.g. Zarroca et al., 2013).

Fieldwork observations also support that the local knickpoint found in basin 32 could indicate a river capture, causing the shifting of SE draining rivers to their present position. We identified a sand point bar (Figures 4.14 and 4.17.D) in a terrace located above Oligocene materials to the east of the knickpoint of basin 32, showing paleo-streams towards the SE, supporting the results obtained by the morphometric analysis.

Figure 4.16. *Fieldwork photographs. A: Fluvial terraces in the watershed of the Tine River. B: Folded fluvial Plio-Quaternary sediments. C: El Alia-Teboursouk fault zone (ETF). D: Sub-vertical Plio-Quaternary deposits on the footwall of the ETF fault. E and F: Striated pebbles on a terrace of the Tine River valley.*

***Figure 4.17**. Fieldwork photographs. A: Dkhila fault folding and putting vertical Plio-Quaternary terraces (i.e. strata are marked in black). B: Dextral striae in Eocene limestones. C: Dextral strike-slip fault near a reverse fault. D: Sand point bar indicating paleocurrents towards the SE. E: Probable co-seismic cracks. The red box highlights striae in N130ºE and N45ºE fractures. F: Two different families of probable co-seismic event, N130ºE and N45ºE.*

4.3.6. Seismic potential of active structures

Through the empirical equations for the earthquake magnitude estimations, we calculate the maximum magnitudes expected for the slip of the two faults recognized by fieldwork: El Alia-Teboursouk (ETF) and Dkhila (DF) faults. For this calculation, we selected different fault segments susceptible to break in an eventual seismic event. Fault segmentation of the most active segments has been done by: a) geometric criteria, b) field observations, c) morphometric and

geomorphological criteria by DEM analysis, and d) information from bibliographic references (e.g. Mejri et al., 2010; Bahrouni et al., 2014; Rabaute and Chamot-Rooke, 2015). Moreover, maximum magnitude for each entire fault has also been calculated to provide an upper bound value.

The empirical values and equations used are the ones from Wells and Coppersmith (1994) and Wesnousky (2008). Reverse fault values and equations are used for the ETF fault while strike-slip values are selected for the DF fault. Although both faults display oblique movements, the ETF shows a predominant reverse motion while the DF is characterized by a mainly strike-slip displacement.

As shown in Table 4.2 and Figure 4.18, we identified five segments susceptible to break along the ETF (ES1, ES2, ES3, ES4 (ES2+ES3) and ES5), while for the DF we only obtained two main segments (DS1 and DS2). Moreover, we calculated the entire fault longitudes (EST and DST). The magnitudes obtained for each fault and methods are shown in Table 4.2.

Faults	Segments	Rupture length (km)	Magnitude (Mw)	
			Wells and Coppersmith (1994)	Wesnousky (2008)
El Alia - Teboursouk	ES1	15.8	6.5	6.4
	ES2	9.8	6.2	6
	ES3	13.5	6.4	6.2
	ES4 (ES2 + ES3)	23.3	6.7	6.7
	ES5	9.7	6.2	6
	EST	97	7.4	7.8
Dkhila	DS1	10.8	6.3	6.5
	DS2	8.8	6.2	6.4
	DST	30	6.8	6.8

Table 4.2. *Moment magnitudes (Mw) calculated for the different segments of ETF and DF faults on the basis of empirical relationships. Maximum moment magnitudes (Mw) have been calculated for the entire El Alia-Teboursouk (EST) and Dkhila (DST).*

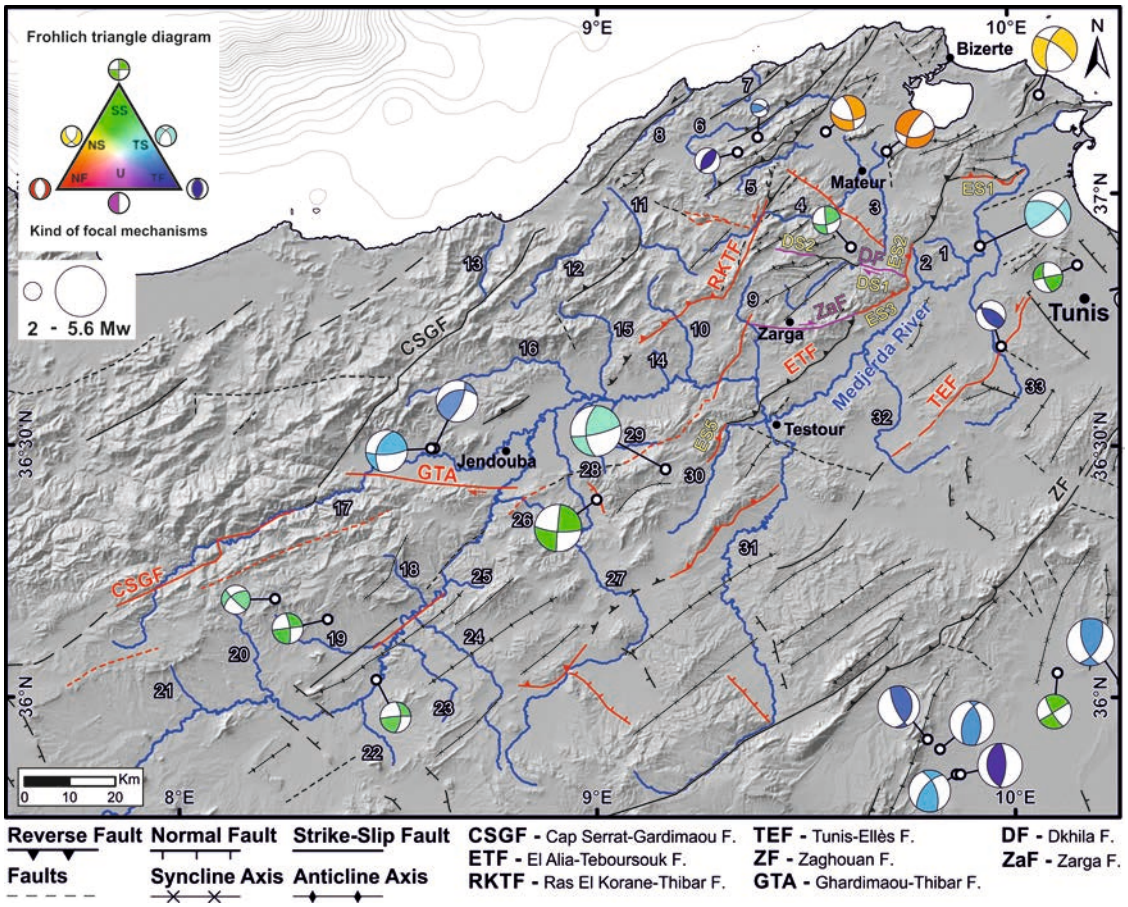

***Figure 4.18**. Northern Tunisia active tectonics map derived from this work. In red are shown the active faults. In purple are shown the active faults described in this work for the first time (Dkhila and Zarga faults). In marine blue are shown the main rivers. Tectonic structures include data from Melki et al. (2012), Bahrouni et al. (2014) and Rabaute and Chamot-Rooke (2015), as well as our own field data. Focal mechanisms solutions extracted of the compilation of Soumaya et al., (2015). The Focal mechanisms solutions are plotted in the barycentre of the epicentral and weighted by magnitudes. The colour of focal mechanisms type is based on the Frohlich triangle diagram (above left); NF: normal faulting, TF: thrust faulting, SS: strike-slip faulting, TS: thrust to strike-slip faulting, and NS: normal to strike-slip faulting.*

4.4. Discussion

4.4.1. Drainage network anomalies associated to active faulting

Most of the ksn anomalies observed in Northern Tunisia are parallel and delineate the uplifted faults blocks developed in the context of NW-SE convergence between Nubia and Eurasia plates (e.g. McClusky et al., 2013; D'agostino and Selvaggi, 2004; Serpelloni et al, 2007; Noquet, 2012) (Figure 4.6). Figure 4.18 shows the active faults derived from the morphometric analysis carried out in this work. As depicted in Figure 4.18, active faults show a scattered distribution agreeing with the sparse seismicity recorded in Northern Tunisia (Meghraoui et al., 1996b; Serpelloni et al.,

2007; Nocquet et al., 2012; Bahrouni et al, 2014; Soumaya et al., 2015; 2018). These faults match with the current transpressive to compressive regime of Northern Tunisia (e.g. Meghraoui and Pondrelli, 2012; Nocquet et al., 2012; Soumaya et al., 2015), and are either reverse-sinistral faults like the El Alia-Teboursouk fault and their associated folds, or dextral and normal faults, which we will discuss next. Furthermore, in some cases these anomalies delineate faults that have not been previously mapped, but that are mapped thanks to a morphotectonic analysis, and later ground-truthed in the field (Figure 4.18). This is the case of the WNW-ESE Dkhila dextral-reverse fault. This fault reaches a length of approximately 30 km and shows evidence of recent activity, cutting Pleistocene terraces and the Tine River valley (Figure 4.18).

The main reverse/left-lateral fault that show a morphotectonic signal and has been ground-truthed in Northern Tunisia is El Alia Teboursouk fault, one of the most important sinistral faults in the region (Figure 4.18). The recent activity of the ETF fault was proved by Plio-Quaternary fluvial sediments verticalized by the thrust activity recognized in fieldwork (Figures 4.14 and 4.16.D). Although not as evident as in the ETF fault, the CSGF, RKTF and TEF faults show morphometric signal and field evidences in the case of TEF fault, supporting recent tectonic activity (Figure 4.6). These faults are NW-dipping reverse-sinistral faults displaying a main NE-SW trend and represent most of the active faults recognized in this work, in agreement to previous works (Rouvier, 1977; Gueddiche et al., 1992; Ben Ayed, 1993; Bahrouni et al., 2014; Soumaya et al., 2015, Essid et al., 2016; Soumaya et al., 2018). Furthermore, most of the thrust focal mechanisms display NE-SW trending nodal planes that agrees with the trending of the delineated faults (Figure 4.18). The hypsometric curves also support uplift in some areas, interpreted as related to the sinistral-reverse fault motion, as for the lower parts of basins 23 and 24 (Figures 4.9 and 4.10).

Dextral faults are interpreted as conjugate to sinistral faults, or as transfer faults of reverse faults and have WNW-ESE trends that clearly match with the regional NW-SE tectonic compressional vector (e.g. DeMets et al., 1994; Sella et al., 2002; Calais et al., 2003; McClusky et al., 2013; D'agostino and Selvaggi, 2004; Serpelloni et al, 2007; Noquet, 2012). Although focal mechanisms clearly show dextral strike slip events with ~W-E trending focal planes (Figure 4.18), few dextral active faults are described in the literature for Northern Tunisia, except for the right-lateral Ghardimaou-Thibar accident, that our analysis also proved as active (high ksn values on the southern block, Figure 4.6) (Amiri et al., 2011; Bahrouni et al., 2014; Soumaya et al; 2015, 2018). Nevertheless, we identified some new WNW-ESE active faults in the field, like the Dkhila's and Zarga faults (Figures 4.14 and 4.18). These faults cut Pleistocene sediments (Figure 4.15) and,

together with the ETF, form an uplifted block that may have isolate the upper part of the Tine River and favoured its capture by the Medjerda main channel (Figure 4.14).

The normal faults of Northern Tunisia show a NW-SE trending and develop small tilted basins hosting alluvial fans (e.g. Belguith et al., 2011; 2013, Soumaya et al., 2015). Moderate ksn values on the footwall areas of these faults suggested their activity. This is clear in the southeastern sector of the studied region (upper parts of basins 31 and 27) or in the Mateur's fault zone where normal component focal mechanisms have been computed (Figures 4.6 and 4.18). The movements of most of the above described faults may cause landscape readjustments that induce river captures as described below. Some of these faults have associated minor or local knickpoints (Figures 4.6). The low ksn values related to these knickpoints may indicate that the activity of these structures is low. This observation fits well with the overall topography in Northern Tunisia, with gentles slopes and no deeply incised canyons (Figure 4.1). However, a low slip-rate for these faults does not mean that they cannot generate important earthquakes, but that their recurrence periods are probably longer. Some field features related to these faults, as the open cracks probably are co-seismic effects of major events, which support its potentially seismogenic nature (Figures 4.17.E and 4.17.F).

Moderate knickpoints are found associated to the competent rocks of the Tellian domain (e.g. basins 12, 15 and 17) or with isolated outcrops of competent rocks (Eocene carbonates in basin nº 4, Figure 4.6). Moderate knickpoints associated to the competent rocks of the Tellian domain agree with the positive anomaly in ksn values parallel to the thrust contact between the Tellian and the Atlas domains (Figure 4.6). This contact places less erosional sandstones above mostly pelitic rocks of the Atlas domain. The local knickpoint in the Medjerda south-west to Tebourba, despite not lying directly over the Dkhila fault itself, it could be related to the uplift generated by the block formed by the ETF, Zarga and Dkhila faults (Figure 4.14).

Moderate and major knickpoints are found in the upper reach of the Medjerda River some kilometers upstream Jendouba, in transverse channels 18, 19, 20, 23, 24, 25 and 26 (Figure 4.6). They agree with higher ksn segments (automatic and regressed segments, Figure 4.6), MaxC/MaxL groups of the normalized profiles and convex hypsometric curves (Figures 4.5 and 4.10), and could be related to a more general drainage reorganization taking place in Northern Tunisia, capturing valleys to the east (see Section 8.2 in Chapter 8).

Furthermore, some knickpoints are also located over the contact with Triassic evaporites (basin 24, west of Kef village (Figure 4.13)). The high lithological contrast, together with the possibility of halokinesis could also play a role by "accelerating" knickpoint formation and upstream

migration. In these areas, additional field mapping and a fine structural analysis will shed light on the matter.

River captures are the main fluvial mechanism in Northern Tunisia driving a general fluvial network reorganization. We have identified several fluvial captures throughout the studied area. These captures are evidenced by different features such as abandoned fluvial channels and terraces, knickpoints and morphometric results. The overall capturing process is well depicted in the Chi profiles for the main channels, those profiles show how the Medjerda main channel is gaining area as its slope is higher in its upper parts compared to the lower parts (Figure 4.7.a). A nice example of these captures can be viewed in the Tine River near Zarga village. The joint activity of the ETF, Zarga and Dkhila faults produced and uplifted a block that isolated the upper reach of the Tine River, boosting its capture by the Medjerda main channel towards the east (Figure 4.14).

Finally, fieldwork evidences of recent activity obtained by the DF and ETF faults confirmed the observations made through the morphometric analysis and prove active tectonic activity with potentially seismogenic character. Using two different empirical equations (Wells and Coppersmith, 1994 and Wesnousky, 2008) significant maximum magnitudes (M_w) of 6.7 and 6.5 have been obtained for fault segments of the ETF and DF faults, respectively. These values are similar to the maximum estimated magnitude of M_w 6.8 for the destructive historical earthquake of Tunis in A.D. 856 (Ksentini and Romhdane, 2011). Although we do not have slip-rate velocities for the faults, we can assume return periods of hundred to thousand years, due to the slow convergence rates defined in this zone (e.g. McClusky et al., 2003; Serpelloni et al., 2007; Noquet, 2012). Low slip-rates are also supported by the low ksn values associated to fault-related knickpoints observed in Northern Tunisia (Figure 4.6). Because of that, the risk will not be as high as we expected for the magnitudes obtained. Even so, the large magnitudes obtained together with the evidence of important historic earthquakes in the region (e.g. Ambraseys, 1962; Ksentini and Romhdane, 2011; Bahrouni et al., 2014; Ksentini and Romhdane, 2014) suggested a considerable seismic hazard in the zone.

4.5. In summary

The morphometric analysis carried out in this chapter revealed several active faults matching with the current NW-SE convergence setting between Nubia and Eurasia plates. The active faults observed show an sparse distribution and low slip-rates throughout the studied area, in agreement to the sparse and scarce seismicity in Northern Tunisia (see Section 2.1.3 of Chapter 2 for further

information). Three families of active faults have been identified: NE-SW reverse-sinistral faults, WNW-ESE dextral faults and NW-SE normal faults. The main reverse-sinistral fault that show a morphotectonic signal and has been ground-truthed is the NE-SW reverse El Alia Teboursouk fault. These NE-SW reverse-sinistral faults represent the main family of active faults recognized in Northern Tunisia. Evidence of recent activity as Plio-Quaternary fluvial sediments verticalized by the slip of the ETF fault were recognized on the field and proved its recent activity. Regarding to dextral faults, we could identify two new ones never earlier described, the Dkhila's and Zarga faults. These dextral faults are interpreted as conjugate to sinistral faults or as transfer faults of reverse faults. Morphotectonic signal (as ksn anomalies or knickpoints) delineate these faults and evidence recent activity later identified in the field (as folded Pleistocene terraces and probably seismogenic cracks associated to the Dkhila fault). Finally, active normal faults developing small tilted basins have also been recognized. Moderate ksn values on the footwall of these normal faults suggested their recent activity.

Several river captures have been identified throughout the studied area. Different morphometric indices in the upper reach of the Medjerda River evidence fluvial network reorganization also supported by Chi profiles, which indicates that its catchment area has grown through time by capturing other longitudinal valleys to the east of its initial drainage divide. These series of captures formed transverse tributaries to the Medjerda River that show the highest convexity and hypsometric integral values. In some cases, these captures could have been driven by an increase in incision rate of the Medjerda tributaries, related to uplift associated with active tectonic structures.

Lithologic contrasts between the Tellian sandstone units and more erodible North Maghrebian paleomargin-derived rocks also seem to influence the drainage in northern Tunisia. The contact between these domains is marked by a clear ksn anomaly and coincides with the main division between basins draining to the Algero-Balearic Basin and the northern tributaries of the Medjerda River that drains into the Gulf of Tunis.

El Alia Teboursouk and Dkhila faults have also been proved to be active in the field and co-seismic evidences have been identified. The estimated maximum earthquake magnitudes for the susceptible segments to break of the ETF and DF faults are 6.7 and 6.5 (M_w) respectively. These magnitudes together with the evidence of significant historical earthquakes in the region suggested a considerable seismic hazard in Northern Tunisia.

CHAPTER 5

Geomorphology and morphostructure of the North Tunisian continental margin

5.1. Introduction

The North Tunisian continental margin is a poorly explored area located just at the transition between the Western and the Eastern Mediterranean Sea. Although there are few published works in the literature (e.g. Auzende, 1971; Auzende et al., 1974; Maldonado and Stanley, 1976; Gennesseaux and Stanley, 1983; Tricart et al., 1994, Catalano et al., 2000; Dinarès et al., 2003), in this work we present the first comprehensive modern marine geophysical dataset of the offshore North Tunisian margin. This dataset consist of a high resolution multibeam bathymetric map and a suite of parametric echosounder and TOPAS profiles acquired during the Geomargen-2 and Geomargen-2AA cruises. In this Chapter we analyse this dataset and present the unprecedented detail of the geomorphologic and morphostructural observations of the offshore North Tunisian margin.

Following the aim of this PhD Thesis to characterize and investigate active tectonic processes in this region, in this Chapter we focus on the geomorphological and morphostructural analyses as the first step to identify recent and active tectonic structures in the North Tunisian continental margin. We describe sedimentary, erosive and tectonic features shaping the seafloor surface and sub-surface to understand the currently active processes occurring in the area as well as to identify fault-related seafloor traces.

5.2. Methodology

To characterize the geomorphology and morphostructure of the North Tunisian continental margin we use high-resolution parametric echosounder profiles and high-resolution bathymetric data (acquired with the high-resolution sub-bottom profilers TOPAS PS 18 and Innomar SES-2000 Compact and the high-resolution multibeam echosounders EM712 and ELAC Seabeam 1050D). The bathymetric map covers an area of 15,600 km^2 between 9°3.6'E-11º16.6'E and 37°14.7'N-38°41.2'N, while Innomar parametric echosounder profiles totalized more than 8,445 km and TOPAS profiles more than 3,500 km. This dataset was acquired during the Geomargen-2 and Geomargen-2AA cruises on-board the RV "García del Cid" and "Ángeles Alvariño", respectively.

To identify seafloor fault-related features and highlight subtle seafloor morphologies and particularly enhance continuity of the seafloor traces of faults and lineaments we filtered our bathymetric mosaic using the high-pass filtering of the topography (Howell et al., 2015) and the Red Relief Image Map (RRIM) (Chiba et al., 2008). We also use morphometric analyses to study the seafloor relief, such as swath profiles and a spatial auto-correlation technique for the hypsometric integral (see Chapter 3 for further information).

5.3. Geomorphological and morphostructural analysis of the North Tunisian margin

The North Tunisian continental margin is characterized by a complex topography with different geomorphological and morphostructural features, as well as specific physiographic domains. In this section, we first introduce the geomorphology and morphostructure of the area describing the main geomorphological features identified. We use morphometric analyses in order to characterize the regional relief of the explored region (Section 5.3.1). Later, we analyse the geomorphology and morphostructure of the different domains in which we classify the study area (Section 5.3.2). Finally, we describe in detail the morphological and morphostructural evidences of sedimentary, erosional and tectonic features that are shaping the seafloor of the North Tunisian continental margin (Section 5.3.3).

5.3.1. Regional geomorphology and morphotectonic structure

a) Brief description of the main geomorphological and morphostructural features of the explored area

In this section we briefly present the main features identified on the bathymetric map. These include the following elements: A) Contourites, moats and cold-water coral mounds; B) Folds and faults, C) Pockmarks, D) Collapse pockmarks, E) Basement highs, F) Slide scars and Mass Transport Deposits and G) Layered sedimentation.

Contourites, moats and cold-water coral mounds (A)

In the explored area of the North Tunisian margin, contourites usually show long and narrow elongated mound shapes with an adjacent, concave moat, parallel or slightly oblique to edges, faults or cold water coral mounds (CWCM) (Figures 5.1.A1, 5.1.A2, and 5.1.A3). Morphologically, contourites are recognizable as elongated drift structures with adjacent moats parallel to the structures along which deep-water bottom-currents flow (Figure 5.1.A3). In the echosounder profiles (Figure 5.1.A1), contourites are recognizable by having offlap bedding when approaching the moats. On the other hand, cold-water coral mounds (CWCM) are typically recognized on the seafloor bathymetry as elongated snake-shaped geo-forms (Figure 5.1.A3). In the parametric echosounder profiles CWCM are recognized as prominent vertical structures displaying transparent facies, due to the accumulation and stacking of coral and reef rubble (Figure 5.1.A1). The nature of CWCM was ground-truthed with 5 cores and 5 dredges recovering coral rubble in several locations.

Folds and faults (B)

Folds caused by faults in recent sediments and therefore by recent tectonic activity also occur in the area (Figures 5.1.B1, 5.1.B2 and 5.1.B3). Due to the restricted penetration of the parametric echosounders they image only the shallowest layers (maximum penetration reached below seafloor is ~0.73 s TWTT or ~61 m) (Figures 5.1.B1 and 5.1.B2). In consequence, faults at depth are not visible, but the superficial response of their motion through the observation of a deformed terrain. For instance, Figures 5.1.B1 and 5.1.B2, show the fault causing surface folding for the western fold but not for the eastern one. Moreover, most of the locally observed deformation at the surface might be related to large fault at depth that branches to shallow depth. The expression of these folds in the seafloor is usually weak (Figure 5.1.B3), but filtered topography maps permit their identification much clearly (see section 5.2).

Pockmarks (C)

Because of their usually characteristic morphological definition, an easy way to identify pockmarks is through the study of bathymetric data (Figure 5.1.C3). We found a large variety of pockmarks of those described by Judd and Hovland (2007), such as: i) standard circular and elliptical pockmarks, as the eastern pockmarks in Figures 5.1.C1, 5.1.C2 and 5.1.C3; ii) composite pockmarks, as the ones occurring when individual pockmarks merge; iii) elongated pockmarks and troughs, which tend to be elongated following the axis of the troughs; iv) giant pockmarks that are anomalously large when compared to other surrounding pockmarks; v) partially filled pockmarks covered by sediments derived from different mechanisms; for example the western pockmark in Figures 5.1.C1, 5.1.C2 and 5.1.C3.

Collapse pockmarks (D)

Collapse pockmarks are also found in the studied area, and we relate them to an evolutionary stage of the pockmarks or perhaps related to the presence of strike-slip faults. These collapse pockmarks may be formed either by the simple evolution of pockmarks to more mature stages or by the presence of long strike-slip faults that generate pull-apart basins and subsequent depressions (Figures 5.1.D1, 5.1.D2 and 5.1.D3).

Basement highs (E)

Several basement highs crop out within the North Tunisian continental margin (Figures 5.1.E1, 5.1.E2 and 5.1.E3). In TOPAS profiles the basement highs characteristically lack stratification and commonly display a strong top reflection caused by the indurated nature of the seafloor that has a comparatively higher acoustic impedance (Figure 5.1.E1).

Slide scars and Mass Transport Deposits (F)

Slide scars and associated Mass Transport Deposits (MTD) are common features identified throughout the explored region (Figures 5.1.F1, 5.1.F2 and 5.1.F3). Slide scars cut the seafloor and are consequently easily identifiable both on TOPAS profiles and on the bathymetric map (Figures 5.1.F1 and 5.1.F3). MTDs are clearly displayed on TOPAS profiles as transparent bodies due to their lack of internal structure (Figures 5.1.F1 and 5.1.F2) but they are not so evident in the bathymetric dataset. In fact, filtered topography (Figure 5.1.F3) turns out to be a good methodology to display the rough seafloor topography of MTDs, in comparison to neighbouring areas.

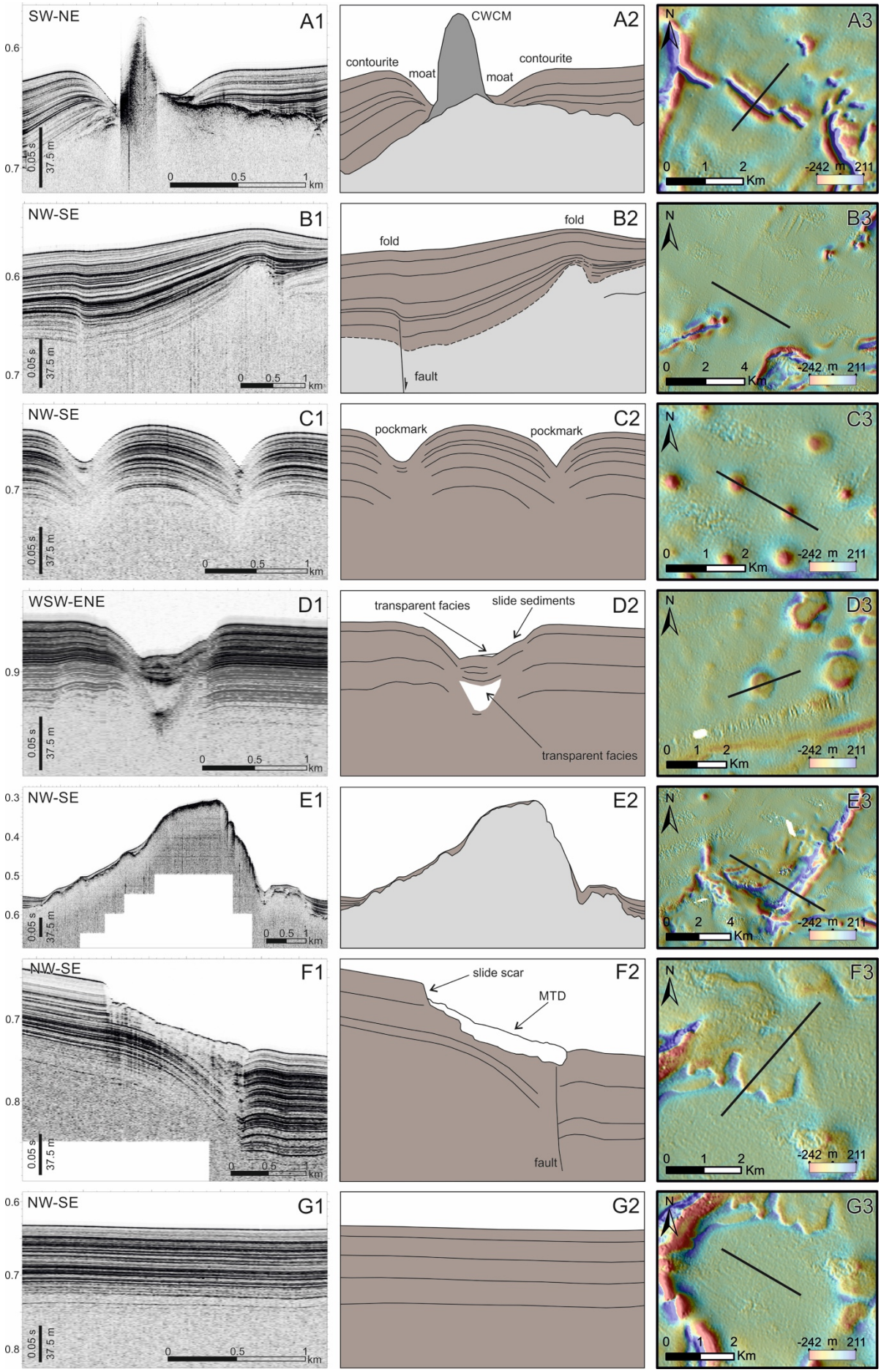
SW-NE
A1
A2
CWCM
contourite
moat
moat
contourite
A3
N
0 1 2 Km
-242 m 211
NW-SE
B1
B2
fold
fold
fault
B3
N
0 2 4 Km
-242 m 211
NW-SE
C1
C2
pockmark
pockmark
C3
N
0 1 2 Km
-242 m 211
WSW-ENE
D1
D2
transparent facies
slide sediments
transparent facies
D3
N
0 1 2 Km
-242 m 211
NW-SE
E1
E2
E3
N
0 2 4 Km
-242 m 211
NW-SE
F1
F2
slide scar
MTD
fault
F3
N
0 1 2 Km
-242 m 211
NW-SE
G1
G2
G3
N
0 1 2 Km
-242 m 211
0.05 s
37.5 m
0 0.5 1 km

Figure 5.1. *Description of the different geomorphological and morphostructural elements identified and its main seismic and morphologic characteristics observed. Column 1: TOPAS parametric echosounder profiles; Column 2: Interpretation of the TOPAS profiles; Column 3: Filtered topography overlapped on top of the original bathymetric shaded relief map. Colour scale ranges from red to blue corresponding from concave to convex morphologies, respectively. The TOPAS profiles are located by a black line. Geomorphological and morphostructural elements are as follows: A: Contourites, moats and cold-water coral mounds (CWCM); B: Folds and faults; C: Pockmarks; D: Collapsed pockmarks; E: Basement high; F: Slide-scar and Mass Transport Deposits (MTD); G: Layered stratification.*

Layered sedimentation (G)

Several regions appear tectonically inactive areas as clearly shown in TOPAS images with a continuous, homogeneous and layered stratification without any disturbance affecting those areas (Figures 5.1.G1, 5.1.G2 and 5.1.G3).

b) Morphometric analyses of the seafloor bathymetry

In this section we describe the regional relief of the explored region by using morphometric analyses like a spatial auto-correlation technique for the hypsometric integral and swath profiles.

Spatial autocorrelation technique for the hypsometric integral

The map of the spatial autocorrelation technique for the hypsometric integral (Hi) (Figure 5.2) reveals a clear preferential distribution of clusters of high Hi values to the east of the Bizerte Canyon. These clusters of high Hi values seem to correlate with pockmark fields (see zooms in Figures 5.2.a and 5.2.b). In contrast, clusters of low Hi values seem to be more distributed throughout the study area, and lower-end values are observed at the eastern side of the Bizerte Canyon in correlation to Cold Water Coral Mounds (CWCM) (Figure 5.2.c). Both, high- and low-value clusters show that the sector to the east of the Bizerte Canyon is characterized by a more complex relief than the smoother sector located to the west of the Bizerte Canyon.

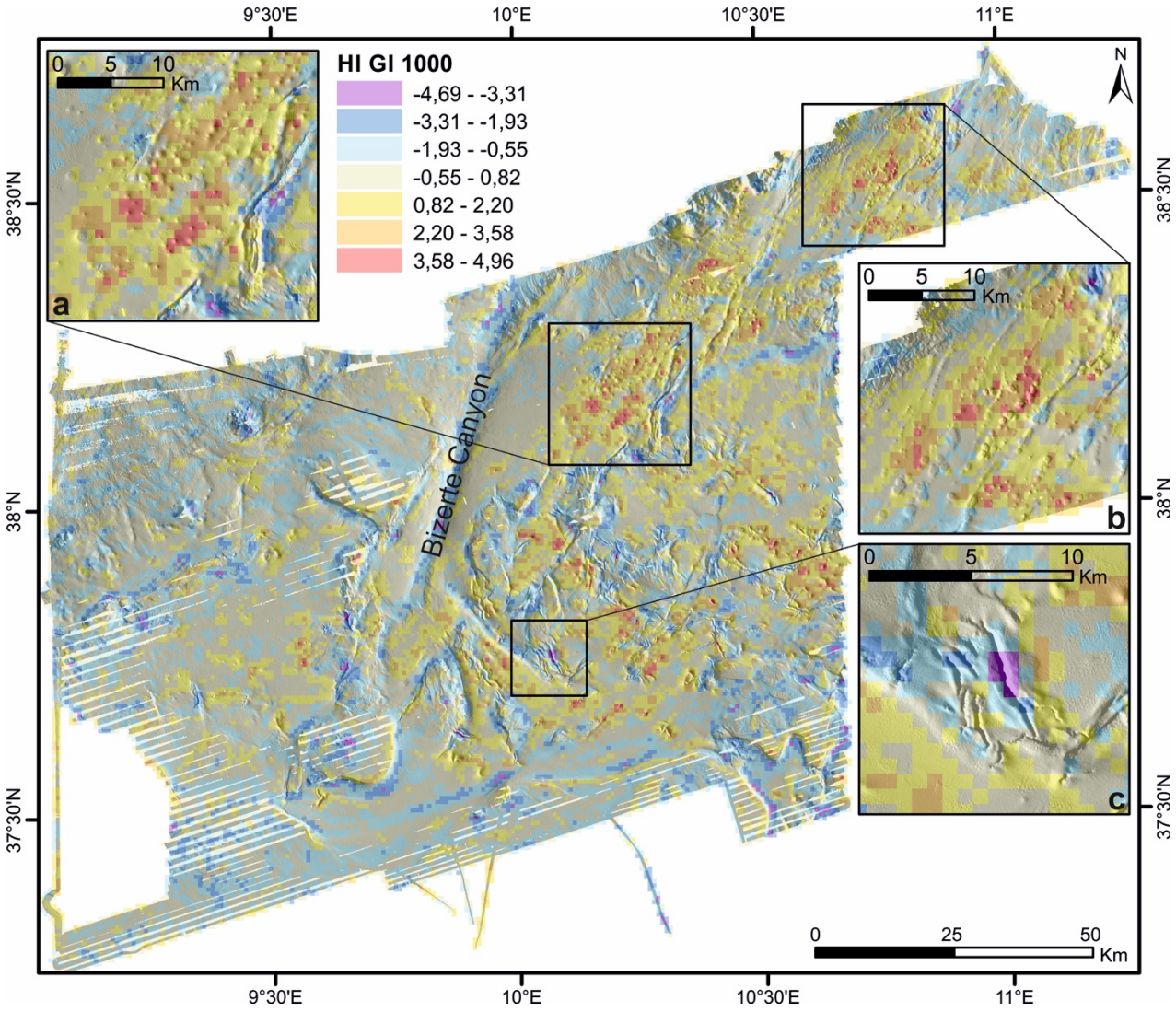

Figure 5.2. *Gedis-Ord statistic estimation for the Hypsometric Integral (HI) values using a 30 m bathymetric map and analysing a grid with a pixel size of 750 m. a) and b) Zoom of clusters of high HI values coinciding with high-density pockmark fields, c) Zoom of a cluster of low HI values coinciding with Cold Water Coral Mounds (CWCM).*

Swath profiles

A total of 36 profiles extracted from the North Tunisian continental margin were stacked and plotted in three different patterns (i.e. continuous, dashed and dotted lines), in order to differentiate the profiles corresponding to northern, central and southern sectors, respectively (Figure 5.3). In general, swath profiles in Figure 5.3.a display the same trend as the one observed with the hypsometric analysis (Hi) explained above.

Although standard deviation values (dark grey area in Figure 5.3.a) for the western sector are higher than the ones of the eastern part, the profiles of the eastern sector are more intertwined and display a higher chaotic aspect than the western ones (i.e. where profiles are more parallel among

themselves). Thus, despite being smoother in the long wavelengths, the eastern sector has a more complex small-scale relief, with more variable seafloor roughness. On the other hand, the western sector profiles are more parallel among them and the standard deviation values are directly related to the depth variability. This variability is induced by the north-western slope, the large Sentinelle and Estafette Banks and the western flank of the Bizerte Canyon.

Regarding the northern profiles (continuous lines), they are parallel in the westernmost sector following the NW slope and the Sentinelle Bank (Figure 5.3.a). However, at the eastern sector and beyond the slope of the eastern flank of the Bizerte Canyon, profiles become more intertwined (Figure 5.3). A similar pattern is displayed by the profiles of the central area (dashed lines). The western sector is characterized by a stripe of parallel profiles displaying the smooth area between the Spiss Bank and the Shelf (Figure 5.3). To the east of the Bizerte Canyon area (dashed red line in Figure 5.3.a) the pattern of the profiles becomes more chaotic. Finally, the southern profiles (dotted lines) also display the same trend with the eastern sector profiles being more intertwined than the western ones (Figure 5.3). Generally, swath profiles show a more variable seafloor roughness in the eastern sector than in the western one.

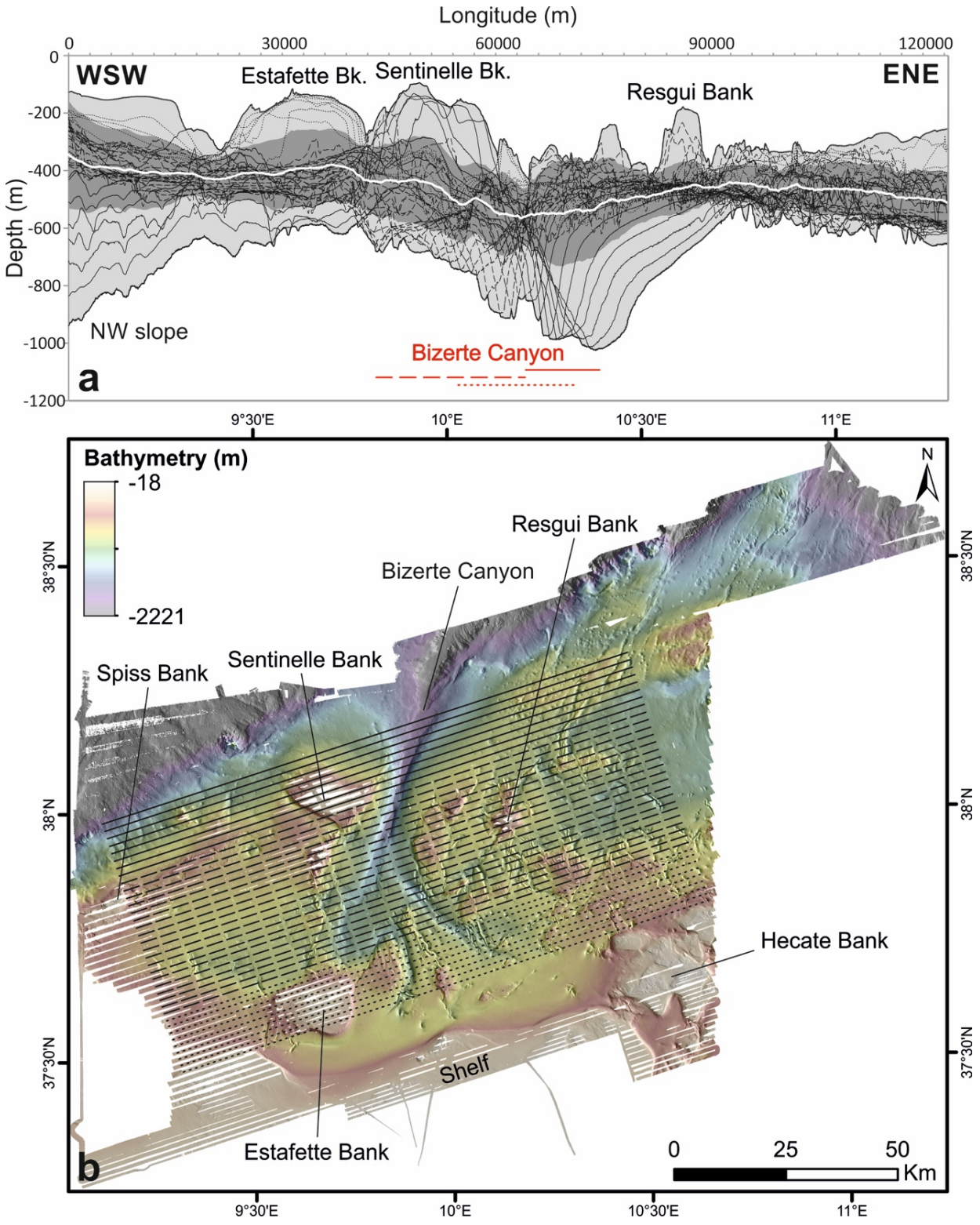

Figure 5.3. *a) Overlapping plot of a total of 36 swath profiles extracted from the North Tunisian continental margin. Three groups of swath profiles are differentiated as continuous, dashed and dotted lines. The red lines below the Bizerte Canyon correspond to the area influenced by the canyon among the three groups of profiles. The white line shows the mean value. The dark grey area correspond to the standard deviation values and the light grey area to the extreme values, b) Bathymetric map of the surveyed area offshore Northern Tunisia with the tracks of the 3 categories of swath profiles displayed, following the pattern shown in (a).*

5.3.2. Geomorphological domains

The offshore area (white polygon in Figure 5.4) is characterized by two main domains, described below: i) a small part of the continental shelf, and ii) the plateau-slope area, which covers most of the mapped region. Besides these two main domains, we also identified other much smaller-scale physiographic domains in the area, such as several structural blocks and the Bizerte Canyon system.

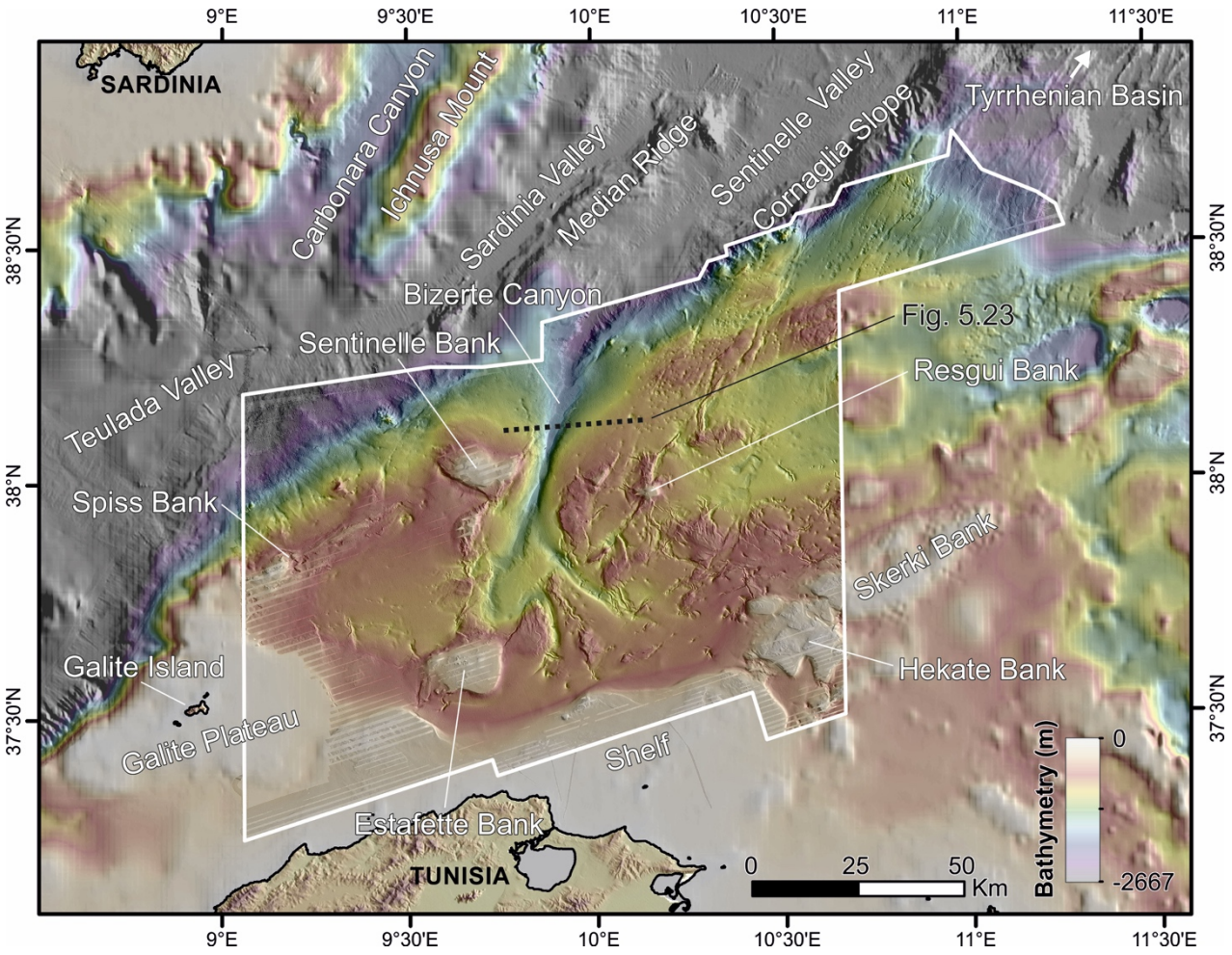

Figure 5.4. *Bathymetric map of the offshore North Tunisian margin. The white polygon outlines the study area. The bathymetric data of adjacent areas correspond to a compilation of different datasets (EMODnet, 2018) with an illumination azimuth of 72° and an altitude of 45°. The dashed black line across the Bizerte Canyon shows the location of seismic profile depicted in Figure 5.23.*

a) The continental shelf domain

The continental shelf, characterized by a depth range between -80 m to -290 m, has a generally smooth seafloor, with a slope gradient of 1° with few local rough areas (Figures 5.5 and 5.6). These rough areas display high-backscatter values that suggest the presence of an indurated rock at the seafloor (Figure 5.6.b). These rocky outcrops are also evidenced in the high-resolution parametric

echosounder profiles (Figure 5.6.d). Rough outcrops along the shelf, span from 10 to 90 km^2 in surface, with a tabular morphology that rises about 20 m from the surrounding seafloor (rough areas in Figure 5.5). The rough morphology contains small ridges and mounds up to 10 m high (i.e. rough areas with salient outcrops as defined in Figure 5.5). Despite the chaotic and rough relief of these outcrops, there is an evident preferential direction of their bounding scarps, coinciding with ENE-WSW and NW-SE trends (Figure 5.5). The shelf edge, delimited by the 200 m isobath, also displays ENE-WSW and NW-SE trends and shows a gentle gradient towards the north (Figure 5.6.a and 5.6.b). These gentle gradients are related to the occurrence of prograding thin Quaternary sequences. In fact, these prograding sediments are clearly displayed in high-resolution TOPAS profiles showing clinoform morphologies and thinning of the sediment layers downslope (Figure 5.6.c).

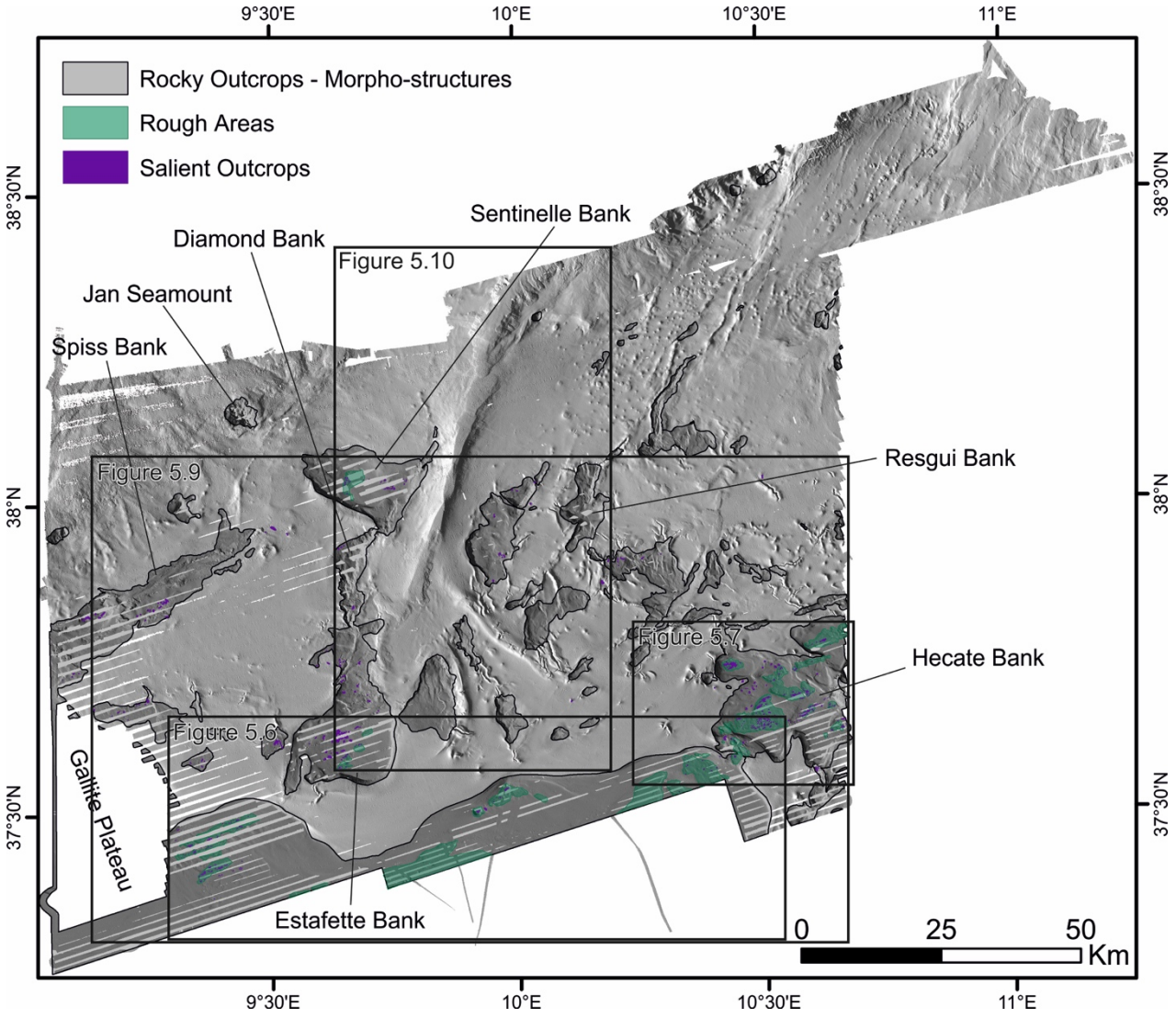

Figure 5.5. *Rocky outcrops mapped within the study zone overlaid on the bathymetric shaded relief map (with an illumination azimuth of 72° and an altitude of 45°). Outlined black boxes show the location of the different domains, corresponding to Figures 5.6, 5.7, 5.8 and 5.9.*

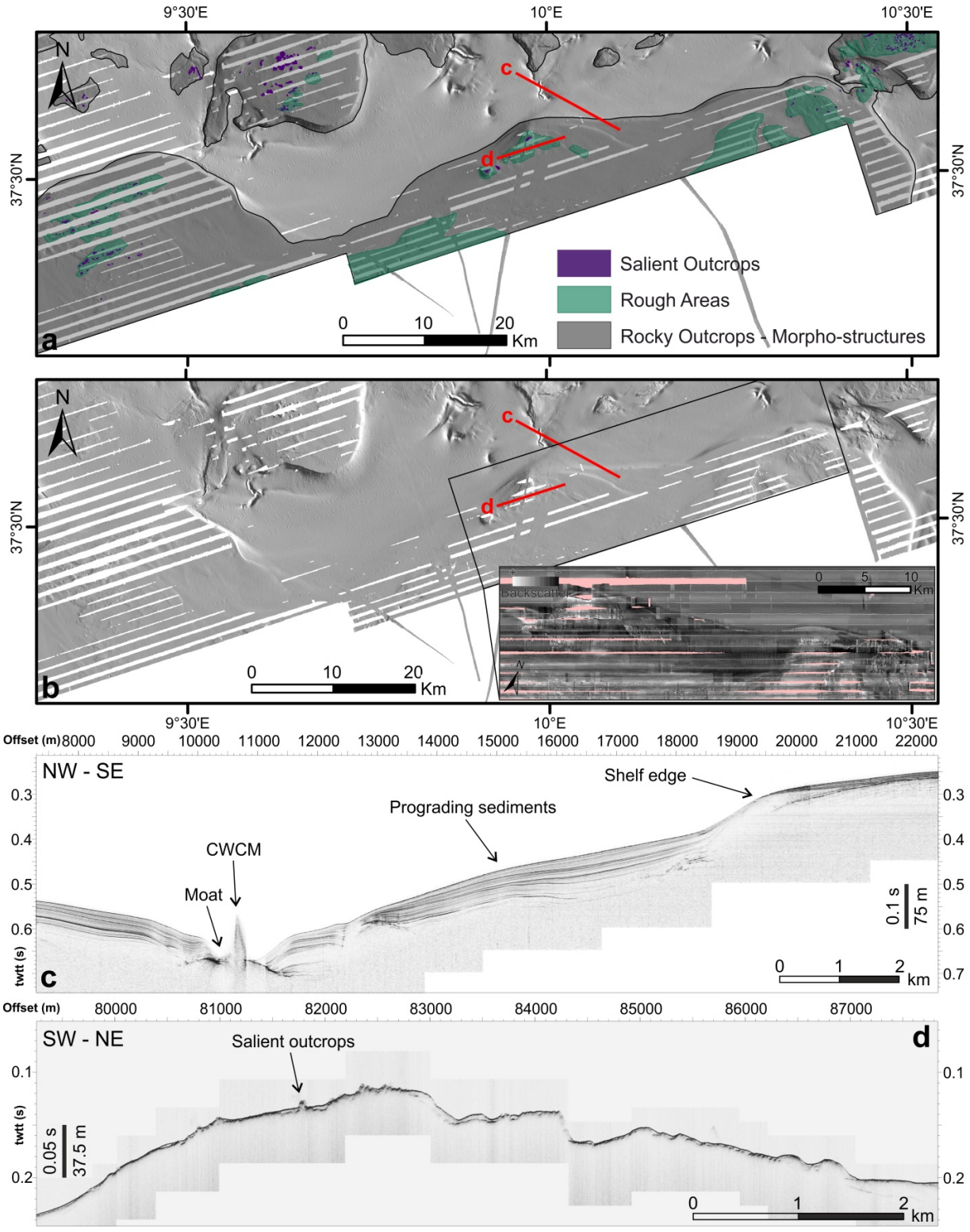

Figure 5.6. *Detail of the outer shelf region with the rocky outcrops mapped. a) Interpreted shaded relief map (illumination azimuth of 72° and altitude of 45°); b) Shaded relief map with a zoom of the acoustic backscatter map. Pink colour background correspond to areas with no backscatter data; c) TOPAS parametric echosounder profile showing prograding sediments; d) Innomar parametric echosounder profile showing the rough seafloor with rocky outcrop areas in the shelf. Location of these profiles are located in (a) and (b). Vertical scales of the profiles are in seconds (Two-way Travel Time). A time-depth conversion has been carried out taking into account sonic velocities of 1500 m/s. Location of this figure is shown as a black rectangle in Figure 5.5.*

b) Large scale structural blocks

The study area is characterized by massive structural blocks (Figure 5.5). The largest structural block is the Hecate Bank (as part of the Skerki Bank; Würtz and Rovere, 2015) located to the east of the continental shelf. This block is 20 km wide, covers a surface of around 300 km^2 and in plan-view displays a straight and angular shape (Figure 5.7). The block base is at around -300 m depth, and rises up to 220 m above the surrounding seafloor. Its steepest flanks are in the south, with ~30º maximum slope values, while to the north it shows a smooth topography with gentle gradients that transition to the surrounding seafloor (Figure 5.7). The top of the block, located at -150 to -80 m depth, shows a smooth seafloor alternating to rough areas from 20 to 40 m high (Figure 5.8.a). These rough areas usually show salient outcrops from 5 to 10 m high on their tops (Figure 5.8.a).

In Figure 5.8.b we observe the occurrence of gas flares over the Hecate Bank indicating active fluid flow and/or gas seepage. In fact, abundant gas flares have been recognized in the explored region at depths ranging between -37 m and -257 m, i.e. along the continental shelf and at the Hecate, Sentinelle, Estaffete Banks and the Gallite Plateau (Figure 5.9). Flares have been identified on most seismic profiles across the areas described above and display either a spotty random distribution or are grouped in fields up to ~5 km wide (Figure 5.9). Both bathymetric data and parametric echosounder profiles show that the occurrence of largest gas flares coincide with the rough and irregular seafloor areas of the shelf (Figure 5.9). In the parametric echosounder records, flares appear as vertical traces, with a maximum height of up to 25 ms above the seafloor (i.e. about ~19 m assuming 1500 m/s sound velocity of the water column) (Figure 5.8.b).

In addition to the Hecate Bank, two other large-scale blocks are displayed in the area with similar morphological aspect. These features occur at the head of the Bizerte Canyon (i.e. Estafette Bank; Würtz and Rovere, 2015) and along its west flank (i.e. Sentinelle Bank, Würtz and Rovere, 2015). They cover a surface of up to 160 and 140 km^2 respectively, with their bases located at a depth ranging between -350 to -500 m and rising above the seafloor up to 260 m (Figure 5.5). Their tops, located between -190 and -120 m deep, also display a smooth and flat morphology. Their central sector is characterized by rough and irregular outcrops less than 100 m high and gently dipping towards the N-NW. Up to 200 m high and a maximum of 30º steep slopes bound these structural highs along the eastern and southern flanks while the northern boundaries are rather smoother. All these features display slightly tilted blocks towards the N-NW (Figure 5.10.a and 5.10.c). South of the Sentinelle Bank, a diamond-shaped smaller high with a top less than -200 m

deep is observed and we name it Diamond Bank (Figure 5.5). Again, it displays steep eastern flanks while the western ones show lower gradients.

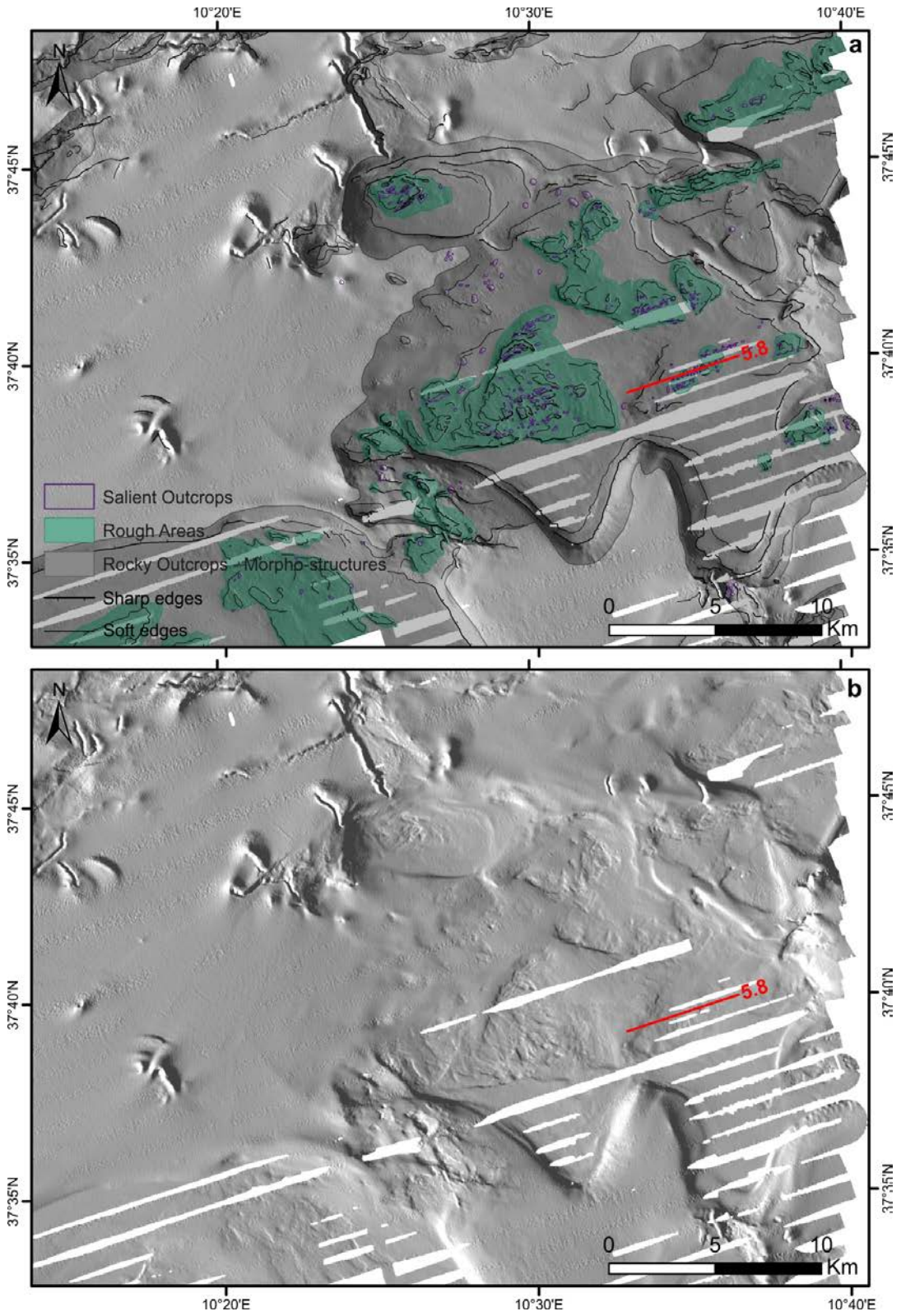

Figure 5.7. *Detail of the Hecate bank. a) Interpreted shaded relief map with an illumination azimuth of 72° and an altitude of 45°, b) Shaded relief map. Location of the profile from Figure 5.8 is depicted with a red line. Location of Figure 5.7 is shown by a black box in Figure 5.5.*

More to the west, the Spiss Bank (Würtz and Rovere, 2015) constitutes an elongated WNW-ESE-trending promontory of about 45 km long and a complex morphology along its axis (Figure 5.9). This structural high connects to the SW with the Gallite Plateau. The height of the Spiss Bank increases towards the southwest as it approaches to the Gallite Plateau, reaching a minimum depth of -115 m. More to the east, a narrow elongated 8.5 km-long-feature rises up 80 m from the surrounding seafloor, reaching a minimum depth of -250 m (Figure 5.5). In addition, a small block with a flat and smooth top, the Resgui Bank (Würtz and Rovere, 2015), is located east of the Bizerte Canyon. This block has its base at a depth of around -440 m and its top at -185 m depth, covering a surface of 60 km^2. It shows an elongated morphology following the NE-SW regional structural trend. Resgui Bank displays steeper slopes along the eastern flank (Figure 5.5). Aside from all these structural highs explained above, several smaller-scale rocky outcrops are observed throughout the study region but mostly distributed to the east of the Bizerte Canyon (Figure 5.5).

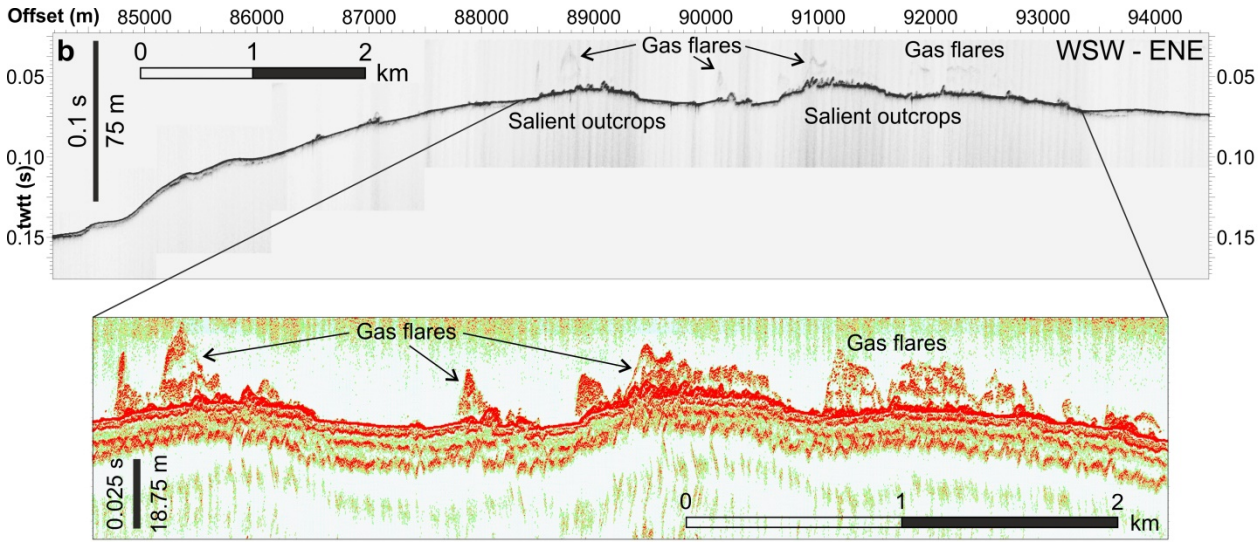

Figure 5.8. *Images of salient outcrops and gas flares above the Hecate Bank. a) Innomar parametric echosounder profile showing salient outcrops and gas flares above the Hecate Bank; b) Zoom of the Innomar high-frequency parametric echosounder profile where gas flares are clearly displayed. Depths are in seconds two-way travel time (TWTT) below sea level. Location of the record is depicted in Figure 5.7.*

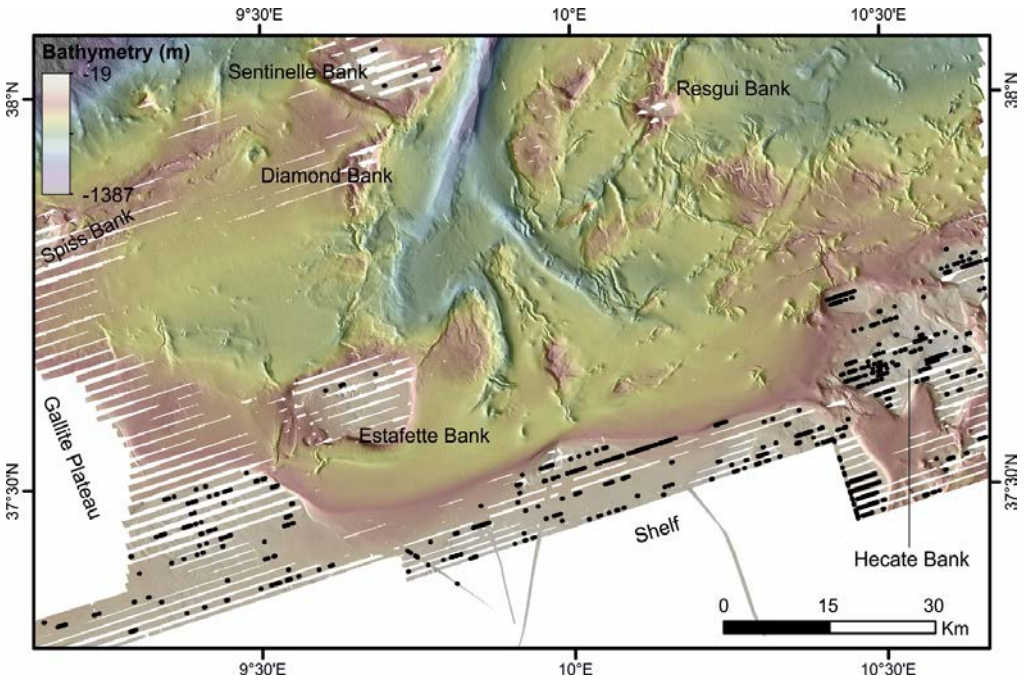

Figure 5.9. *Gas flares identified and mapped based on the analysis of the high-frequency Innomar parametric echosounder profiles. Black dots depicted on the coloured shaded relief map (illumination azimuth of 72° and altitude of 45°). Location of this Figure is shown in Figure 5.5.*

c) The Bizerte Canyon

The Bizerte Canyon is a prominent geomorphological feature of the North Tunisian continental margin. It extends for 80 km in the central sector of the study region, ranging from -500 to -1.400 m depth and following a NNE-SSW structural trend. To the northeast, the canyon extends beyond our mapped area towards the Sentinelle Valley (Figure 5.4). The head of the canyon is characterized by two elongated depressions: one following a NNW-SSE trend and the other one a NW-SE trend, probably corresponding to old, inactive tributary channels nowadays disconnected from the main channel (Figure 5.10.a). These branches were identified long ago (Genneseaux and Stanley, 1983), and were related to paleo-drainage systems.

Bizerte Canyon corresponds to a linear feature, incised about 400 m and 4 to 10 km wide. It shows abrupt irregular physiography, with a topographic high in a central-position along the canyon axis (Figures 5.10.a and 5.10.d). Swath profiles along its axis show a U-shaped morphology with a broad flat floor and steeper slopes at the eastern margin of the central sector of the canyon (Figures 5.10.b and 5.10.e). Furthermore, the canyon head is disconnected from the Tunisian shelf margin. The bathymetry shows numerous slide scars mainly located at the head of the canyon and at the north-eastern segment connecting to the Sentinelle valley (Figure 5.10.a). The mass-transport phenomena from the canyon walls to the thalweg is recorded by the transparent facies in TOPAS profiles (Figure 5.10.f).

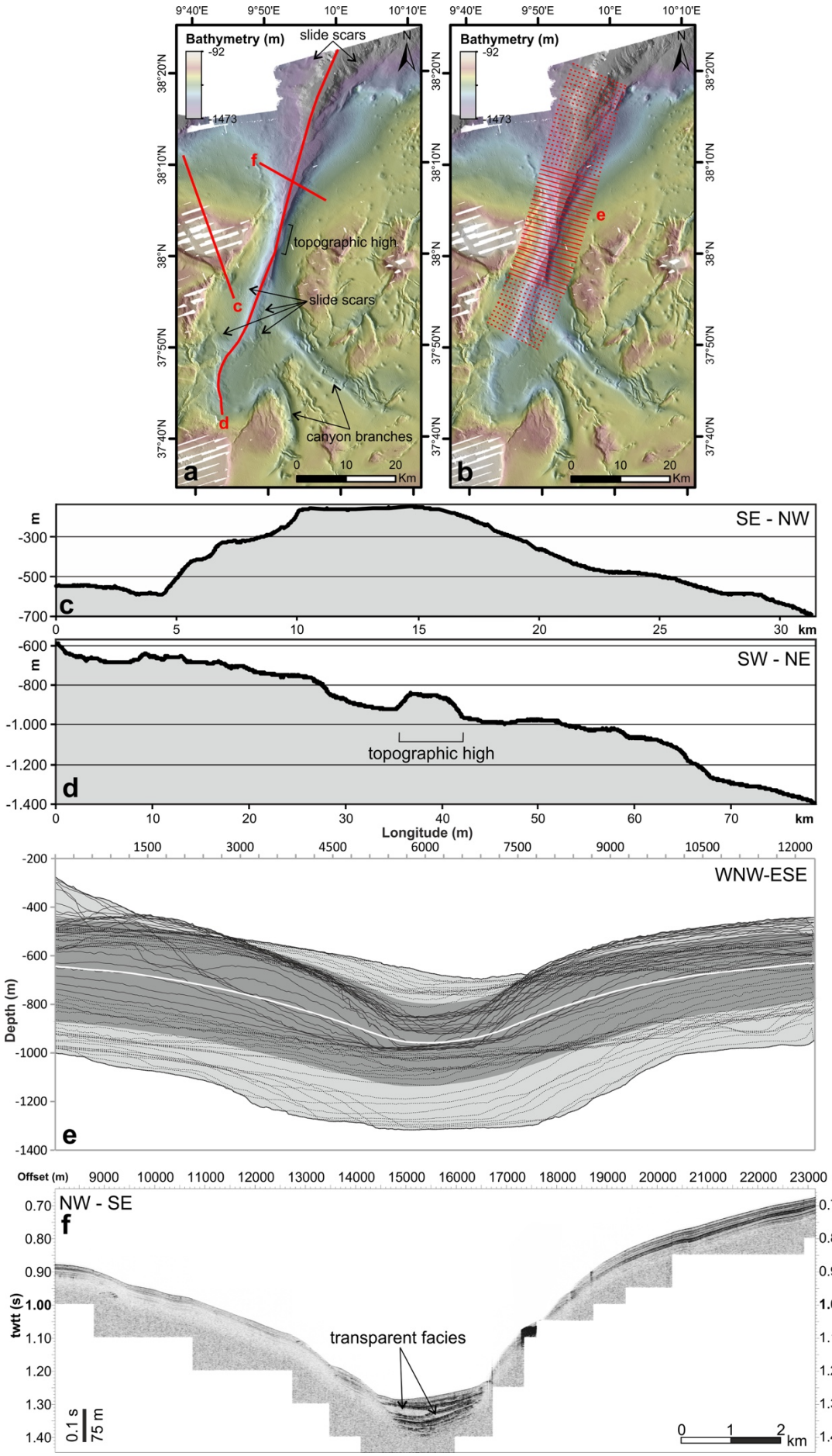
9°40'E
9°50'E
10°E
10°10'E
38°20'N
38°10'N
38°N
37°50'N
37°40'N
Bathymetry (m)
-92
-1473
slide scars
N
f
topographic high
c
slide scars
d
canyon branches
e
0
10
20
Km
a
b
SE - NW
m
-300
-500
-700
c
0
5
10
15
20
25
30
km
SW - NE
-600
-800
-1.000
-1.200
-1.400
topographic high
d
0
10
20
30
40
50
60
70
km
Longitude (m)
1500
3000
4500
6000
7500
9000
10500
12000
WNW-ESE
Depth (m)
-200
-400
-600
-800
-1000
-1200
-1400
e
Offset (m)
9000
10000
11000
12000
13000
14000
15000
16000
17000
18000
19000
20000
21000
22000
23000
NW - SE
f
twtt (s)
0.70
0.80
0.90
1.00
1.10
1.20
1.30
1.40
transparent facies
0.1 s
75 m
0
1
2
km

Figure 5.10. *Detail of the Bizerte Canyon. a) Colour-shaded relief map of the Bizerte Canyon (illumination azimuth of 72º and an altitude of 45º), with the location of the across Sentinelle Bank profile (c), along-axis profile (d) and across-canyon profile (f); b) Same map with the location of the swath profiles at the central part of the Bizerte Canyon; c) Bathymetric cross-section along the Sentinelle Bank, d) Bathymetric cross-section along the Bizerte canyon; e) Swath profiles extracted for the Bizerte canyon (The profiles in a middle position are displayed in continuous lines while the northern and southern ones are displayed as dotted lines. The white line shows the mean value, the dark grey area corresponds to the standard deviation values and the light grey area the extreme values). Location of the records is imaged in b; f) TOPAS profile across the Bizerte canyon (depths are in seconds two-way travel time (TWTT) below sea level.); Location of the Figure is depicted as a black rectangle in Figure 5.5.*

d) The plateau-slope domain

The Eastern plateau-slope sector

East of the Bizerte Canyon, the plateau-slope domain displays a complex morphology (as seen through the morphometric analysis above). This complexity is mainly produced by a dense network of small-scale structural highs (Figure 5.5, 5.11, 5.12, 5.13 and 5.14). These structural blocks rise 50 to 250 m high from their base at -400 and -500 m depth. The tops of most of them are gently tilted toward the west. They display sharp scarps facing the east with NNE-SSW trending walls up to 190 m high and 20° steep (Figures 5.11, 5.13 and 5.15.a). In contrast, some other features dip gently towards the east, while its corresponding scarps are oriented towards the west and north-northwest (Figure 5.11, 5.14 and 5.15.b).

In the north-eastern sector, a partially surveyed 45 km long and 15 km wide WSW-ENE trending high rises 200 m in average above the surrounding seafloor that we name Bizerte Ridge (Figures 5.11, 5.12 and 5.13). The height of this promontory increases north-eastwards to ~350 m above the surrounding seafloor. In general, the seafloor is not as rocky as at the structural highs described above (Figures 5.11, 5.12 and 5.15.c), with the exception of small outcrops along the high.

These outcropping structural highs bound several small basins filled with sediment sequences. Near these small basins, a large basin spans across the eastern sector. This basin, roughly delineated by the -500 m isobaths, is bounded to the north by the Bizerte Ridge described above and by the Hecate Bank to the south (Figure 5.11). Longitudinally, seafloor structural highs (including Resgui Bank), bound its western sector, while the eastern end was not entirely mapped during Geomargen-2 cruises (Figure 5.11). However, EMODnet-HRSM bathymetry (EMODnet, 2018) delineates the extension to the east, with a large structural high in a central position (Figure 5.11).

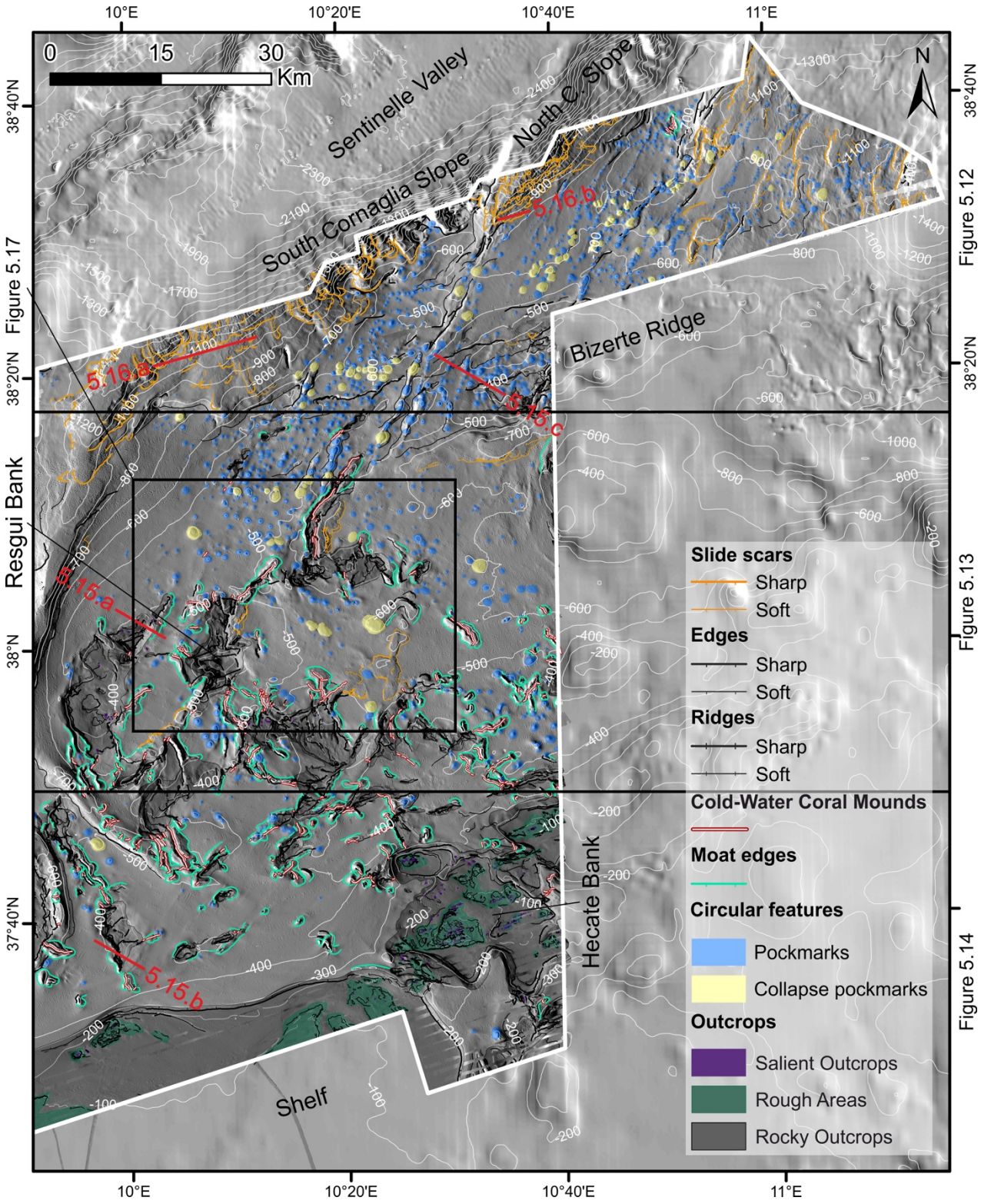

Figure 5.11. *Geomorphological map of the Eastern plateau-slope sector. Diverse morphological elements are mapped above our dark-grey shaded-relief map (bounded by a thick white line). In light-grey is depicted the surrounding area corresponding to a compilation of different datasets (EMODnet, 2018) (with an illumination azimuth of 72° and altitude of 45°). This figure is divided into three rectangles, each one related to Figures 5.12, 5.13 and 5.14, respectively. Thick red lines show the location of TOPAS records illustrated in Figures 5.15 and 5.16. The black box locates Figure 5.17.*

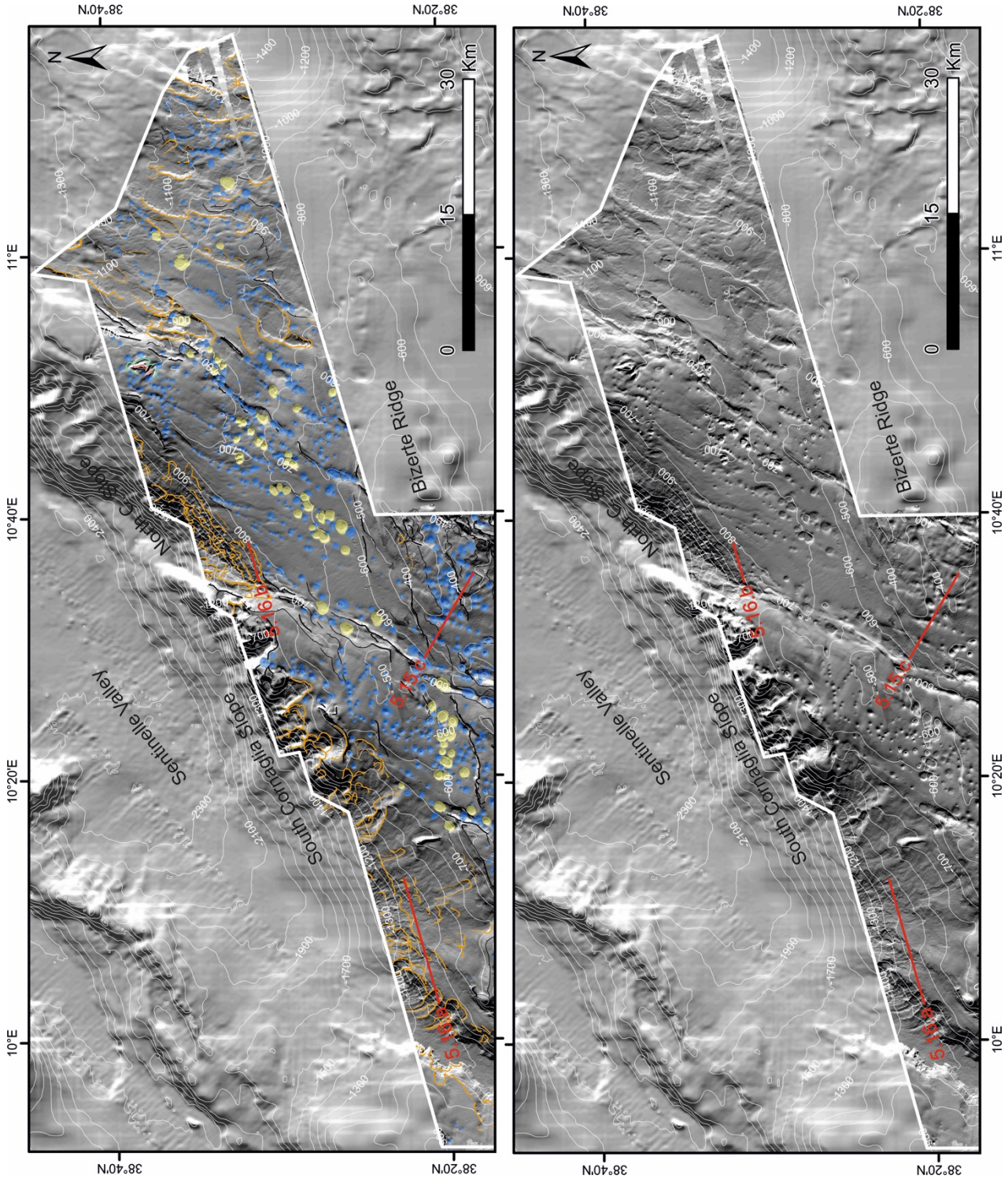

Figure 5.12. *Zoom of the northern sector of the eastern plateau-slope geomorphological map. a) Interpreted shaded relief map; b) Shaded relief map. Both maps have an illumination azimuth of 72° and an altitude of 45°. Profiles of Figures 5.15.c and 5.16.a,b are depicted in red.*

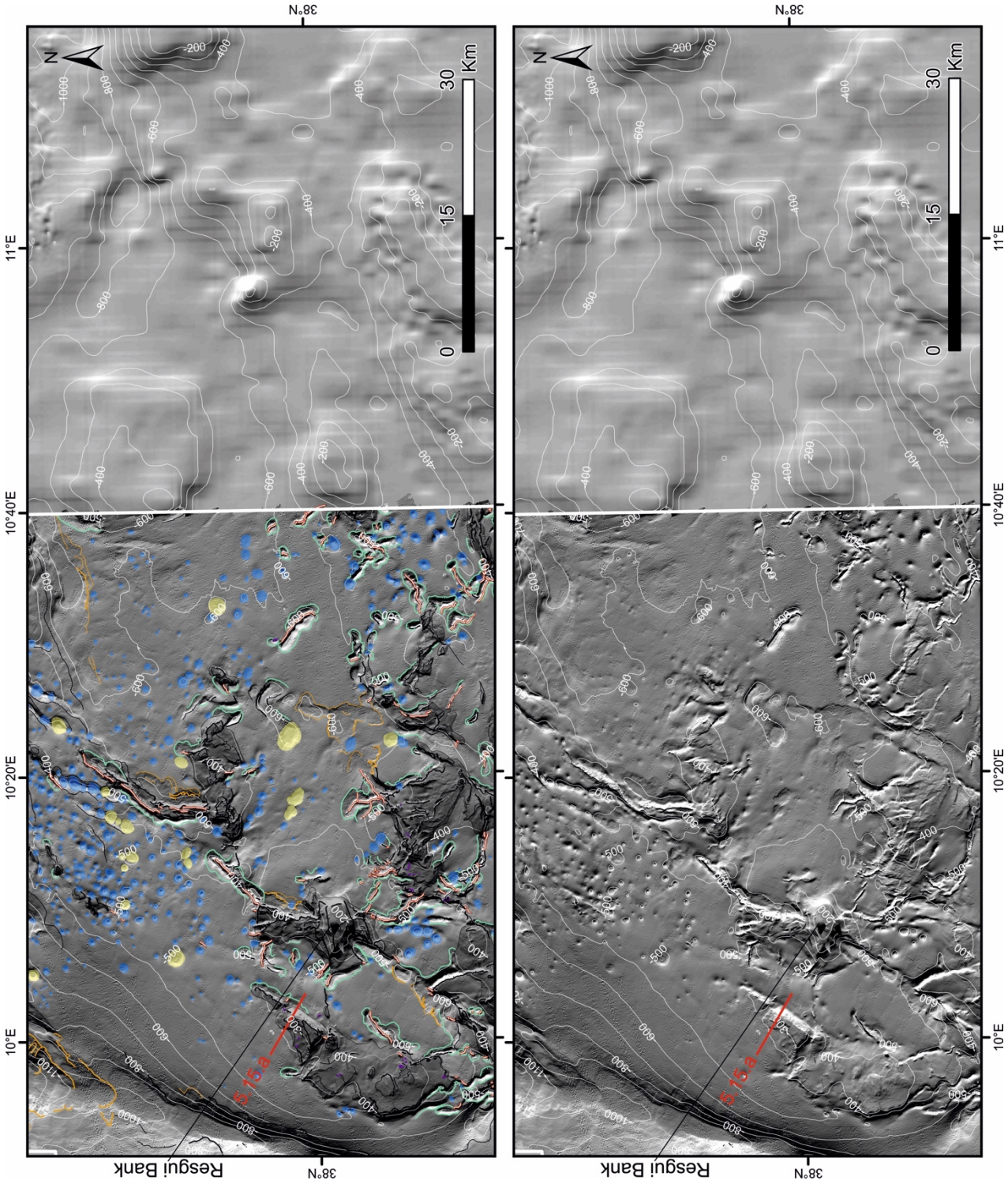

Figure 5.13. *Zoom of the central sector of the eastern plateau-slope geomorphological map. a) Interpreted shaded relief map; b) Shaded relief map. Both maps have an illumination azimuth of 72° and an altitude of 45°. Resgui Bank is located. Profile of Figure 5.15.a is depicted in red.*

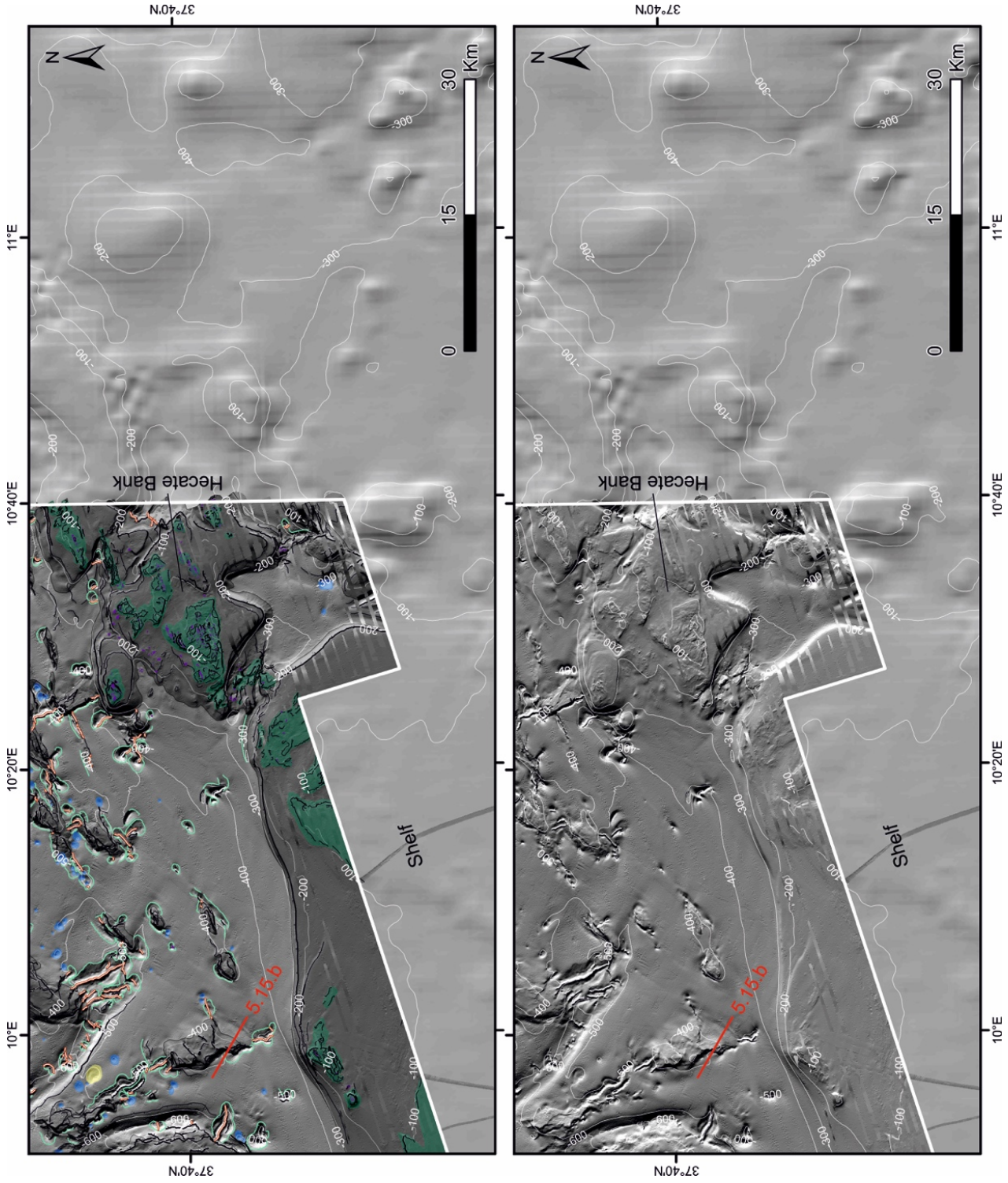

Figure 5.14. *Zoom of the southern sector of the eastern plateau-slope geomorphological map. a) Interpreted shaded relief map; b) Shaded relief map. Both maps have an illumination azimuth of 72° and an altitude of 45°. Hecate Bank is located. Profile of the Figure 5.15.b is depicted in red.*

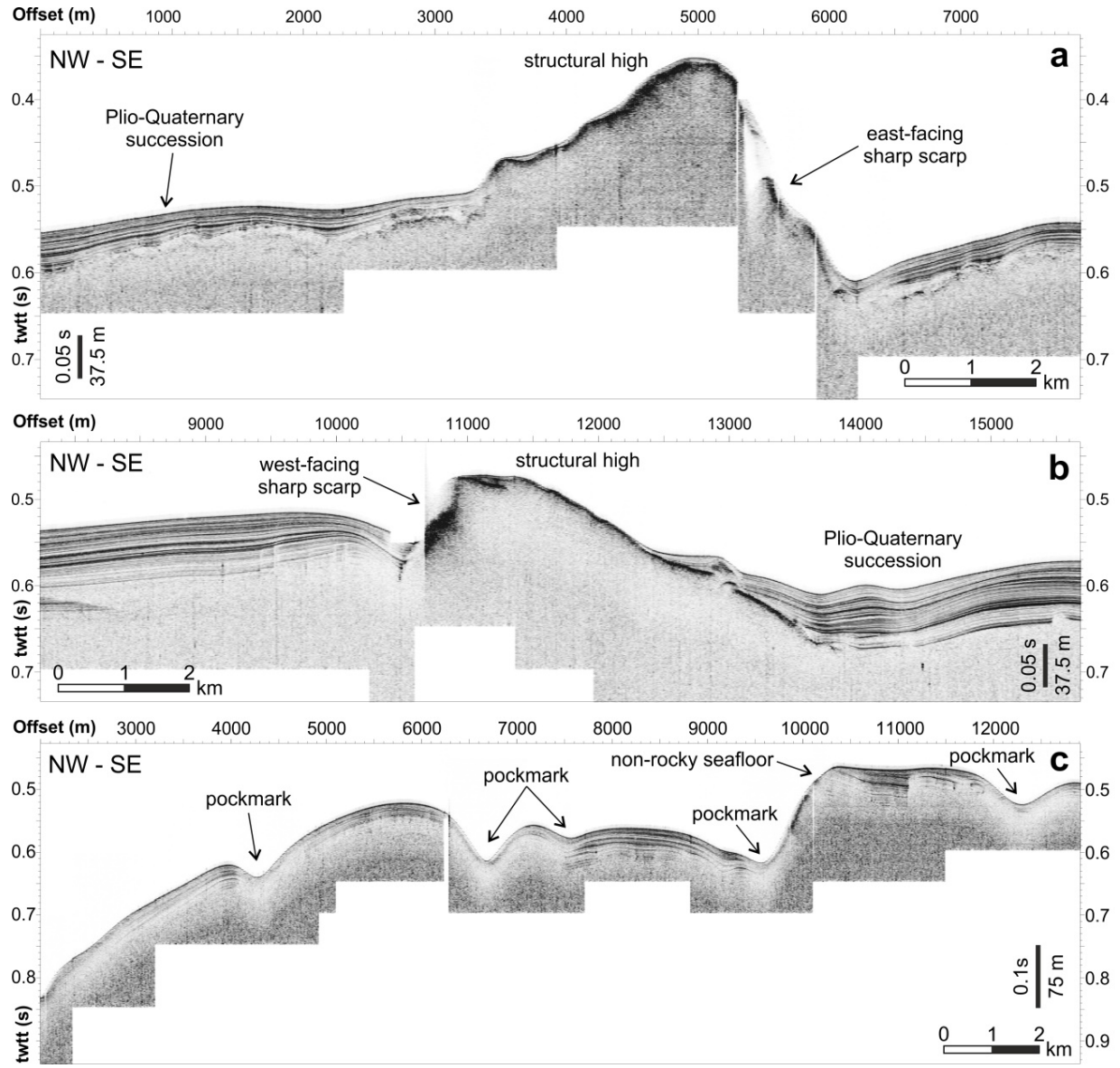

Figure 5.15. *TOPAS profiles of the Eastern plateau-slope structural highs. a) Example of a structural high displaying a steep east-facing scarpment; b) Example of a structural high displaying a steep west-facing scarpment; c) Bizerte Ridge in a stratified sedimentary sequence. Locations of the records are outlined in Figures 5.11, 5.12, 5.13 and 5.14.*

To the north of the Bizerte Ridge, there are two steep slopes in a NE-SW trend that are referred as south and north Cornaglia Slopes. These slopes are eroded by numerous mass transport phenomena evidenced by landslide scars and MTDs occurring along the slope, which have been filling the Sentinelle Valley (Figures 5.11, 5.12, 5.16.a and 5.16.b). At the easternmost sector of the mapped region depth increases to -1500 m and numerous slide scars and MTDs take place again, with sediment deposited to the east. In addition to these north slides related to the steep Cornaglia Slope, south of the area numerous scars, slides and slumps (and its corresponding MTDs) have been identified within the Tunisian Plateau, although here the terrain is often fairly smooth (Figure 5.17, 5.18.a and 5.18.b).

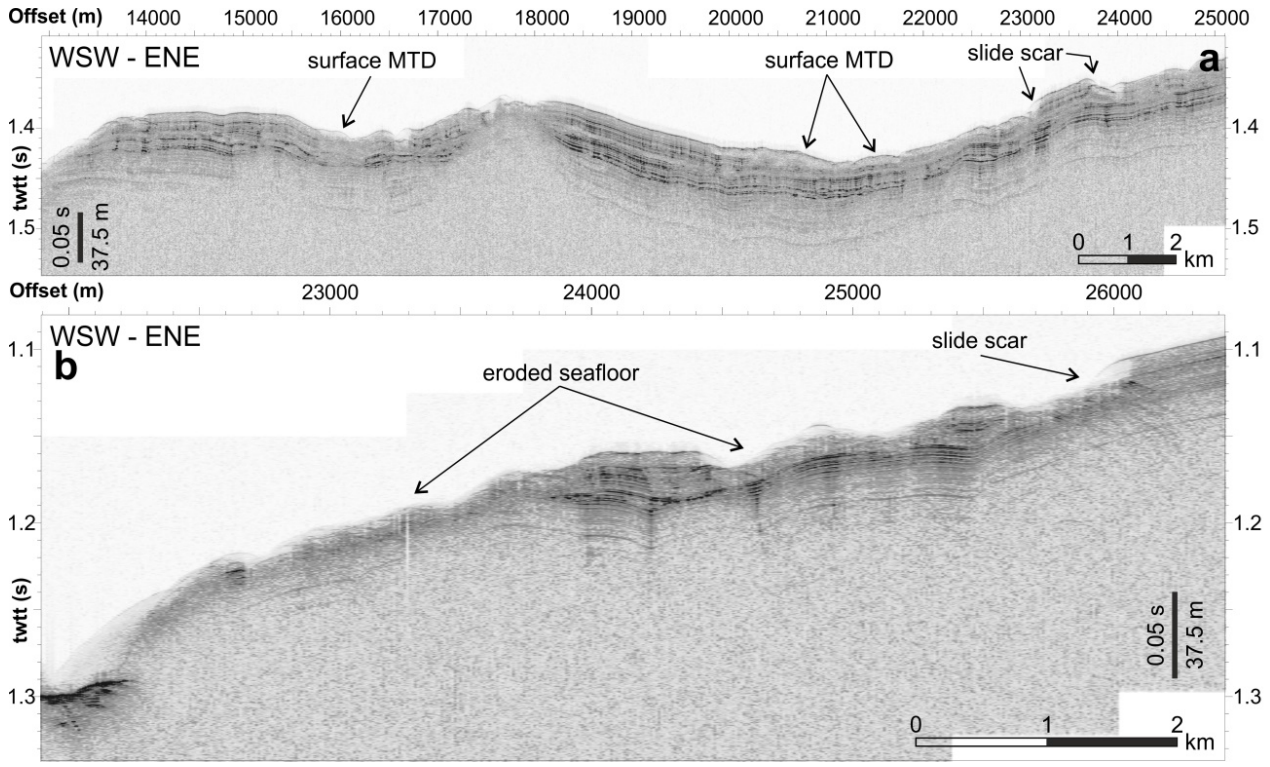

Figure 5.16. *TOPAS profiles of the north-eastern slope slides. a) Example of the South Cornaglia Slope slides; b) Example of the North Cornaglia Slope slides. Profiles are located in Figures 5.10 and 5.11. MTD: Mass-transport deposits.*

Besides the prominent structural highs on the eastern plateau-slope sector, pockmarks and cold-water coral mounds (CWCM) are conspicuous in the eastern area, and are far less frequent in other mapped areas.

The eastern plateau-slope sector accumulates most pockmarks in the region, containing 1353 pockmarks of the total amount of 1469 (Figure 5.11). Collapse pockmarks display the same distribution pattern, with 82 of 84 located in the eastern region. Pockmarks are distributed at a depth range of -276 to -1188 m (Table 5.1), covering the entire region except the top of the structural highs that contain indurated material. However, most pockmarks are located at depths of -400 to -500 m. Mapped pockmarks display a sub-circular to elongated shape (Figures 5.17 and 5.19.a), covering areas from 0.008 to 1.8 km^2 and displaying diameters ranging from 0.111 to 1.8 km (Table 5.1.a). On the other hand, collapse pockmarks display sub-circular to irregular shapes (Figures 5.17 and 5.19.b), covering larger areas from 0.1 to 5.9 km^2 and diameters between 0.4 and 3.3 km (Table 5.1.b). Pockmark depths (calculated from the pockmark's rim to the deepest point of the bowl) range between -2 and -105.4 m but show the higher density of features between -10 to -25 m (with 865 of 1469 features between this range), as suggested by the low standard deviation value (Table

5.1.a). In addition, collapse pockmark depths range from -9 to -103 m (Table 5.1.b) with a higher occurrence between -25 and -45 m, showing larger mean values than pockmarks.

Pockmarks (a)	**Seafloor depth (m)**	**Pockmark depth (m)**	**Area (km^2)**	**Diameter (m)**
Min	-275.640	-2.026	0.008	0.111
Max	-1187.823	-105.360	1.798	1.850
Mean	-632.097	-19.493	0.283	0.619
St. Deviation	172,805	-12.989	0.263	0.286
Collapse Pockmarks (b)	**Seafloor depth (m)**	**Pockmark depth (m)**	**Area (km^2)**	**Diameter (m)**
Min	-470.546	-8.928	0.125	0.439
Max	-1042.708	-103.454	5.942	3.338
Mean	-651.486	-40.394	1.181	1.341
St. Deviation	118.459	-19.145	0.930	0.517

Table 5.1. *Morphological characteristics of a) mapped pockmarks and b) collapse pockmarks.*

Within the eastern sector, pockmarks occur sparsely, either in small groups or clustered in a large system in the north-easternmost region (Figure 5.11). In contrast, scattered pockmarks do not display any preferential direction in their distribution. Clustered pockmarks display a clear pattern of distribution, forming alignments following a NE-SW preferential direction, similar to the orientation of the main regional morphological scarps (Figures 5.11 and 5.12). Collapse pockmarks display a sparse distribution with a higher concentration of features towards the north-easternmost sector (Figures 5.11 and 5.12).

CWCMs are widely distributed with an exceptional total number of 286 mounds exposed at the seafloor. CWCMs ridges are few hundred meters wide at their base, 20 m to 100 m high, and a few tens of meters to a maximum of 6.5 km long. High-resolution acoustic records show that structural highs, particularly their edges and scarps, are preference sites of CWCM development (Figures 5.17 and 5.20). Thus, the orientation of CWCMs shows to be roughly parallel to the main structural trends. In most cases, CWCM are a prolongation of NE-SW oriented scarps (Figures 5.17 and 5.20.a) or align NW-SE parallel to structural escarpments (Figures 5.17 and 5.20.b). About 80% of the CWCM are distributed over a ~3,000 km^2 wide sector of the plateau east of Bizerte Canyon, where most rocky outcrops occur (Figure 5.11). In addition, a few CWCMs occur inside the tributary channels to Bizerte Canyon, along paths of past and possibly on-going sediment transport direction (Figures 5.11 and 5.14).

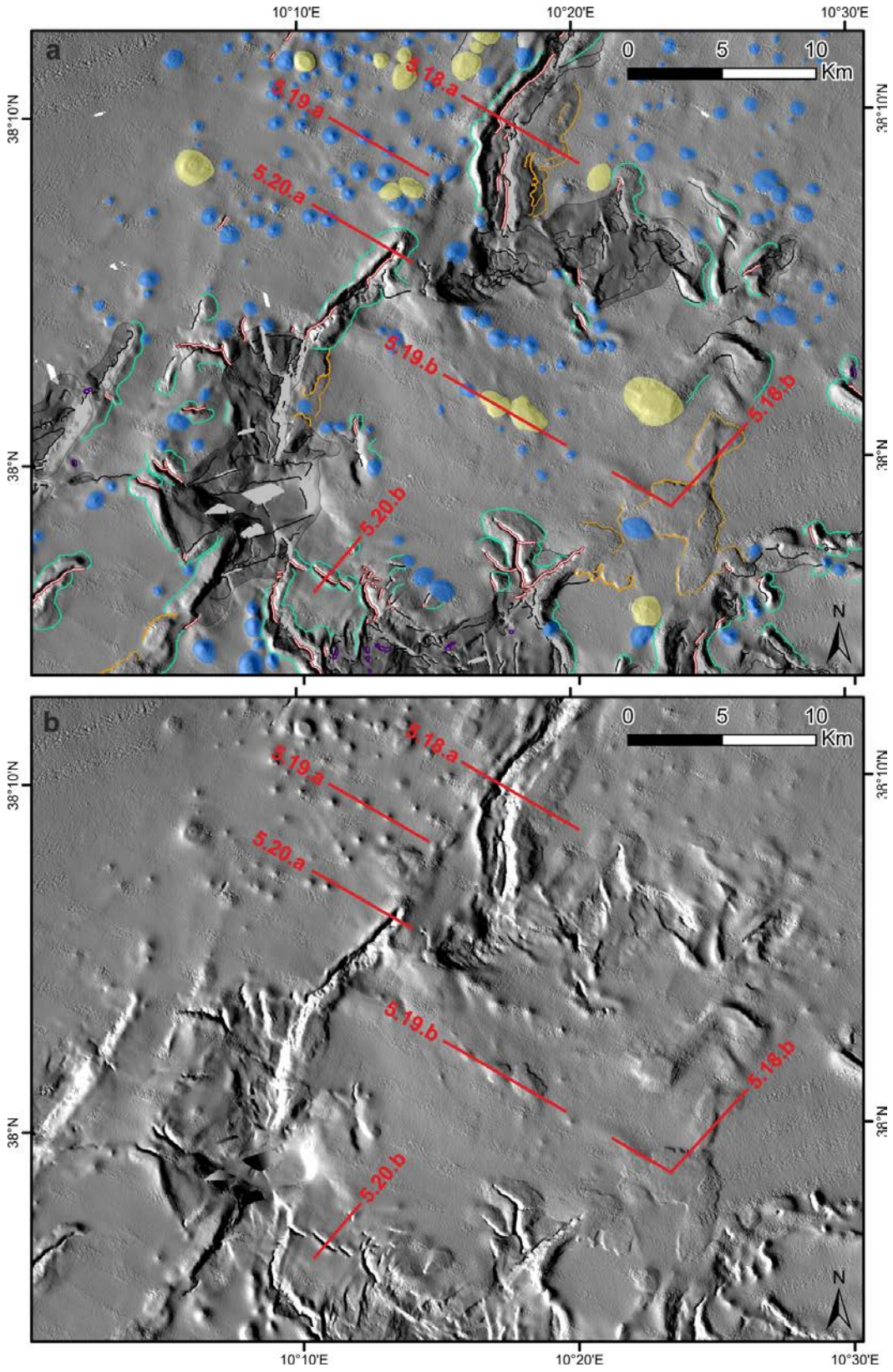

Figure 5.17. *Shaded relief map of the central area of the eastern plateau-slope sector (with an illumination azimuth of 72° and an altitude of 45°). a) Shaded relief map; b) Interpreted shaded relief map; Legend is shown in Figure 5.11. This figure is located by a black box in Figure 5.11. Red lines show the location of the different TOPAS records corresponding to Figures 5.18, 5.19 and 5.20.*

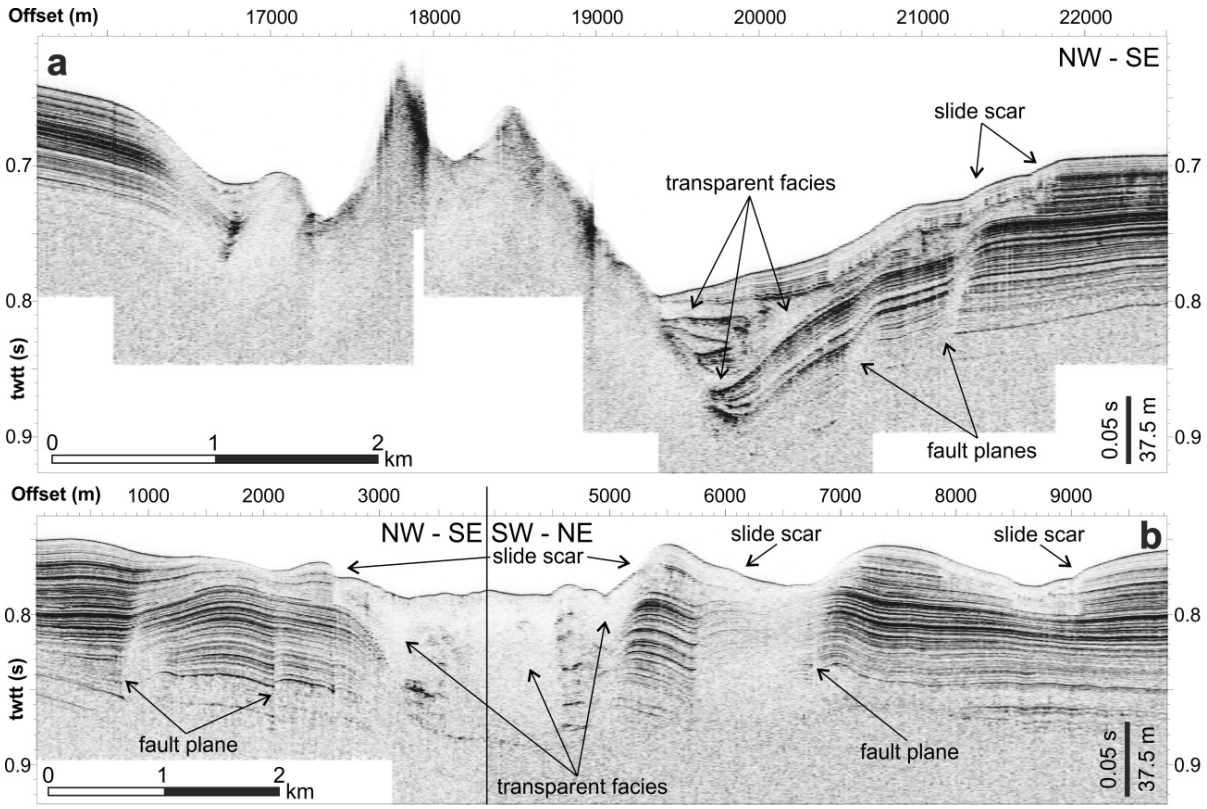

Figure 5.18. *TOPAS profiles of submarine slides within the eastern plateau-slope sector. a) Example of slide scars affecting a huge contourite deposit and transparent facies related to slide deposits filling in the contourite moat; b) Example of slide deposits and slide scars in relatively flat areas. Locations of the records are outlined in Figure 5.17.*

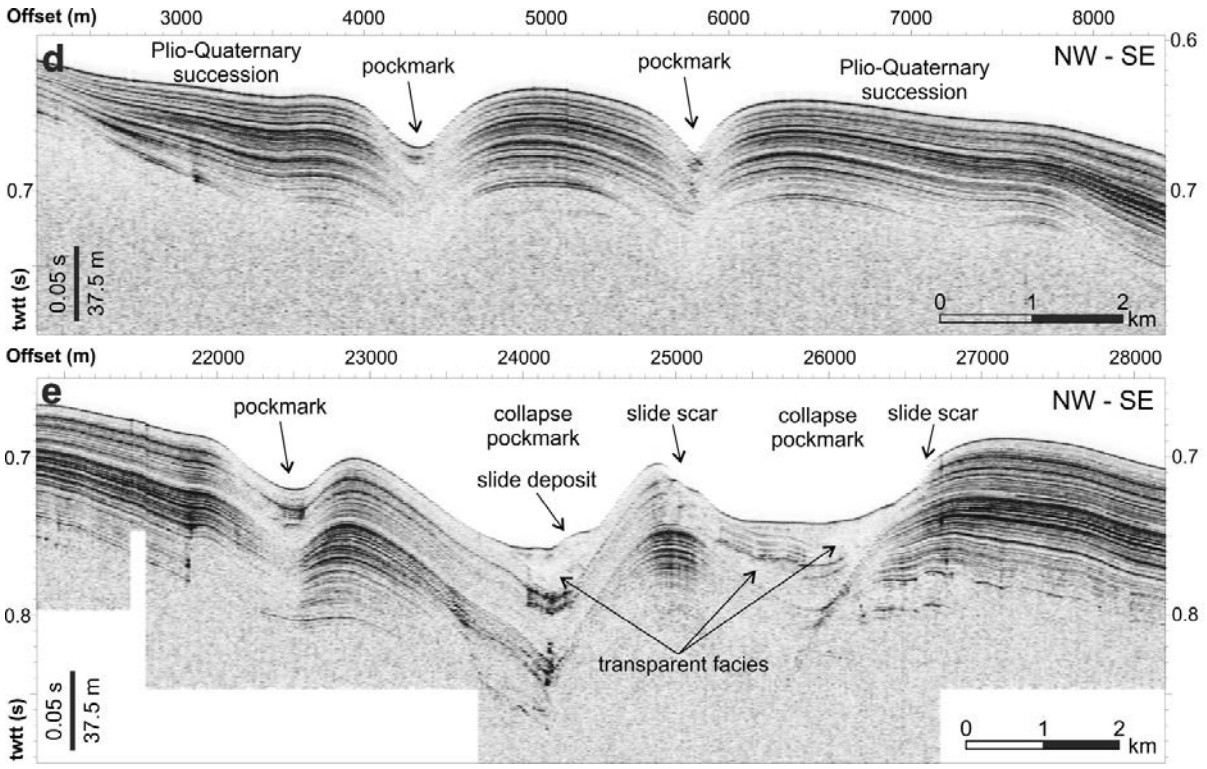

Figure 5.19. *TOPAS profiles showing examples of (a) pockmarks and (b) collapse pockmarks as well as other related features. Both profiles are located in Figure 5.17.*

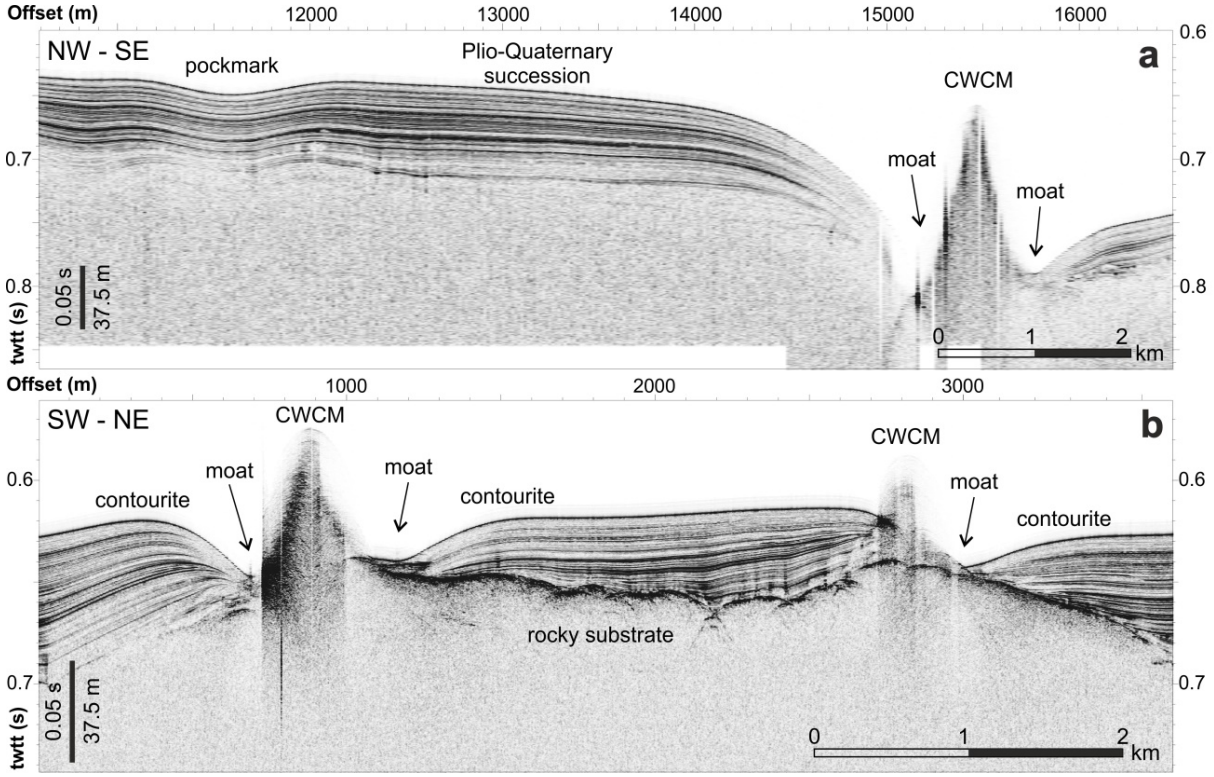

Figure 5.20. *TOPAS profiles showing examples of cold-water coral mounds (CWCM). a) A CWCM aligned following the main NE-SW direction of the observed linear escarpments; b) A CWCM aligned in a NW-SE direction as the linear escarpments of the structural high located southwards (Figure 5.17). Both profiles are located in Figure 5.17.*

The Western plateau-slope sector

The western plateau-slope sector extends west of the Bizerte Canyon. As the eastern plateau, it displays an irregular physiography but comparatively more uniform (Figures 5.21 and 5.22). A gentle slope occurs from the outer shelf at around -230 to -380 m depth (Figures 5.21 and 5.22). Downwards from the gentle slope area, a concave-up depressed sector is located at an average depth of 440 m and delineated by the -400 m isobath (Figures 5.21 and 5.22). This depressed area is bounded to the east by the Estafette, Sentinelle and Diamond Banks, to the north and west by the Spiss Bank (described above), and to the south by a few small-scale rocky outcrops (Figures 5.21 and 5.22). The deepest points of this depressed area (deeper than -500 m) correspond to erosive contourite moats, incising around 20 m following CWCMs (Figures 5.21 and 5.22).

To the north of the Spiss and Sentinelle Banks, occurs the slope area of the plateau-slope system. Average gradient increases to 2.5º up to the north-west in the deepest sector of the explored area, coinciding with the Teulada Valley at about -2220 m depth. Here, a NE-SW striking slope is carved by slide scars draining sediment towards the Teulada Valley (Figures 5.21 and 5.22). The largest scar in the NW area occurs between -1200 and -1400 m with a failure area of about 50 km^2

and 60-100 m depth, implying a total sediment volume of ~4 km^3 moved in one or several episodes. More to the east, a conical comparatively large feature with a volcano shape occurs, and we name it Jan Seamount. It is ~500 m high rising from -1200 to -800 m (Figures 5.21 and 5.22a).

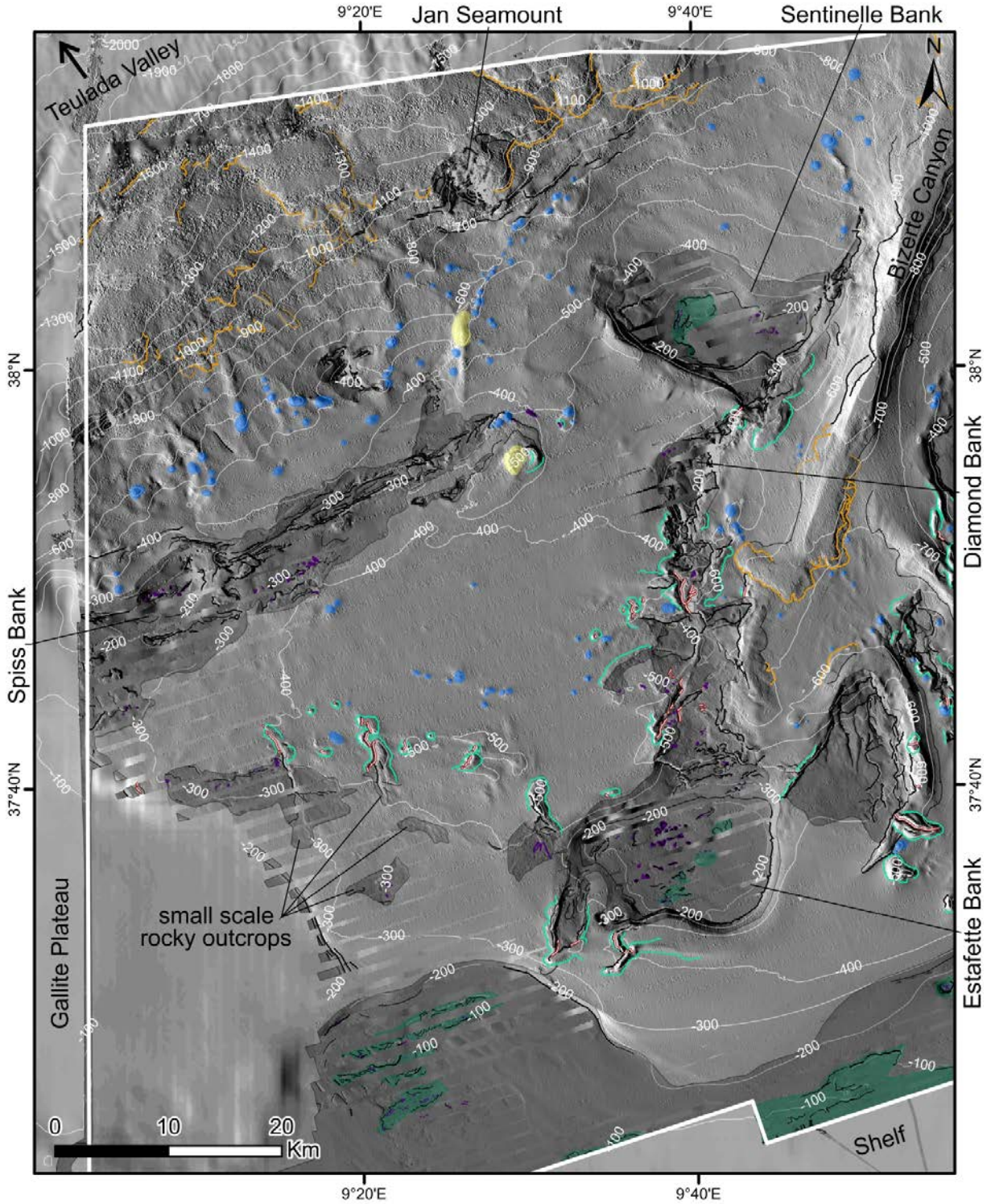

Figure 5.21. *Geomorphological map of the western plateau-slope sector. Cartography over a shaded map of our bathymetric data (bounded by a thick white line) and a mosaic of different datasets for the adjacent areas (all of them with an illumination azimuth of 72° and altitude of 45°) (EMODnet, 2018).*

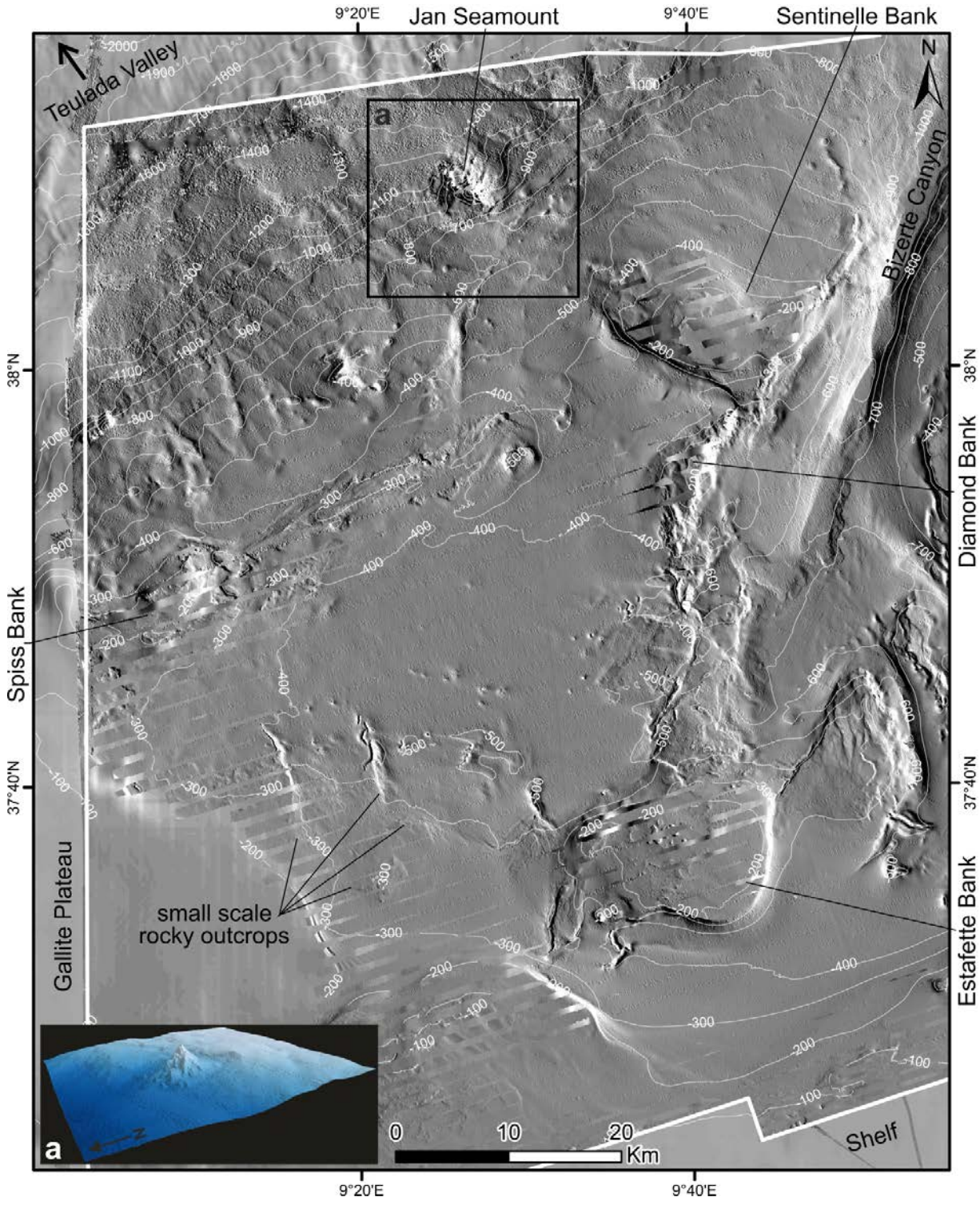

Figure 5.22. *Shaded relief map of the western plateau-slope sector (bounded by a white line) and a mosaic of different datasets for the adjacent areas (all of them with an illumination azimuth of 72° and altitude of 45°) (EMODnet, 2018). a) 3D Digital Elevation Model of the volcano-shaped structural high (named Jan Seamount); location of (a) is outlined in a black box on the shaded relief map.*

5.3.3. Geomorphological and morphostructural evidence of sedimentary, erosive and tectonic features

a) Sedimentary features

Smooth seafloor areas bounded by topographic highs correspond to sedimentary basins. These basins cover most of the mapped region, with scattered comparatively mid-scale basins and one large basin in both Western and Eastern plateau-slope sectors, at depth ranges of around -400 to -500 m and -500 to -700 m respectively (Figures 5.11 and 5.21).

Contourite deposits are common sedimentary structures throughout the area, which appear mainly parallel or slightly oblique to block-margins, faults or CWCM (Figures 5.11, 5.20 and 5.21). The relative abundance of these relief features (including CWCM) at the eastern sector explains the preferential location of contourites there.

Mass Transport Deposits (MTD) are associated to high-gradient slopes and occur mainly across the northern slopes (Figures 5.11, 5.12 and 5.16.a) or Bizerte Canyon (Figures 5.10.a and 5.10.e). Nevertheless, intra-continental margin MTDs are displayed associated to the largest contourite deposits (Figures 5.17 and 5.18.a), and a few in rather smooth areas (Figures 5.17 and 5.18.b). In some cases the transparent MTDs facies occur next to slide scars upslope (Figure 5.18.a), whereas in other cases sediment transport is not such evident, because scars and MTDs occur in flat areas, where enclosing scars makes difficult to determine any sediment flow (Figure 5.18.b).

b) Erosive features

As described above, most mapped structural highs display abrasion platforms as flat tops with rough patches and an average depth of around -200 m (Figure 5.5). Bathymetric and parametric data show gas/fluid flares from basically all flat-top structurally high areas including the shelf, the Gallite Plateau and the Hecate, Estafette and Sentinelle Banks (Figures 5.8 and 5.9). Furthermore, the highest concentration of flares commonly occurs related to rough areas with high-backscatter values suggesting the presence of rocky seafloor.

Significant erosive contourite moats, up to 13 km long and tens of meters deep (Figures 5.17, 5.20.a and 5.20.b), are common erosive features. Moats generally cut strata at the base of the scarp walls, reflecting the action of erosive flows flowing along the bases of rocky highs, cold-water coral mounds, or along fault traces. In fact, CWCM are one of the most important features providing

positive reliefs in the explored region (as shown by the low HI value clusters in Figure 5.2), and a significant amount of moats occur associated to these mounds.

Slide scars mainly occur along the northern slopes (Figures 5.11, 5.16.a, 5.16.b and 5.21) and the head of the Bizerte Canyon (Figure 5.10) although like MTDs, are also found scattered within the eastern sector of the plateau (Figures 5.17, 5.18.a and 5.18.b).

c) Tectonic features

Linear scarps delimiting the base of some structural highs likely correspond to fault planes. Moreover, escarpments at the north-eastern sector are morphological expressions of faults deforming strata and the seafloor with NE-SW trend (Figure 5.11). These NE-SW faults might have an important role controlling the up-flow migration of gas-rich fluids and consequently in the generation and preservation of the pockmarks. In addition to this main trend, minor faults with N-S or NNW-SSE strike also possibly occur. Some small-scale seafloor ridges, sub-parallel to the faults, denote the associated folding. This NE-SW trend, with minor N-S to NNW-SSE striking faults, extends to the south, except in the southernmost region. In this southernmost region of the Eastern plateau-slope sector, the escarpments of several small-scale rocky outcrops as well as the northern escarpments of the Hecate Bank are the expression of faults trending WSW-ENE and are delineated also by CWCM following the escarpments.

Further west, the Bizerte Canyon is the morphological expression of a major fault in a NNE-SSW trend. Its straight morphology together with its abrupt and irregular longitudinal profile with alternating topographic highs and lows reflects a tectonic control in the canyon development, despite of a regular equilibrated concave-up profile, generally observed along submarine canyons regulated by sedimentary flows (Figures 5.10.a and 5.10.d). Deep penetrating seismic profiles from oil industry support that Bizerte Canyon runs along a major normal fault dipping to the east (M. Ouadday, Tunis University, personal communication 2017). The canyon thalweg displays a broad flat floor with an average width of 2 km, except for an 8 km long sector at a depth range of -920 to -970 m, where a morphological obstruction dramatically reduces its extension to less than 200 m (Figures 5.10.a and 5.10.c). This sector of the thalweg corresponds to a structural high rising up ~110 m (Figures 5.10.a and 5.10.d).

The western plateau-slope sector lacks TOPAS coverage and only bathymetry and parametric echosounder profiles are available (Figures 5.21 and 5.22). Comparing to the Eastern plateau-slope sector it is clear that the western one has a smoother topography lacking a surface expression of

major faults. Some lineation with NE-SW trend at the northwest of the Sentinelle Bank may be the surface expression of faults. The eastern edge of the Sentinelle and the Diamond Banks are also possibly fault traces trending NE-SW and NW-SE, perhaps related to the major fault under Bizerte Canyon.

5.4. Discussion

The analysis of high-resolution bathymetry and high-resolution echosounder data of the North Tunisian continental margin show a complex structure with different geomorphologic and morphostructural features. Below, we interpret the sedimentary, erosive and tectonic processes shaping the current seafloor morphology.

5.4.1. Influence of sedimentary, erosive and tectonic processes on seafloor morphology

The recent sediment infill of basins of the Tunisian plateau is remobilized by bottom water currents. The large amount of widespread contourite deposits, and their related adjacent erosive moats (Figure 5.11) reflect the active hydrodynamics and sediment transport processes in the area. The Tunisian plateau is part of the Sardinian-Sicilian sill between the eastern and western Mediterranean waters. Here different surface and intermediate water flows occur (e.g. Sammari et al., 1999; Astraldi et al., 1999, 2002; Onken and Sellschopp, 2001). Topographic obstacles as the Gallite and Skerki Banks influence the circulation and water mass distribution funnelling the water along slopes causing erosion and building contourite deposits (Sammari et al., 1999; Onken and Sellschopp, 2001).

The explored area actually hosts 286 CWCMs that correspond to the highest density mapped in the Mediterranean (e.g. Schembri et al., 2007, Orejas et al, 2009, Vertino et al., 2010, Taviani et al. 2011, Lo Iacono et al., 2014; 2018) and probably the densest CWCM field ever mapped in oceanic margins explored until the present-day (Figures 5.11 and 5.21). The local distribution of mounds indicates that the tectonic setting is the main factor governing their orientation, since mounds are in most of cases aligned along NE-SW and NW-SE oriented scarps (Figure 5.17), coinciding with the main orientation of the structural trends.

Slide scars and associated MTDs are mainly located along the northern slopes or along the Bizerte Canyon (also noted by Maldonado and Stanley, 1976) (Figures 5.11 and 5.21). Most slides occurred at unstable seafloor escarpments associated to high-gradient slopes. Several fault traces cutting the seafloor support a relation to some slides in the Cornaglia Slope as already discussed by

Mascle et al. (2004). The intra-plateau slides are associated to contourite deposits or occur in flat areas, and we interpret that the destabilization of the sediment is likely a coseismic effect of earthquakes. Fault planes reaching close to the surface and affecting the shallow sediments supports a relation between earthquake shaking and sliding phenomena (Figures 5.18.a and 5.18.b). Thick transparent deposits located near flat areas, where MTDs would not be expected, supports this hypothesis. Many MTDs throughout the area, including the northern slopes, are not draped by visible hemipelagic sediment supporting their recent occurrence (e.g. Figure 5.18.b).

Abrasion platforms localized on several structural highs suggest a glacio-eustatic sea level oscillations shaping the highs summits (Figure 5.7). These flat-topped blocks were possibly exposed and eroded during the Plio-Quaternary lowstand sea level phases (e.g. Chiocci and Orlando, 1996; Lobo et al., 2008).

The presence of salient outcrops in some sectors of the shelf together with the preferential trends of their bounding scarps supports that these areas consist of eroded structural highs (Figures 5.6.a and 5.6.b). The same features are displayed by several other rocky highs scattered throughout the margin, supporting a tectonic control in their formation (Figure 5.5). Seismic reflection profiles indicate that this region of the Tunisian plateau is composed of a S- to SE-directed imbricated of fold and thrust belt system (Tricart et al., 1994) (see Section 2.2.2 in Chapter 2). Thus, the structural highs mapped throughout our studied region possibly represent the surface expression of anticline folds (with fold axis ~ NNE-SSW oriented) or thrust sheets cropping out of the fold and thrust belt. This ENE-WSW trend corresponds to a series of overthrust faults proposed by Gennesseaux and Stanley (1983) along the area (see Section 2.2.2 in Chapter 2). Modern seismic images from oil industry support that most structural highs are anticline folds (M. Ouadday, Tunis University, personal communication 2017). The steeper slopes of the southern and eastern flanks of most of the large scale structural blocks (Hecate, Estafette, Sentinelle and Resgui Banks) and the gently dipping towards the NW of some of them correspond well to the S-SE verging fold-thrust configuration. Gas flares are observed along tabular area coinciding with the continental shelf and with the Hecate, Sentinelle and Estaffete Banks and the Gallite plateau (Figure 5.9). Flares do not seem to be related to local tectonic structures, such as fault scarps or other tectonic lineaments. The fact that flares are limited to these high regions (large scale structural blocks and the shelf) and that commonly occur related to rough areas can suggest a structural control in the local active fluid circulation. In fact, gas seems to be escaping through anticlines axis due to subaerial erosion of the anticlinal tops during the last glacial maximum, where the sea level dropped about 100 m.

Surface lineaments related to recent faults mark a main regional trend with NE-SW orientation (particularly clear in the north-eastern sector) (Figures 5.11 and 5.12), i.e. perpendicular to the NW-SE plate convergence between Nubia and Eurasia (e.g. Serpelloni et al., 2007). The occurrence of the highest density of pockmarks along these NE-SW tectonic lineaments in the north-eastern sector (Figures 5.11 and 5.12) supports a recent tectonic control in fluid circulation, probably related to fault structures reaching some reservoir. The high pockmarks density may support more intense recent tectonic activity in the north-eastern sector, which would favoured expulsion of gas-rich fluids. Recent tectonic activity has been proposed along the north Corgnalia slope with recent folding at the foot of the Corgnalia scarpment and recently broken micritic concretions inferred to relate to reactivation of major faults (Mascle et al., 2004).

The irregular physiography of Bizerte Canyon together with its irregular longitudinal profile, its U-shaped transverse morphology, and the disconnection of its canyon head with the shelf margin suggest that the canyon has little current sediment transport activity. The canyon floor around 38º5'N shows a sucession of sediments, some of transparent facies (Figure 5.10.f), supporting lack of sediment transport. Nevertheless, 3 sand turbidite flows in a sediment core of the Sentinelle valley covering the last 80 ky have been assigned to the Bizerte Canyon, proposing some activity by a canyon not fed by emerged area or a fluvio-deltaic system, but a wide submarine plateau (Budillon et al., 2009). Our data supports that activity is possibly constrained to the end segment, near the Sentinelle Valley. Early sparker and 3.5 kHz profiles across the canyon were interpreted supporting a tectonic control on Bizerte Canyon (Figure 5.23) and Carbonara Canyon (offshore south Sardinia, Figure 5.4), with similar trends (Maldonado and Stanley, 1976).

Overall, there are clear qualitative and quantitative morphologic differences between eastern and western sectors. The morphometric analyses show a different morphologic pattern (Section 5.3.1) between the eastern and western sectors of the Bizerte Canyon, with the eastern region having more irregular topography. All geomorphological features defined in this study predominate through the Eastern plateau-slope sector, which shows more irregular seafloor morphology contrasting to the western relief (Figures 5.2 and 5.3). This E-W morphologic difference may be explained by the geological setting. The western sector corresponds to the "Kablylian Equivalent" unit overlain by up to 2 km thick Early Miocene arkosic turbidites (CPK Zone from Tricart et al. (1994) in Figure 2.12, see Section 2.2.2 in Chapter 2). The thick turbidite layer above the "Kabylian Equivalent" unit produces a smooth relief in the western sector. In the eastern region, the thrust sheets of the Tellian domain and the autochthonous Tunisian Atlas domain crop out causing a more irregular topography.

The thick Early Miocene turbidites cover does not provide hard substrata, which could explain the dominant occurrence of CWCM in the eastern sector (where thrust anticlines form rocky outcrops). The preference location of CWCM to the east contributes to a more complex relief causing low Hi clusters (Figure 5.2).

Recent tectonics seems to be another factor influencing seafloor relief. The highest density of pockmarks along NE-SW tectonic lineaments in the north-eastern sector support higher recent tectonic activity in that area, causing a more irregular seafloor topography in that area.

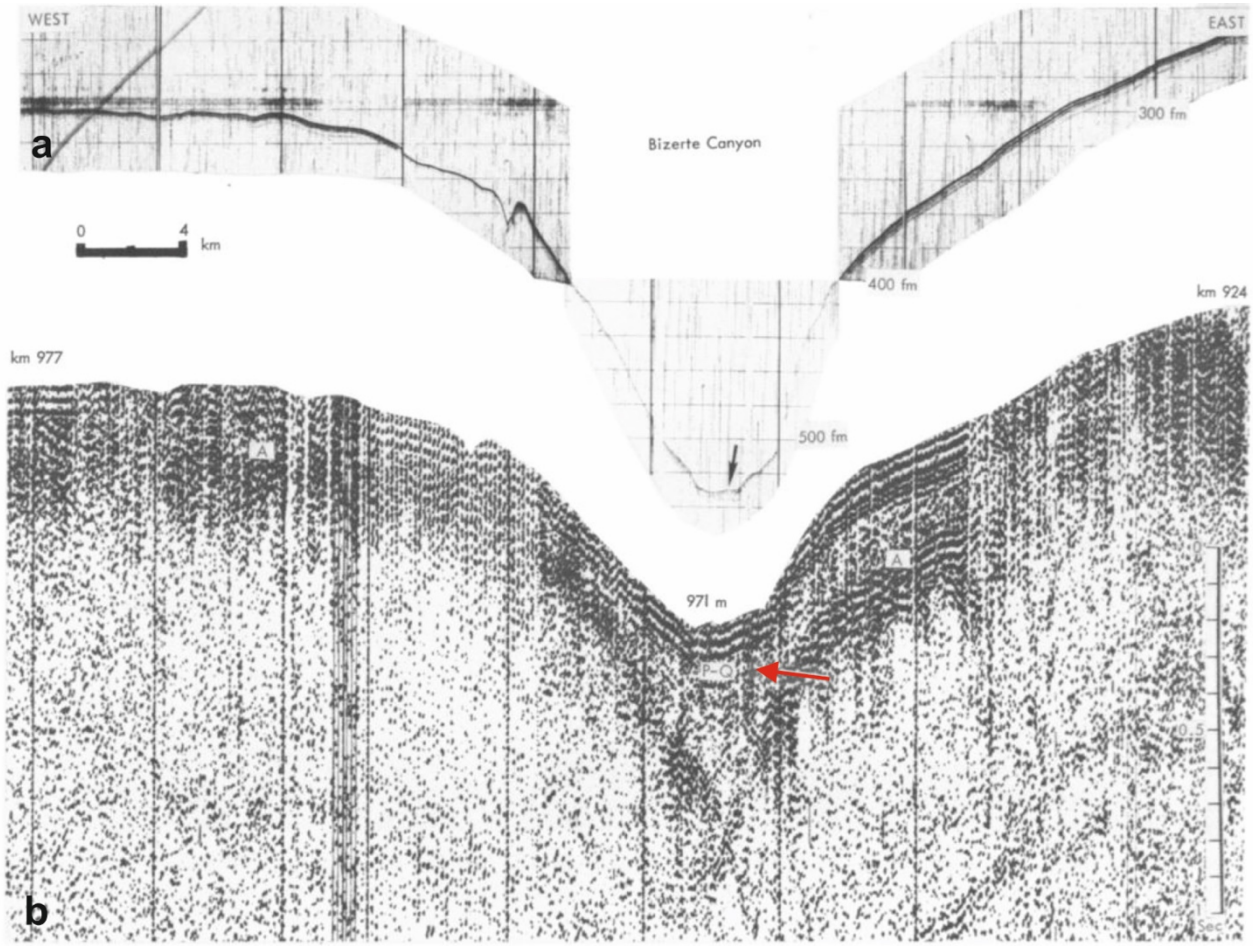

Figure 5.23. *A 3.5 kHz profile (a) and an old Sparker profile (b) taken from Maldonado and Stanley (1976). The arrow of the 3.5 kHz profile (a) shows the irregular configuration of the valley floor that they relate to slumped sediments. The red arrow of the Sparker profile (b) shows fault displacement. Location of the profile is outlined in Figure 5.4.*

5.5. In summary

The analysis of the geophysical dataset acquired across a portion of the outer shelf and a large sector of the continental plateau-slope system shows a complex geomorphology and morpho-structure. The coexistence of a wide range of geomorphic features, such as contourites, moats, CWCMs, folds and faults, pockmarks and collapse pockmarks, basement highs, slide scars and mass transport deposits (MTD), the Bizerte Canyon and the rough shelf coupled with active gas release represents a complex scenario, where sedimentary, erosive and tectonic processes interplay to shape the seafloor and shallow strata.

Large contourite deposits throughout the area support intense hydrodynamic and sediment transport processes. These processes relate to the location of the study region in the Sardinian-Sicilian sill linking eastern and western Mediterranean water masses. Here, topographic obstacles such as structural blocks or CWCM influence water currents, resulting in erosion and building up of thick contourite deposits.

A total of 286 CWCMs have been identified and mapped, which correspond to the highest density of CWCMs ever mapped in the Mediterranean and probably the densest CWCM field mapped in the world. The location in the area of the mounds appears to be related to the tectonic setting since CWCMs occur along NE-SW and NW-SE oriented scarps, following the main structural trends. Thick turbidite layers covering the western sector may prevent the occurrence of CWCMs in that region.

Most of slide scars and associated MTDs are localized and associated to high-gradient slopes. However, several slide scars and MTDs occur in nearly flat regions of the margin and have been interpreted as coseismic effects of earthquakes.

Pockmark fields and gas flares mapped in the explored area give evidence of gas-rich fluid seepage occurring in the offshore Northern Tunisia. Morphometric analysis suggests a relevant role of tectonic processes controlling fluid circulation both at a regional scale, with pockmark dense fields more distributed throughout the eastern sector (i.e. the Tellian and Atlas domains sector), and at a local scale, with pockmarks aligned along NE-SW trending recent fault scarps. The occurrence of highest density of pockmarks along these NE-SW faults of the north-easternmost sector suggests a major recent tectonic activity in this region. Furthermore, flare occurrence is likely to be structurally controlled in their distribution probably escaping from eroded anticlines.

The base of the flanks of some structural blocks likely corresponds to fault traces. The escarpments of the north-easternmost area are surface expressions of recent faults and display a NE-SW main trend (although N-S and NNW-SSE trends have also been identified throughout the explored area). The Bizerte Canyon runs over a major NNE-SSW fault with some normal component dipping to the east.

The margin, composed of S- to SE-directed imbricated thrust sheets, displays an irregular bathymetric physiography that reflects the deep complex structural control at the scale of the margin, corresponding to the straight morphology of the shelf, large-scale tilted structural blocks and by the Bizerte Canyon. The large structural blocks and parts of the continental shelf are surface expression of anticline folds of the north African belt, with fold axis ENE-WSW oriented. The abrasion platforms are recent features caused by subaerial erosion during a glacio-eustatic sea level drop.

The region shows a clear morphologic difference between eastern and western sectors from the Bizerte Canyon, likely resulting from the geologic configuration and recent tectonics along the margin. The western sector is underlain by the “Kabylian Equivalent” domain coverered by up to 2 km of thick Early Miocene turbidites smoothing seafloor topography. In contrast, in the eastern sector the fold and thrust sheets of the Tellian and Atlas domains crop out and display a more complex relief. Recent tectonics are more intense in the north-eastern area where the seafloor displays structures that indicate the presence of active faults and recently active abundant pockmarks, that form the more complex relief of the region.

CHAPTER 6

Quaternary seismo-stratigraphy and tectono-sedimentary evolution of the North Tunisian continental margin

6.1. Introduction

Offshore Northern Tunisia has been poorly studied with only a handful of, mostly relatively old, studies that provide basic knowledge about the current tectonic setting (e.g. Auzende, 1971; Auzende et al., 1974; Maldonado and Stanley, 1976; Gennesseaux and Stanley, 1983; Tricart et al., 1994, Dinarès et al., 2003). We carried out the first comprehensive bathymetric and high-resolution seismic work in the region that provides a large database to study recent and active tectonic and sedimentary processes. Recent tectonic processes to the east (north of Sicily) and west (north of Algeria) sectors of this plate boundary region are comparatively better understood from more numerous recent studies (e.g. Auzende et al., 1975; D'Agostino and Selvaggi, 2004; Goes et al., 2004; Déverchère et al., 2005; Billi et al., 2007; Kherroubi et al., 2009; Yelles et al., 2009; Strzerzynski et al., 2010; Billi et al., 2011). Northern Tunisia occurs in the region where the deformation of the north African margin reactivated in Algeria transitions to the reactivated margin of north Sicily by poorly understood tectonic processes. Thus studying the continental margin of Northern Tunisia provides information on a poorly known, large and complex zone of deformation.

Quaternary south-dipping faults located at the foot of the central and eastern Algerian margin have been interpreted to represent an incipient stage of subduction of the Neogene oceanic lithosphere (e.g. Auzende et al., 1975; Déverchère et al., 2005; Kherroubi et al., 2009; Yelles et al., 2009; Strzerzynski et al., 2010). The reactivation of the Algerian margin is causing uplift along the costal domain (onshore and offshore) (Yelles et al., 2009; Strzerzynski et al., 2010), as predicted by models of subduction initiation processes (e.g. Faccenna et al., 1999; Mart et al., 2005). A similar tectonic pattern is also observed offshore northern Sicily, where plate convergence is mainly

accommodated along an E-W trending active thrust system that reactivates inherited faults of the southern Tyrrhenian (D'Agostino and Selvaggi, 2004; Goes et al., 2004; Billi et al., 2007, 2011). As for northern Algeria, northern Sicily is undergoing recent tectonic uplift (Holocene age), which has also been proposed to result from an early stage of contraction previous to a foreseeable subduction initiation (Billi et al. 2007).

In this chapter, we focus on the Quaternary seismic stratigraphy of the North Tunisian continental margin, and characterize the active tectonic structures that affect the recent sediment sequences. To age constrain recent tectonic deformation of the North Tunisian continental margin, we calibrated the stratigraphy with the information from a giant piston core collected ~60 m from one of our TOPAS profiles (Dinarès-Turell et al., 2003). We defined and calibrated six seismic horizons and their corresponding units in our parametric echosounder TOPAS profiles. We used these horizons and units to compute Isochore and Sediment Accumulation Rate (SAR) maps and with the analysis of their geometry and distribution from TOPAS profiles we interpreted the recent tectono-sedimentary evolution of the area. The horizons and units defined in the TOPAS profiles provide data on the last 1,724 ky evolution (from early Calabrian).

6.2. Data and methodology

We use high-resolution parametric echosounder TOPAS profiles to define Plio-Quaternary seismo-stratigraphic horizons and units. TOPAS profiles totalized more than 3,500 km in length, covering an area between 9º43'E-11º18'E and 37º33'N-38º41'N corresponding to a total of 6,434 km^2 (see Chapter 3 for further information on TOPAS acquisition).

To define the seismo-stratigraphic units we used the giant piston core LC07, acquired in 1995 with the CALYPSO system of the French RV "Marion Dufresne" in the frame of the EU-MAST-II "PALAEOFLUX" project (Rothwell, 1995; Dinarès-Turell et al., 2003). The correlation between the core LC07 and our TOPAS data, and a chrono-stratigraphic framework for the Quaternary sedimentary history were done using "IHS Kingdom Suite" software. We defined six regional seismic horizons to study the sediment distribution within the area and characterize the Quaternary tectonic evolution.

We mapped the seismic horizons to construct time-contour maps for each horizon. With these time-contour maps we calculated thickness maps for each seismic unit (isochore maps). Finally, we calculated sediment accumulation rate maps for all seismic units, using the ages of the horizons

from the LC07 piston core calibration. These maps are restricted to the area covered by our TOPAS profiles, i.e. a NE-SW area covering part of the eastern sector and the north-easternmost sector of the explored region (Figure 6.1).

6.2.1. The LC07 giant piston core and horizon calibration

The LC07 giant piston core was collected at 38º8.72'N and 10º4.73'E and it is located 63 m north of one of our TOPAS profile (Figure 6.1.b). Due to the smooth topography of the area, with ~0.5 m depth difference between the core site and closest point on the TOPAS profile, we plotted the core data into the "IHS Kingdom Suite" software without applying any depth correction. This 0.5 m is somewhat less than the accuracy of the multibeam-echosounder bathymetric resolution (Kongsberg, 2018a). Since strata layering is fairly sub-horizontal, we placed de information of core LC07 directly on the TOPAS profile "20131206100824" (Figure 6.1.b), at coordinates 38º8.69'N and 10º4.71'E.

Log data were not available for this core, and no physical properties (i.e. Vp sonic velociy, density) exist to calculate the depth of the different seismic reflections (from now on referred as horizons). Therefore, we used the mean sonic velocity in the seawater (1,500 m/s) because the sonic velocity of unconsolidated sediments does not usually change significantly. We computed depth also with 1550 m/s to evaluate depth uncertainty from small but realistic changes in seismic velocity. Given the seismic data resolution, depth differences do not considerably change the age of horizons (Figure 6.1.c). For instance, the difference ranges from 0.135 milliseconds (ms in TWTT) in the uppermost age of 249 ky, to 0.375 ms (TWTT) in the deeper one of 695 ky (see Table 6.1). These depth uncertainties could change the ages in 7, 15 and 20 ky from the top to the deepest horizon sampled by the core, so the age of the horizons does not change substantially using a range of realistic sonic velocities considering the relatively extensive age period we study (~1.7 Ma to present).

Finally, the age of the three horizons deeper than the core (HIV, HV, HVI in Figures 6.1.a and 6.1.c) is derived from the mean sediment accumulation rate (2.16 cm/ky) in the core sediment (Dinarès-Turell et al., 2003, Figure 6.2). In addition, Dinarès-Turell et al. (2003) describes a sandy interval of less than 1 m just above horizon HIII (695 ky) (Figure 6.2) that matches with a seismically transparent layer -often interpreted as sand bodies- in the TOPAS image (Figures 6.1.a and 6.1.c). This observation supports our correlation between the sedimentological data of LC07 piston core and the TOPAS image (line 20131206100824).

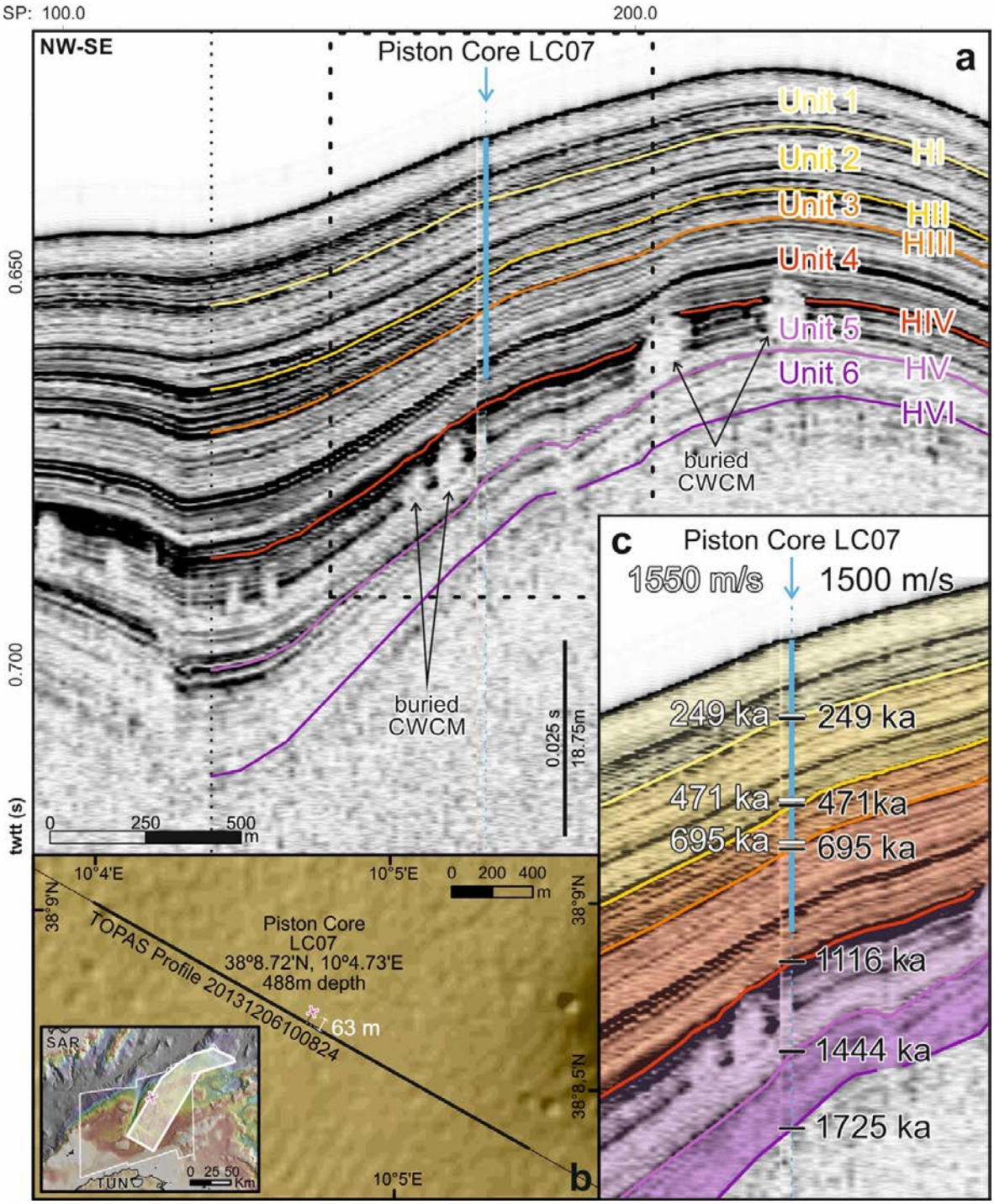

Figure 6.1. *Correlation between the TOPAS seismic data and the piston core data of Dinarès-Turell et al. (2003). a: TOPAS profile number 20131206100824 with the location of the LC07 piston core. Depths are in seconds two-way travel time (TWTT) below sea level. The black dashed rectangle shows the frame of Figure 6.1.c. The W sector of the profile is shown without the interpretation. b: Bathymetric map with the location of TOPAS profile number 20131206100824 and the location of the LC07 piston core. At the bottom left corner it is displayed the regional location of the LC07 piston core within the explored area (TUN: Tunisia, SAR: Sardinia). The white shaded polygon shows the area covered by the TOPAS profiles. c: Zoom of the TOPAS profile number 20131206100824 and location of the LC07 piston core. The ages of the horizons are calculated following two possible sound velocities: 1500 m/s (at the right side of the core, in black colour) and 1550 m/s (at the left side of the core, in white colour).*

Ages (ky) / Depth (mbsf) (Dinarès-Turell et al., 2003)	Depth (s TWTT)		Depth difference (s)
	1500 m/s	1550 m/s	
249 / 6.18	0.64113	0.64086	0.000135
471 / 13.03	0.65027	0.64968	0.000295
695 / 16.48	0.65487	0.65412	0.000375

Table 6.1. *Depth comparison for the three upper reflectors using 1500 m/s and 1550 m/s sonic velocities.*

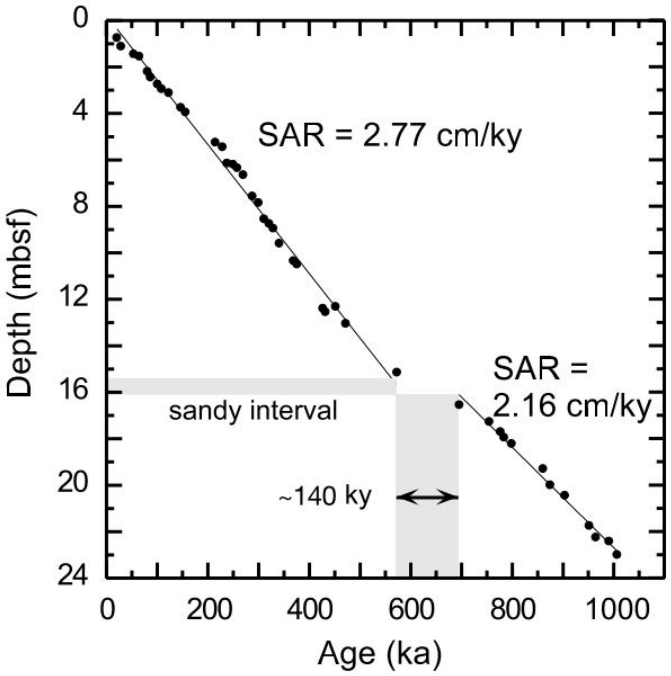

Figure 6.2*. Age control points used to derive the age model of the long piston core LC07 in Dinarès-Turell et al. (2003). The mean sediment accumulation rates (SAR) are shown. The SAR of the deep segment is the one used on this work to derive the ages of the three deepest horizons, which are HIV, HV and HVI (Figure 6.1.c).*

6.3. Seismo-stratigraphy

To interpret the recent seismo-stratigraphic history of the margin, we defined different seismic horizons. We use "horizon" as "An interface that might be represented by a seismic reflection, such as the contact between two bodies of rock having different seismic velocity, density, porosity, fluid content or all of those" (Oilfield Glossary, 2017). Acoustic reflections defining the different horizons were selected on the basis of their high amplitude and lateral continuity, which made them easily detectable and continuous throughout the study area. In total, we defined six seismic horizons that correspond to six distinct seismic units (Figure 6.1).

6.3.1. Seismic Horizons and Units

Following we describe units HI to HVI from TOPAS parametric echosounder images. Most of units display sediment drapes in the middle of the basins that locally evolve to contourites along the boundaries.

Unit 1) The uppermost Unit 1 consists of a group of parallel draping reflections characterized by an intermediate high-amplitude reflection that divides the unit in low reflections above and high reflections below. The bottom boundary of the Unit 1 is defined by the horizon HI, located at 6 mbsf at the LC07 core site (Figure 6.1.a), that is characterized by 3 superposed reflections of moderate amplitude easily identifiable throughout the study area (Figure 6.3). The HI horizon has been calibrated as 249 ky old (Dinarès-Turell et al., 2003) corresponding to the late mid Pleistocene.

Unit 2) The Unit 2 consists of a group of parallel draping reflections characterized by high-amplitude reflectors in between layers of transparent facies and locally display transparent bodies related to Mass Transport Deposits (MTDs) (Figure 6.1.a). Its bottom boundary, the horizon HII, is a high amplitude reflection identified at 13 mbsf in the sediment core (Figure 6.1.a) and it has been dated at 471 ky in Dinarès-Turell et al. (2003), corresponding to mid-middle Pleistocene age.

Unit 3) The Unit 3 is a narrow unit of about 3 m at the core site characterized by a group of draping parallel high-amplitude reflections, easily detectable throughout the explored area (Figures 6.1 and 6.3). Its bottom boundary is the horizon HIII that is identified at 16 mbsf in the sediment core, and has been dated at 695 ky in Dinarès-Turell et al. (2003), thus of early middle Pleistocene age (Figure 6.1). Unit 3 contains the sand interval interpreted to represent a winnowed lag deposit (deposit where the finer portion was removed by physical action) (Dinarès-Turell et al. (2003). We correlate it to Unit 3 lower transparent layers, best developed to the SE along the TOPAS profile (Figure 6.1.a).

Unit 4) The Unit 4 is formed by parallel facies of moderate amplitude with a characteristic high-amplitude middle reflection (Figure 6.1.a). The bottom boundary of the Unit 4 is the horizon HIV and it is characterized by a prominent high-amplitude reflection identified at 25 mbsf in the sediment core (Figure 6.1.a). Horizon HIV is not imaged at times due to lack on energy penetration in the deeper occurrences. It has been dated at 1,116 ky extrapolating from the LC07 core in Dinarès-Turell et al., (2003), corresponding to mid-late Calabrian age.

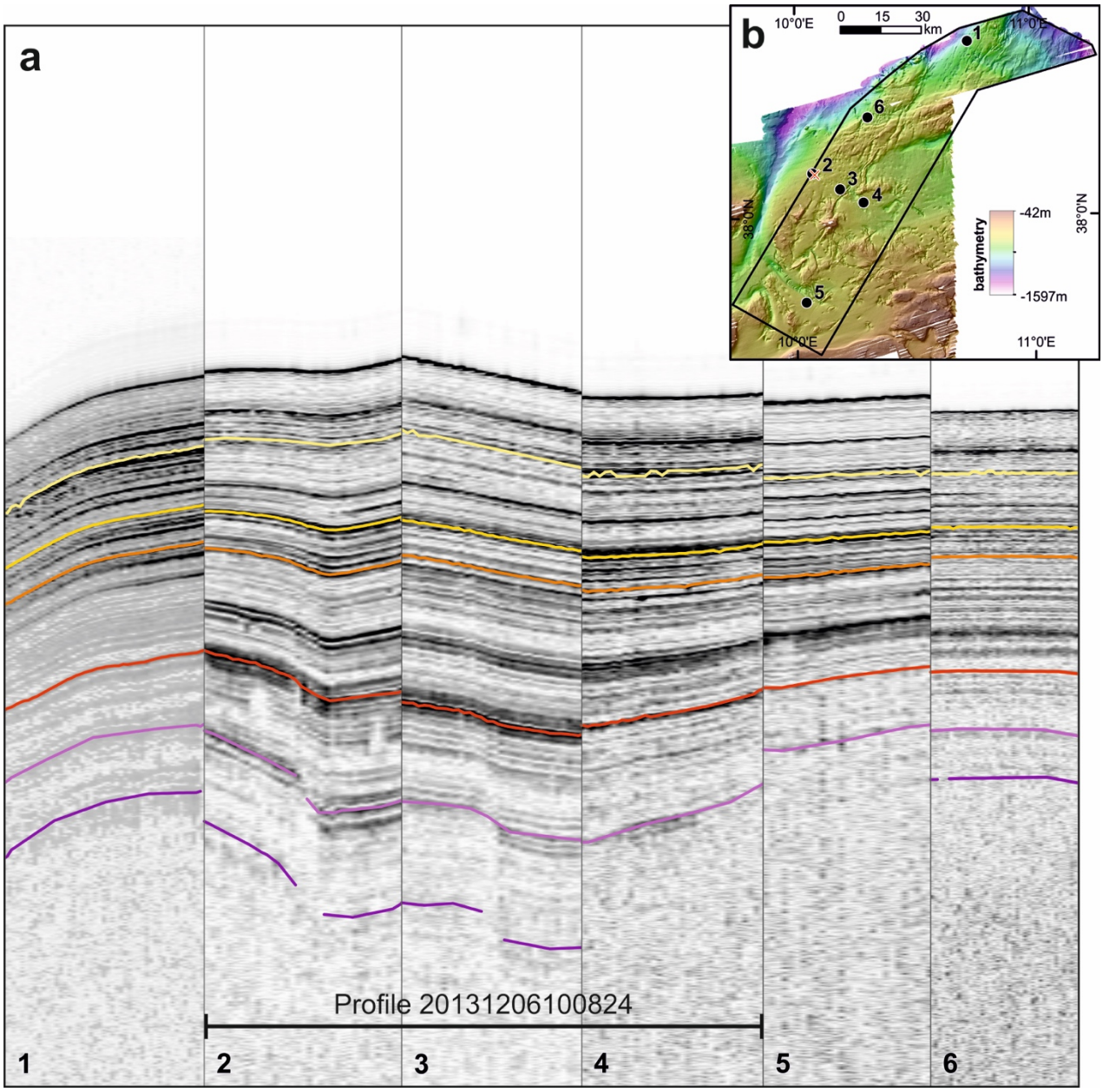

Figure 6.3. *a) Correlation of seismic profiles through the study area. b) Bathymetric map with the location of each of the 6 TOPAS section marked as black dots. Profiles number 2, 3 and 4 are the ones corresponding to profile 20131206100824, where the long piston core LC07 was collected. The red cross indicates the location of core LC07.*

Unit 5) The Unit 5 is a characteristic unit that has transparent facies in the central-lower layers and locally display several transparent sub-vertical bodies that may be interpreted as cold-water coral mounds growing from a lower transparent comparatively thick layer that may represent a sandy interval (buried CWCM in Figure 6.1.a). The bottom boundary of the Unit 5 is the horizon HV characterized by a high-amplitude reflection identified at 32 mbsf in the sediment core (Figure 6.1.a), that often is not imaged because of its depth. The age of HV extrapolated from LC07 core is

1444 ky in the early-mid Calabrian age (Dinarès-Turell et al., 2003). HV occurs as a relatively high-amplitude reflection separating two transparent bodies (Figure 6.3).

Unit 6) The deepest Unit 6 is internally mainly transparent, occasionally displaying weak amplitude reflections. The character may be due to the poor recovery of energy. Its bottom boundary is the horizon HVI that corresponds to the deepest level described at the sediment core at 38 mbsf (Figure 6.1.a). This reflection has been dated at 1725 ky extrapolating from the LC07 core in Dinarès-Turell et al. (2003). Dating is from early Calabrian Age, almost reaching to the Calabrian-Gelasian boundary (1,800 ky). HVI is discontinuous where visible and only mapped in part of the study area.

We could map horizons HI-IV throughout the whole area, HV across most the region and HVI locally (Figure 6.3) using the "IHS Kingdom Suite" software.

6.4. Quaternary sedimentary evolution

The orography of the area played a role in the recent sediment distribution history of the continental margin. The orography forced sediment to distribute in different basins located in between basement highs, depicted in dashed blue lines in Figure 6.4. As an example, the isochore map of Unit 1, between HI and the seafloor (Figure 6.4), shows several small depocenters (i.e. locations with greater sediment thickness) distributed throughout the area, although they are more abundant towards the southern sector (i.e. basins A, B, C, D, F and G; Figures 6.4, 6.5 and 6.6). The thicker deposits mainly located on the southern sector occurs for all Units (Figure 6.7), although it is undetermined for Units 5 and 6 due to the limited data coverage (Figures 6.7.b and 6.7.a respectively).

The greatest thickness for all units occurs in basins A, F and G (note thickness of units in Figures 6.5 and 6.6). Units 1, 2 and 3 have maximum thicknesses of 42.83, 44.63 and 61.35 m in basin A, perhaps related to bottom currents along the canyon building large contourite deposits (Figures 6.5 and 6.7). Unit 4 was not imaged in the basin A, and it shows a maximum thickness of 61.35 m in the basin G (Figures 6.6 and 6.7). Units 5 and 6, are not imaged in the basins A and G, which may explain their maximum thicknesses of 23.1 and 18 m occurring in basin E (Figures 6.5 and 6.7). An area south-east of basin B has also a considerable thickness, but does not correspond to a well-defined basin (Figure 6.4). This is related to sediment accumulation near the continental shelf imaged as a sediment progradation from the shelf into the Tunisian plateau (see Chapter 5).

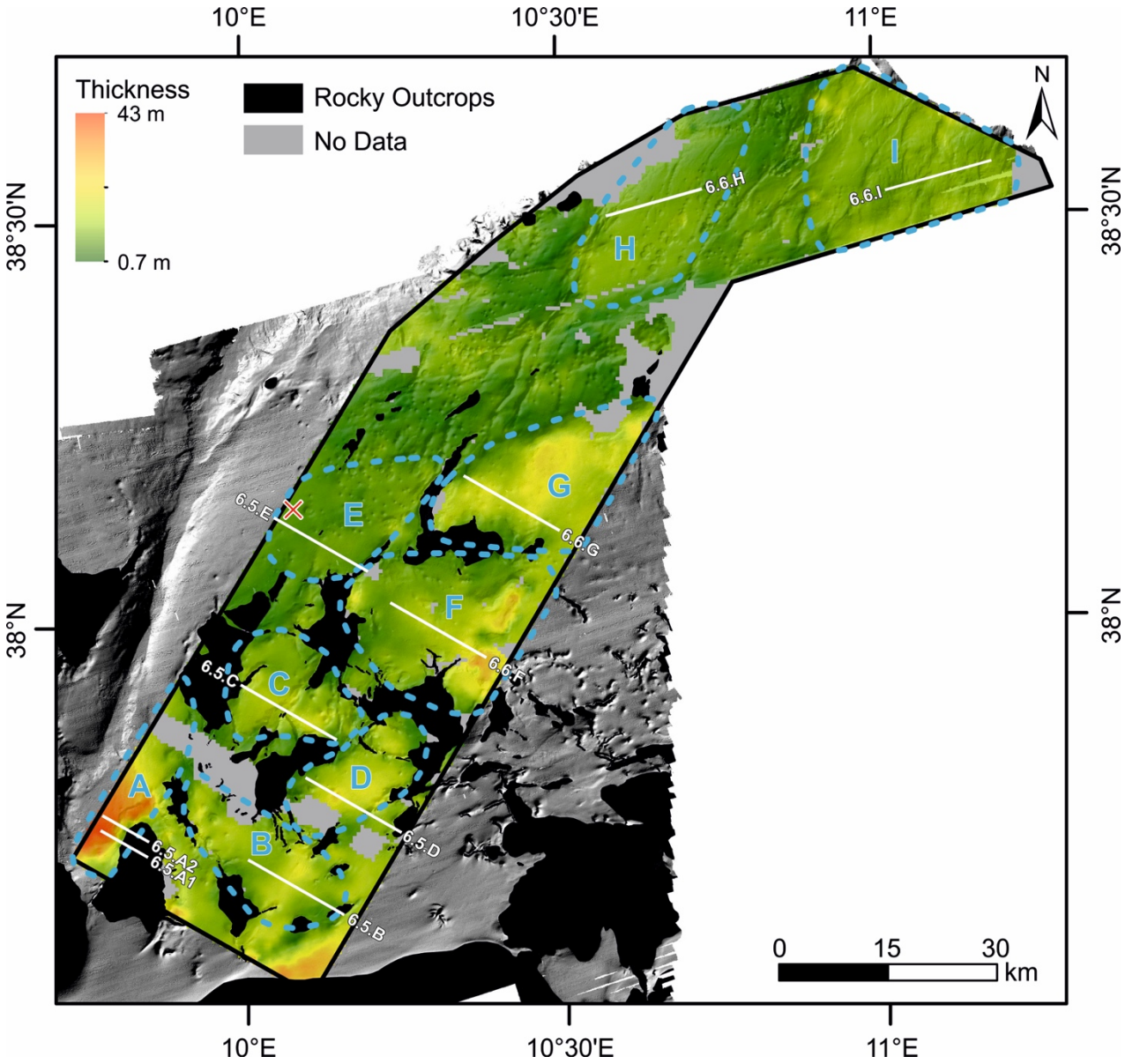

Figure 6.4. *Isochore map of the Unit 1 (located between the horizon HI and the seafloor; corresponding to late middle Pleistocene to present). The different basins defined in this study (A to I) are outlined by dashed blue lines. The red and white X marks core LC07 site location. White lines locate the TOPAS profiles presented in Figures 6.5 and 6.6.*

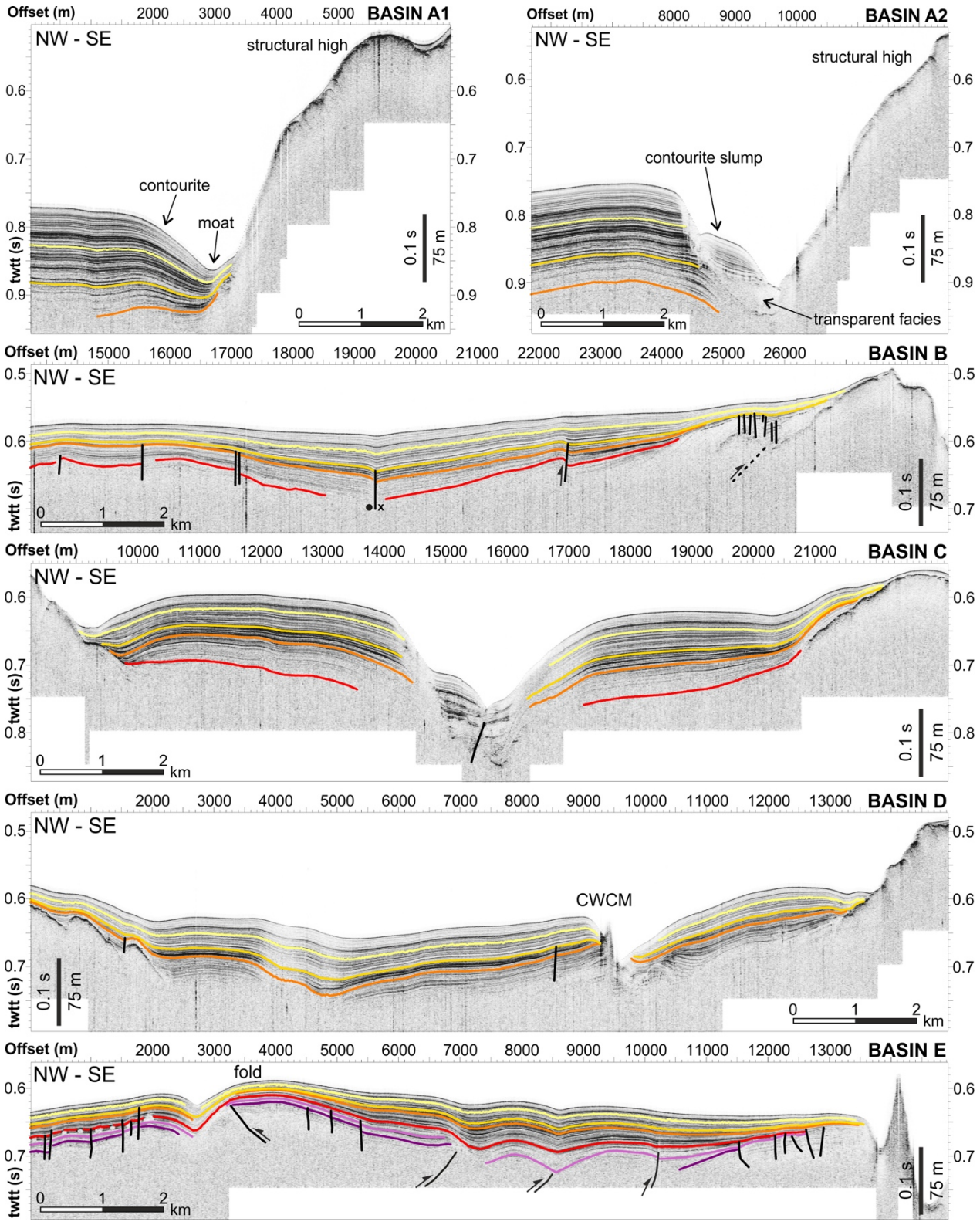

Figure 6.5. *Interpreted TOPAS profiles of basins A, B, C, D and E. TOPAS profiles are shown with the same vertical and horizontal scale, which allows to compare horizons, depths and thicknesses between the plots.*

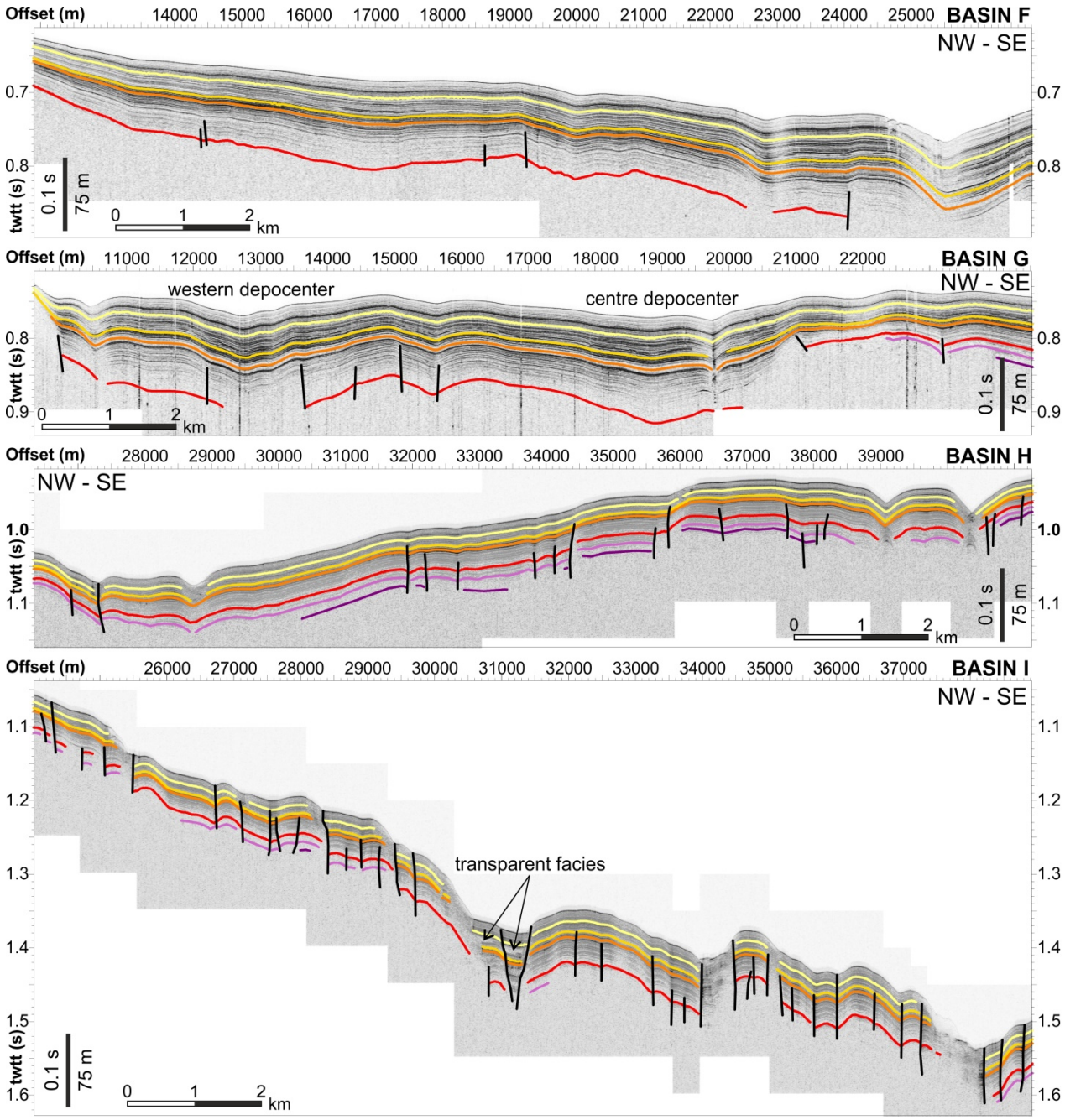

Figure 6.6. *Interpreted TOPAS profiles of basins F, G, H and I. TOPAS profiles are shown with the same vertical and horizontal scale, which allows to compare horizons, depths and thicknesses between the plots.*

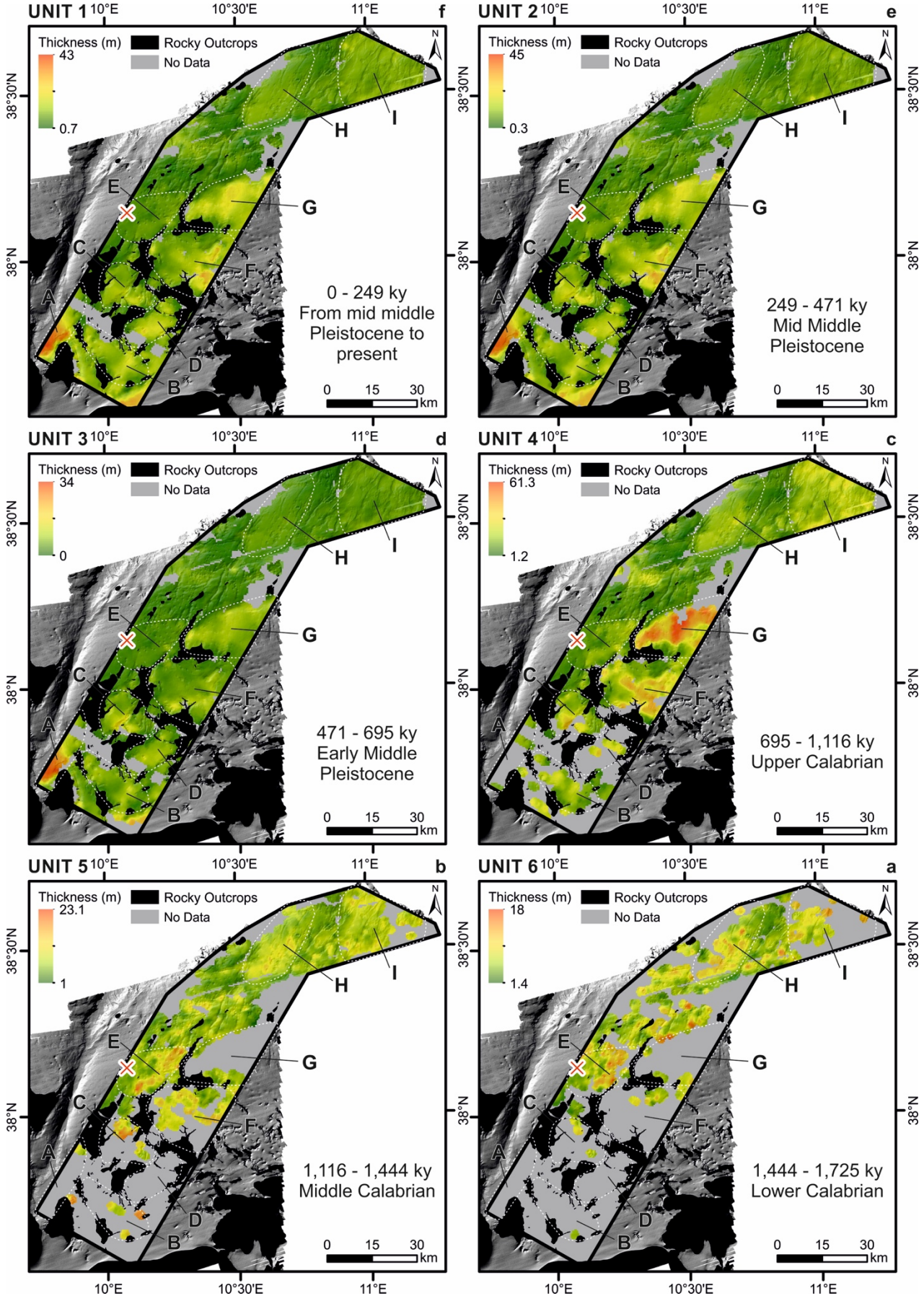
UNIT 1
f
Thickness (m)
43
0.7
Rocky Outcrops
No Data
0 - 249 ky
From mid middle
Pleistocene to
present
UNIT 2
e
45
0.3
249 - 471 ky
Mid Middle
Pleistocene
UNIT 3
d
34
0
471 - 695 ky
Early Middle
Pleistocene
UNIT 4
c
61.3
1.2
695 - 1,116 ky
Upper Calabrian
UNIT 5
b
23.1
1
1,116 - 1,444 ky
Middle Calabrian
UNIT 6
a
18
1.4
1,444 - 1,725 ky
Lower Calabrian
10°E
10°30'E
11°E
38°30'N
38°N
A
B
C
D
E
F
G
H
I
0 15 30
km
N

Figure 6.7. *Isochore maps for all the units (in meters), from Present to Lower Calabrian. Colour scales of the maps, corresponding to thickness, vary according to the boundary values of each unit. The different basins defined in this study (A to I) are outlined by dashed white lines. Location of the different basins are shown in capital letters (from A to I). The red and white X marks core site location.*

6.4.1. Sediment accumulation rate

The sediment accumulation rate (SAR) of each seismic unit is shown in the maps of Figure 6.8. These maps permit to compare SAR over time, from present-day to Lower Calabrian (Early Quaternary). To analyse the results, we plotted individual SAR values for all nine basins (Figure 6.9). SAR values represent well sediment Units 4 to 1, as Units 5 and 6 lack full coverage. In these plots, the mean SAR value for all basins is displayed as a red line, the mean SAR value of each basin is displayed as a blue line, the maximum SAR value of each basin (i.e. the maximum depocenter) is displayed as a dark green line, and the upper-3th-quartile mean value is displayed by a light green line (i.e. a proxy for the mean value of the greatest depocenters). Thus, we can compare mean SAR values of each basin with mean values of the entire study region through different time-periods. Moreover, we can easily compare the depocenters of the different basins.

These maps show how SAR values change over time, while main depositional locations have not considerably changed. The depocenters in Figure 6.7 experienced different sedimentation rates over time, without significant spatial changes within basins (Figure 6.8). The most significant feature revealed by these maps is the clear decrease in SAR values during the deposition of Unit 3 (Figure 6.8.d), corresponding to the early Middle Pleistocene (471 – 695 ky). This pattern is also displayed by the red line (i.e. representing the mean SAR value for all basins) in Figure 6.9, with the lowest value of 28 mm/ky during the deposition of Unit 3.

The SAR map of the lower Calabrian Unit 6 (1725-1444 ky; Figure 6.8.a) has considerable gaps -particularly in the south- because horizons HVI and HV are either too deep to image or are not present in areas with buried highs of older indurated material. In general, SAR values are low, with a maximum value of 64 mm/ky in basin E.

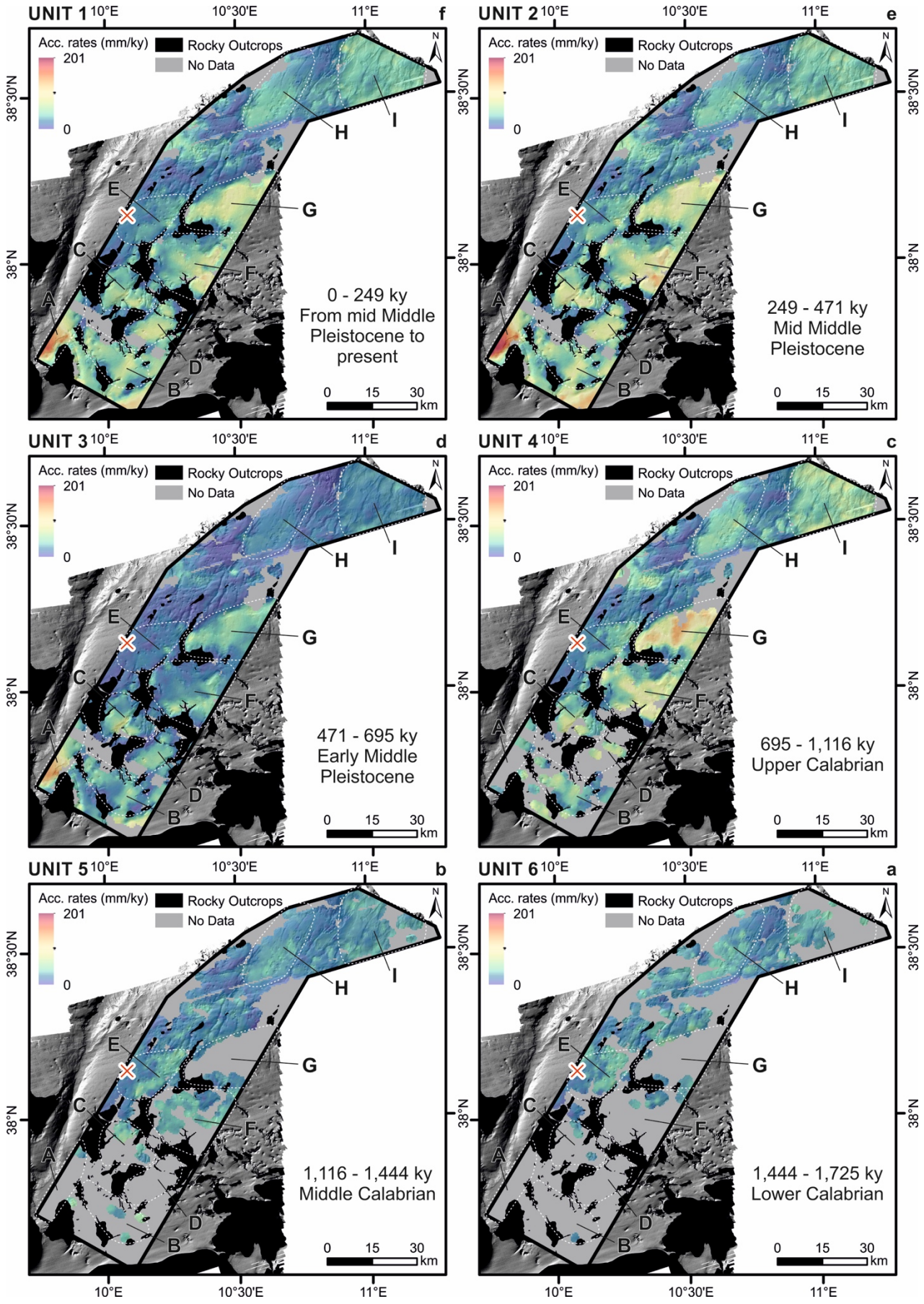
UNIT 1
f
0 - 249 ky
From mid Middle
Pleistocene to
present
UNIT 2
e
249 - 471 ky
Mid Middle
Pleistocene
UNIT 3
d
471 - 695 ky
Early Middle
Pleistocene
UNIT 4
c
695 - 1,116 ky
Upper Calabrian
UNIT 5
b
1,116 - 1,444 ky
Middle Calabrian
UNIT 6
a
1,444 - 1,725 ky
Lower Calabrian
Acc. rates (mm/ky)
201
0
Rocky Outcrops
No Data
10°E
10°30'E
11°E
38°30'N
38°N
N
A
B
C
D
E
F
G
H
I
0 15 30
km

Figure 6.8. *Sediment accumulation rate (SAR) maps for all the units (in mm/ky). All the maps are displayed with the same colour scale, taking the upper end SAR value as the maximum SAR value for all Units (the one from the Unit 2, mid middle Pleistocene). The different basins defined in this study (A to I) are outlined by dashed white lines. The location of the different basins (from A to I) are displayed in capital letters. The red and white X marks core site location.*

The SAR map of the middle Calabrian Unit 5 (1444-1116 ky; Figure 6.8.b) covers basins E, H, F and I. Generally, SAR values are similar to SAR of underlying Unit 6. Unit 5 displays mean SAR values of 26 mm/ky while the Unit 6 shown 27 mm/ky. Basin E shows similar SAR and sedimentation areas to those of Unit 6. However, Unit 5 occurs in two main depocenters. One occurs in the south-eastern sector of the basin, with an elongated shape, east of an uplifted fold in a NNE-SSW trend (Figure 6.5), and the other occurs on the north-eastern sector, likely related to a normal slip of an oblique fault of similar trend. SAR of basin H is similar to Unit 6 map (Figure 6.8.c). Better coverage of basins H and I indicate that changes in SAR values are related to fault slip and associated sediment thickening. Basin F displays maximum SAR of 47 mm/ky, but the deep HV here prevents good coverage of the basin.

Unit 4 of upper Calabrian and earliest Middle Pleistocene age (1116-695 ky; Figure 6.8.c) is mapped nearly across the whole area, with the exception of the southernmost basins, where HIV is too deep for imaging. Unit 4 map (Figure 6.8.c) displays comparatively higher SAR values, up to 156 mm/ky than for older units (Figure 6.9.G). The highest SAR occurs at basin G centre, where an elongated depocenter follows a NNE-SSW orientation, similar to the main regional fault trend (Figure 6.8.c). Basin G has two additional depocentres with SAR values up to 134 mm/ky for both locations, east and west of the main depocentre. Neighbouring basin E shows in the south-east the same depocenter of Unit 5, east of a NNE-SSW trending recent fold that limits the sedimentation to the eastern sector of the basin. This elongated depocenter extends towards the south and connects to basin C, where SAR values reach up to 101 mm/ky (Figures 6.9.C and 6.8.c). Unit 4 is the oldest mapped across nearly the entire basin F, where it reaches SAR values up to 115 mm/ky (Figure 6.9.C). High SAR values occur along the eastern part of the basin possibly related to slip on a normal fault with a NNE-SSW strike (Figure 6.8.c). Basin B is the best-mapped southern basin, with SAR values up to 79 mm/ky (Figure 6.9.B). Two NE-SW trending depocenters are possibly controlled by strike-slip faulting (Figure 6.5). Basins H and I have SAR values up to 79 and 92 mm/ky, respectively (Figures 6.9.H and 6.9.I).

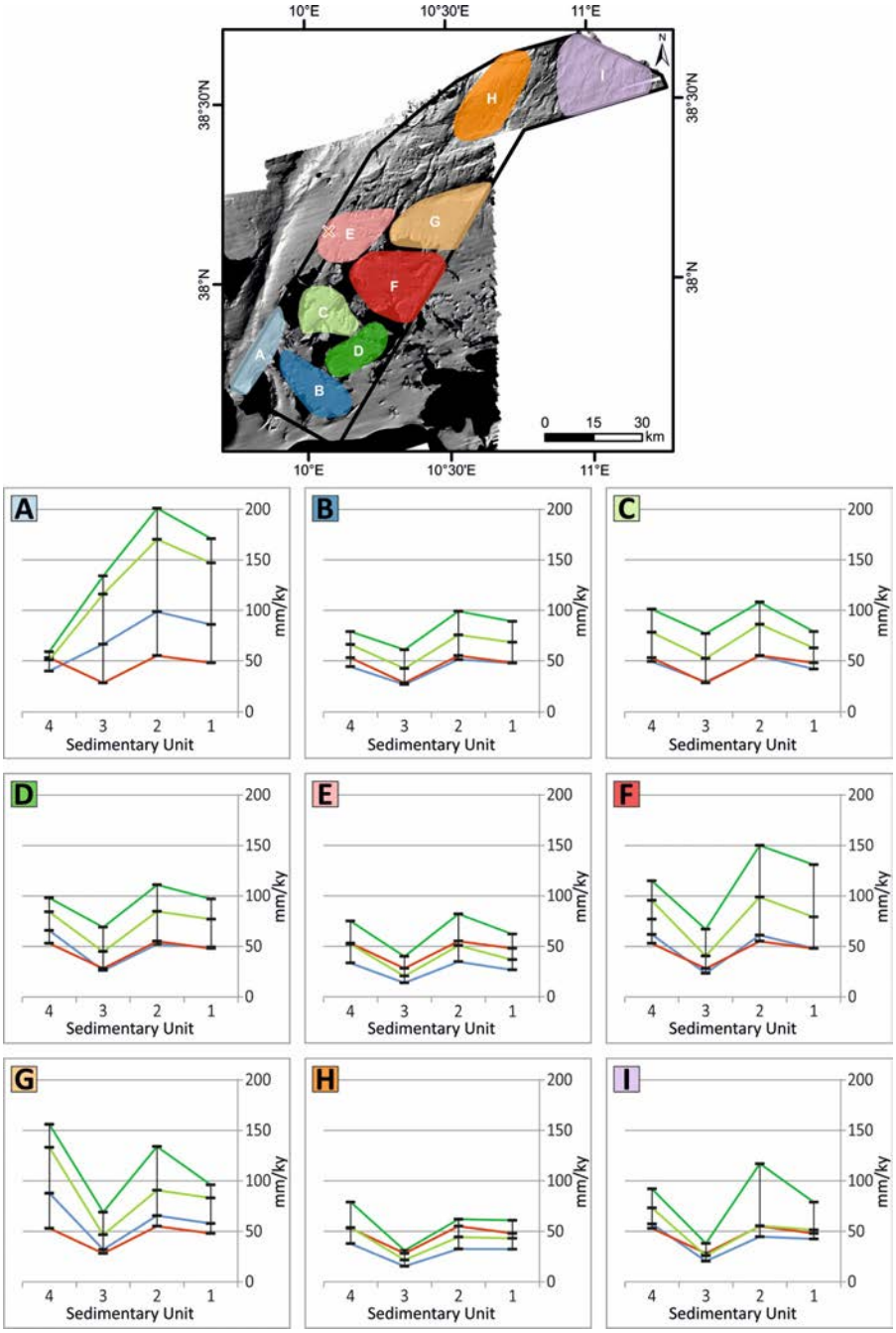

Figure 6.9. *Sediment accumulation rate (SAR) plots for all the basins (from A to I). The X-axis represents the Sedimentary Units (from 4 to 1) and the Y-axis corresponds to the sediment accumulation rate values (SAR) in mm/ky. The red line displays de mean SAR value of all the basins, the blue line corresponds to the mean SAR value of each basin, the dark green line the maximum SAR value for the deepest depocenter of each basin and the light green line the upper-3th-quartile mean value (i.e. a proxy for the mean value of the largest depocenters). The red and white X of the map marks core site location.*

Unit 3 implies a marked decreased in SAR mean values from 695-471 ky (early Middle Pleistocene), diminished to about half (from 53 to 28 mm/ky) for the entire study area (Figures 6.8.d and 6.9). Unit 3 SAR map across all basins shows for the first time values for basins A and D. Basin A has a high maximum SAR value of 134 mm/ky (Figure 6.9.A), possibly related to bottom currents

running through Bizerte canyon, and building thick contourite deposits. Basin D has SAR values up to ~69 mm/ky (Figure 6.9.D) in an elongated NE-SW trending depocenter (Figure 6.8.d). Finally, basin B has another - two first developed - thinner NE-SW striking depocenters (Figure 6.8.d).

Unit 2 represents a new increase in SAR from 471-249 ky (mid Middle Pleistocene; Figure 6.8.e) following the decrease of Unit 3: The mean SAR values increase from 28 to 55 mm/ky, similar to the SAR values of Unit 4 (red line in Figure 6.9). Although with similar SAR values, Units 4 and 2 have the main depocenters in different locations. A clear example is the depocenter of basins G and F. During the Upper Calabrian (Unit 4), basin G had the depocenter with highest SAR (156 mm/ky), but during Unit 2 (mid Middle Pleistocene), basin F had larger SAR values than basin G (150 mm/ky vs 134 mm/ky respectively) (Figures 6.8.c, 6.8.e, 6.9.F and 6.9.G). Similarly to basin G, the northernmost basins H and I have higher mean SAR values in Unit 4 than during Unit 2 (Figures 6.9.H and 6.9.I). In contrast, basins A, B, C and D in the south have higher mean SAR values in Unit 2 (Middle Pleistocene) than during Unit 4 (Upper Calabrian) (Figures 6.8.c and 6.8.e). This pattern is clear for basins B and C, but it is less obvious for A and D where Unit 4 could only be locally mapped (Figure 6.9). Yet, some small Unit 4 patches within basins A and D show lower SAR values for Unit 4 than for Unit 2 (Figure 6.8.c). In contrast, basin E shows similar SAR values for Units 4 and 2, but with low mean SAR values and the upper-3th-quartile mean values similar to values of basin H (Figures 6.9.E and 6.9.H), which supports that it is related to sedimentation patterns of the northern basins.

Unit 1 shows slightly lower mean SAR values from 249-0 ky (mid Middle Pleistocene to present, Figure 6.8.f) than in the underlying Unit 2 (red line in Figure 6.9), but no changes in main depositional locations are observed. Mean SAR values of ~55 mm/ky during deposit of Unit 2 decrease to ~48 mm/ky during Unit 1.

6.5. Quaternary regional deformation

From the analysis of sediment deposit type and distribution, sediment thickness and SAR, it is clear that syn-sedimentary active tectonic features influence sedimentation. Recent faulting and folding appear to play a key role for the Quaternary sediment distribution and sediment rate throughout the study area. Next, we present some of the most relevant tectonic features that affect recent sedimentation.

Most of depocenters within the study region have geometries that support their association to syn-sedimentary active faults (see section 6.4). A clear example is the depocenter of basin F (Figure 6.4), with the eastern boundary rotated by a comparatively major NNE-SSW normal fault dipping to the NW and the basin developing on the hanging wall (Figure 6.10.b). Basin H depocenter is related to a small pull-apart basin formed by sinistral motion of a strike-slip fault (Figure 6.10.c). Thickening of sediment units into the pull-apart basin and sediment sliding with clear scar and transparent slide facies support active slip on the fault, which seem to affect sediments of Units 1 and 2 (Figure 6.10.c). Depocenters of basin I (Figure 6.8) are related to mass transport phenomena, represented by Mass Transport Deposits (MTDs) that produce thickening of some sediment units in the basin (Figures 6.10.d and 6.11). MTDs may result from slip of faults during deposition of Unit 2 from 471-249 ky (mid Middle Pleistocene). Their wedge morphology and proximity to the faults support a causal link between MTDs and slip faults (Figures 6.10.d, 6.11.a, and 6.11.b). We interpret MTDs with a tectonic origin, although a fault is not always imaged nearby on the TOPAS profile Figure 6.11.c. Unit 2 contains 15 MTDs, mostly located within basin I. The abundance of MTDs in basin I anomalously increases the thickness of Unit 2 there (Figure 6.9.I).

Unit 3 has comparatively lower SAR values (Section 6.4). As a result, although the Units 1-3 represent similar age periods (224 ky Unit 3, 222 ky Unit 2, and 249 ky Unit 1), Unit 3 is everywhere clearly thinner in seismic images (Figure 6.10). Likewise, Unit 3 mean thickness values are <1/2 of the mean values of Unit 4 that represents 421 ky, twice as long in time as Unit 3. Thus, Unit 3 represents the most significant departure in mean SAR values, followed by a change in sedimentation pattern (section 6.4).

This change consists in new strata geometrical relationships, with onlap geometries of most layers of Units 2 and 1 with underlying reflections in the hanging wall of the major normal fault of basin F (Figure 6.10.b). The layers geometry shows an abrupt change during deposition of lower strata of Unit 2 at 402 ± 5 ky (mid Middle Pleistocene) (Figure 6.10.b), and the onlap seems necessarily related to either slip on a new fault or increased slip rate on an existing fault (considering that wedged strata are displayed below the Unit 2 thus likely showing previous slip). The growth-fault geometry of the most recent sediments supports slip of the fault to present day, supported by SAR of the area (Section 6.4.1) that shows an increased SAR during Unit 2 compared to Unit 3 (Figures 6.8 and 6.9).

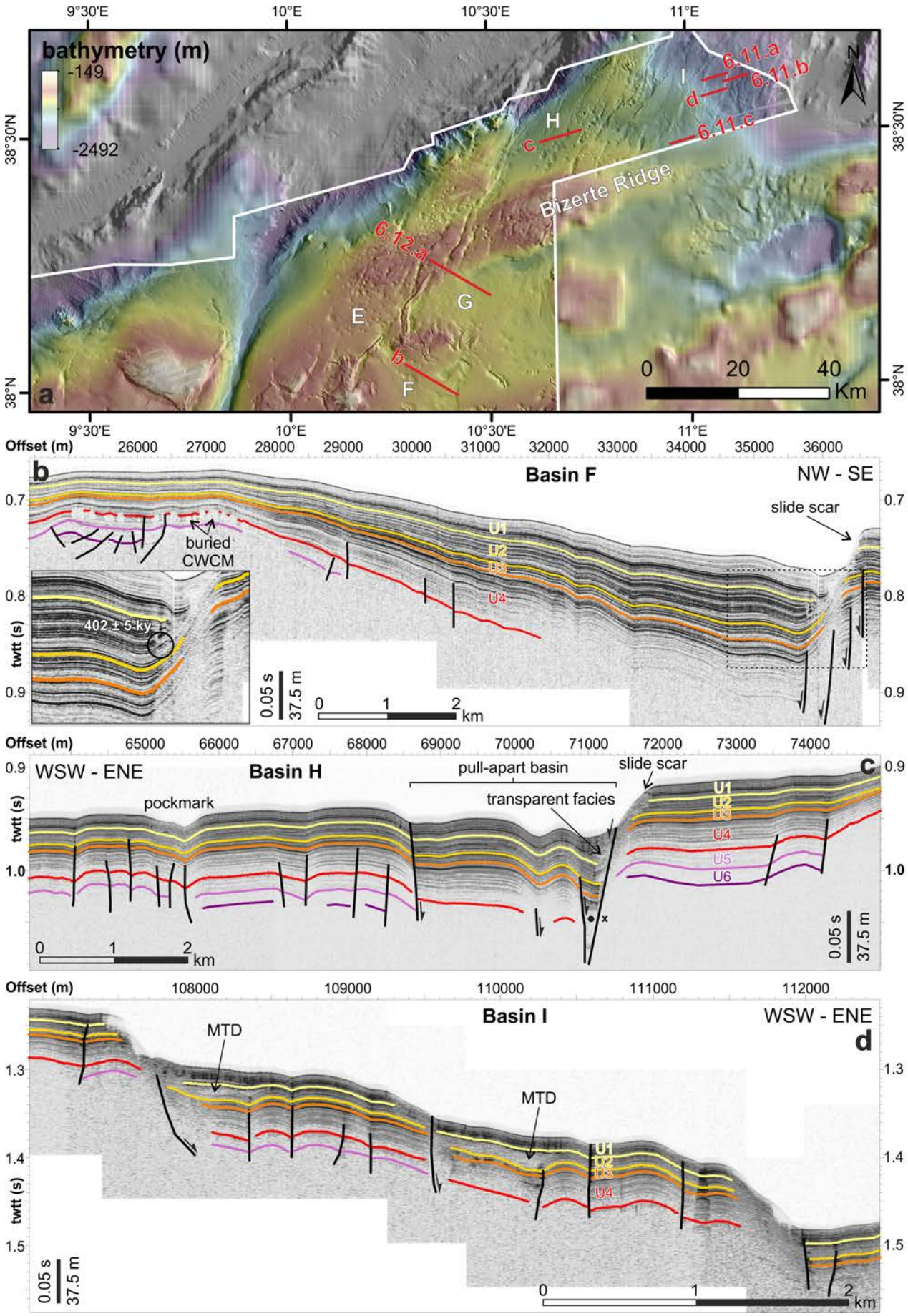
9°30'E
10°E
10°30'E
11°E
38°30'N
38°N
bathymetry (m)
-149
-2492
N
6.11.a
6.11.b
6.11.c
6.12.a
Bizerte Ridge
a
0 20 40 Km
Offset (m)
b
Basin F
NW - SE
slide scar
buried CWCM
U1
U2
U3
U4
402 ± 5 ky
twtt (s)
0.05 s
37.5 m
0 1 2 km
c
WSW - ENE
Basin H
pull-apart basin
slide scar
pockmark
transparent facies
U5
U6
d
Basin I
MTD

Figure 6.10. *Bathymetry of the northern Tunisian Margin and selected TOPAS profiles. a) Bathymetric map showing the location of TOPAS profiles that show different fault-related depocenters within the study area. b) TOPAS profile across basin F, in the line drawing it is shown in a black circle the beginning of the onlap geometries at 402 ± 5 ky. c) TOPAS profile across basin H, and d) TOPAS profile across the basin I.*

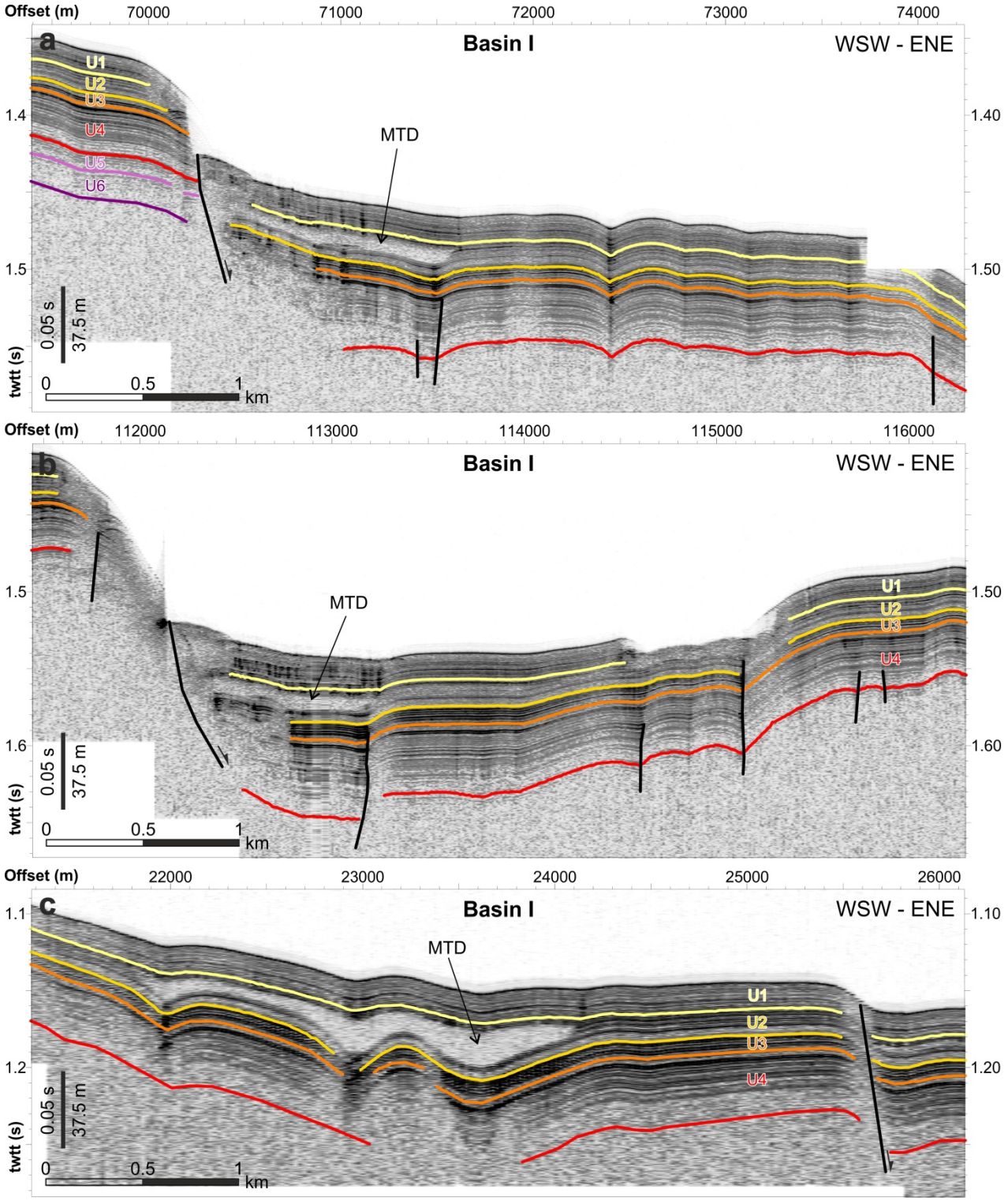

Figure 6.11. *TOPAS profiles showing different fault-related depocenters within the basin I of the study area, referred to as a), b) and c), from north to south. We observe the MTDs resulting from the slip of faults within the Unit 2. Location of the profiles is depicted in Figure 6.10.a.*

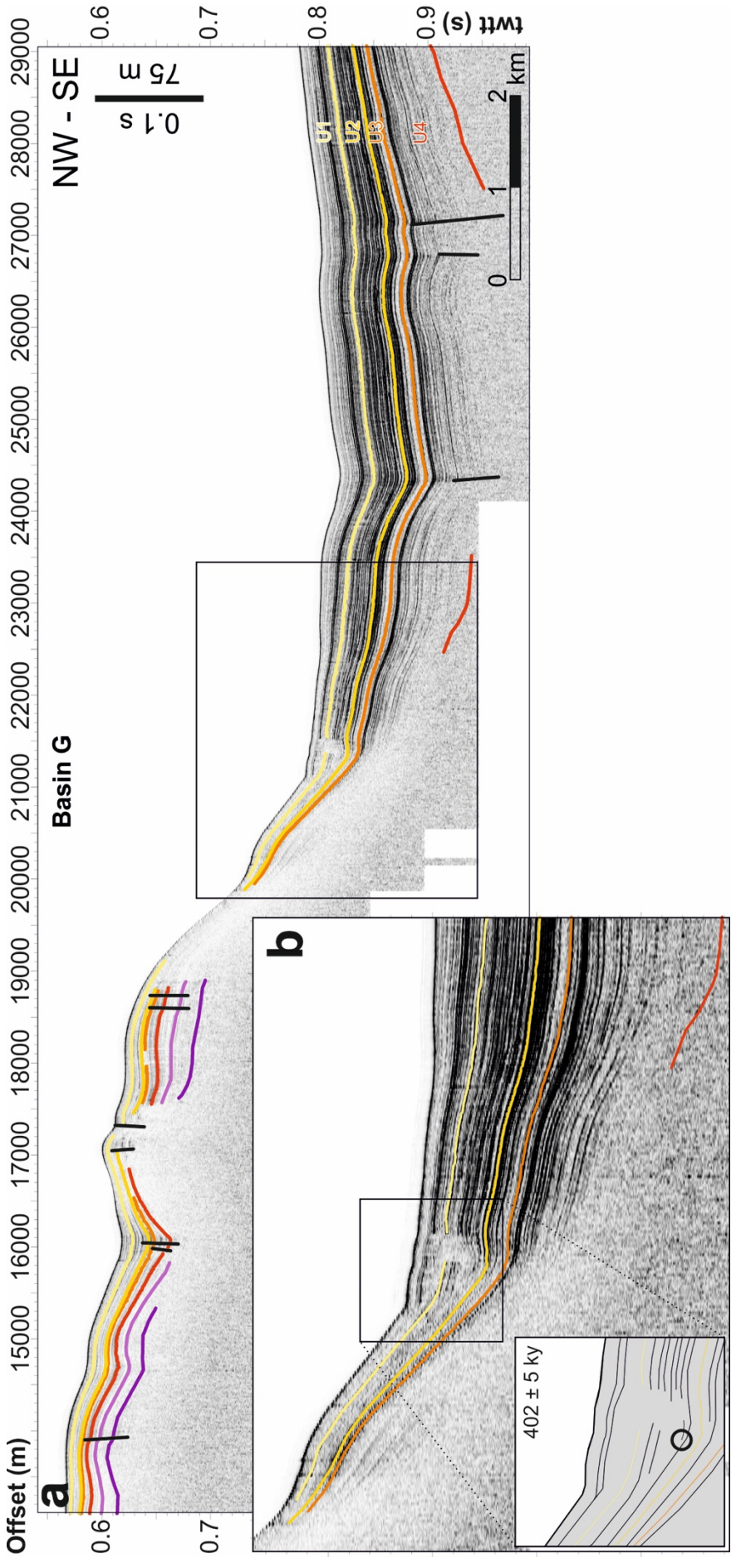

Figure 6.12. *a) TOPAS profile across the basin G. The rectangle shows the contact between the slope and the basin. Location of the profile is depicted in Figure 6.10.a. b) Detailed zoom between the slope and the basin. In the line drawing it is shown in a black circle the beginning of the onlap geometries at 402 ± 5 ky.*

Basin G exhibits a similar sedimentation pattern, with pinch-out geometries and onlap terminations within Units 2 and 1 (Figure 6.12.b). Although growth-strata in all sediment units in the western sector of basin G indicate continuous uplift of the western sector (related to the Bizerte Ridge; Figure 6.10.a), the pinch-out and onlap geometries imaged at the base of the Unit 2 and younger (402 ± 5 ky) (Figure 6.12.b) support a sudden increase in uplift velocity. The intercalated transparent facies and undulated seafloor indicate sediment destabilization probably related to uplift. Further east along the base of the WSW-ENE trending high occurs an elongated seafloor depression containing slide scars and large MTDs (Figure 6.10.a).

6.6. Discussion

6.6.1. Tectono-sedimentary evolution

Our analysis supports a series of inferences on the interrelation between sedimentation and tectonics. The location of most depocenters within the study region appears related to recent tectonics, and seismic images show that most depocenters occur indeed near recent faults. Several depocenters contain MTDs likewise related to -possibly sudden- slip on faults. Yet, a few depocenters appear mainly related to sedimentary processes only, like the large depocenter located within basin A resulting from the build-up of a contourite deposit, and the depocenter at the south-east sector of basin B resulting from prograding sedimentation extending from the continental shelf (Figure 6.4).

Unit 3 SAR shows a clear decrease in sediment accumulation rate from 695-471 ky (early Middle Pleistocene, Figure 6.8.d) with a mean value of 28 mm/ky, (Figure 6.9). This decrease may be partially related to the process creating a sandy interval interpreted as a winnowed lag deposit (Dinarès-Turell et al., 2003), which, given the extension of the layer in seismic images, possibly affected the entire region. This sandy interval separates two general SAR trends from 21.6 to 27.7 mm/ky in the sediment core (Figure 6.2).

The change in internal geometry and distribution of the Units, as well as the SAR variations in depocenters through time, affect all the studied area. The onlap terminations and pinch-out geometries, starting at 402 ± 5 ky (mid Middle Pleistocene), i.e. occurring for most of Unit 2 and Unit 1, indicate a change in either tectonics with new faults or acceleration of the slip rates on existing faults Figures 6.10.a and 6.12. The SAR distribution supports that the change caused new fault kinematics or accelerated slip of existing faults, mainly towards the mid-northern sector. The

15 MTDs within Unit 2 are also mainly localized in the northern sector (Figures 6.10.c and 6.11). Moreover, the northern basins (i.e. basins E, G, H, I) have larger SAR values during the deposit of Unit 4 than for Units 2 and 1, whereas the southern basins show the opposite trend. Assuming a relatively constant sediment supply throughout time indicated by the 2.16-2.77 cm/ky determined in the sediment of piston core LC07 (Figure 6.2) and further supported by its nearly homogeneous grey to olive foraminifer-rich mud sediment (Dinarès-Turell et al., 2002, 2003), spatial changes in SAR may related to tectonics. The onlap and pinch-out geometries towards Bizerte Ridge in the north (e.g. Figure 6.12), support uplift soon after the beginning of Unit 2 (402 ± 5 ky), which likely caused a comparatively reduced SAR across the northern sector.

This change in tectonics inferred from the sudden variation in fault slip (402 ± 5 ky) and occurrence of MTDs within Unit 2 in the mid Middle Pleistocene, is somewhat younger than the tectonic reorganization at around 0.8-0.5 Ma proposed for the south-central Mediterranean (Goes et al., 2004). Goes et al. (2004) interpret this reorganization related to the last stages of the end of back-arc extension of the Tyrrhenian Basin. Extension dominated the Tyrrhenian regional evolution since the Tortonian (10-8 Ma) (Gueguen et al., 1998; Faccenna et al., 2001; Rosenbaum et al., 2002; Faccenna et al., 2004; Pondrelli et al., 2004; D'agostino and Selvaggi, 2004; Jenny et al., 2006) (Figure 6.13). However, the current 5 mm/yr Africa-Europe plate convergence appears to be mainly absorbed in northern Sicily by an offshore contractional belt characterized by frequent moderate thrust earthquakes (Figure 6.14) (e.g. Goes et al., 2004; Billi et al., 2007; Serpelloni et al., 2007; Nocquet, 2012; Palano et al., 2012; Presti et al., 2013; Totaro et al., 2016; Chiarabba and Palano, 2017). This seismicity delineates the currently-active deformation zone within the Nubia-Eurasia plate-boundary offshore northern Sicily, which extends to the west with our study area. Thus, the abrupt tectonic change inferred from the relations between sedimentation and faulting, and the uplift of our northern sector, is likely related to the accommodation of the current plate convergence by deformation along this boundary. In agreement, further west the Nubia-Eurasia boundary exhibits Quaternary reactivation along northern Algeria (Déverchère et al., 2005; Domzig et al., 2006; Kherroubi et al., 2009; Yelles et al., 2009; Strzerzynski et al., 2010; Arab et al., 2016). Kherroubi et al. (2009) proposed a west to east migration of the tectonic activity along the Algerian margin with the eastern sector undergoing tectonic activity since 0.9-0.6 Ma compared to 1.2 Ma to the west. Thus, the 0.9-0.6 Ma tectonics in eastern Algeria (Kherroubi et al. (2009), and 0.8-0.5 Ma in northern Sicily (Goes et al., 2004) are reasonably similar to the 402 ± 5 ky age obtained in this study. The differences in timing may be due to differences in resolution or uncertainty or imply an evolutionary process with time and space migration of the deformation across this sector of

Nubia-Eurasia convergent boundary. Furthermore, it is possible that deformation had begun before in the Tunisian continental margin, as it can be depicted in the wedged sediments of Figure 6.10.b below the 402 ± 5 ky reflector. Déverchère et al., (2005) proposed incipient southward subduction of the Algero-Balearic oceanic basin under the Algerian margin, and Billi et al. (2007) proposed that the young southern Tyrrhenian margin is in an early stage of contraction, compressively reactivating or inverting north-dipping inherited faults from the opening of the Tyrrhenian basin. Several works have also locally described minor phases of inversion along the northern edge of the Tunisian plateau in the Sardinia Channel area (e.g. Tricart et al., 1990; Tricart et al., 1994; Mascle et al., 2001; Mascle et al., 2004). The location of our study area next to the south Tyrrhenian contractional belt, and from the region of reactivation in Algeria, further supports that our study area is in an early stage of contraction.

No deep-penetration seismic image has been published to our knowledge from the structure uplifting the northern sector of the study region. The SAR distribution supports uplift in the region limited by the southern flank of the Bizerte Ridge to the south, and the Cornaglia slope to the north. This region also contains the highest density of pockmarks and recent NE-striking faults (Figure 6.10.a). The pockmarks aligned on NE-striking faults further support recent tectonic activity in the north-easternmost sector. The interpretation of uplift of the northern region discussed in this Chapter, agrees with inferences based on morphology of recent tectonic activity in the northern sector discussed in Chapter 5.

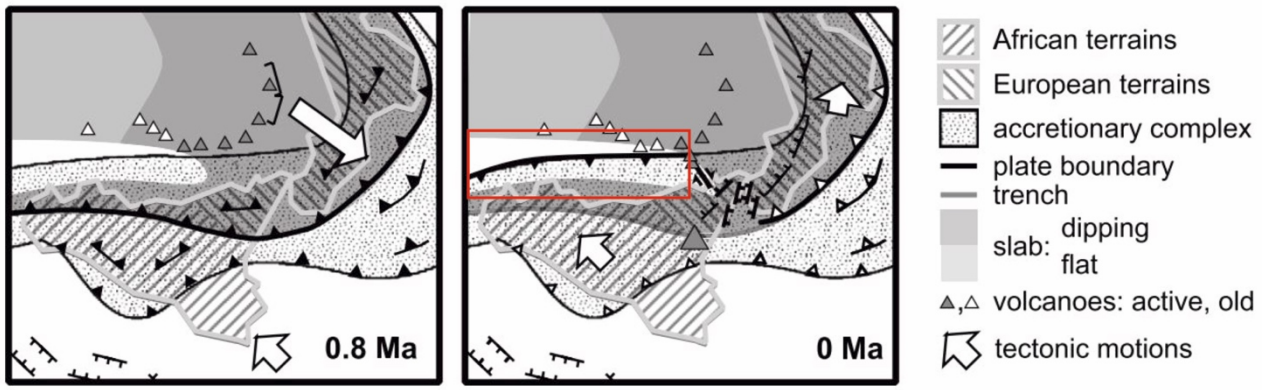

Figure 6.13. *Sketch of the recent tectonic evolution (0.8 to 0 Ma) of the Sicily–Calabrian area. To the right, the red box displays the new offshore contractional belt located in northern Sicily. Modified from Goes et al. (2004).*

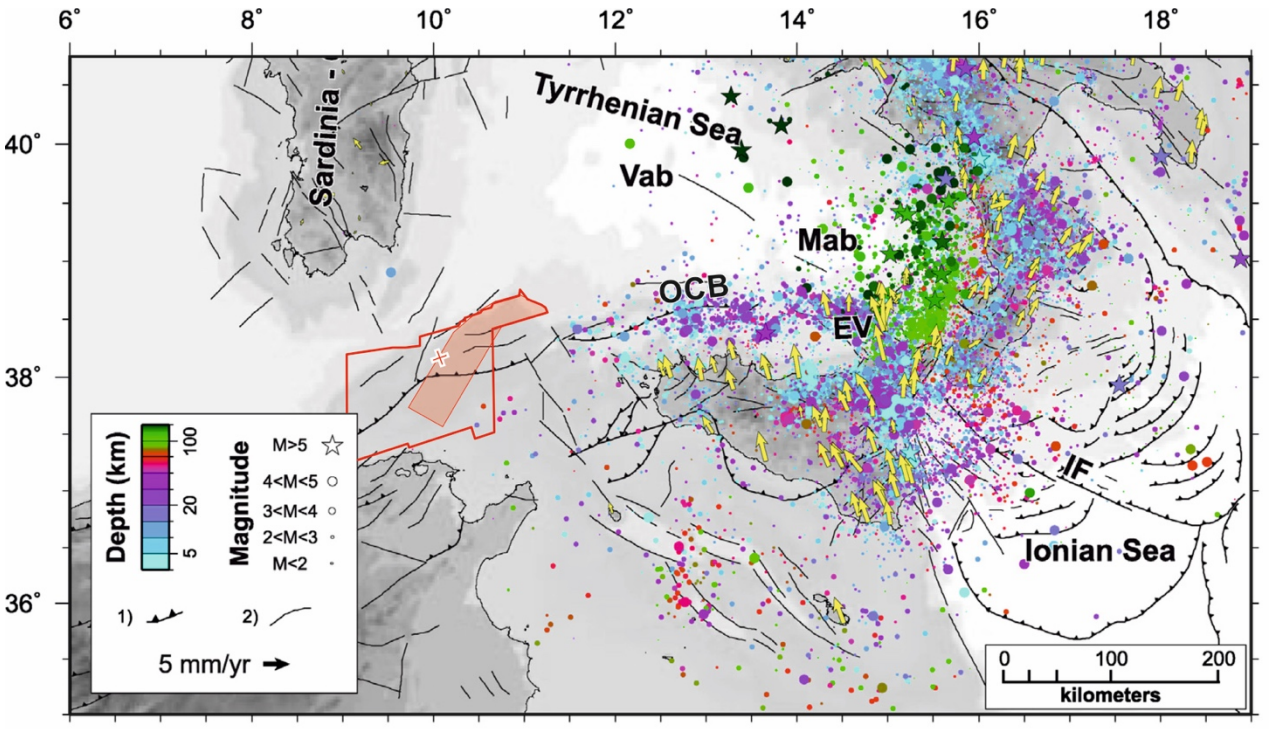

Figure 6.14. *Tectonic map with the instrumental seismicity (1981-2013) of the central Mediterranean area. Earthquakes are colored as a function of the focus depth. Different symbols indicate their magnitude. The red polygon delineates our study zone. The red and white X of the map marks core site location. Present-day GPS motion vectors (yellow arrows) are in a fixed Eurasian reference frame. Abbreviations: EV, Aeolian Volcanoes; Mab Marsili basin; Vab, Vavilov basin; IF, Ionian fault; SPb, Sardinia-Provençal basin, OCB, Offshore contractional belt. Modified from Chiarabba and Palano, 2017).*

6.7. In summary

The seismo-stratigraphic analysis of the Quaternary deposits shows that individual basins developed syn-tectonic to faulting. Faulting may represent a reactivation of existing faults, or acceleration of the slip of pre-existing faults. The location of the depocenters of the basins, which in some cases contain abundant MTDs, occurs next to active faults imaged in sub-bottom profiles.

The study of Sediment Accumulation Rates (SAR) of the depocenters provides information of the tectonic evolution of the region. SAR values of the northern basins (i.e. E, G, H and I) were larger before the deposition of Unit 3 than during Units 2 and 1. Unit 3 has the lowest SAR possibly related to an erosive event creating a winnowed lag sand deposit mapped across the region.

The TOPAS profiles show, in addition to the change in SAR, a change in the strata geometry of the units next to faults during the early deposition phase of the Unit 2. Unit 2 and 1 display onlap terminations and pinch-out geometries indicative of syn-tectonic sedimentation, as well as -possibly

fault-related- MTDs within Unit 2. The internal structure of Units 6-3 is generally a drape with regional changes in thickness and indicates a comparatively quiescence tectonic period. The stratigraphy supports that the change in active faulting intensity occurs at 402 ± 5 ky, in the mid Middle Pleistocene.

The location of onlap terminations and pinch-out geometries supports uplift of the northern sector, which may explain the comparatively lower SAR values obtained in this sector after the deposit of Unit 3.

The change in tectonic activity close to the base of Unit 2 (402 ± 5 ky) is slightly younger that the age proposed for reactivation and early stage contraction of the south Tyrrhenian area (Goes et al., 2004). This initiation of contraction may relate to the NW-SE convergence between Nubia and Eurasia, and probably marks the stop of the Tyrrhenian back-arc extension. If this inference is correct, lithospheric collision between Nubia and Eurasia plates is probably the main driving force governing tectonics in the central Mediterranean region at the present day.

CHAPTER 7

Active tectonics of the North Tunisian continental margin

7.1. Introduction

The study region of the North Tunisian continental margin is located offshore, at the diffuse boundary between the Nubia and Eurasian plates. The region is currently in a contractional tectonic setting within a NW-SE convergence regime. The North Tunisian margin shows no tele-seismic activity along the inferred plate boundary region (Serpelloni et al., 2007). The neighboring eastern and western regions of northern Algeria and northern Sicily currently display abundant seismicity concordant with a compressional regime (i.e.) and are better known (e.g. Meghraoui and Doumaz, 1996; Hollenstein et al., 2003; Stich et al., 2006; Serpelloni et al., 2007, Billi et al., 2011; Nocquet, 2012; Totaro et al., 2016;). Offshore North Tunisia the lack of seismicity and limited seismic profiling information prevented any detailed tectonic study of the area.

In this Chapter we present a structural analysis to study active tectonics of the North Tunisian continental margin. The main aim is to integrate bathymetric maps with parametric echosounder images to study the shallow structure of the area and to identify potentially active tectonic structures, and determine faulting style and kinematics. The result of integrating high-resolution TOPAS profiles and a high-resolution bathymetric is a fault map of the region with unprecedented detail. Finally, we compute the maximum magnitude of potential earthquakes along segments of active fault systems, providing the first seismic hazard assessment of the offshore region.

7.2. Methodology

To characterize active tectonic processes offshore North Tunisia we use high-resolution parametric echosounder profiles and high-resolution bathymetric data. Thus, we use the same data

sets used to characterize the geomorphology and morpho-structure of the offshore area in Chapter 5. Integrating the geomorphological and morpho-structural analysis of the area with the tectono-sedimentary evolution (Chapters 5 and 6 respectively), provides the observations needed to identify fault-related features. We evaluate their kinematics and compute the possible maximum earthquake magnitudes using two empirical relationships (i.e. Wells and Coppersmith, 1994 and Wesnousky, 2008) (see Chapter 3 for further information about these empirical relationships).

7.2.1. Criteria for fault classification

In this work, we classify faults in four different groups: Possible faults, Inferred faults, Blind faults and Surface rupture faults:

i) Possible Faults are interpreted only from geomorphologic structures because either we do not have TOPAS data or seismic images do not provide information (e.g. regions of low TOPAS penetration).

ii) *Inferred Faults* are interpreted from coincident geomorphologic and seismic structures, although fault offsets are not imaged, strata geometry (e.g. growth strata or tilted strata) in TOPAS profiles supports recent or ongoing tectonic activity.

iii) *Blind Faults* have offsets imaged in seismic data and associated geomorphologic relief but the fault plane does not reach the seafloor. These faults cutting strata in the TOPAS profiles are Quaternary and younger than ~1,725 ky (lower Calabrian). Although there is some debate to define active faults based on the timing of the last event when a fault was active, it is commonly accepted that a fault is considered to be potentially active if it has moved during the Quaternary (e.g. Keller and Pinter, 2002). However it has to be considered that Quaternary has been re-defined and now extends further back to 2.58 Ma, according to the International Commission on Stratigraphy (ICS, 2018). Thus, we interpret that blind faults mapped in our data can be considered active faults (with maximum ages of about 1.7 Ma). Blind fault traces are displayed in yellow in our maps and TOPAS profiles. In the maps, these faults are classified as “main” and “secondary” faults depending on their significance.

iv) *Surface Rupture Faults* are defined with both morphological and seismic evidences. They cut the seafloor and strata imaged in TOPAS profiles. Faults active during the Holocene (past 10 ky), are always considered active faults (Keller and Pinter (2002). Surface ruptures are displayed in red color in our maps and TOPAS profiles. In the maps,

these faults are classified as "main" and "secondary" faults depending on their significance.

The fault classification criteria used in this Chapter is summarized in the Table 7.1 below:

Fault type			Bathymetric evidence	TOPAS evidence		
				Do not cut strata	Cut strata	Cut surface
Possible Fault			■			
Inferred Fault			■	■		
Blind Fault	Main	*Strike-Slip*	■		■	
		Normal	■		■	
		Reverse	■		■	
	Secondary	*Strike-Slip*	■		■	
		Normal	■		■	
		Reverse	■		■	
Surface Rupture Fault	Main	*Strike-Slip*	■		■	■
		Normal	■		■	■
		Reverse	■		■	■
	Secondary	*Strike-Slip*	■		■	■
		Normal	■		■	■
		Reverse	■		■	■

Table 7.1. *Fault classification criteria applied in our work.*

In addition, recent folding in the study region is classified by its dimensions as "main" folds or "secondary" folds.

7.3. Tectonic domains

TOPAS profiles acquired during the Geomargen-2AA cruise (Figure 7.1) display the shallow structural style of recent tectonics in a wide sector of the margin. About 3,500 km of TOPAS profiles cover a region of ~6,434 km^2, mainly in the eastern and north-eastern sectors of the study region, that we interpret as representing tectonics active in the whole explored region. Based on active tectonic structures within the area, we have defined 3 main tectonic domains:

i) The North-eastern Domain that is bounded to the west by the Bizerte Canyon and to the south by the southern flank of the Bizerte Ridge (Figure 7.1).

ii) The Eastern Domain that covers the area east of the Bizerte Canyon, bounded to the north by the Bizerte Ridge (Figure 7.1).

iii) The Western Domain that covers the area west of the Bizerte Canyon (Figure 7.1).

Next, we describe each of these tectonic domains and estimate the seismic potential of the most relevant active faults.

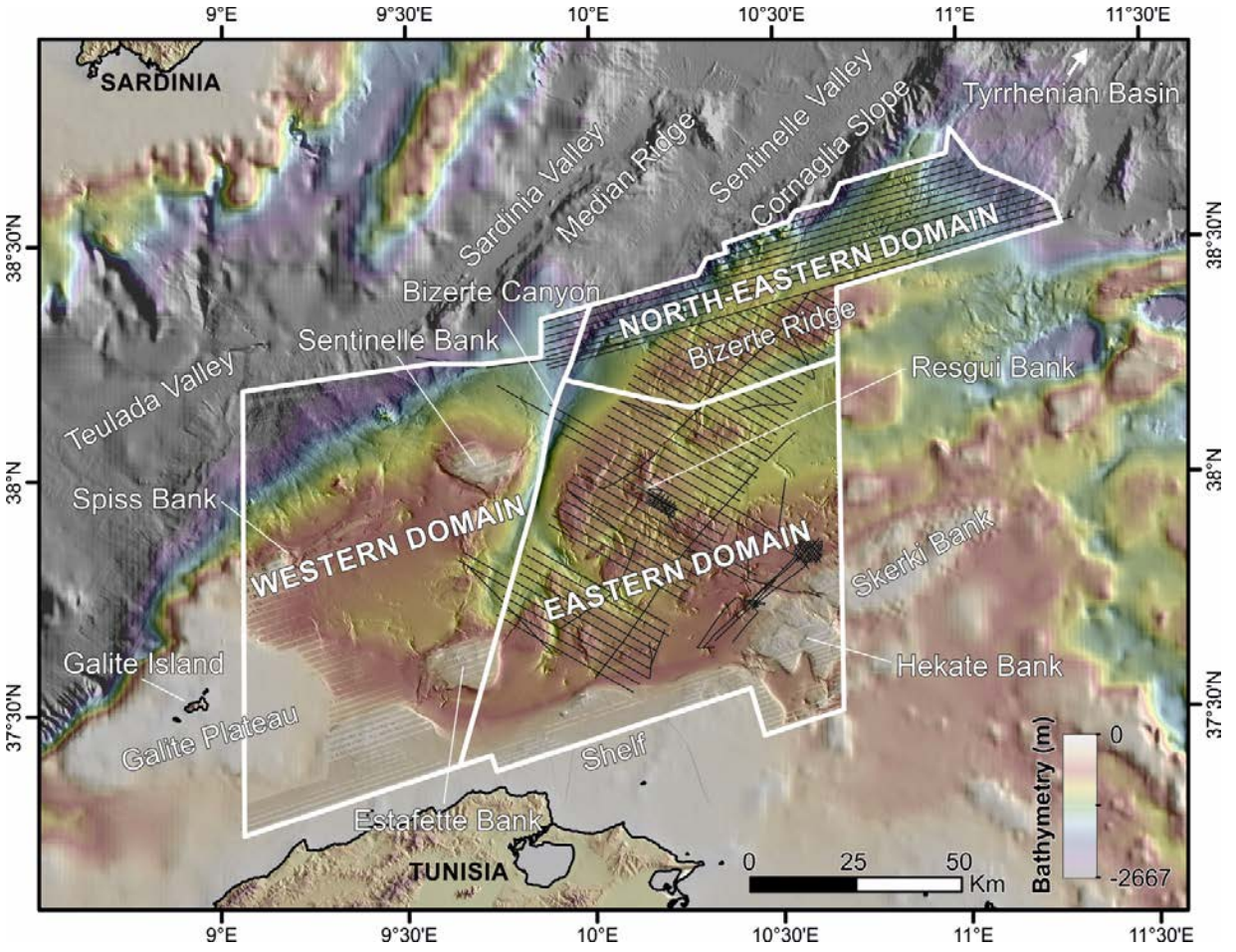

Figure 7.1. *Bathymetric map of the North Tunisian Margin. The three main tectonic domains interpreted in the north Tunisian continental margin are bounded by the white polygons. TOPAS tracks are depicted in thin black lines.*

7.3.1. The North-eastern Domain

Bathymetric data covering the North-eastern Domain shows elongated troughs with pockmarks aligned along them. The troughs are the surface expression of fault traces (described in Chapter 5). Fault traces in the North-eastern Domain show a main average trend of N25º-N30º (Figures 7.2 and 7.3). Meanwhile, fault-associated folds are sub-parallel to the fault traces, and therefore their axes follow the same trend. In addition to the N25º-N30º main trend, minor fault trends occur at N15º-N25º and N30º-N40º (Figures 7.2 and 7.3).

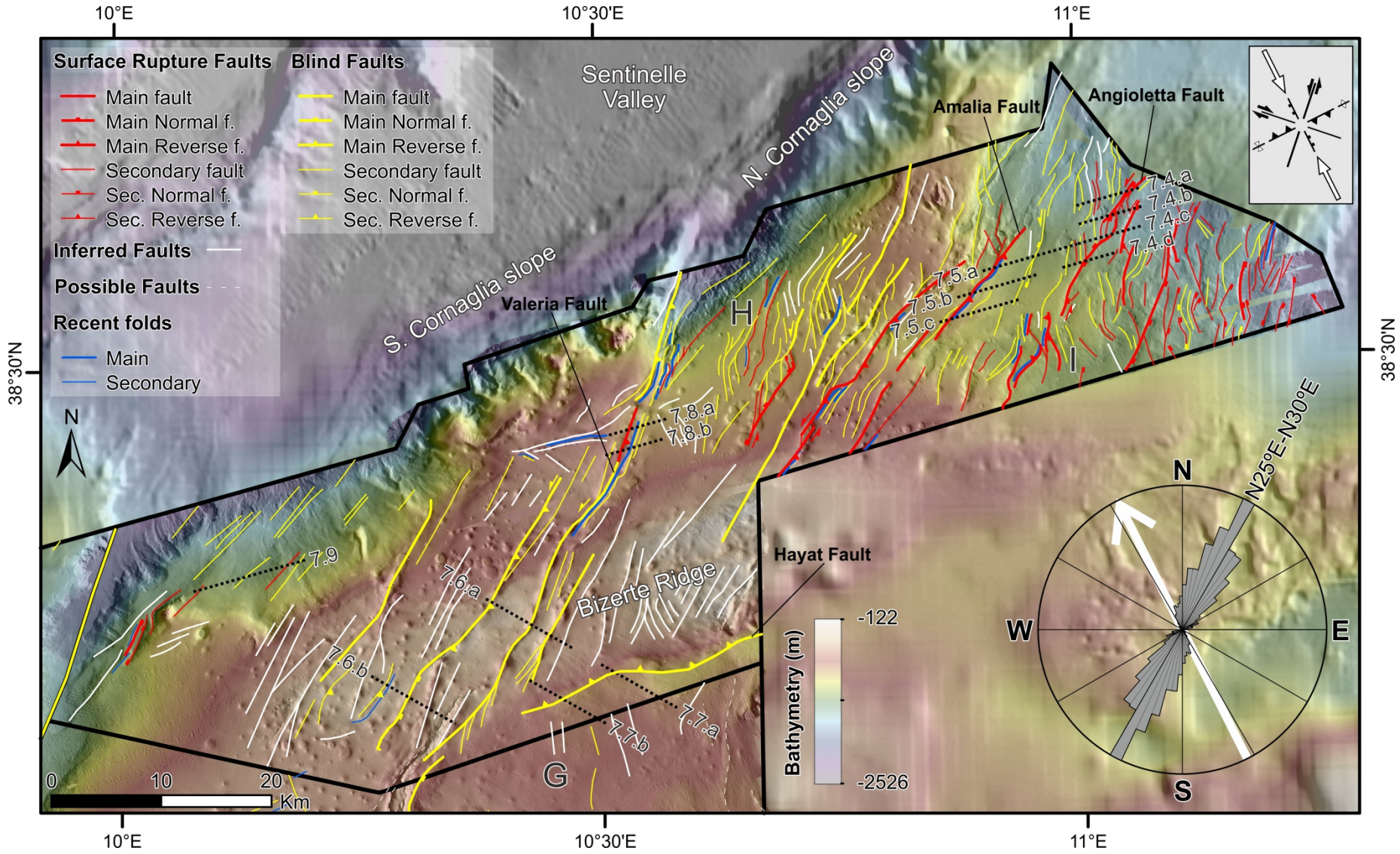

Figure 7.2. *Recent tectonic framework of the North-eastern Domain (faults and folds). The rose diagram shows the average orientation of the North-eastern Domain faults clustered at 5° groups. The white arrow shows the GPS horizontal velocity of the closer permanent station, MILO in western Sicily, (Serpelloni et al. 2007) relative to the Eurasian plate; The absolute kinematic rate in MILO station is 3.5 ± 0.6 mm/yr with an*

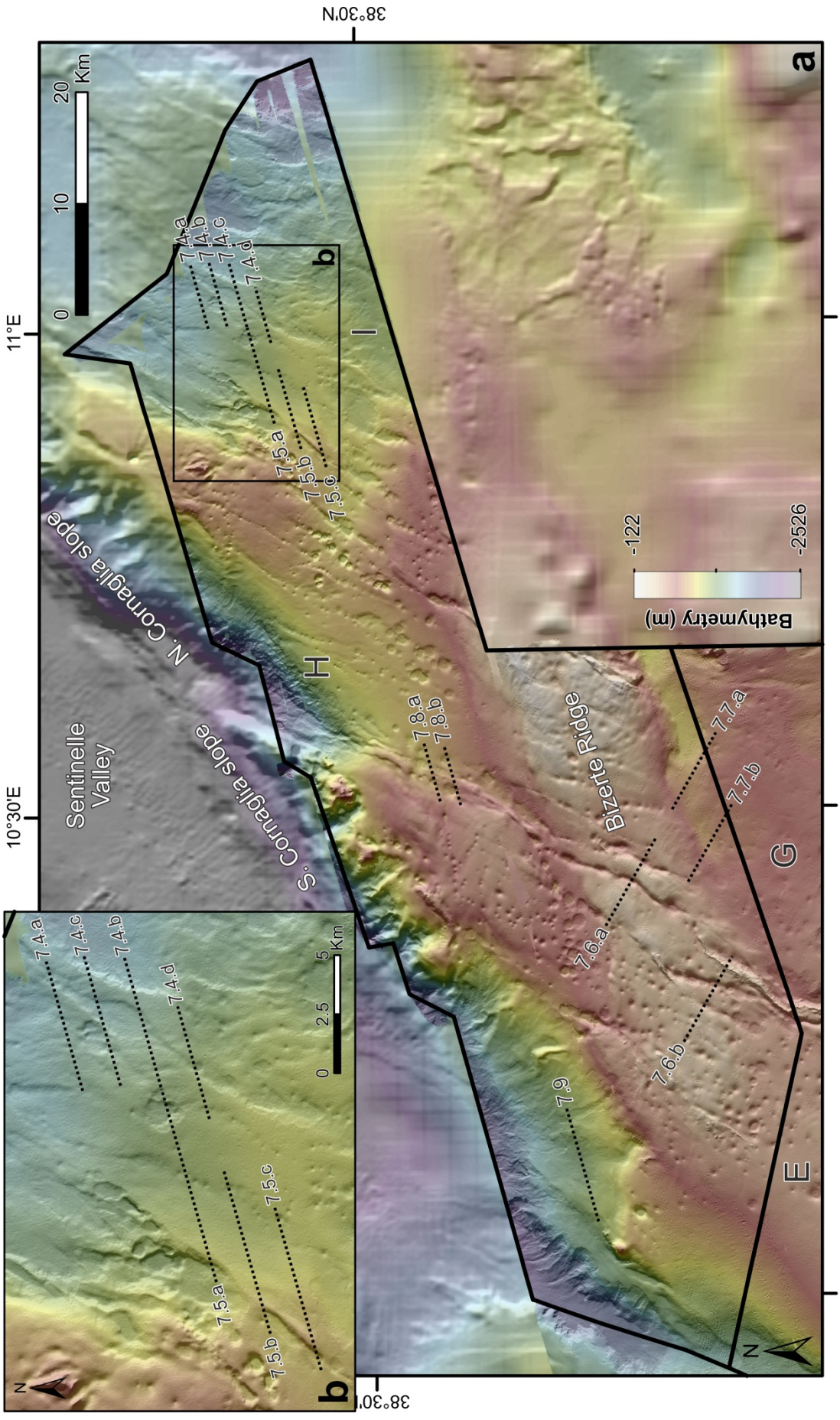

***Figure 7.3**. North-eastern tectonic Domain; a) Coloured shaded relief bathymetric map b) Zoom of the area showing the pull-apart basin of the Angioletta fault and the Amalia reverse fault. Location of TOPAS profiles is depicted by dashed black lines (Figures 7.4, 7.5, 7.6, 7.7, 7.8 and 7.9).*

Left-lateral pull-apart basins (Figures 7.2, 7.3 and 7.4) are recognized throughout the North-eastern Domain. A clear example shows a pull-apart basin resulting from the slip on a fault, named Angioletta Fault (Figure 7.4). Angioletta fault is affecting the seafloor, which supports that the structure is currently active. The pull-apart basin geometry indicates a left-lateral strike-slip motion of the fault, clearly shown in map view (Figures 7.2 and 7.3) and in the TOPAS image (Figures 7.4.b and 7.4.c). North and south of the pull-apart basin (Figures 7.4.a and 7.4.d), the Angioletta fault changes its relative displacement from reverse to normal, respectively. This characteristic trend is observed in other strike-slip faults in the area, displaying sub-vertical fault planes with changes in the along-strike slip component (normal to reverse). Moreover, several NNW-SSE trending *en-echelon* traces observed within the North-eastern Domain display oblique sinistral strike-slip faulting (Figures 7.2 and 7.3). The sinistral strike-slip component matches with the regional stresses inferred from the SE-NW convergence between Nubia and Eurasia in this sector to the south-west of the Tyrrhenian Sea. A rose diagram shows that the ~N30ºW convergence vector (white arrow) is oblique to the main N25ºE-N30ºE fault trend (Figure 7.2).

Besides a dominant strike-slip component, pure normal (Figures 7.4.b and 7.4.c) and reverse faults also occur in the North-eastern Domain. The normal SE-dipping fault of Figure 7.4.b and 7.4.c cuts to the seafloor supporting recent activity. Moreover, mass transport deposits (MTDs) imaged along the hanging-wall of the normal fault may have resulted from co-seismic shaking (discussed in Chapter 6). This kind of slide deposits, and slide scars, are common features within the North-eastern Domain. A SE-dipping reverse fault folding the seafloor, that we named Amalia fault has syn-tectonic sediment deposits that thicken towards the east, which together with onlap terminations towards the west indicate uplift of the western flank (Figure 7.5). Chaotic facies and slide scars on the western flank of the Amalia-fault fold erode the most recent sedimentary layers (Figures 7.5.a and 7.5.b). These features suggest that recent sliding likely resulted from slip of the Amalia fault, further supporting recent tectonic activity. Pure normal and reverse fault slip also match the oblique convergence of the region. Reverse faults seem to have a predominant ENE-WSW trend, striking roughly perpendicular to the main convergence vector (Figure 7.2). Normal faults characteristically trend NNE-SSW being highly oblique to the plate convergence vector (Figure 7.2).

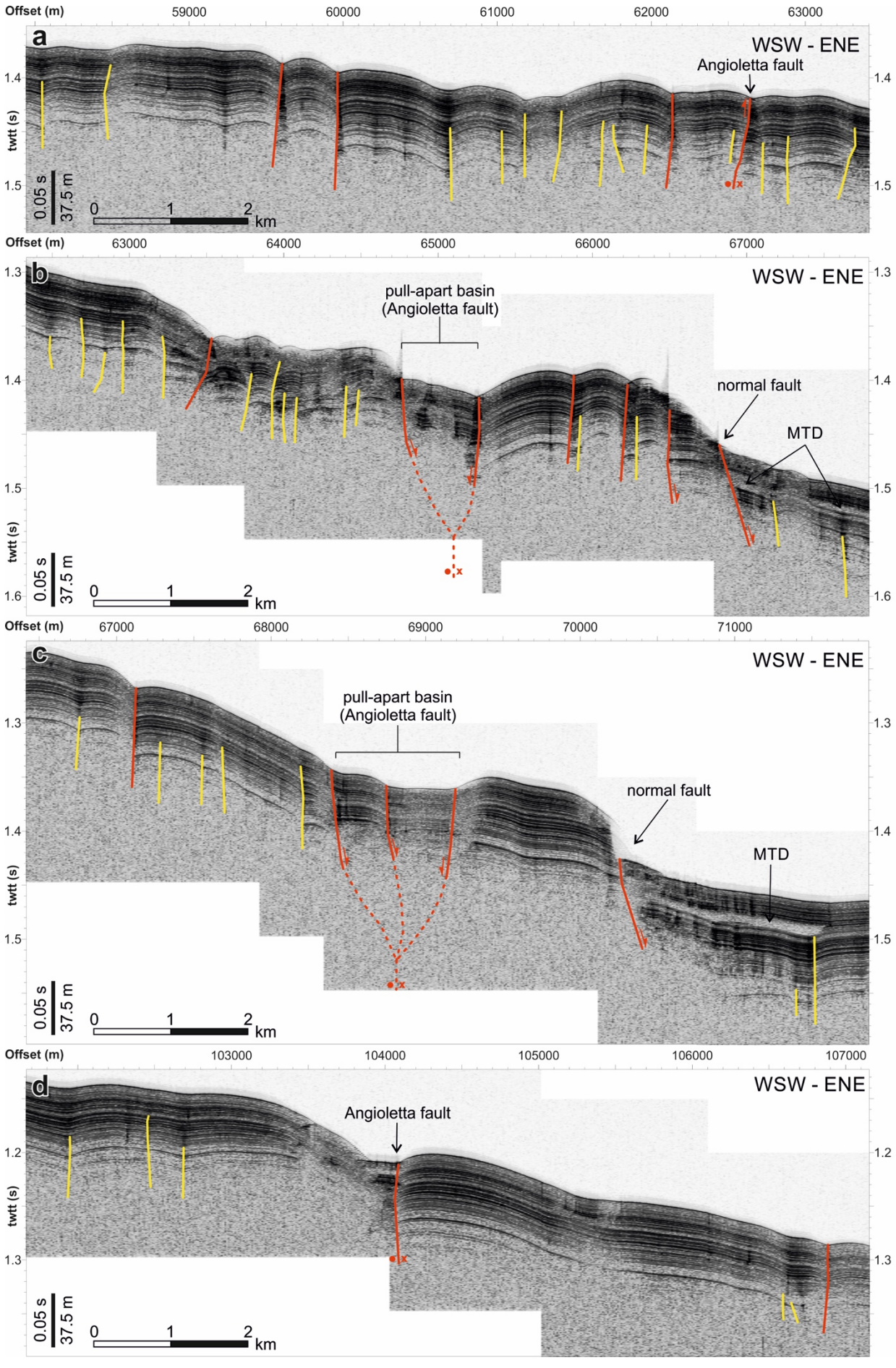
Offset (m)
59000
60000
61000
62000
63000
a
WSW - ENE
Angioletta fault
1.4
1.5
twtt (s)
0.05 s
37.5 m
0
1
2
km
Offset (m)
63000
64000
65000
66000
67000
b
WSW - ENE
pull-apart basin
(Angioletta fault)
normal fault
MTD
1.3
1.4
1.5
1.6
twtt (s)
0.05 s
37.5 m
0
1
2
km
Offset (m)
67000
68000
69000
70000
71000
c
WSW - ENE
pull-apart basin
(Angioletta fault)
normal fault
MTD
1.3
1.4
1.5
twtt (s)
0.05 s
37.5 m
0
1
2
km
Offset (m)
103000
104000
105000
106000
107000
d
WSW - ENE
Angioletta fault
1.2
1.3
twtt (s)
0.05 s
37.5 m
0
1
2
km

Figure 7.4. *TOPAS profiles showing the pull-apart basin of the Angioletta fault (a, b, c and d). Faults with seafloor rupture are represented in red colour, while Blind faults are shown in yellow. Location is shown in Figures 7.2 and 7.3.*

In the southernmost sector, faults with a N25º-N30º average trend occur across the Bizerte Ridge (Figures 7.2 and 7.3). In Figure 7.6 two TOPAS images show the main faults across the Bizerte Ridge, which do not cut the shallow-most sediments indicating that they may be secondary to deeper faults or have not been recently active. The deformation of the seafloor supports that some deep faults are active (e.g. reverse fault at offset ~12,500 in Figure 7.6.b). The main faults are associated to troughs in the bathymetry, but the steep walls of the fault scars prevent imaging of the termination of strata in the TOPAS profiles (main faults in Figure 7.6). The extension of the faults towards the north and south along flat seafloor supports that these troughs delineate the faults. The steepness of the faults indicates a predominant strike-slip motion, as in the northernmost areas. Comparatively fewer reverse and normal component faults occur. In general, all faults keep the trend observed in the north, with strike-slip faults changing slip component along-strike.

The Bizerte Ridge is probably the surface expression of a large anticline fold formed above a S- to SE-directed thrust of the set originally created within the early-middle Miocene north African belt of imbricated thrust sheets (discussed in Chapter 5). Its south-eastern flank displays onlap terminations and pinch-out geometries of the most recent sediment layers indicative of contemporaneous uplift supporting recent/ongoing fault activity (also discussed in Chapter 6). Images display tilted strata likely corresponding to the forelimb of the fold creating the Bizerte ridge (Figure 7.7). This structural configuration supports a S-verging thrust fault under the south-east flank of the Bizerte Ridge, that we name Hayat fault. The Hayat fault is a regional reverse blind fault that likely caused the uplift of the northern sector of the study region, possibly much of it related to the current NW-SE kinematics of the Central Mediterranean (discussed in Chapter 6). This fault is highly orthogonal with respect to the Nubia-Eurasia convergence vector so that its relief appears related to recent slip re-activation (Figure 7.2).

TOPAS images show slide scars, transparent-facies sediment packages, and tilted blocks indicative of mass transport deposits (MTD) along the depression (Figure 7.7), likely related to the uplift of the Bizerte ridge, and possibly also by the occurrence of minor reverse N-verging faults within basin G (Figure 7.7.a). TOPAS images also show that fault-related structure is more significant towards the east (Figure 7.7.a), supporting that the Hayat fault grows towards the west (Figure 7.7.b). Taking into account the seismostratigraphy in the Chapter 6 and assuming that the strata was originally deposited fundamentally with a sub-horizontal attitude, the current strata

geometry supports an uplift-rate estimated as ~ 0.24 mm/yr for the last 471 ky due to the slip of the Hayat reverse fault. Assuming a 45º dip for the Hayat fault this uplift-rate would correspond to 0.33 mm/yr slip-rate during the last 471 ky. This value is estimated from the strata geometrical relationship imaged on the TOPAS profile of Figure 7.7.a, thus in the western sector of the fault where the smaller offset occurs compared to the eastern segment, so that a larger slip-rate may be associated to the Hayat fault there.

Another important active feature in the North-eastern Domain corresponds to a fault system that bounds the basin H to the west (Figures 7.2 and 7.3). This system, with a NE-SW orientation, extends from the Sentinelle Valley in the north through the Bizerte Ridge in the south (Figures 7.2 and 7.3). The main structure of this system, named Valeria fault, cuts to the seafloor, generating a wide fold, which support recent activity (Figure 7.8). Seafloor morphology above the sub-vertical Valeria fault plane support that the fold is a pressure ridge formed by the interaction of Valeria fault with secondary faults. Valeria fault has a sub-vertical plane slightly dipping towards the east, with sediment layers thinning towards the fold indicating reverse slip on the fault (Figures 7.8). The activity of this fault system in the northern and southern sectors is not as clear because rougher topography, makes difficult to determine recent activity and slip component (as for faults in Figure 7.6). The S-shaped morphologies of the seafloor along the fault corridor (Figures 7.2 and 7.3) may indicate a sinistral strike-slip system, with changes in slip along-strike indicated by locally clear reverse slip (e.g. Figure 7.8).

Along Cornaglia slope (i.e. south and north as displayed in Figures 7.2 and 7.3) numerous faults follow a similar NE-SW main regional trend (Figures 7.2 and 7.3). The detailed trace of the faults is not evident due to slide scars carving the slope seafloor surface. These slide scars display a clear trend following the main NE-SW faulting trend that support that they initiate along the trace of faults. A profile along the south Cornaglia slope strike displays little faulting, slide scars and smooth strata geometry (Figure 7.9). The sub-vertical fault planes with small vertical offset, cutting the seafloor in some instances, support strike-slip fault kinematics.

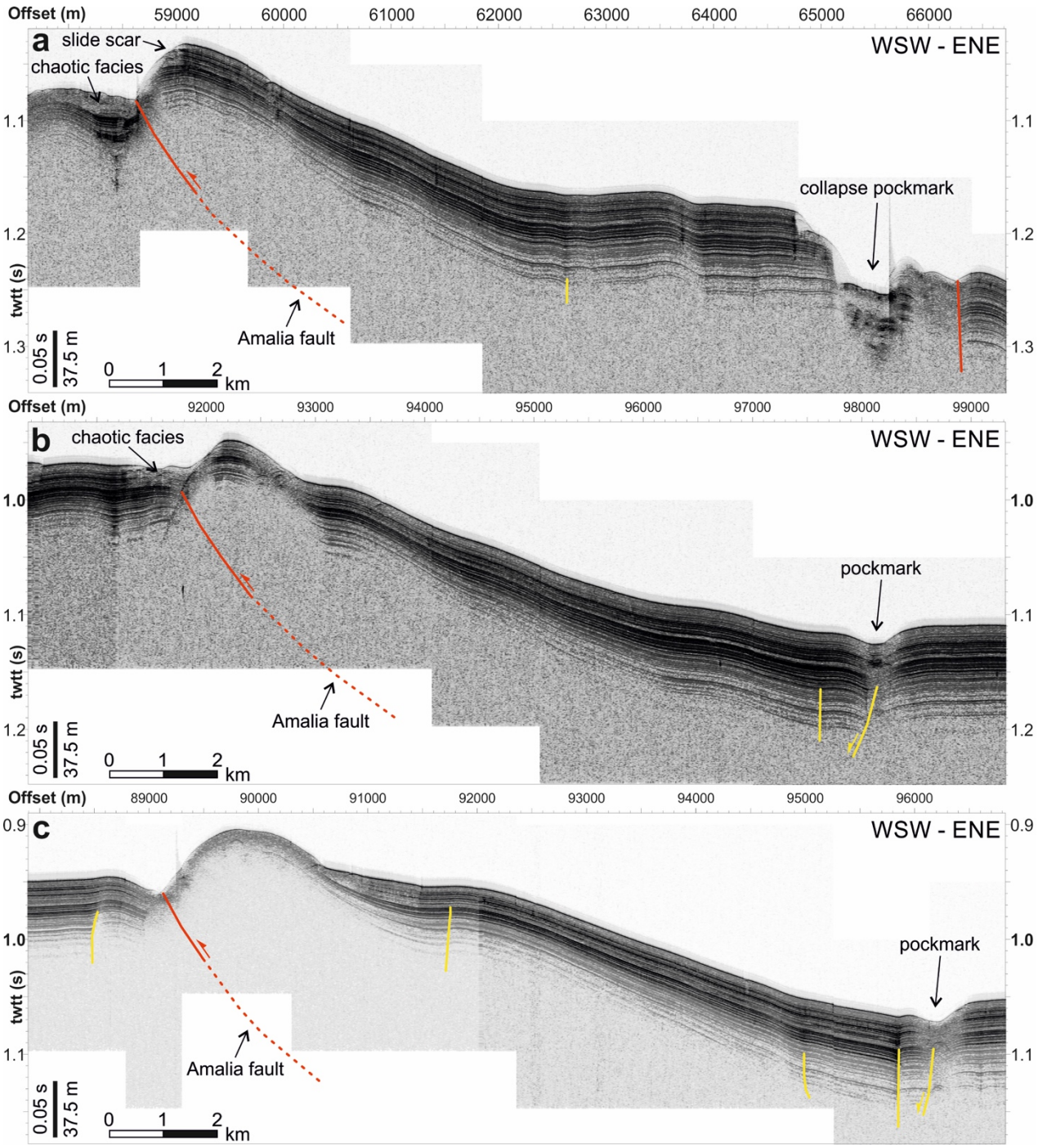

Figure 7.5. *Three parallel TOPAS profiles showing the Amalia active reverse fault (in red). Blind faults are shown in yellow colour. Location is shown in Figures 7.2 and 7.3.*

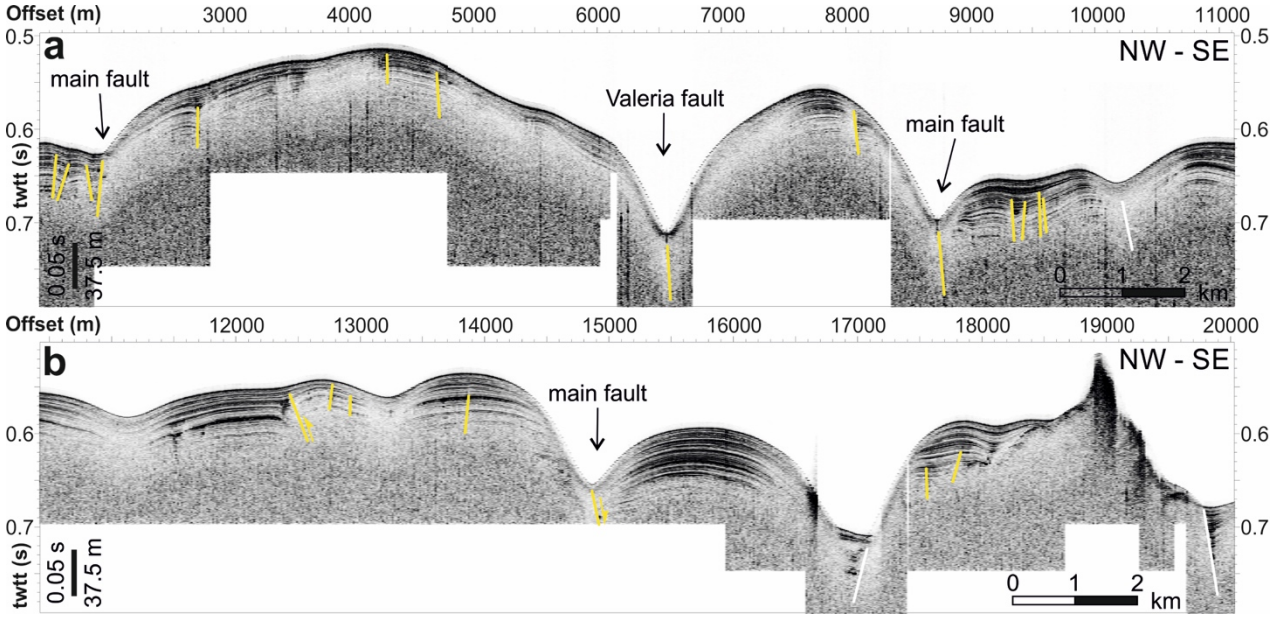

Figure 7.6. *TOPAS profiles showing Blind and Inferred faults (in yellow and white respectively) across the Bizerte Ridge (Valeria fault is depicted in a). Location is shown in Figures 7.2 and 7.3.*

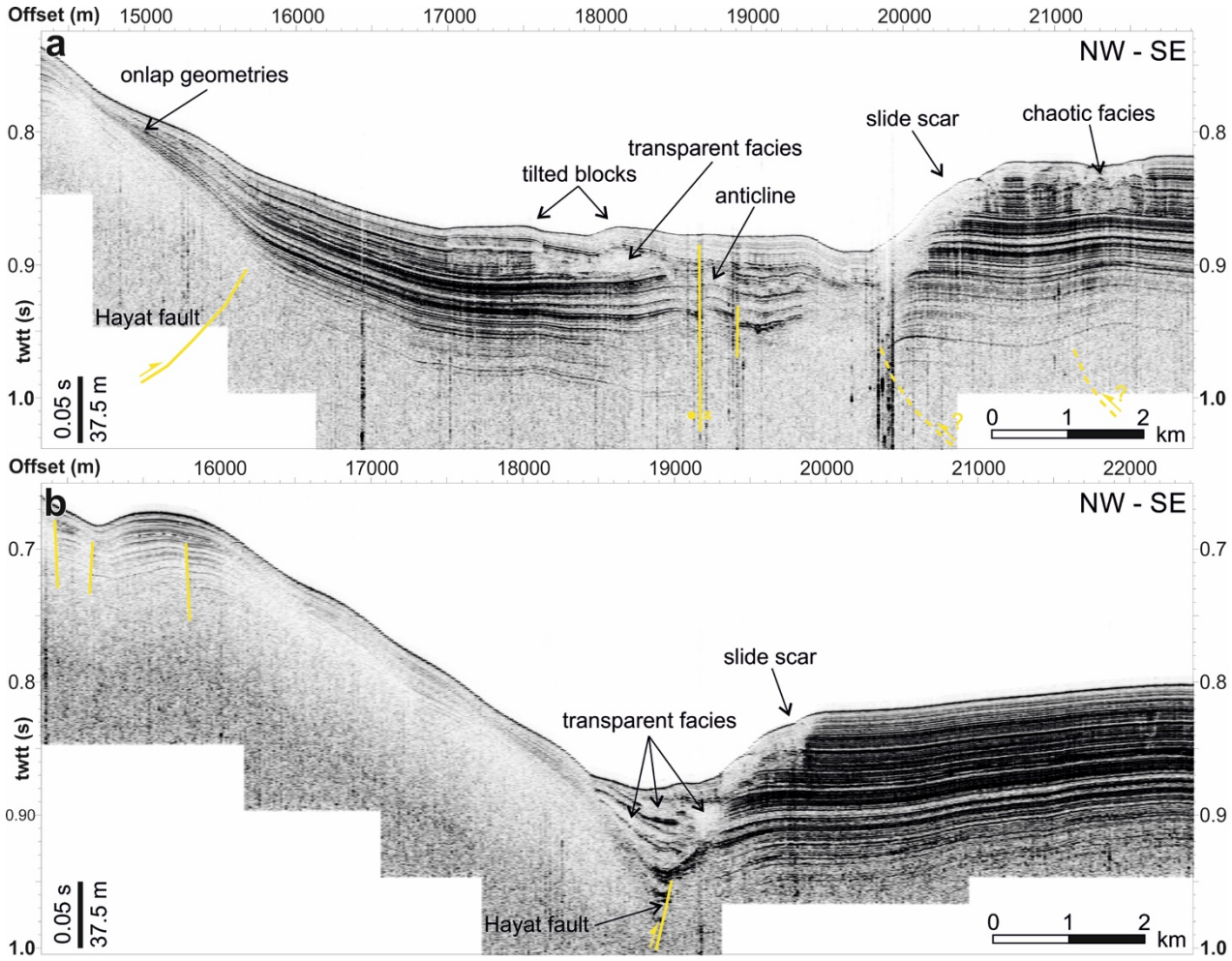

Figure 7.7. *TOPAS profiles showing the southeastern boundary of the Bizerte Ridge and Hayat fault-related features. Blind faults are represented in yellow colour. Transparent facies and slide scars are identified. Location of these profiles is shown in Figures 7.2 and 7.3.*

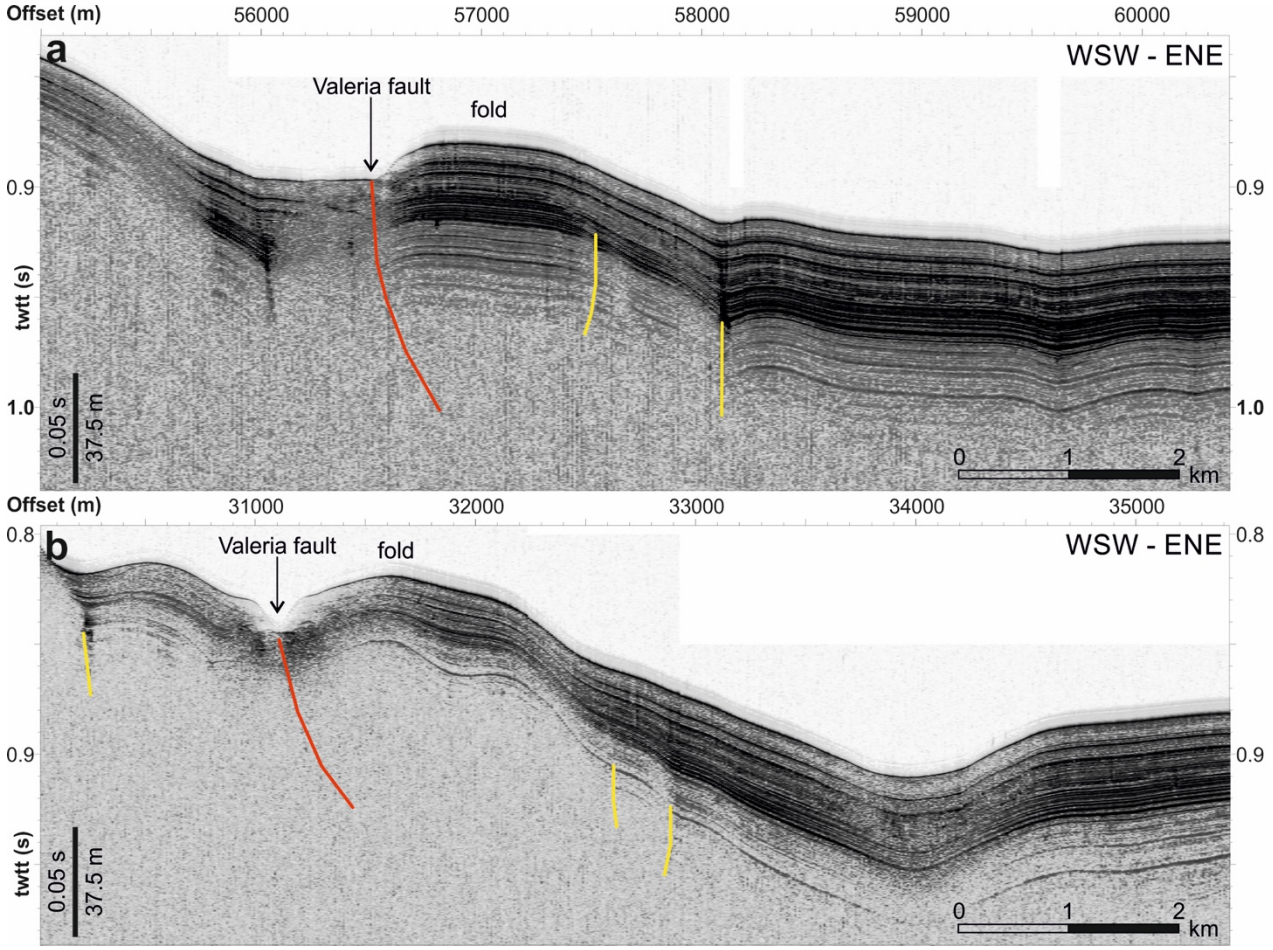

Figure 7.8. *TOPAS profiles showing the Valeria fault (i.e. the main fault of the NE-SW fault corridor). Lines location is shown in Figures 7.2 and 7.3.*

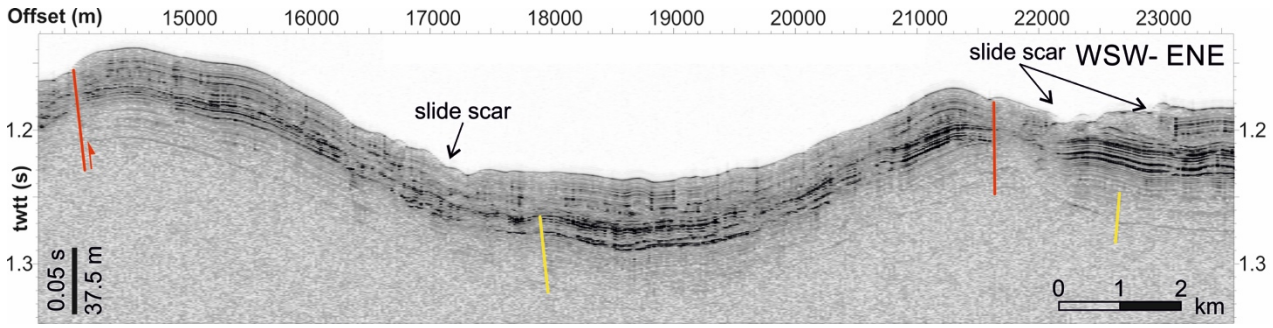

Figure 7.9. *TOPAS profile showing little faulting along the South Cornaglia slope. Several slide scars disturb otherwise regular sedimentary layering. Line location is shown in Figures 7.2 and 7.3.*

7.3.2. The Eastern Domain

The Eastern Domain seafloor displays few active fault traces compared to the North-eastern Domain. The fault lineaments forming elongated troughs containing pockmarks described in the North-eastern Domain do not have a clear continuation towards the south. Therefore, in the Eastern Domain mapping of tectonic structures imaged by TOPAS profiles is more challenging because their seafloor expression is comparatively subdued with no clear morphological expressions. Nevertheless, some recently active tectonic structures are recognized throughout the Eastern Domain, mainly following the regional NE-SW main trend.

A significant tectonic feature of the Eastern Domain is the extension in the south of the NE-SW fault corridor (Valeria fault system) described in Section 7.3.1. Across the northernmost sector of the Eastern Domain, this fault corridor changes from a NE-SW orientation to a N-S trend, delineating an S-shaped bathymetric high, that we name Snake Ridge (Figures 7.10 and 7.11). A significant normal fault, with conjugated faults and associated transparent deposits and tilted strata, delineates the eastern flank of this high (Figures 7.12.a and 7.12.b). The recent MTDs support the sudden slip of faults (see also Chapter 5). Nevertheless, although recent, the MTDs are covered by a thin undisturbed sediment veneer indicating some elapsed time since the last slip on the fault that caused sliding, or that the fault has not slipped since ~146 ky (age derived from the seismo-statigraphic study carried out in Chapter 6). Towards the south-west, the fault corridor may link to or dissect the Resgui Bank (Figures 7.10 and 7.11). Although the structure of the connection is not clear on TOPAS images, seafloor relief support the structural continuity. The S-shaped topographic high relief of the north-eastern sector of the Resgui Bank is similar to the NE-SW trending Snake Ridge described above (Figures 7.10 and 7.11).

The fault corridor continues south of the Resgui Bank, where MTDs along a NE-SW trending confined depression seems related to a NE-SW trending significant fault activity (Figures 7.12.c and 7.12.d). However, the images do not show cut strata so that we classify it as Inferred fault. The sinuous shape of the corridor within the Eastern Domain indicates a sinistral strike-slip component, similar to structures in the North-eastern Domain (Section 5.3.1).

A major tectonic feature of the Eastern Domain is the NE-SW Samia fault bounding to the east the basin F (Figure 7.10). The NW dipping Samia fault (discussed in Chapter 6) is imaged as a blind fault, but the transparent facies at the seafloor in places near the Samia fault support that is active or was very recently active (see Chapter 5 for images of MTDs).

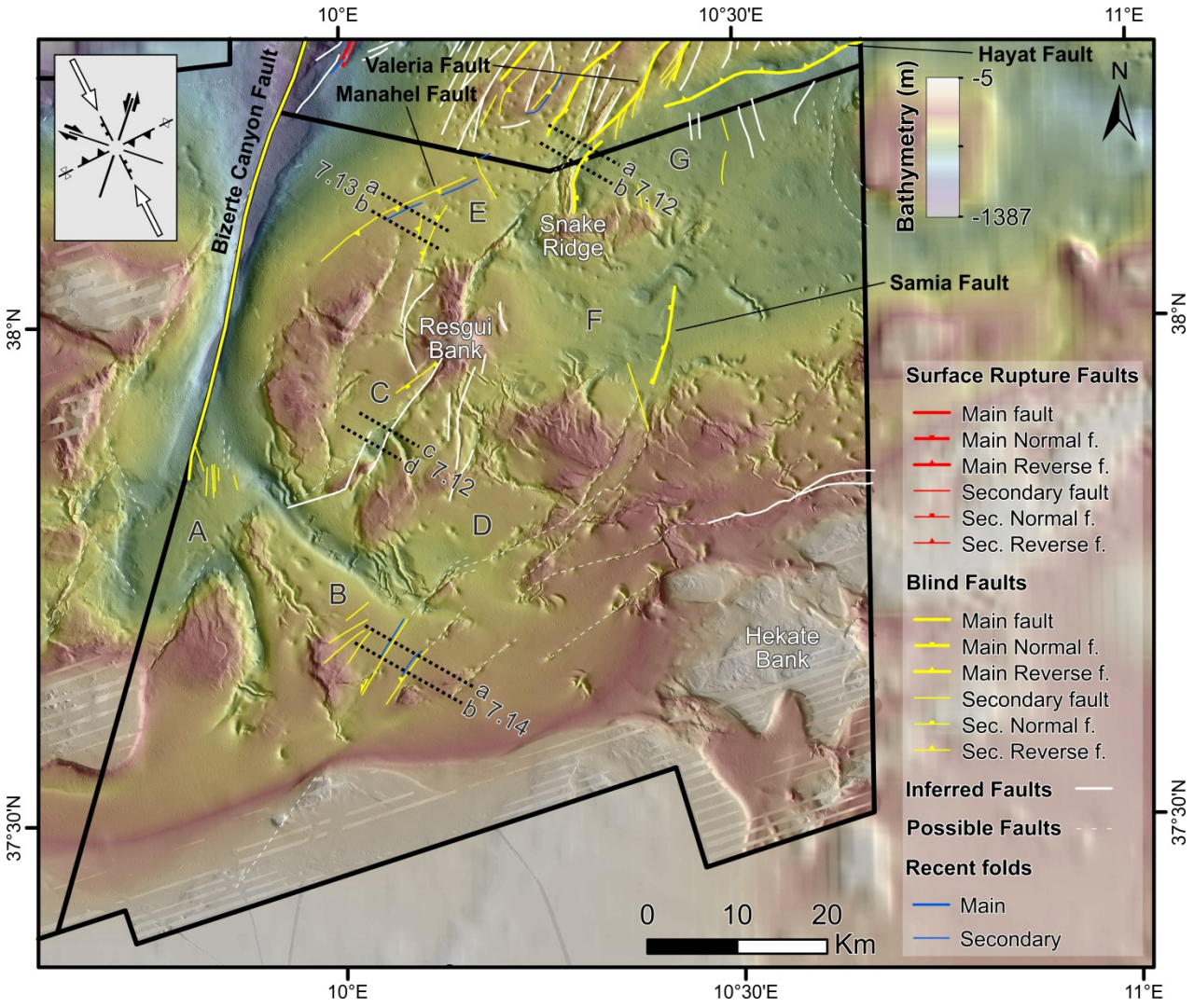

***Figure 7.10**. Framework of recent tectonics in the Eastern tectonic Domain (faults and folds). Location of TOPAS profiles is depicted by dashed black lines (Figures 7.12, 7.13 and 7.14).*

Recent fault activity has also occurred within basin E, where a major NE-SW trending fold generated by the slip of a reverse blind fault delineates the Manahel fault (Figures 7.10, 7.11 and 7.13). The Manahel reverse fault dips SE and uplifts the west-central sector of basin E shown by the pinching out of strata towards the fold (Figure 7.13). The thicker sedimentation of the basin center is deformed by back-thrusting, which seem to be largely currently inactive or strongly slowed down since ~1,116 ky (according to the seismo-stratigraphic study carried out in Chapter 6). The Manahel reverse fault strikes NE-SW, roughly perpendicular to the regional convergence vector between Nubia and Eurasia (Figure 7.2), while the associated faults are NNE-SSW, oblique oriented to the regional contractional direction.

Southward near the boundary with the Western Domain, around the head of the Bizerte Canyon faulting decreases (Figures 7.10 and 7.11). Here faults display a normal component and are

compatible with the N30ºW convergence between Nubia and Eurasia (Figure 7.2). The faults are likely related to the head of the Bizerte Canyon, which runs along a major NNE-SSW trending fault (Figure 7.10; see Chapter 5,), possibly active as indicated by strata offsets observed under the canyon in a 3.5 kHz profile (Maldonado and Stanley, 1976) (see Chapter 5 for further details). Although with normal displacement component, this main fault probably has a current left-lateral strike-slip component as displayed by other faults with the same NNE-SSW trend, thus oblique to the regional compressional vector (Figure 7.10). Compagnoni et al. (1989) based on multi-channel seismic data proposed a sinistral strike-slip component fault underlying Bizerte canyon.

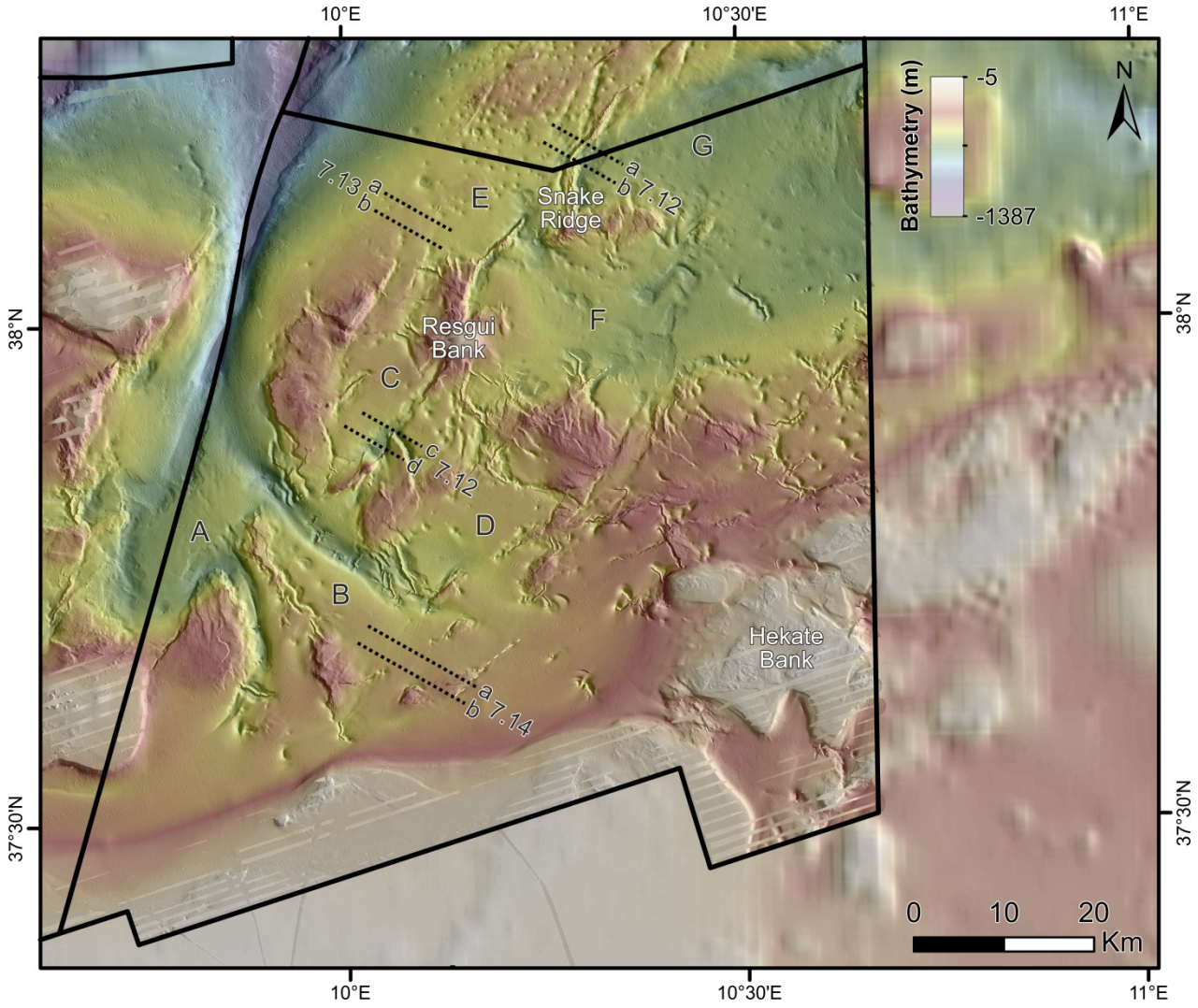

***Figure 7.11**. Coloured shaded relief map of the Eastern tectonic Domain. Location of TOPAS profiles is shown as dashed black lines (Figures 7.12, 7.13 and 7.14).*

NE-SW fault-controlled depocenters support some recent tectonic activity within basin B (see Chapter 6), in the southernmost sector of the Eastern Domain. Growth-strata thinning to the eastern sector of the basin and fold development support active uplift by reverse faulting (Figures 7.10, 7.11 and 7.14). The core of the fault-controlled active folds appears to contain old sediments folded

in a previous tectonic phase. The faults located within basin B, are sub-vertical and display little strata deformation, which supports a sinistral strike-slip faulting component within the regional N30ºW convergence (Figures 7.10 and 7.14).

Some Inferred and Possible E-W-trending faults occur in the south-eastern sector of the Eastern Domain, north of the Hecate bank, but their structure is poorly imaged in the data.

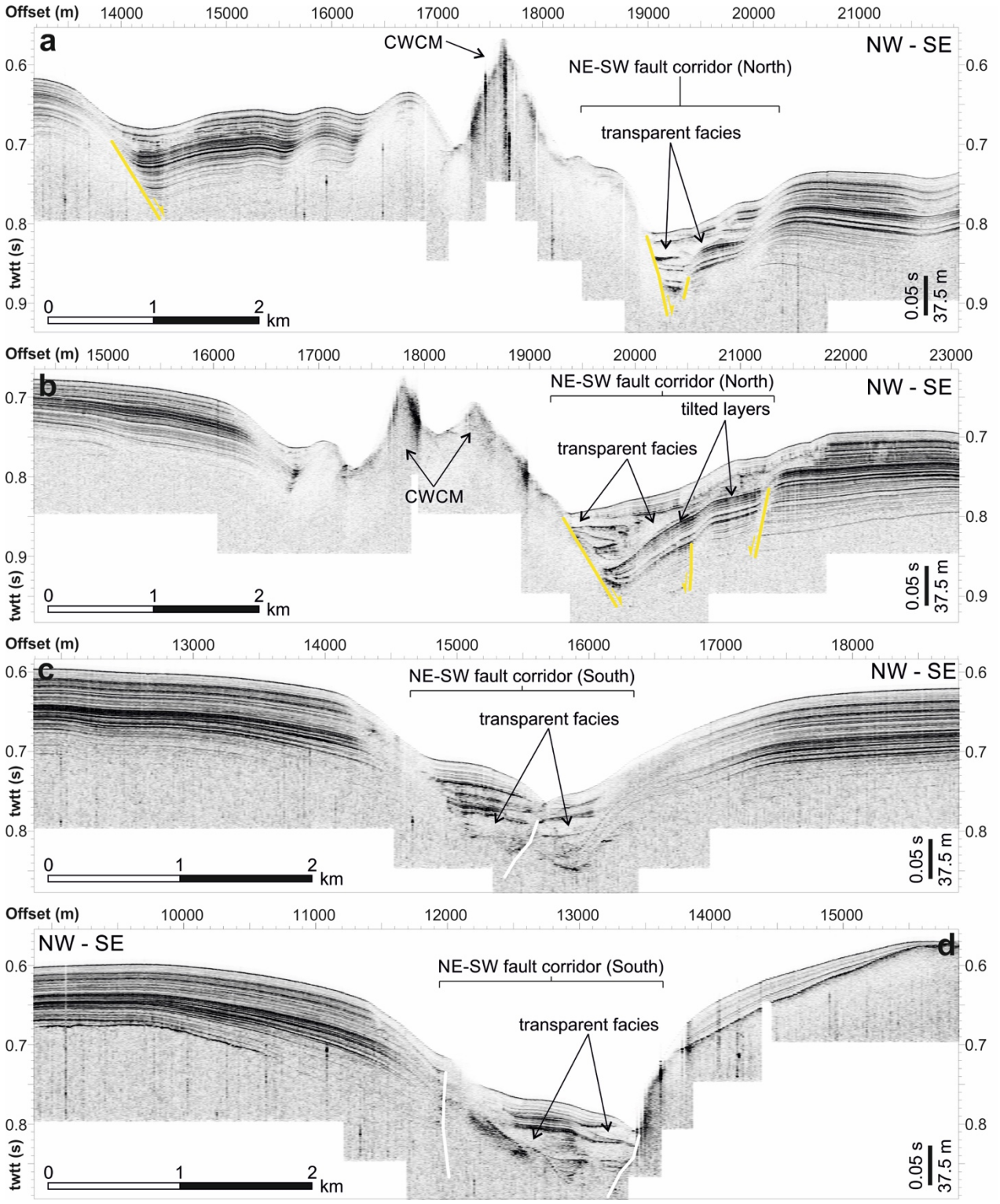

Figure 7.12. *TOPAS profiles showing the NE-SW corridor within the Eastern Domain. TOPAS profiles a) and b) showing the north-easternmost sector and c) and d) the south-westernmost one. Transparent facies correspond to MTDs. Layers tilted by faults are also depicted. In yellow colour are represented the Blind faults while in white are shown the Inferred faults. Location is shown in Figures 7.10 and 7.11.*

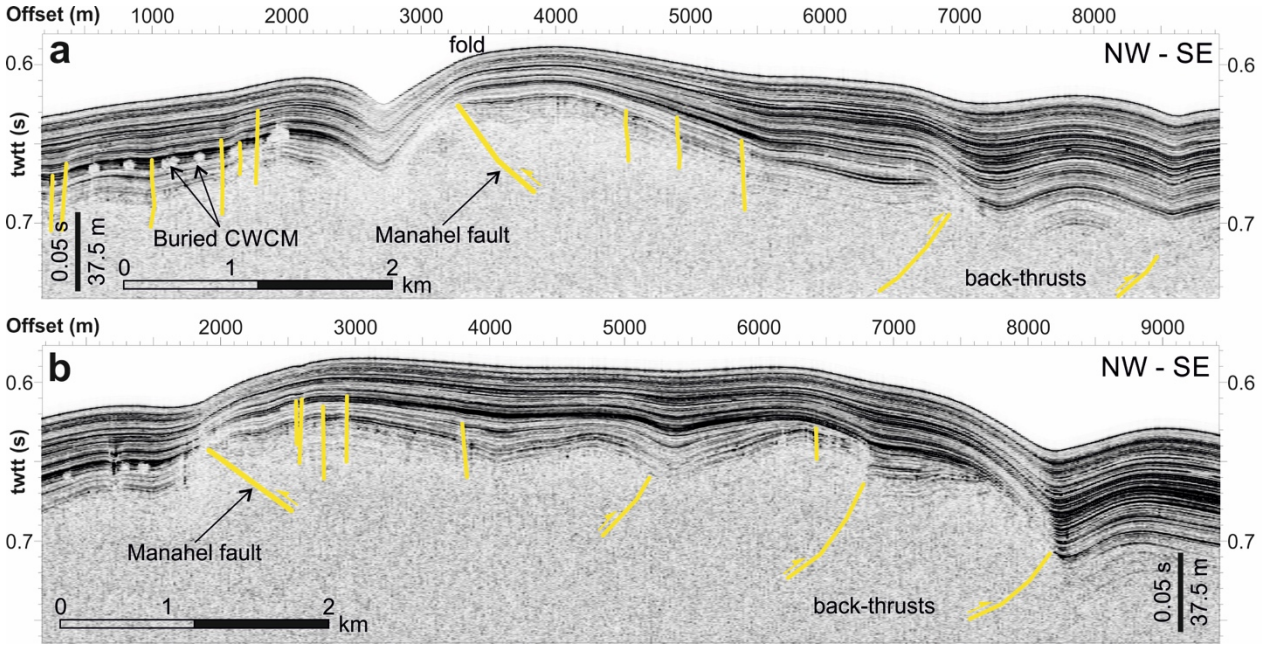

Figure 7.13. *TOPAS profiles showing the folding and Blind faulting within the basin E. The Manahel Blind reverse fault is depicted. Location is shown in Figures 7.10 and 7.11.*

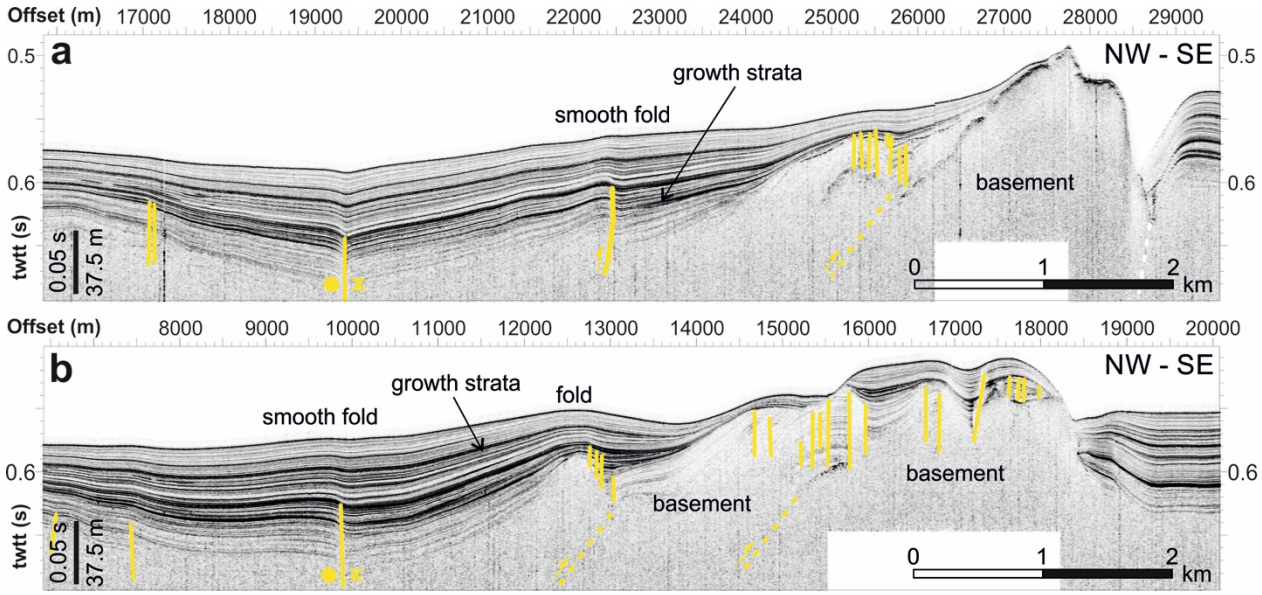

Figure 7.14. *TOPAS profiles showing the faulting within the basin B. Smooth folding and growth strata are identified. In yellow colour are represented the Blind faults while in white dashed lines are shown the Possible faults. Location is shown in Figures 7.10 and 7.11.*

7.3.3. The Western Domain

The Western Domain displays comparatively little evidence of tectonic activity, and we used only geomorphological features to interpret tectonic features because no TOPAS profiles were acquired in this region, so that mainly Possible faults are displayed (Figures 7.15 and 7.16). NE-SW trending lineaments to the NW of the Sentinelle Bank may be fault traces. These lineaments follow the NE-SW faulting trend of the main strike-slip faults in the other domains. The relief lineaments linking the eastern flank of the Sentinelle Bank to the Estafette Bank display the geometry of a potential system of fault traces following NE-SW and NW-SE trends, and might be related to the major fault under Bizerte Canyon.

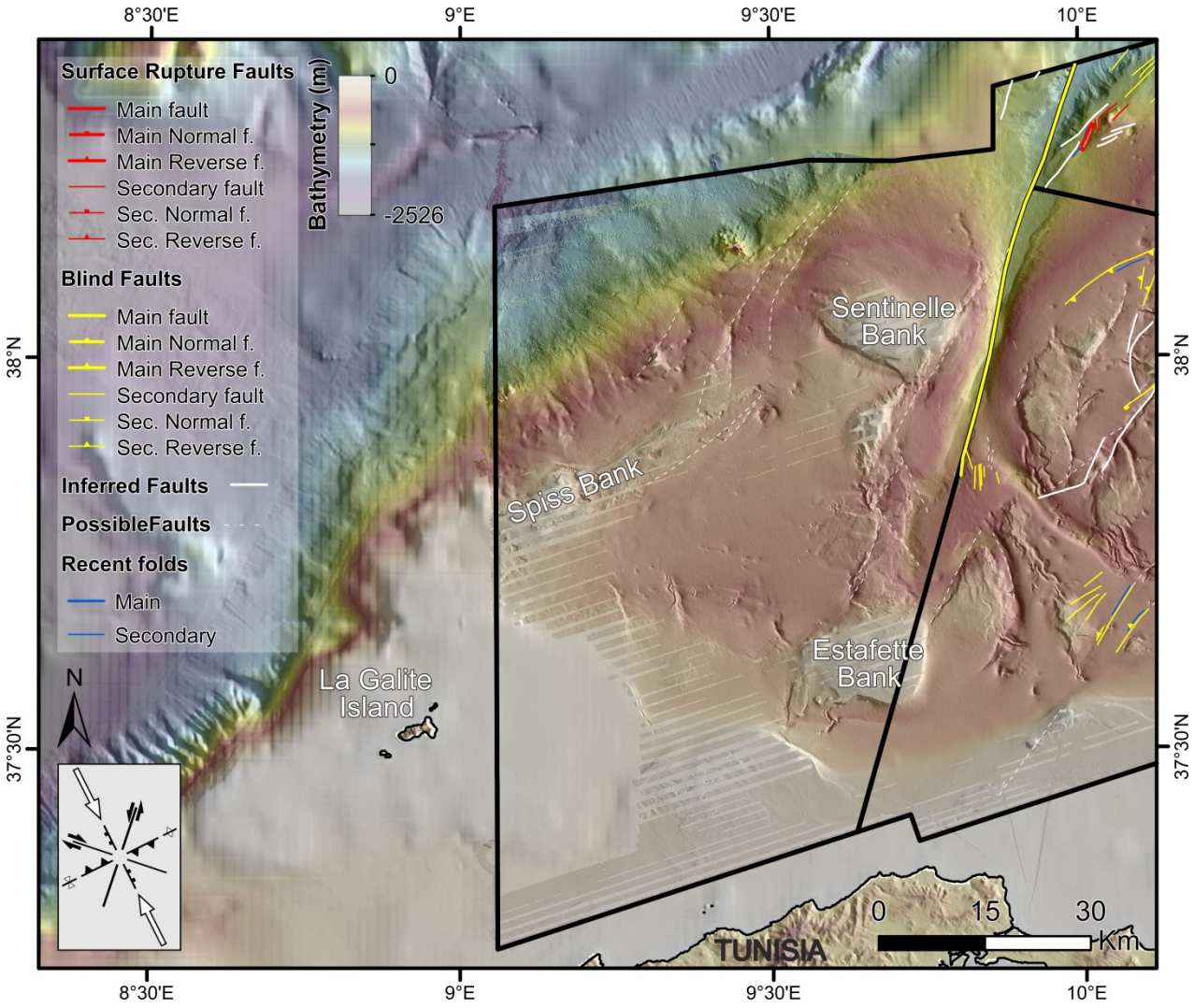

***Figure 7.15**. Framework of recent tectonic structures of the Western tectonic Domain.*

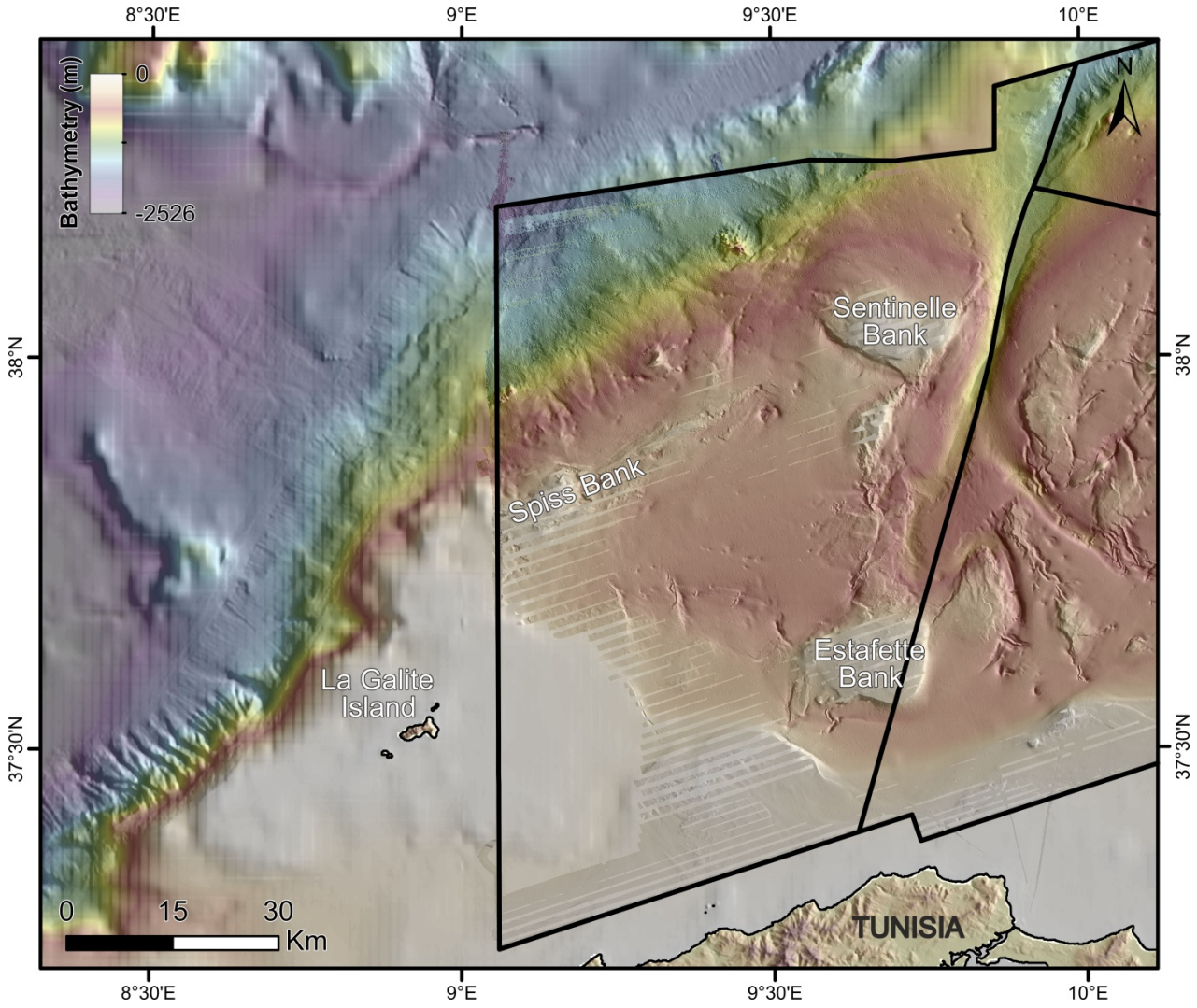

***Figure 7.16**. Colored shaded relief map of the Western tectonic Domain, with the main banks labeled (Spiss Bank, Sentinelle Bank and Estafette Bank).*

7.3.4. Seismic potential of active structures

As carried out in Chapter 4 for the onshore North Tunisian region, here we calculate the potential maximum moment magnitudes (M_w) for the offshore area. For this calculation we selected different fault segments of fault systems susceptible to rupture during a seismic event. This segmentation of the faulting is defined on the basis of geomorphological observations and tectonic evidence identified in TOPAS profiles. In order to calculate the maximum expected magnitudes, we selected the northern segment of the Amalia fault of Figure 7.5 and the entire Hayat fault of Figure 7.7. Both faults display the longer and best defined segments of reverse faults in the region and show evidences of recent tectonic activity (see Section 7.3.1). Although the Amalia fault shows evidence of potentially more recent activity, the highly perpendicular strike of the Hayat fault to the regional convergence vector (Figure 7.2) suggest a major seismic potential for the latter. Based on

empirical relationships the 10.7 km long segment of the Amalia fault might generate up to Mw ~6 (Wesnousky, 2008) to ~6.25 (Wells and Coppersmith, 1994) earthquake. The trace of the Hayat fault that runs within the study area has 23.46 km in length, being able to generate Mw ~6.6 (Wesnousky, 2008) to ~6.7 (Wells and Coppersmith, 1994) earthquake. Nevertheless, the structure associated to the Hayat fault appears to extend further east in the lower resolution bathymetry out of the mapped area (Figures 7.2 and 7.3). Interpreting that the Hayat fault may be ~39 to ~67 km long, and depending on that length, we estimate it could generate earthquakes Mw ~6.9 - ~7.10 (Wesnousky, 2008) or ~7.2 - ~7.54 (Wells and Coppersmith, 1994).

7.4. Discussion

7.4.1. Active Tectonic Structures

The map of recent tectonics (Figures 7.2, 7.10 and 7.15), shows that active faults (i.e. Surface Rupture Faults and Blind Faults, respectively) are mainly located within the eastern domains and particularly in the North-eastern Domain. Blind faults occur in both domains and Surface Rupture faults are largely restricted to the North-eastern Domain.

The North-eastern Domain shows most of the Blind and Surface Rupture faults within the study region with the latter being mainly located at the north-easternmost sector of this domain. Faulting within this domain trends mainly NE-SW forming small pull-apart basins of NNW-SSE *en-echelon* geometries, bounded by sub-vertical fault planes (Figures 7.2, 7.3 and 7.4) with a main oblique sinistral strike-slip component. Strike-slip faults tend to change orientation giving rise to pure normal or pure reverse component segments. The ENE-WSW trending faults typically have reverse component (Figures 7.2 and 7.3), while NNE-SSW trends dominantly have normal components (Figures 7.2 and 7.3). The ENE-WSW trends are perpendicular to the main convergence vector (i.e. rose diagram in Figure 7.2) while the NNE-SSW trends tend to be oblique to the convergence vector (Figure 7.2). These observations are consistent with the present-day plate convergence and the associated regional NW-SE contractional stress field (e.g. McClusky et al., 2003; Goes et al., 2004; Serpelloni et al., 2007), clearly displaying a transpressive regime. The North-eastern Domain, with most active faults, matches with the northern "recently" (since 402 ± 5 ky, see Chapter 6) uplifted area, which clearly shows that current tectonics focus on this North-eastern Domain. Faulting within this domain shows a preferential SE dip, except for faulting at the south-eastern boundary of the Bizerte Ridge (Hayat fault), which dips towards the NNW.

The Eastern Domain does not display Surface Rupture Faults and Blind Faults occur in a comparatively scattered and sparse distribution. The main fault trend is NE-SW direction similar to systems in the North-eastern Domain. Numerous faults have associated MTDs particularly in the main fault corridor (Figures 7.10, 7.11 and 7.12) and within basin F (Figures 7.10 and 7.11). Blind faults deforming the seafloor occur within basins E and B. Basin E faults display pure NE-SW reverse kinematics and NNE-SSW back-thrusts that match the regional stress field. In contrast, basin B contains strike-slip faults and some west-dipping reverse faults that uplift the eastern basin edge. Minor faults at the head of the Bizerte canyon seem to be related to the Bizerte Canyon underlying main fault, which may currently have a sinistral strike-slip component, matching the current N30ºW contractional regime (e.g. Serpelloni et al. 2007). In contrast to the North-eastern Domain where faulting generally dip towards the E or SE, in the Eastern Domain in addition to the E or SE dip, an opposite NW fault dip occurs (in basins F and B).

The relief map of Figures 7.2 and 7.3 show that the NE-SW trending faults of the North-eastern Domain extend north of our study area, into the Tyrrhenian Basin. NE-SW trending faults dipping preferentially towards the south-east, have been imaged along the south-western boundary of the Tyrrhenian Basin, across the north Sicily Margin (Guzman, 2015) (Figure 7.17). These faults form a horst and graben system related to the opening of the Tyrrhenian Basin. Most faults in the western sector of the MCS profile of Figure 7.17 (thus north of our study region) dip eastward, indicating that the shallow SE-dipping active faults identified in the North-eastern Domain and northern sector of the Eastern Domain might be related to extensional faults formed during slab rollback-related migration of the Apennines-Calabrian subduction front (Malinverno and Ryan, 1986; Trincardi and Zitellini, 1987; Mascle and Rehault, 1990; Faccena et al., 2001; Rosenbaum et al., 2002) formed ~8-6 Ma (Trincardi and Zitellini, 1987; Mascle and Rehault, 1990; Rosenbaum et al., 2002). These ancient Tyrrhenian faults are currently being inverted in a transpressional system in the frame of the present NW-SE convergence framework between the Nubia and Eurasian plates (Figure 7.2). Undifferentiated Plio-Quaternary minor phases of inversion and recent compressive folding have been described along the edge of the Tunisian plateau in the Sardinia Channel area (Tricart et al., 1990, 1994; Mascle et al., 2001, 2004).

The south Tyrrhenian active contractional belt north of Sicily (to the east of the North-eastern Domain) has an overall E-W trend, proposed to be segmented by a succession of ENE-WSW and NE-SW trending reverse faults, and NW-SE right-lateral strike- and oblique-slip faults from the analysis of seismological and structural data from coastal outcrops onshore (Billi et al., 2007) (Figure 7.18). Based on focal mechanisms, the ENE- to NE-striking faults are proposed to be high-

angle south verging faults interpreted to be either i) inherited low-angle thrust zones steepened by the emplacement (at their footwall) of foreland piggyback thrust sheets, or ii) inherited high-angle basin-bounding normal faults being currently inverted (Billi et al., 2007). The Hayat fault along the south-eastern flank of the Bizerte Ridge displays a pattern supporting the reactivation of an inherited NW-dipping fault with the stresses of the current NW-SE compressional setting of the Nubia-Eurasia convergence. Thus, the current convergence between Nubia and Eurasia possibly reactivates as strike slip transtensional or transpressional faults originally formed by the opening of the Tyrrhenian Basin (i.e. SE-dipping, NE-SW trending faults of the North-eastern Domain), and also reactivates older faults from the fold-and-thrust belt system formed in the African margin during the opening of the Algero-Balearic Basin at ~17-14 Ma (i.e. NW-dipping NE-SW trending faults of the North-eastern and Eastern domains).

The estimated ~0.33 mm/yr slip-rate for the Hayat fault during the last 471 ky is significantly larger than the slip of any other NE-SW reverse fault of the North-eastern Domain, that have smaller offsets. The highly orthogonal attitude of the Hayat fault with respect to the Nubia-Eurasia convergence vector and strongly tilted strata at the forelimb of the Bizerte Ridge suggests that Hayat fault is likely a major fault accommodating much of the convergence between plates in the studied region (Figure 7.2). Furthermore, the Hayat fault slip appears to control the topographic evolution of the northern sector, and is responsible of its uplift (discussed in Chapter 6).

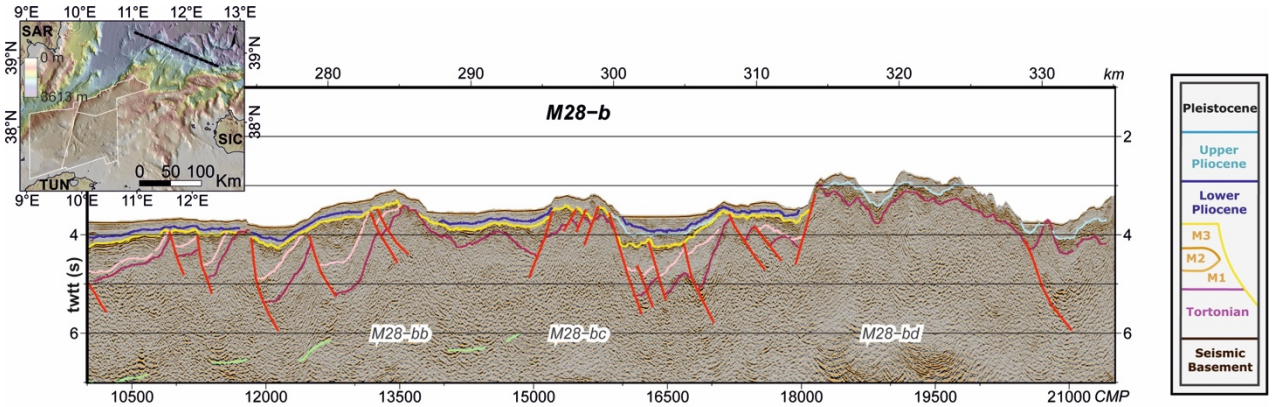

Figure 7.17. *Interpreted multi-channel seismic (MCS) profile across the North Sicily margin taken from Guzman (2015). Recent faults and seismo-stratigraphic sequence, from Pleistocene to Tortonian are depicted. Inset: Coloured bathymetric map of the North Tunisian Margin with the location of the MCS profile in a black line (TUN: Tunisia, SAR: Sardinia, SIC: Sicily).*

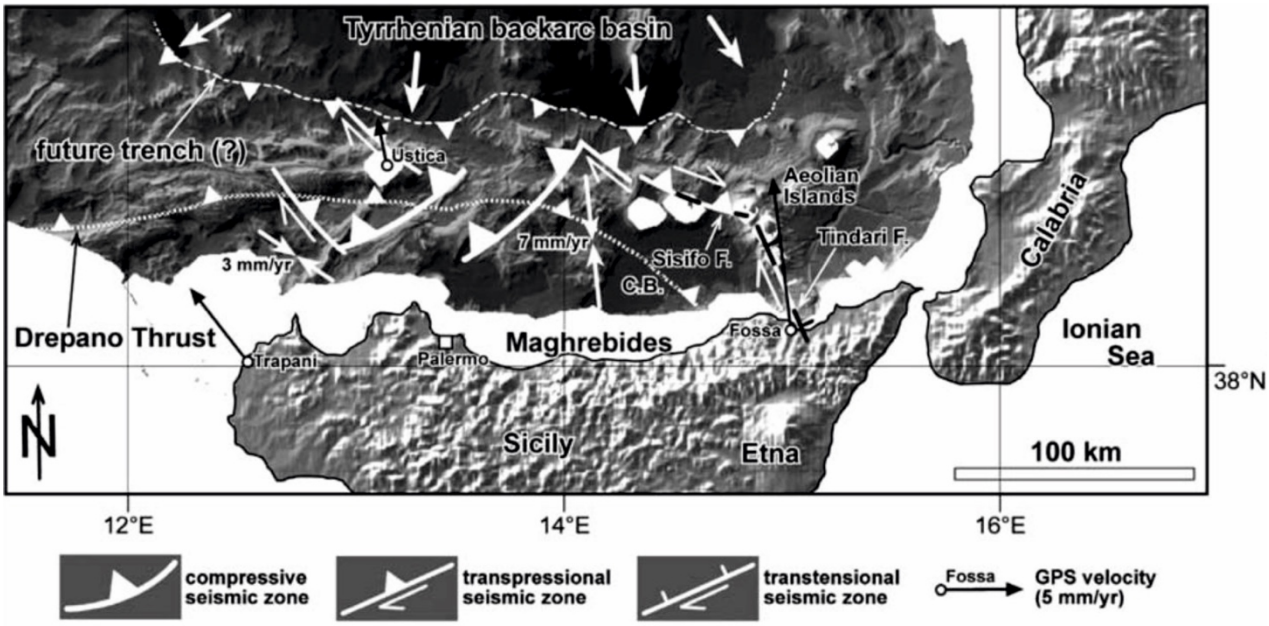

Figure 7.18. *Model showing the active tectonics of the south Tyrrhenian contractional seismic belt as proposed by Billi et al. (2007). The belt involves NE and NW trending faults. The NE trending faults are thrust faults, whereas the faults trending NW and WNW are interpreted as right-lateral strike-slip faults, which transfer the compressional displacements towards the southeast (Goes et al., 2004). Most seismogenic faults cut through the Oligocene age Drepano Thrust (Pepe et al., 2005). The kinematics of the south Tyrrhenian belt is consistent with GPS data (D'Agostino and Selvaggi, 2004). In particular, two pairs of converging white arrows with associated numerical values (i.e. 3 and 6 mm/yr) are representative of the direction and rate of tectonic convergence computed after the GPS velocity vectors from Fossa, Trapani and Ustica stations. A forthcoming evolution of this belt may involve the subduction of the Tyrrhenian oceanic lithosphere toward the south, underneath the Maghrebian fold-and-thrust belt. The trench may eventually develop at the back of the south Tyrrhenian seismic belt, as indicated in the Figure as potential future trench. C.B.: Cefalú Basin.*

The current pattern of deformation in the central Mediterranean Sea between the Nubia and Eurasian plates is ~5 mm/yr, with a NW-SE trending convergence (Figure 7.19) (McClusky et al., 2003; Goes et al., 2004; Serpelloni et al., 2007; Noquet, 2012; Palano et al., 2012). Several seismo-tectonic and GPS studies and different geodetic datasets support that east of our study region the total amount of convergence is currently being completely or largely absorbed across the southern Tyrrhenian seismic belt (Figure 7.19) (e.g. Agate et al., 2000; Hollenstein et al., 2003; D'Agostino and Selvaggi, 2004; Goes et al., 2004; Tondi et al., 2006; Serpelloni et al., 2007; Billi et al., 2011; Nocquet, 2012; Totaro et al., 2016). While to the west, along Algeria, it is estimated that ~2-3 mm/yr of convergence are currently accommodated in a narrow belt along the north-Algerian margin (Figure 7.19) (e.g. Meghraoui and Doumaz, 1996; Stich et al., 2006; Serpelloni et al., 2007). Although we have not estimated cumulative strain, it appears that a considerable amount of the total convergence is being accommodated within our study area (mainly by the Hayat fault). Serpelloni et al. (2007) noted that the residual shortening of the NW-ward 2.3 ± 0.5 mm/yr drift of Sicily has

to be accommodated northward, between Ustica (in NW Sicily) and the Corsica-Sardinia block, i.e. northeast of our study region. Due to the lack of instrumental seismic events along this region, Serpelloni et al. (2007) suggest that compression is probably transferred northwards, in Liguria, where active thrusting has been described (e.g. Larroque et al., 2001; Bigot-Cormier et al., 2004). Although part of the convergence may be absorbed in Liguria, our study reveals that part of the shortening is accommodated within our study region, mainly by the Hayat fault and across the North-eastern Domain sinistral fault system. The main NE-SW trending sinistral strike-slip system in a transpressive regime defined in our study area differs from the faulting in northern Sicily and Algeria. There, both areas display compressional regimes with prevailing thrust focal mechanisms (e.g. Serpelloni et al., 2007; Billi et al., 2011).

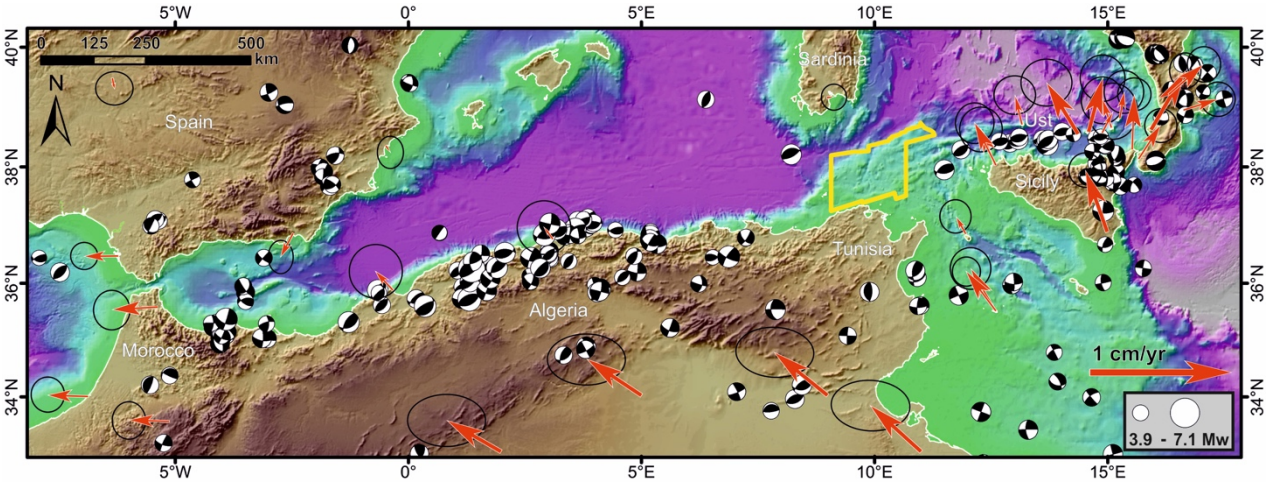

Figure 7.19. *Focal mechanism solutions of the western Mediterranean region. Data taken from the Global CMT catalog for the period between 1976 and 1996 (Global CMT, 2015) and the RCMT catalog between 1997 and 2015 (RCMT, 2015). Horizontal velocities (with 95% error ellipses) given with respect to the Eurasian plate (modified from Serpelloni et al. (2007)) along the Nubia-Eurasia boundary in western Mediterranean. The location of the study area is displayed by a yellow polygon. Ust = Ustica island.*

7.4.2. Faulting and seismic activity

The maximum magnitudes (M_w) of 6.25 to 7.54 (Wells and Coppersmith, 1994; Wesnousky, 2008) estimated for the reverse fault segments within the North-eastern Domain are moderate to large. As discussed in Chapter 4, although there are no slip-rate velocities for the faults, we speculate that return periods are long, of several hundreds to thousands of years, due to the slow convergence rate defined for our study area and distributed deformation (e.g. McClusky et al., 2003; Serpelloni et al., 2007; Noquet, 2012). No co-seismic major tsunami is expected due to the thin water layer, the faulting generally oblique strike-slip and the maximum magnitudes obtained (6.25

– 7.54 Mw) that are too weak to trigger significant tsunamis (Bryant, 2014). Furthermore, we interpret that the absence of significant instrumental seismicity for the study region could be induced by the fact that shortening is distributed along numerous small-scale faults, instead of being absorbed by a limited set of large faults capable of generating medium magnitude earthquakes on a regular basis. However, it must be kept in mind that our work offshore has only studied the seafloor and near surface expression of active faults, and that we do not have information on how these faults extend into deeper crustal layers. In particular, we do not know whether some of the fault segments identified in our maps merge at depth into larger structure. This scenario could imply seismogenic faults larger than those considered here, because inherited tectonic structures may be larger than their surface expression due to reactivation in a new stress field and with slip vector that are different to previous tectonic phases. Seismic data imaging the crustal-scale tectonic structure of the region are necessary to finalize hazard analysis of shallow faults that we have identified as currently re-activated structure.

7.5. In summary

The structural analysis carried out in this Chapter reveals a series of active faults defined for the first time in the explored area. Most Surface Rupture and Blind faults (i.e. active faults) are localized within the North-eastern Domain. These faults mostly are SE-dipping NE-SW trending faults possibly originally formed during the opening of the Tyrrhenian Basin (at ~8-6 Ma), and currently being reactivated with strike-slip displacement and inverted in compression by the current NW-SE contractional setting due to convergence of the Nubia and Eurasian plates. The kinematic indicators of the faults of the North-eastern Domain support a transpressional regime with a main sinistral strike-slip faulting style. NW-dipping NE-SW trending faults related to an older fold-thrust belt system, formed during the early-middle Miocene opening of the Algero-Balearic basin, have also been identified. Some of these faults are also being reactivated and display different fault kinematics, with some reverse faults that occur in basin B and normal faults in basin F. The most important structure is the Hayat fault, a major WSW-ENE reverse major fault located south of the Bizerte Ridge that is likely accommodating much of the convergence within the studied region. Hayat fault recent slip is also responsible of the uplift of the North-eastern Domain.

Active faulting within the study region appears to accommodate a significant part of the current NW-SE shortening in the Tunisia margin related to convergence between Nubia and Eurasian plates. Shortening in the study region appears widely distributed in a suite of relatively short faults

that may prevent generation of large magnitude earthquakes. Classical empirical relationships used to estimate the maximum magnitudes indicate that active faults in the area could generate up to Mw 7.54 earthquakes. This significant magnitude indicates a moderate seismic risk, particularly considering the long distance between earthquake sources and inhabited areas. Furthermore, no major tsunamis are expected in the study region, where water layer is thin, faulting is generally oblique strike-slip and estimated magnitudes (6.25 – 7.54 Mw) are weak to generate a large tsunami. However, the fault segments identified at the surface and shallow depth may link deeper into larger structures and deep seismic data should be collected and evaluated to better constrain the tectonic structure and hazard analysis of the region.

Part IV

DISCUSSION

CHAPTER 8

Discussion

The discussion chapter of this PhD Thesis aims at summarizing and integrating the different observations presented in chapters 4-7 and present them under the unifying framework of the Mediterranean geodynamic evolution since about middle Miocene. This chapter focuses further into the currently active tectonics and the present-day geodynamic setting of the Nubia-Eurasia boundary within Northern Tunisia. The multi-disciplinary approaches and multi-scale datasets used provide the information to jointly analyze recent tectonic structures onshore and offshore of the North Tunisian land and continental margin.

8.1. Active faulting in the North Tunisian land and continental margin

The morphometric analysis of relief data together with the complementary fieldwork carried out onshore North Tunisia revealed a sparse distribution of the active faulting with three different families of faults: a) NE-SW reverse-sinistral faults, b) WNW-ESE dextral faults, and c) NW-SE normal faults (Figure 8.1). The most frequent active fault families onshore Northern Tunisia is the NW-dipping NE-SW trending reverse-sinistral faults, which largely control the present-day relief evolution of the region. The most important reverse-sinistral active fault of this family is the El Alia-Teboursouk (ETF) fault that show a morphotectonic signature suggesting current tectonic activity (Figure 8.1). Moreover, fieldwork observations, such as Plio-Quaternary folded fluvial terraces verticalized by thrust faulting activity of the ETF fault support a recent activity. Furthermore, we interpret dextral WNW-ESE faults as conjugate to sinistral faults or as transfer segments of reverse faults. The Dkhila fault (DF) is one of these dextral WNW-ESE trending faults that also show evidence of recent activity in the field (Figure 8.1). Finally, NW-SE trending normal

faults currently associated to the development of small tilted basins also show morphotectonic signals evidencing recent activity (Figure 8.1).

The main faulting trend onshore extends offshore, and recent faulting within the whole plateau-slope system of the offshore North Tunisian margin shows a NE-SW trend. These NE-SW faults generally show oblique sinistral strike-slip components, although they may work as pure normal or pure reverse depending on their strike (i.e. ENE-WSW trending faults show reverse components while NNE-SSW show normal components). Sinistral strike-slip component is mainly observed in the North-eastern plateau-slope Domain (NE-domain in Figure 8.1), where sub-vertical fault planes bound small pull-apart basins showing NNW-SSE *en-echelon* geometries. The scattered pattern of the active faulting observed onshore Northern Tunisia is also maintained in the nearshore areas of the offshore study region, i.e. in the Eastern plateau-slope Domain (E-domain in Figure 8.1). The Eastern Domain contains sparse NE-SW trending active (blind) faults (Figure 8.1). This pattern changes northward, where most offshore recent faulting occurs. The North-eastern Domain contains most blind faults and all surface rupture faults identified offshore (Figure 8.1). The similar main NE-SW trends of onshore and offshore faulting are formed by fault systems dipping in different directions. The main NW-dipping fault system onshore Northern Tunisia appears to extend to the nearshore offshore area of the Eastern Domain (Figure 8.1). In contrast, the northern sector of the Eastern Domain NE-SW trending faults dip SE-wards (Figure 8.1). In the North-Eastern Domain, SE-dipping sub-vertical faults prevail, except for the Hayat fault (Figure 8.1).

The few previous studies of active faulting in North Tunisian support transpressive to compressive slip (e.g. Meghraoui and Pondrelli, 2012; Nocquet et al., 2012; Soumaya et al., 2015) concordant to the current NW-SE-trending compressive regime between the Nubian and Eurasian plates (e.g. McClusky et al., 2013; D'agostino and Selvaggi, 2004; Serpelloni et al, 2007; Noquet, 2012). Two faulting provinces are observed offshore in the study region: i) one restricted to the North-eastern Domain and the northernmost sector of the Eastern Domain (Figure 8.1), and ii) the rest of the Eastern domain, where faulting matches the pattern observed onshore. Thus, two major faulting systems emerge when analyzing the whole studied region (onshore and offshore):

i) The Northern system, which includes the North-eastern Domain and the northern sector of the Eastern Domain with several SE-dipping NE-SW trending faults that display oblique sinistral components (Figure 8.1).

ii) The Southern system, which includes most of the Eastern Domain and the onshore North Tunisian studied area. Active faulting here shows a more sparse distribution,

characterized by NW-dipping NE-SW trending faults with reverse to sinistral components (Figure 8.1).

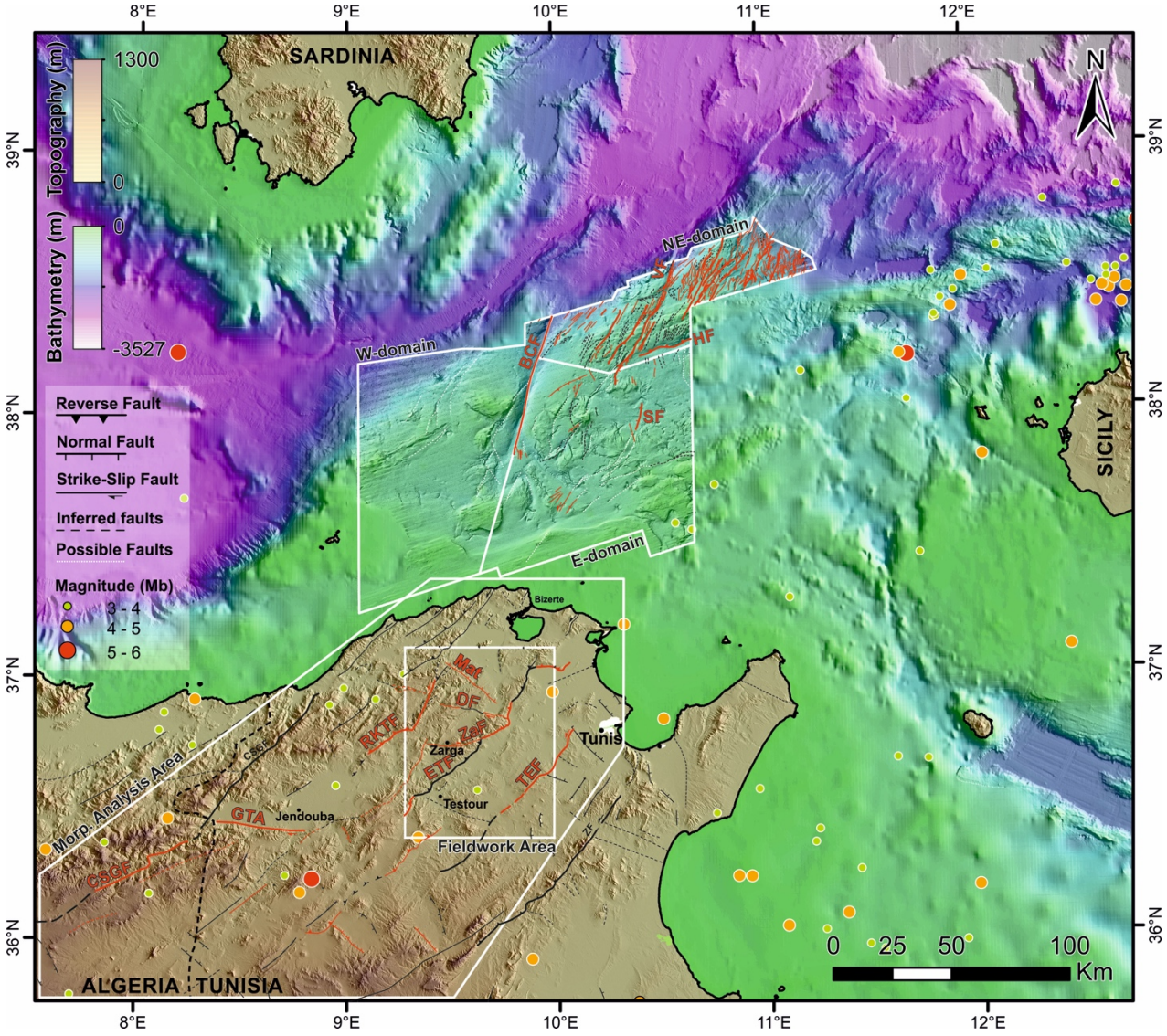

Figure 8.1. *Topography, bathymetry and active faults of the North Tunisian land and continental margin (red faults). Epicentres of magnitude M_b between 3 and 6 are from the International Seismological Centre (ISC, 2018). The location of the study areas (onshore and offshore) are represented by white polygons. The white rectangle depicts the fieldwork area. Dashed line depicts the boundary between Algeria and Tunisia. Tectonic structures onshore include data from Melki et al. (2012), Bahrouni et al. (2014) and Rabaute and Chamot-Rooke (2015), as well as our own field data. Mat: Mateur fault, Df: Dkhila fault, ZaF: Zarga fault, CSGF: Cap Serrat-Gardimaou fault, RKTF: Ral El Korane-Thibar fault, ETF: El Alia-Teboursouk fault, TEF: Tunis-Ellès fault, ZF: Zaghouan fault, GTA: Ghardimaou-Thibar accident, SF: Samia fault, HF: Hayat fault, VF: Valeria fault, BCF: Bizerte Canyon fault .*

The SE-dipping NE-SW trending faults of the Northern system correspond to extensional faults formed ~8-6 Ma related to slab rollback during migration of the Apennines-Calabrian subduction front (Malinverno and Ryan, 1986; Trincardi and Zitellini, 1987; Mascle and Rehault, 1990;

Faccena et al., 2001; Rosenbaum et al., 2002) and recently reactivated (see Chapter 7). In contrast, the NW-dipping NE-SW trending faults mainly grouped in the Southern group are older faults formed in early-middle Miocene during the development of the North Africa fold-and-thrust belt system, as a consequence of the collision between the Kabylides block onto Africa, and derived from the rollback of the Tunisian slab (e.g. Bracene and Frizon de Lamotte, 2002; Benaouali-Mebarek et al., 2006; Abbassene et al., 2016; Leprêtre et al., 2018) and recently reactivated. Thus, both fault systems appear to form on inherited structures formed by currently inactive geodynamic processes, and that have been reactivated with slip vectors related to the present-day stress field due to convergence between African and Nubian plates.

Long significant-magnitude earthquake recurrence periods are expected for the analysed faulting of the North Tunisian continental margin due to the low NW-SE convergence rate in the region (~0.5 cm/yr) (e.g. McClusky et al., 2003; Serpelloni et al., 2007; Noquet, 2012). This is also supported by the morphometric relief analysis onshore (i.e. low ksn values recorded in fault associated knickpoints). Regarding the magnitude of the expected seismic activity, instrumental measurements recorded low to moderate magnitude events (M_w 2 to 5.5) for the past century (Gueddiche et al., 1998; Ksentini and Romhdane, 2014). However, historical events describing the destruction of Roman and Arabic settlements evidence intensities between VIII to X on the MSK scale (e.g. Ambraseys, 1962; Vogt, 1993; Mejri et al., 2010; Bahrouni et al., 2014; Ksentini and Romhdane, 2014; Kharrat et al., 2018). Our fieldwork carried out in onshore Northern Tunisia discovered structures potentially linked to co-seismic effects, such as the open cracks located at the western segment of the Dkhila fault (Figure 8.1). Furthermore, in the offshore study region several mass transport deposits (MTDs) may be related to co-seismic deformation. The location of these MTDs in areas of smooth seafloor relief, in the vicinity of recently active faults support that significant seismic events occurred in the whole studied area. Sedimentary dikes along striated fault planes observed in the Corgnalia slope (Sicily Channel) might be related to Plio-Quaternary earthquakes (Mascle et al., 2004). Furthermore, several MTDs at the seafloor offshore Northern Tunisia also support significant recent seismic events.

Earthquake magnitudes have been estimated for a selection of significant faults in the studied region using empirical relationships (Wells and Coppersmith (1994); Wesnousky 2008). Onshore Northern Tunisia maximum M_w of 6.5 and 6.7 have been estimated for fault segments of potentially seismogenic faults identified in the field (i.e. the DF and ETF faults, respectively). Offshore, the northern segment of the Amalia fault and the entire Hayat fault have been evaluated (Figure 8.1). Maximum earthquake magnitudes of M_w 6.25 and 7.54 have been estimated for the Amalia and

Hayat faults respectively. These estimated magnitudes obtained onshore support a considerable seismic hazard in Northern Tunisia. However, long recurrence periods may lower the immediate hazard expected, taking into account the magnitudes obtained. Offshore, the largest potentially seismogenic fault is far from inhabited zones, which indicates a relatively low seismic risk. Furthermore, coseismic large tsunamis are not expected for the identified faults offshore, mainly due to shallow water and the moderate maximum magnitudes estimated (M_w 6.25 – 7.54) that are weak to generate significant, destructive tsunamis (Bryant, 2014). However, it must be kept in mind that our work offshore has only studied the surface and near surface expression of active faults and that we do not have information on how these faults extend into deeper crustal layers. In particular, some of the fault segments identified could merge at depth into larger structure, implying larger seismogenic faults than those considered here. Deep penetrating data of the region are necessary to finalize hazard analysis of faults that we have identified as currently re-activated structures.

8.2. Drainage reorganization in onshore Northern Tunisia and relationship to regional tectonics

Convergence in active collisional continental plate boundaries favours the development of transverse drainages that route sediments from the orogenic wedge towards the foreland basin system (DeCelles and Giles, 1996). In these orogenic regions, the interplay between active tectonic structures such as thrusts, antiformal folds or lateral ramps, greatly determine the geometry of the drainage pattern, especially the relationship between transverse and axial drainage systems (e.g. Hirst and Nichols, 1986; Burbank et al., 1996; Jones, 2004). The natural evolution of rivers draining mountain belts is to develop incipient axial drainages, parallel to local tectonic structures that progressively evolve to transverse drainages following the main topographic gradient in latter stages (Babault et al., 2012). It is well known that crustal thickening related to plate convergence and associated shortening structures, together with upper-mantle flow, produces a dynamic topography that influences the drainage systems in active plate boundaries (Braun, 2010; Husson et al., 2012). In fact, relative small-scale dynamic topography is especially important in regions with narrow underlying lithospheric slabs, like in the Western Mediterranean (e.g. Faccenna and Becker, 2010; Faccenna et al., 2014b; Petit et al., 2015; Booth-Rea et al., 2018; Spakman et al., 2018). Geodynamic mechanisms such as slab pull, slab tearing, slab dragging, slab delamination or flow in the upper mantle exert an important influence on local, crustal topography that can be largely independent of the crustal structure (e.g. Missenard et al., 2006; Gogus and Pysklywec, 2008; Mancilla et al., 2015; Spakman et al., 2018). Moreover, other factors such as lithology, inherited

geological features or fluvial captures can play an important role in drainage organization (e.g. Harvey and Wells, 1987; Stokes et al., 2008; Giaconia et al., 2012a).

The interaction between all these different factors can result in anomalous drainage patterns in respect to the direction of regional convergence. This might occur in Tunisia, where the main catchment draining the orogenic wedge is the Medjerda River, which runs NE-SW for 400 km from northern Algeria to the Gulf of Tunis, perpendicular to the regional NW-SE plate convergence (Figure 8.2). The NE Tunisia drainage network has basically two general river orientations (see Chapter 4): axial rivers striking NE-SW parallel to the compressional structures, and transverse channels striking NW-SE to NNW-SSE. The transverse channels of the eastern side of the Medjerda river present higher *ksn* trends, convex hypsometric curves and higher values of MaxC/MaxL (see Section 4.3 of Chapter 4 for further explanations), thus suggesting that the capture process is driven by the replacement of the axial drainage by a transverse one. This observation agrees with the expected behaviour in the normal evolution of a drainage network in a mature relief developed under a NW-SE compressional setting, where high structural reliefs and steep regional slopes favours the development of a transverse drainage system (Babault et al., 2012). However, the Medjerda River remains as the "main attractor" for the whole drainage system, despite maintaining a general trend parallel to the main structural relief, which can be considered as an anomalous flow in the described tectonic configuration. Moreover, the Medjerda River main channel is gaining area with respect to its subsidiaries by means of capturing processes towards the east (Chapter 4). One of these captures was clearly described by fieldwork near Zarga village, where the activity between the ETF, Zarga and Dkhila faults uplifted a block that resulted in the capture of the Tine River by the Medjerda main channel.

Although tectonic transport related to thrusting in Tunisia has been mainly towards southeast, the filtered topography map (Figure 8.2) shows a regional long-wave topographic-high that coincides with the southwest Atlassic front, along the boundary between the Sahara and Tunisian Atlas. This region is also characterized for its seismicity with dominant strike-slip focal mechanisms (Figure 8.2) and by the presence of active dextral WNW-ESE oriented faults, like the Gafsa fault (Ben Hassen et al., 2014). The high altitude within this region results in a general topographic gradient towards the northeast favouring the development of large axial catchments, such as the Medjerda River. The Medjerda River valley drains towards a general depression in the filtered topography (Figure 8.2). Onshore, palustrine environments and lakes with outlets towards the Sicily channel and the Gulf of Gabes characterize the coastal areas of this topographically depressed region. Considering the rather uniform crustal thickness of Tunisia in a NE-SW direction (Research

Group for Lithospheric Structure in Tunisia, 1992) it is possible that this topographic low region may be related to some dynamic topography effect. Actually, this topographically depressed area lies above the region where a slab body imaged in the Tunisian upper mantle would link with the African lithospheric mantle (Wortel and Spakman, 2000; Piromallo and Morelli, 2003; Fitchner and Villaseñor, 2015). Although the slab images in this region are poorly resolved by seismic tomography because of poor seismic ray coverage under Tunisia, independent active-source wide-angle seismic data show the presence of a reflector at the top of a high-velocity body at 87 km under this region (Research Group for Lithospheric Structure in Tunisia, 1992), which together with intermediate depth seismicity in the Sicily Channel (Chiarabba and Palano, 2017) supports the presence of a slab under Tunisian possibly connected with the African mantle lithosphere (Booth-Rea et al., 2018) (Figure 8.3). This slab may possibly link with the African lithosphere under the southernmost segment of the South Atlassic fault and under the North-South Axis, producing a dynamic topography in the form of a depression from the Gulf of Gabes towards the Sicily channel (Booth-Rea et al., 2018) (Figure 8.3). Thus, dynamic topography related to slab pull together with tectonic activity along the south Atlassic mountain front, are probably important factors determining the apparently anomalous longitudinal orientation of the Medjerda River. Uplift along the south Atlassic dextral transfer zone might also be related to upper-mantle flow through a Tunisian Atlas slab window between the Sahara and Tunisian Atlas (Figures 8.2 and 8.3). This boundary must have worked as a dextral STEP (Subduction-Transform Edge Propagator) boundary since the Middle Miocene, namely the Tunisian Atlas Transfer Fault (TATF in Figure 8.3).

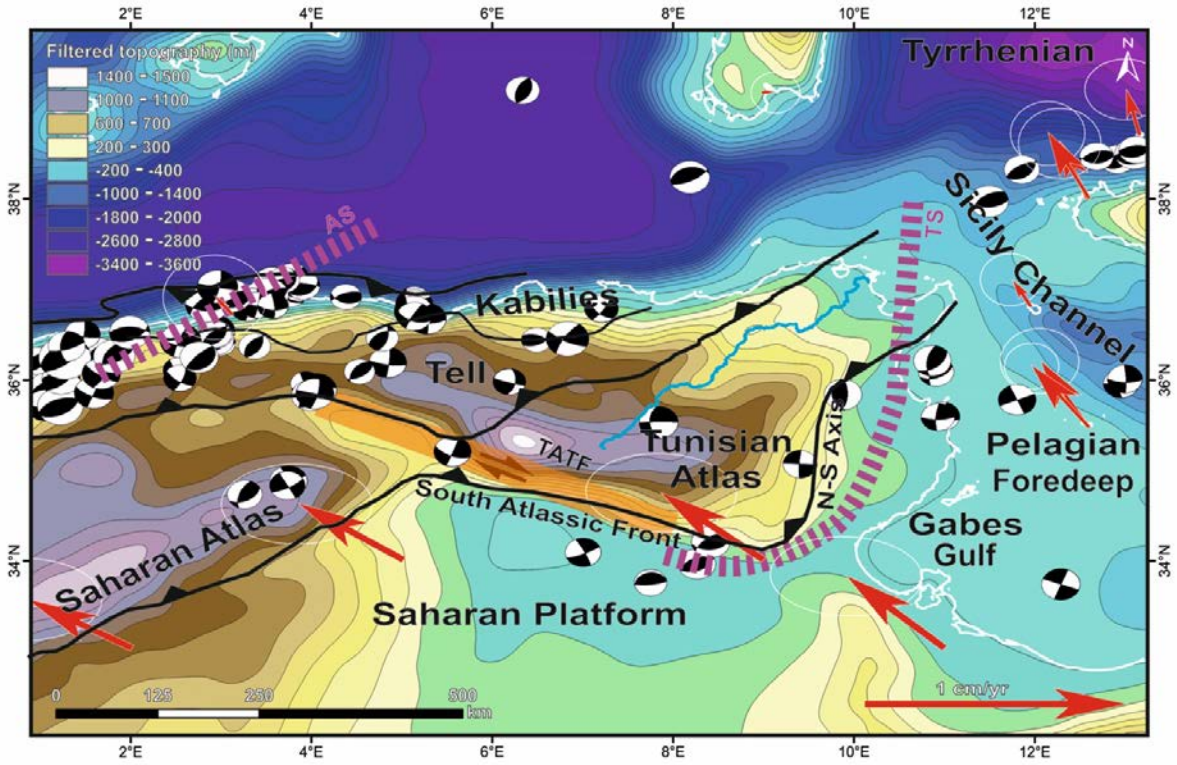

Figure 8.2. *Spatial distribution of moment tensor solutions and horizontal velocities (with 95% error ellipses) given with respect to the Eurasian plate (modified from Serpelloni et al, 2007), along the Nubia-Eurasia boundary in the western Mediterranean. Focal mechanisms are obtained from the Global CMT catalogue for the 1976-1996 period and from the European-Mediterranean RCMT catalogue for the 1997-2015 period. Focal mechanisms are plotted in the barycentre of the epicentres and weighted by earthquake magnitudes. The background shows a filtered topography (25 km radius mean filter) that highlights the regional topographic trends. Dashed purple lines depict the location of the slabs (AS: Algerian Slab, TS: Tunisian Slab).*

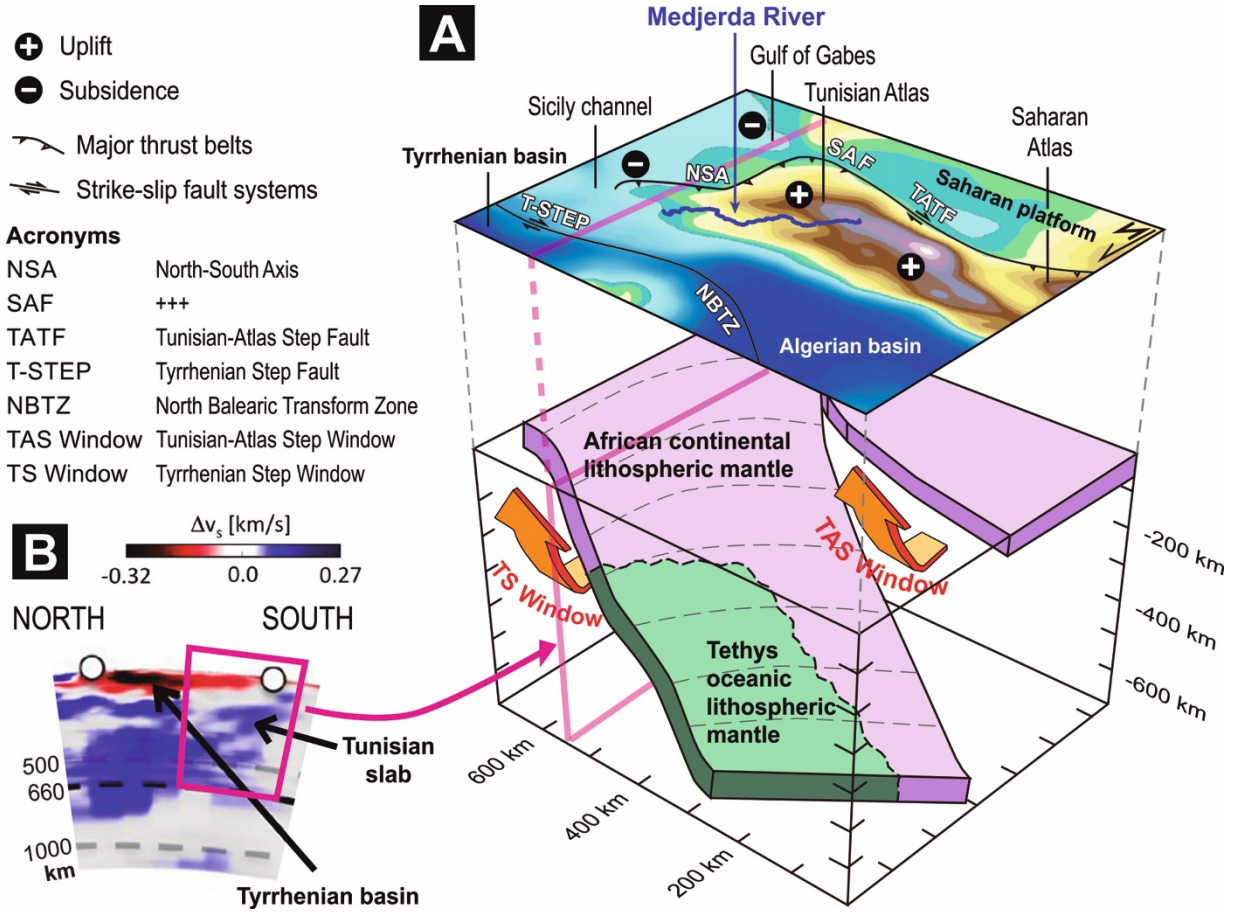

Figure 8.3. *3D-model of the tectonic setting and its influence on topography and drainage in Northern Tunisia (modified after Booth-Rea et al., 2018). A) Filtered topography showing the general topographic gradients in the region and their possible relation to the interplay between plate convergence and deep mantle processes. The Tunisian slab has been drawn, on the basis of the model proposed by Booth-Rea et al, (2018). Slab pull would drive negative buoyancy in the Sicily channel and the Gulf of Gabes, while positive uplift would occur above delaminated regions of Northern Tunisia in the headwaters of the Medjerda River, or related to transpressive tectonics along the Tunisian Atlas STEP boundary. Continental-mantle slab tearing along this STEP boundary developed the Tunisian Atlas Slab window (TAS). B) Tomographic profile crossing Northern Tunisia from South to North (extracted from Fichtner and Villaseñor, 2012).*

8.3. North Tunisia in the current Western Africa-Eurasia plate boundary setting

Most of the shallow (<30 km deep) teleseismic seismicity in the western Mediterranean is related to the NW-SE convergence between Nubia and Eurasia plates, which is causing the tectonic inversion of the western Mediterranean basins. In turn, this inversion is also causing the formation of a new crustal-scale shear zone boundary between Nubia and Eurasia that in the Maghreb region occurs along the southern margin of the Algero-balearic Basin (Billi et al., 2011; Giaconia et al., 2015). Reverse N-verging blind faults along the central Algerian offshore margin may evidence

ongoing underthrusting of the Neogene oceanic domain (Déverchère et al., 2005) probably marking the onset of a new subduction zone (Auzende et al., 1975). Fault inversion along the North Algerian margin has been reported by many authors (e.g. Domzig et al., 2006; Kherroubi et al., 2009; Yelles et al., 2009; Strzerzynski et al., 2010, Maouche et al., 2011; Bouyahiaoui et al., 2015), and it is supported by the instrumental seismicity recorded along a narrow belt parallel to the Algerian coast (e.g. Serpelloni et al., 2007; Beghoul et al., 2009; Meghraoui and Pondrelli, 2012; Nocquet, 2012). Eastward, seismicity becomes sparser and covers a broad region extending towards the south when approaching Tunisia (e.g. Nocquet, 2012). In fact, from easternmost Algeria to Tunisia main seismicity concentrates along the south Atlas front, where strike-slip focal mechanisms occur along the front, while reverse mechanisms have been recorded to the SE, along the boundary between the Tunisian and Saharan Atlas (Soumaya et al., 2015; 2018) (Figure 8.4). This pattern of seismicity delineates the deformation front probably related to the NW-SE plates convergence and the geometry and dynamics of the slab underlying Tunisia. This may be still linked to Africa lithosphere under the Tunisian Atlas segment (Fichtner and Villaseñor, 2015) where the Atlas deformation region widens (Figure 8.4). The displacement towards the south of the south Atlassic thrust front from SE Algeria to Tunisia occurs above the edge of the slab segment that may be still attached to the African lithosphere (Figure 8.3). This boundary between the Tunisian and Saharan Atlas works as a dextral STEP fault boundary, represented at the surface by ~NW-SE-oriented dextral strike-slip structures like the Gafsa fault that produce a strip of seismicity with strike-slip focal mechanisms (Figure 8.2).

Even though the location of the deformation fronts may be driven by a narrow segment of the underlying slab, the broadening of the deformation region from East Algeria to Tunisia may be related to the Africa-Western Mediterranean crustal and lithospheric structure. In most of Algeria the location of recorded seismicity is narrow and roughly maps the transition from the thick African lithosphere to the thinner Algerian Basin Miocene oceanic-type lithosphere (e.g. Serpelloni et al., 2007; Beghoul et al., 2009; Meghraoui and Pondrelli, 2012; Nocquet, 2012). In contrast, the displacement towards the south of the deformation together with the broad seismicity band occurring in Tunisia might be related to the fact that the north African lithosphere converging to the NW is encountering the continental lithosphere of Sardinia-Corsica, and not a thin oceanic plate (Soumaya et al., 2015). Northern Sicily is relatively similar to Algeria in that it shows a well-defined seismicity band that occurs near the boundary between the continental and proto-oceanic crust of the Tyrrhenian Basin (Prada et al., 2014). The reactivation of the northern Sicily margin has been already described, although it seems to be in a comparatively earlier stage of contraction (e.g. Billi

et al., 2007, 2011; Pierdominici and Heidbach, 2012; Presti et al., 2013). Tunisia, in contrast, has an extended continental shelf made of continental crust that connects with the continental crust of Sardinia. This configuration may promote the formation of a broad diffuse deformation zone in Tunisia, in comparison to the neighbouring regions where two crustal domain contrast in thickness and rheology. This proposal is in agreement with the widespread instrumental seismicity compared to the narrow seismic belts of Northern Algeria and North Sicily (e.g. Serpelloni et al., 2007; Beghoul et al., 2009; Meghraoui and Pondrelli, 2012; Nocquet, 2012).

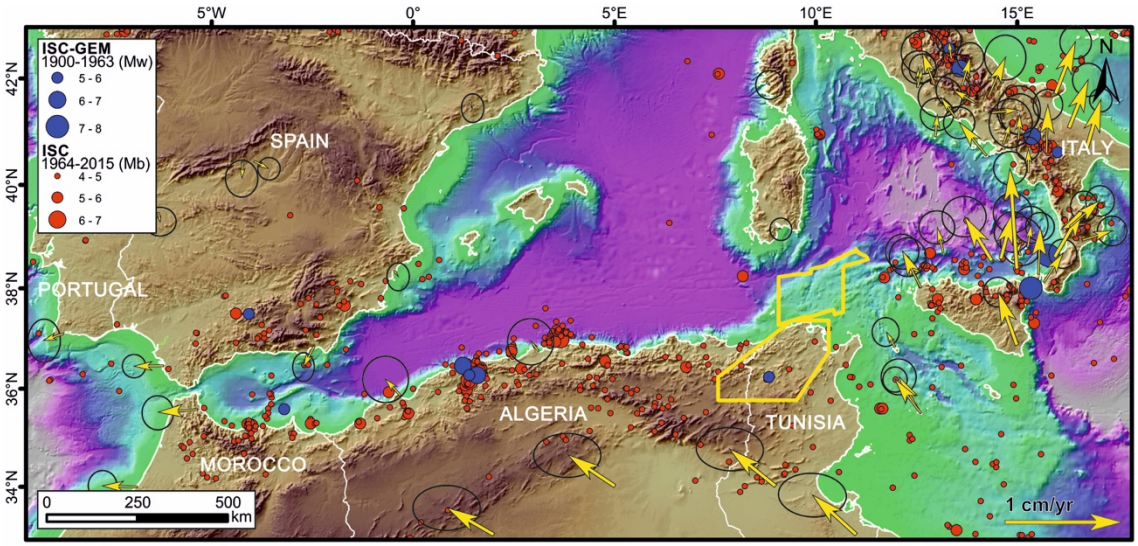

Figure 8.4. *Seismicity distribution and present-day GPS motions of the western Mediterranean region. Blue circles are from the ISC-GEM catalogue (ISC-GEM, 2018) and red circles from the ISC (ISC, 2018). The yellow polygons show the location of the study areas (onshore and offshore). Yellow arrows depict horizontal velocities (with 95% error ellipses) given with respect to the Eurasian plate (modified from Serpelloni et al, 2007), along the Nubia Eurasia boundary in the western Mediterranean.*

8.4. Geodynamic evolution of Northern Tunisia

Most models proposed for the geodynamic evolution of the Western Mediterranean consider slab-rollback the main driving force for the opening of the Western Mediterranean basins (e.g. Rehault et al., 1984; Faccenna et al., 2004; Schettino and Turco, 2006; Jolivet et al., 2009; Carminati et al., 2012; Faccenna et al., 2014a). Although models agree in the driving force, there are two different proposal: i) Models considering a continuous and unique slab running from the northern Apennines to the Alboran region (e.g. Rehault et al., 1984; Faccenna et al., 2004; Schettino and Turco, 2006; Jolivet et al., 2009; Carminati et al., 2012; Faccenna et al., 2014a) (Figure 8.5), and ii) Models considering a segmented slab with different geodynamic evolution for each segment depending on regional stresses (e.g. Wortel and Spakman, 2000; Spakman and Wortel, 2004;

Vergés and Fernàndez, 2012; Chertova et al., 2014; van Hinsbergen et al., 2014; Spakman et al., 2018) (Figure 8.6). Most of these geodynamic models consider that subduction is still accommodating much of the NW-SE trending Nubia-Eurasia convergence at present (Figure 8.5.f), particularly that the Tyrrhenian subduction roll-back is still active, and that reactivation in compression of inherited faults is only local (e.g. S-dipping thrust front in offshore Northern Africa in Figure 8.6).

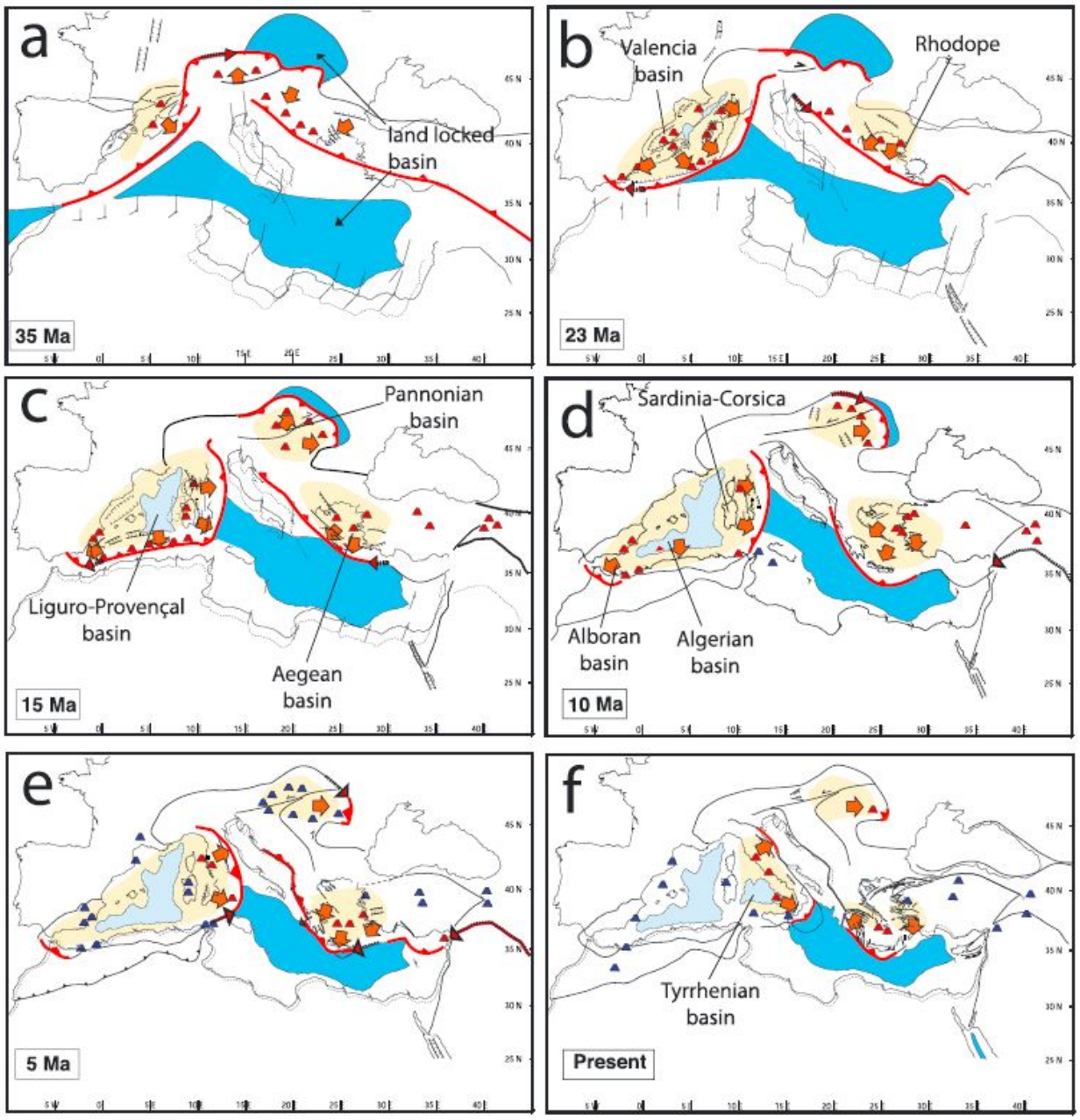

Figure 8.5. *Geodynamic evolution of the Mediterranean region. Red thick lines indicate active subduction fronts. Red and blue triangles indicate calcalkaline and anorogenic volcanic edifices, respectively. Yellow areas indicate areas of extension and arrows depict the direction of the stretching. Light blue depicts oceanic crust. Dark blue correspond to land-docked basins. Extracted from Faccenna et al. (2014a).*

The results obtained in this PhD Thesis agree better with Western Mediterranean geodynamic models that consider a segmented slab (e.g. Wortel and Spakman, 2000; Spakman and Wortel, 2004; Vergés et al., 2012; Chertova et al., 2014; van Hinsbergen et al., 2014). As discussed in Section 8.2, the main catchment of Northern Tunisia, the Medjerda River, shows an anomalous NE-SW-trending flow running perpendicular to the NW-SE Nubia-Eurasia convergence. This trend is opposite to the transverse drainage system expected for mature reliefs in the normal evolution of drainage networks (Babault et al., 2012). In fact, the anomalous flow of the Medjerda River is explained by dynamic topography related to slab-pull forced by the Tunisian slab under the southernmost segment of the South Atlassic Fault and the North-South Axis (Figure 8.3). Moreover, the Tunisian Atlas Transfer Fault worked as a dextral STEP (Subduction-Transform Edge Propagator) boundary of the Tunisian slab that probably favoured upper-mantle flow through the slab window causing the uplift along the south Atlassic dextral transfer zone (Figure 8.3). It is clear then, that the successive observations indicating that the flow of the Medjerda River is anomalous support a segmented slab scenario, where the Tunisian slab migrated in a NW-SE direction from the Algero-Balearic Basin towards Tunisia.

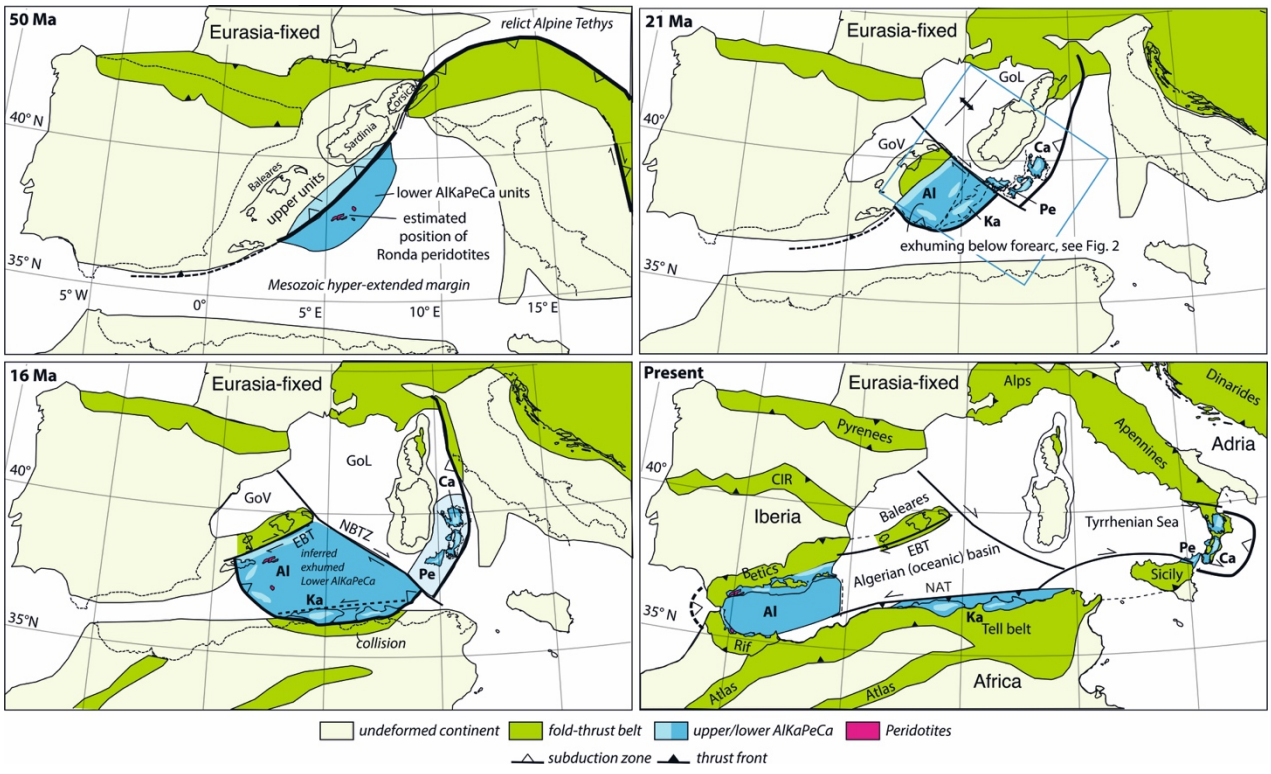

Figure 8.6. *Cartoon showing the reconstruction of the Western Mediterranean evolution since 50 Ma (Early Eocene) to Present. Al = Alboran; Ca = Calabria; CIR = Central Iberian Ranges; EBD= Emile Baudot Transform; GoL= Gulf of Lyon; GoV= Gulf of Valencia; Ka=Kabylides; NAT= North African Transform; NBTZ= North Balearic Transform Zone; Pe= Peloritani Mountains. Extracted from van Hinsbergen et al. (2014).*

Our results support the recent reactivation of inherited faults both onshore and offshore (Figure 8.1). Northern Tunisian land and continental margin show active faults that slip in agreement to the current NW-SE compressive regime between the Nubian and Eurasian plates (e.g. McClusky et al., 2013; D'agostino and Selvaggi, 2004; Serpelloni et al, 2007; Noquet, 2012) (Figure 8.1). The offshore seismo-stratigraphic analysis (Chapter 6) identified several sedimentary features that indicate a widespread sudden slip of faults and uplift of the northern sector during a clear tectonic change in style or deformation rate at 402 ± 5 ky (mid Middle Pleistocene). Although our ages are somewhat younger, this tectonic change is probably related to a tectonic reorganization during the last stages of the end of the back-arc extension of the Tyrrhenian Basin described by Goes et al. (2004) for the south-central Mediterranean area. This differences in time may be due to our more accurate calibration of the events, or to the location of our study area west of the actively-deforming south Tyrrhenian contractional belt (e.g. Goes et al., 2004; Billi et al., 2007; Serpelloni et al., 2007; Nocquet, 2012; Palano et al., 2012; Presti et al., 2013; Totaro et al., 2016; Chiarabba and Palano, 2017), so that the deformation may have migrated in space through time. Our study region is east of the region of reactivation in Algeria (Déverchère et al., 2005; Domzig et al., 2006; Kherroubi et al., 2009; Yelles et al., 2009; Strzerzynski et al., 2010; Arab et al., 2016) where initial phases of crustal under-thrusting processes have been described, which agrees with our interpretation that our study area is in an early stage of contraction. The data offshore show reactivation of inherited faults in a region with few neotectonic studies, limited to local studies in the Sicily Channel area (e.g. Tricart et al., 1990, 1994; Mascle et al., 2001, 2004), and with a weak seismicity in comparison to adjacent segments of the Nubia-Eurasia boundary. The scarce seismicity has been interpreted to indicate that the contractional deformation from the Sicily Channel continued only further the north, in the Liguro-Provençal Basin (Billi et al., 2007; Serpelloni et al., 2007; Billi et al., 2011). Our results show that some of the convergence is being accommodated within our study region mainly in the Hayat fault, that is the one responsible of the uplift of the northern sector. The observations support that most of the Western Mediterranean basin boundaries, even with little seismicity, are currently being inverted in compression -to different extents- as a consequence of the present-day NW-SE Nubia-Eurasia convergence (Billi et al., 2011).

In summary, the results of the geomorphologic, tectonic and stratigraphic analyses carried out in this PhD Thesis provide key information to reconstruct the Neogene geodynamic evolution of the North Tunisian continental margin and are relevant to understand the evolution of the western Mediterranean (Figure 8.7). Three major geodynamic stages are identified:

i) Previous work supports that around 30-35 Ma ago (Figure 8.7.a) extension took over after compression in all the back-arc areas of the Western Mediterranean triggered by the rollback initiation and by the consequent retreat of submarine trenches (e.g. Rehault et al., 1984; Rosenbaum et al., 2002; Faccenna et al., 2004; Schettino and Turco, 2011; Jolivet et al., 2009; Carminati et al., 2012; Faccenna et al., 2014a). This first stage of trench migration towards the east caused the rotation of Sardinia, Corsica, the Balearic Islands and the Kabylies, with the consequent opening of the Valencia, Liguro-Provençal, Algero-Balearic and Alboran basins. In Northern Africa, the opening of these basins was coeval to the emplacement of the Kabylies block during the development of the fold-and-thrust system in the North African margin (e.g. Benaouali-Mebarek et al., 2006; Leprêtre et al., 2018). In fact, the tectonic structures that currently display the largest relief in Northern Tunisia -both onshore and offshore- are NE-SW orientated fault-bounded sheets and folds from the fold-and-thrust belt formed as a consequence of the docking of the Kabylies against the African passive margin at 17-14 Ma (Late Burdigalian - Langhian) (Savelli et al., 2002; Abbassene et al., 2016; Chazot et al., 2017) (Figure 8.7.a).

ii) After this first stage of intense tectonic activity affecting Northern Tunisia, a second stage followed marked by the opening of the Tyrrhenian Basin starting at around 10 Ma (Tortonian to Messinian age) (Faccena et al., 2001; Savelli, 2002; Rosenbaum and Lister, 2004) (Figure 8.7.b). The slab rollback migration of the Apennines-Calabria subduction front caused the extension and thinning of the lithosphere with the consequent formation of an extensional horst-and-graben system on the Tyrrhenian continental margins (Malinverno and Ryan, 1986; Trincardi and Zitellini, 1987; Mascle and Rehault, 1990; Sartori et al., 2001). The Tyrrhenian extensional stage is recorded at the North-eastern Domain of the offshore study area by a series of SE-dipping, NE-SW-striking faults extending SW from the Tyrrhenian horst-graben system that are superimposed on the fold-and-thrust belt of the previous stage (Figure 8.7.b and Chapter 7).

iii) Finally, the results of this PhD thesis clearly show how the current NE-SW Nubia-Eurasia convergence is inverting fault structures inherited both, from the middle Miocene North African fold-and-thrust belt, and the Tortonian extensional system derived from the opening of the Tyrrhenian Basin (Figure 8.7.c). This reactivation was accelerated at 402 ± 5 ky (mid Middle Pleistocene), when a sudden tectonic pulse occurred in the offshore study area, probably marking the final stop of the Tyrrhenian

back-arc extension. We interpret that from 402 ± 5 ky on, lithospheric collision has been probably the main driving force governing tectonics in the central Mediterranean region (Goes et al., 2004). Two major fault systems identified in the study region, generally correspond to the reactivated structures of the two tectonic events described in i and ii. The inherited faults are currently being reactivated with differing kinematics and display a transpressive to compressive system (i.e. differing to the pure thrust faulting observed in northern Sicily and Algeria) with a major reactivation of the Northern group (Figure 8.1). The younger faults of the Northern group, mainly related to the opening of the Tyrrhenian Basin (Tortonian), display a larger degree of reactivation compared to the ones of the Southern group. The WSW-ENE trending reverse Hayat fault, formed in the middle Miocene, is located at this Northern sector and displays a larger degree of reactivation compared to the reactivated middle Miocene faults in the south. The North-eastern system of active faults, characterized by NE-SW-trending faults and the major WSW-ENE reverse Hayat fault, may have been more readily reactivated because their location is slightly to the east from the thick continental crust of the Corsica-Sardinia block (see Section 8.3), and closer to the comparatively thinner highly extended crust (Prada et al., 2016) offshore northern Sicily. This scenario implies a rheological contrasting continental-oceanic boundary that facilitates the reactivation of the North-eastern Domain. In contrast, the Southern faulting system onshore Tunisia and the nearshore offshore area are characterized by a sparse distribution of mainly oblique sinistral to reverse NE-SW faults, which may result from the continental-continental crust collision between Northern Tunisia and the Corsica-Sardinia block.

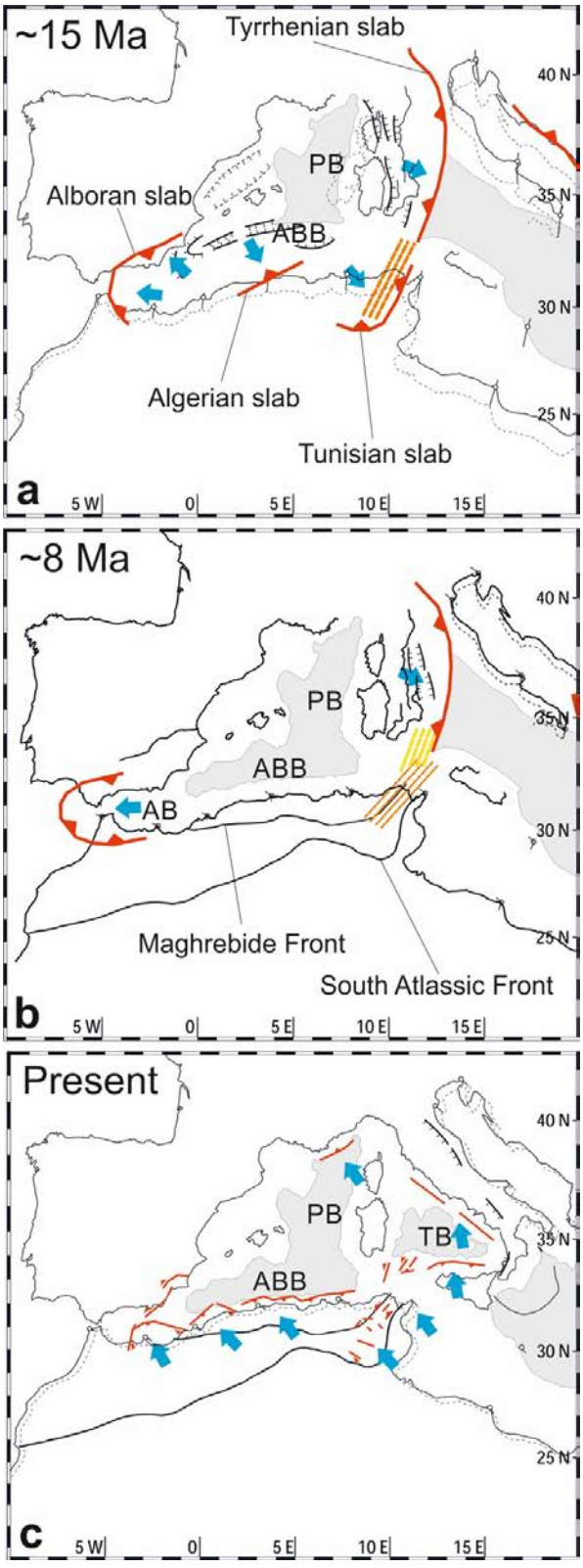

Figure 8.7. *Schematic tectonic evolution of the Western Mediterranean since ~15 Ma based on the modification of previous models with the results of this thesis work. Red lines indicate active subduction fronts and active faults. Orange lines in a and b indicate NE-SW trending faults of the North Tunisian fold-thrust belt formed at 17-14 Ma. Yellow lines in b indicate Tortonian faults from the opening of the Tyrrhenian Basin. Blue arrows show the direction of the stretching. Grey areas indicate oceanic crust. ABB:Algero-Balearic Basin, PB: Provençal Basin, AB: Alboran Basin, TB: Tyrrhenian Basin.*

Part V

CONCLUSIONS & FORWARD LOOK

CHAPTER 9

Conclusions

The results obtained from the morphometric analyses carried out onshore together with the analysis of the geophysical dataset acquired offshore provide new insights into the active tectonics and geodynamic evolution of the Nubia-Eurasia plate boundary in Northern Tunisia. This Chapter summarizes the most relevant findings of my research.

9.1. General conclusions

i) Active faulting shows a transpressive to compressive component in the whole study area of the North Tunisian land and continental margin, resulting from the current NW-SE-trending compressive regime between the Nubian and Eurasian plates.

ii) Two major fault groups -currently reactivated- have been identified and characterized on the basis of their nature and distribution:

   a. The North group is characterized by a dense distribution of SE-dipping NE-SW trending faults. They were originally generated as extensional faults during the opening of the Tyrrhenian Basin caused by the slab rollback migration of the Apennines-Calabrian subduction front since the Tortonian.

   b. The South group shows a sparse distribution of mainly NW-dipping NE-SW trending faults that were originally formed as thrust faults during the collision between the Kabylies block and Africa in the Middle Miocene, a process derived from the rollback migration of the Tunisian slab.

iii) Earthquake magnitudes have been estimated ranging from magnitude (M_w) 6 to 7.54, which together with the identification of potentially indicators of co-seismic effects and historical significant events in the region imply a previously unknown seismic hazard with long recurrence periods. Major tsunamis associated to the seismic activity are not expected to be generated in our study area.

iv) The main mechanisms that influenced the drainage evolution of Northern Tunisia and the anomalous longitudinal orientation of the Medjerda River are: the NW-SE shortening related to the Nubia-Eurasia convergence and the slab-pull under eastern Tunisia, and as a result, the uplift of the western Tunisia along the South Atlassic mountain front that may have worked as a dextral STEP boundary since the Middle Miocene.

v) The sparse seismicity in Tunisia occurs in a broad band that extends towards the south, compared to neighbouring regions. The southern limit delineates a deformation front probably related to the geometry and dynamics of a slab underlying Tunisia. A second factor causing the comparatively broad distribution of seismic events in Tunisia, may relate to the collision of the North African lithosphere with the relatively thick continental lithosphere of Sardinia-Corsica. This scenario contrast with the narrower band of seismicity where continental lithosphere deforms against thinner oceanic plates like north of Algeria and north of Sicily.

vi) During the Middle Miocene Northern Tunisia was affected by an intense tectonic activity due to the collision of the Kabylies block against the African passive margin driven by slab dynamics. As a consequence of this contractional stage, the North-Africa fold-and-thrust belt was established structured with major NE-SW trending structures. Later on, extension due to the opening of the Tyrrhenian Basin affected the Tunisian plateau at around 8-6 Ma (Tortonian to Messinian age) characterized by NE-SW trending extensional faults from the Tyrrhenian horst-graben system. Finally, compression occurred after extension, reactivating ancient structures due to the current NW-SE Nubia-Eurasia boosted at 402 ± 5 ky (mid Middle Pleistocene), when the Tyrrhenian back-arc extension ceased and from that on, lithospheric collision become the main driving force governing tectonics in the central Mediterranean.

9.2. Specific conclusions

9.2.1. Tectonic activity onshore

i) Three main families of active faults have been identified onshore Northern Tunisia: the NE-SW trending reverse-sinistral faults, the WNW-ESE trending dextral faults and the NW-SE trending normal faults. The most frequent family of active faults is the NE-SW trending reverse-sinistral faults.

ii) The main reverse-sinistral fault that show a morphotectonic signal and evidences of activity in the field is El Alia Teboursouk fault.

iii) Two new dextral faults not previously described have been mapped and named as the Dkhila and the Zarga faults.

iv) Evidence of recent slip and associated coseismic effects have been recognized in field structures, related to the Dkhila (DF) and the El Alia Teboursouk (ETF) faults.

v) The estimated maximum earthquake magnitudes for the largest segments of the Dkhila (DF) and the El Alia Teboursouk (ETF) faults are 6.5 and 6.7 (M_w) respectively, which imply a significant seismic hazard for the region.

vi) River captures are the key mechanism that drives the fluvial network reorganization in Northern Tunisia. Morphometric indices evidence fluvial network reorganization that indicate that the catchment area of the Medjerda River has grown through time by capturing other longitudinal valleys to the east of its initial drainage divide. A good example of one of these captures is the Tine River. The interplay of the El Alia Teboursouk, Zarga and Dkhila faults produced an uplifted block that isolated the upper part of the Tine river, boosting its capture by the Medjerda River.

9.2.2. Geomorphology and morphostructure offshore

i) The use of quantitative morphometric analysis offshore similar to that done onshore has produced comparatively little information that can be easily used to understand the offshore evolution. The reasons for this failure are possibly related to the fundamentally different sediment-erosion dynamics on both setting, rather than to differences in tectonic processes.

ii) Large contourite deposits are widespread and imply an intense hydro-dynamism and sediment transport processes along the Tunisian plateau.

iii) The studied area hosts an exceptional number of cold-water coral mounds (CWCM), a total of 286 sites, which corresponds to the highest CWCM density mapped in the Mediterranean and probably the densest field ever mapped and explored until the present-day.

iv) Landslide scars and neighbouring mass transport deposits (MTDs) are typically localized at and near high-gradient slopes, respectively. Further, several slide scars and MTDs occur in nearly flat regions, and we interpreted them as possible co-seismic effects.

v) Pockmark fields and gas flares mapped in the shelf and the whole mapped area give us clear evidence that gas-rich fluid seepage occurs in the offshore Tunisian margin. Fluid circulation is clearly localized and controlled by the tectonic structure of the margin, both at a regional scale, with pockmark dense fields mainly distributed throughout the eastern sector, and at a local scale, with pockmarks aligned along NE-SW trending recent fault scarps.

vi) Active flares do not occur at individual pockmarks or even in the region of pockmark abundance. Their occurrence seems to be structurally controlled at larger scale by the configuration of the margin geological structure formed during Miocene. Surface seepage occurs above anticlinal structures represented by flat-top ridges possibly cut by subaerial erosion during the last glacial maximum, when sea level dropped ~100 m.

vii) Those large structural blocks and parts of the continental shelf are the surface expression of anticline folds S- to SE-directed, which corresponds to imbricated thrust sheets of the North African fold-and-thrust belt showing an ENE-WSW oriented fold axis.

viii) The region is characterized by a distinct morphology between the Eastern and Western sectors from the Bizerte Canyon, which results from the geologic configuration and the recent tectonics occurring in the margin.

9.2.3. Quaternary seismo-stratigraphy and tectono-sedimentary evolution offshore

i) The seismo-stratigraphic analysis of the Quaternary deposits shows that individual basins develop syn-tectonic to faulting. Faulting may represent either a reactivation with new kinematics of pre-existing faults or an increase of the slip rate of pre-existing faults.

ii) The TOPAS images show a change in Sediment Accumulation Rates (SAR) coeval to a change in the strata geometry of the units next to faults. This event occurred during the early deposition phase of the Unit 2, noting a change in active faulting intensity at 402 ± 5 ky, in the mid Middle Pleistocene.

iii) The location of onlap terminations and pinch-out geometries supports the regional uplift of the northern sector that may explain the comparatively low sediment accumulation rates (SAR) values in this sector after the deposition of Unit 3.

iv) The change in tectonic activity occurring at 402 ± 5 ky may relate to the NW-SE convergence between Nubia and Eurasia, and probably marks the end of the Tyrrhenian back-arc extension and subduction trench migration to the SE in the Ionian Basin. This implies a change in driving kinematics supporting lithospheric collision between Nubia and Europe as the main force governing tectonics in the central Mediterranean.

9.2.4. Tectonic activity offshore

i) The structural analysis out of the offshore Northern Tunisia revealed a series of active faults mapped for the first time. Most active faults (i.e. either showing or not a surface rupture) occur within the North-eastern Domain and mostly are SE-dipping NE-SW trending faults, possibly related to the opening of the Tyrrhenian Sea that started at about ~10 Ma. These faults are currently reactivated with different kinematics and inverted in compression by the present-day NW-SE trending contractional setting between the Nubia and Eurasian plates. The faults located in the North-eastern Domain display a transpressional regime showing a dominant left-lateral strike-slip slip.

ii) The NW-dipping NE-SW trending faults related to the old fold-and-thrust belt system associated to the opening of the Algero-Balearic Basin have also been identified and some are reactivated displaying different fault components. The reverse Hayat fault located in the North-eastern Domain is the largest mapped offshore structure and probably the responsible of the uplift of the northern sector.

iii) Active faulting in the study region accommodates part of the current NW-SE shortening between the Nubia and Eurasian plates. The largest accommodation of convergence in one structure occurs in the reverse WSW-ENE trending Hayat fault.

iv) The estimated maximum earthquake magnitudes for the largest offshore segments that might break in one event in our study area range from M_w 6 to 7.54, implying a significant seismic hazard. However, the long recurrence periods expected and the long distance between the seismic sources and inhabited coastal areas may lower the immediate risk. Coseismic significant tsunamis are not expected considering the shallow water and the magnitudes estimated that are not sufficient to generate major, destructives tsunamis.

v) Our work offshore has studied only the surface and near surface expression of active faults, and we do not have information on how these faults extend deeper in the crust. Some of the fault segments identified could merge at depth into larger structures, implying larger-size seismogenic faults than those considered here. Deep penetrating data in the region are necessary to advance hazard analysis of faults that we have identified as currently re-activated structures.

CHAPTER 10

Forward look

The results of this PhD thesis provide new insights concerning active tectonics, sedimentation, the regional tectonic configuration and the geodynamic evolution of the boundary between Nubia and Eurasia in Northern Tunisia. In addition to these major topics, the geomorphology and morpho-structure of the extended continental margin in Northern Tunisia has been revealed with unprecedented accuracy and detail. Previous studies regarding these topics are scarce and almost absent in the offshore studied region. These new findings raise new questions that need additional information to address them. In this Chapter we propose the following topics to answer those open questions.

10.1. Active faulting and seismic hazard onshore

The active faults map provided in the framework of this PhD thesis is based in different approaches and datasets for the onshore and offshore regions. Onshore Northern Tunisia, the location and component of the faults used in this work is based in data from Melki et al. (2012), Bahrouni et al. (2014) and Rabaute and Chamot-Rooke (2015), together with our work on relief analysis and fieldwork. Although the major faults appear well constrained, the mapping of two new large WNW-ESE faults, previously unknown, in the frame of this work suggest that there is room for possibly considerable improvement and more efforts are needed to finalize the fault cartography of Northern Tunisia. Although some cartographies of active tectonics have been recently published (e.g. Bahrouni et al., 2014; Rabaute and Chamot-Rooke, 2015; Soumaya et al., 2018) more detailed analysis of the active fault segments appears necessary to constrain the seismogenic potential of mapped structures.

Taking into account these considerations, we propose to improve the cartography and characterization of active faults in Northern Tunisia considering the new active faults identified in this work, as well as the active tectonics characterization carried out. Although the slow convergence between Nubia and Eurasia derives in low seismic frequency in the region, the historical evidence of destructive earthquakes proves that seismic risk has to be taken into consideration. Furthermore, despite the slow slip rate of the faults, the large dimensions of some of them suggest a significant seismic potential. In fact, maximum potential magnitudes up to 6.7 Mw have been obtained for the ETF fault, one of the most important active faults of the family of NW-dipping NE-SW major structures characterizing Northern Tunisia. In addition to the major NE-SW faults, there are large major faults that act as crustal scale boundaries in central Tunisia, as the NW-SE-oriented dextral strike-slip faults of the south Atlassic STEP boundary (Tunisian Atlas Transfer Fault). All these observations support the importance of continuing with new efforts in the cartography and characterization of active faults in Tunisia to improve the seismic hazard assessment.

10.2. Active faulting, tectonic structure and evolution offshore

Offshore Northern Tunisia, mapping of active faults has been possible in the areas covered by TOPAS profiles but it is uncertain at areas with only bathymetric coverage. Furthermore, an improved characterization of active tectonic structures of the North Tunisian continental margin requires to study the area in greater depth since TOPAS data only image the shallow tens of meters of structures, and some of the identified faults could merge at depth into larger structures implying larger seismogenic faults than those considered here. Moreover, the seismo-stratigraphic work carried out in this PhD thesis has been done using the calibration from one single giant piston core acquired in the frame of the EU-MAST-II “PALAEOFLUX” project (Rothwell, 1995; Dinarès-Turell et al., 2003) and it would be convenient to constrain the analysis with more geological samplings in the area. To solve this issues and better constrain the active faults mapping as well as the tectonic structure and the timing of the slip of the faults of the continental margin of Northern Tunisia we propose to complement the existing data with 11 geophysical transects along which TOPAS and MCS data would be acquired, as well as 7 giant piston cores (Figure 10.1). The total dataset is designed to be able to be acquired in about one month survey with a single ship capable of acquiring piston cores as well as MCS data.

i) Geophysical transects

- Profiles **W1**, **W2**, **W3** and **W4** cut the Western Domain from the Tunisian Shelf to the Teulada Valley in a NNW-SSE direction. They are defined to perpendicularly cut the structural trend of the North African fold-and-thrust belt. These profiles would provide information on the western sector of the study area where no TOPAS data was acquired in the previous surveys. In particular, they would help to constrain the faulting of this sector, where only Possible faults have been able to be defined (faults at the NW and SE of the Sentinelle Bank). Profiles W3 and W4 will provide new data on the Bizerte Canyon underlying fault and the later will also shed light into the NE-SW trending Blind faults within basin B. Profile W3 will also provide information about the nature and formation of the discovered Jan seamount. Furthermore, all these profiles will provide information on the geological configuration of the margin and will help to define the boundary between the Alkapeca internal zone and the allochthonous Tellian domain along the western Tunisian Plateau.

- Profiles **E1**, **E2**, **E3** and **E4** run along the Eastern and North-eastern domains and are designed, similarly to profiles W1-W4, to perpendicularly cut the fold-and-thrust belt related structures. They are defined slightly clock-wise rotated from profiles W1-W4 following the shift of the structures trend from NE-SW to ENE-WSW trends. Profile E1 has been designed to cross the LC07 piston core used in this work to be able to correlate the seismostratigraphic data with the new dataset. Profiles E2, E3 and E4 would help to constrain the Hayat fault and analyze its recent slip and together with profile E1 would help to investigate the expected crustal variations between the Tunisian Plateau and the Sentinelle Valley at the north. Furthermore, all E1-E4 profiles would provide new insights on the Skerki Bank and will help to understand the transition of the structures from the Tunisian Plateau to the easternmost located “south Tyrrhenian contractional belt”.

- Profiles **D1**, **D2** and **D3** are designed to perpendicularly cut the NE-SW Tortonian faults derived from the opening of the Tyrrhenian Basin and reactivated in compression due to the current Nubia-Eurasia convergence. These profiles would help to study the NE-SW Tortonian faults, providing new

insights in fault kinematics and nature, as well as to understand the transition of this system from the Tunisian Plateau to the Tyrrhenian Basin together with the interplay with the middle Miocene fault system. In particular, they would be useful to constrain the NE-SW Valeria fault system as well as the northern segment of the Bizerte Canyon fault. Furthermore, these profiles cut the previous E1-E4 profiles enabling their connection and the seismostratigraphic correlation between the different profiles. Profile D1 is defined to cross the Samia fault in order to better image this structure and study its recent activity as well as its relation with the nearby transparent facies interpreted to be co-seismic.

ii) Piston cores:

- Piston core 1 (**PC1**) is designed to sample de sedimentary layers of the Western Domain. It is placed coinciding with the profile W2 to be able to correlate the sedimentary data with the seismic data. This core is placed at the northern boundary of the major sedimentary basin to be able to sample deeper horizons due to the expected lower sedimentation and to ensure the sample of the sediments in the CPK Zone (Calabro-Peloritani-Kabylian Zone or internal domain).

- Piston core 2 (**PC2**) is placed to sample the growth strata due to the slip of some reverse-to-sinistral NE-SW trending faults that are causing some uplift at the southern sector of basin B. This core will be useful to sample the sediments closer to the shore and it is designed to be placed on top of the W4 profile and a NW-SE TOPAS profile for its correlation.

- Piston cores 3 and 4 (**PC3** and **PC4**) are planned to study one of the faults where the tectonic change described in this thesis at 402 ± 5 ky has been defined. Two piston cores are designed in both walls of the fault (hanging and foot walls) to try to better understand this tectonic change and try to define the start of the slip, since wedged sediments are already found below the horizon at 402 ± 5 ky. Both cores are placed on top of the D1 planned profile to be able to image the sedimentary structure between the sedimentary samples. Furthermore, the sedimentary data acquired in this location will be helpful to check the seismostratigraphic analysis carried out in this work, since the sediment layers

will be able to be correlated with the LC07 piston core following the profile D1 to the NW.

- Piston cores **PC5** and **PC6** are designed similarly to the previous ones to study the Hayat fault, one of the most striking faults in the study area where the tectonic change at 402 ± 5 ky has also been defined. Piston core PC5 has been planned to cut the wedged sediments due to the slip of the Hayat fault and the PC6 to cut the stable area within the basin G. Both cores will be placed on top of the seismic profile E2 and all together will help to study the slip and geometry of the fault as well as the start of the re-activation.

- Piston core **PC7** is placed in the North-eastern Domain, between basins H and I, in an elevated area where the sediment layers are thin, what will help to sample deeper horizons. This core is placed on top of the profiles E4 and D3 as well as an ENE-WSW TOPAS profile to be able to calibrate all of them with a single piston core. This core will help to better constrain the seismostratigraphic analysis of this North-eastern Domain where the re-activated Tortonian faults related to the opening of the Tyrrhenian Basin occur.

This large dataset is planned to be acquired with the main aim to solve open questions raised during this thesis work, in terms of active tectonics and geodynamic evolution of the North Tunisian continental margin. Aside from the tectonic and geodynamic evolution of the area, some other significant topics have been revealed that would be of interest to be studied in more detail. In particular, there are two of these topics that have a significant scientific potential, the massive occurrence of Cold Water Coral Mounds, and gas flares escaping above eroded anticline folds. To study both topics, it would be interesting to plan surveys with the aim to carry out detailed analysis of the structures, probably including the use of ROVs to record CWCM (and check if they are alive) or gas flares (and check the areas where the gas is scaping) as well as to pick up geological samples.

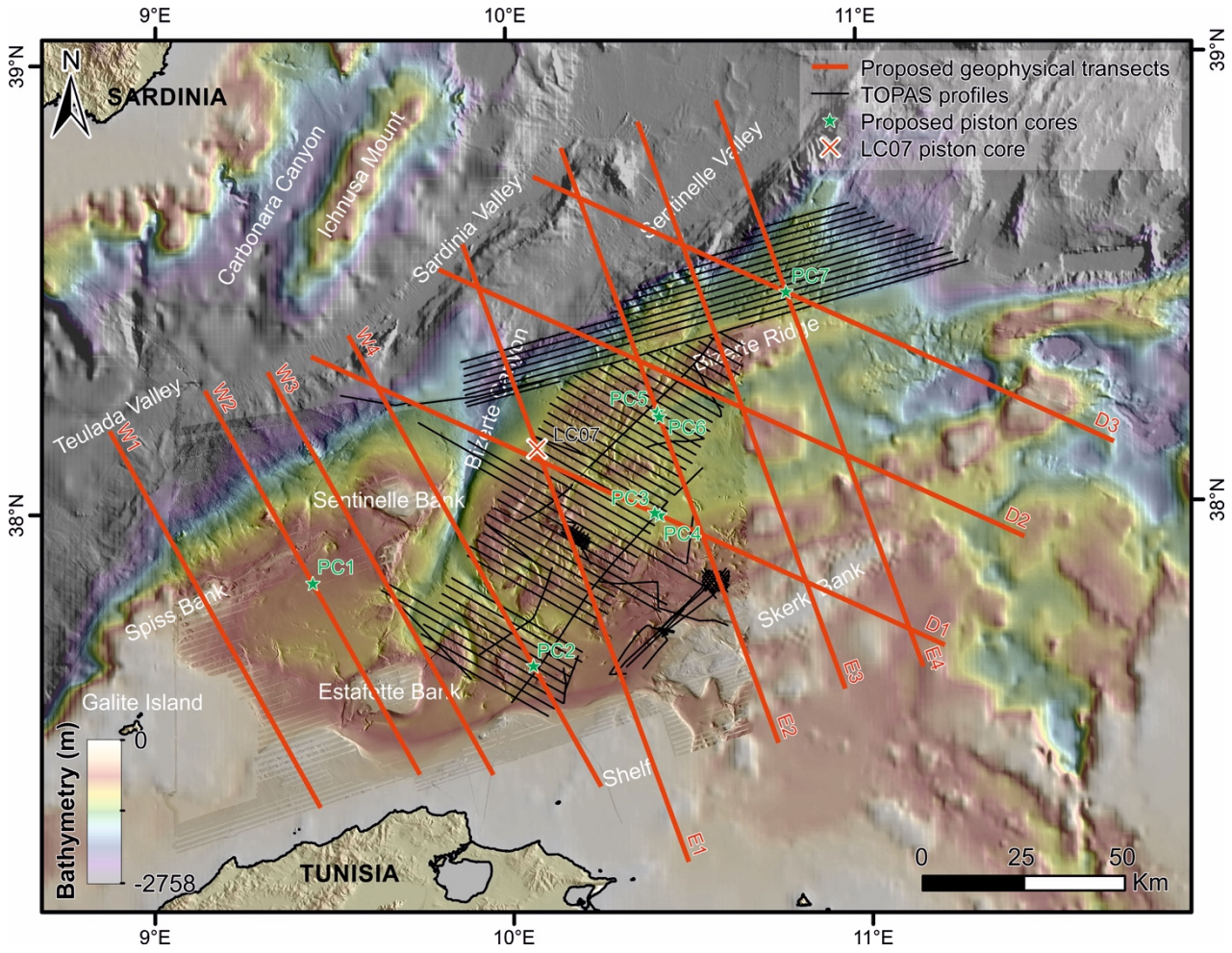

Figure 10.1. *Geophysical and drilling proposal.*

References

Abbassene, F., Chazot, G., Bellon, H., Bruguier, O., Ouabadi, A., Maury, R.C., Déverchére, J., Bosch, D. and Monie, P. (2016). A 17 Ma onset for the post-collisional K-rich cal-alkaline magmatism in the Maghrebides: Evidence from Bougaroun (northeastern Algeria) and geodynamic implications. *Tectonophysics*, 674, 114-134.

Agate, M., Beranzoli, L., Braun, T., Catalano, R., Favali, P., Frugoni, F., Pepe, F., Smriglio, G. and Sulli, A. (2000). The 1998 offshore NW Sicily earthquakes in the tectonic framework of the southern border of the Tyrrhenian Sea. *Mem. Soc. Geol. It.*, 55, 103–114, doi: https://doi.org/10.15713/ins.mmj.3.

Alonso, B., Ercilla, G., Casas, D., Stow, D.A.V., Rodríguez-Tovar, F.J., Dorador, J. and Hernández-Molina, F.J. (2016). Contourite vs gravity-flow deposits of the Pleistocene Faro Drift (Gulf of Cadiz): Sedimentological and mineralogical approaches. *Marine Geology*, 377, 77-94, doi: https://doi.org/10.1016/j.margeo.2015.12.016

Alyahyaoui, S. and Zouari, H. (2014). Synsedimentary folding process and transtensive tectonic during Late Miocene to Quaternary in northeastern Tunisia: case of Mateur-Menzel Bourguiba region. *Arabian Journal of Geosciences*, 7, 4957-4973.

Ambraseys, N. (1962). The seismicity of Tunis, *Annals of Geophysics*, 15, 233-244.

Amiri, A., Chaqui, A., Hamdi Nasr, I., Inoubli, M.H., Ben Ayed N. and Tlig, S. (2011). Role of preexisting faults in the geodynamic evolution of Northern Tunisia, insights from gravity data from the Medjerda valley. *Tectonophysics*, 506, 1–10, doi:10.1016/j.tecto.2011.03.004.

Andreani, L. and Gloaguen, R. (2016). Geomorphic analysis of transient landscapes in the Sierra Madre de Chiapas and Maya Mountains (northern Central America): implications for the North American-Caribbean-Cocos plate boundary. *Earth Surface Dyn*amics, 4, 71–102, doi:10.5194/esurf-4-71-2016.

Andresen, K.J., Huuse, M., Schødt, N.H., Clausen, L.F. and Seidler, L. (2011). Hydrocarbon plumbing systems of salt mini basins offshore Angola revealed by three-dimensional seismic analysis. *American Association of Petroleum Geologists Bulletin*, 95, 6, 1039–1065, doi: https://doi.org/10.1306/12131010046.

Arab, M., Rabineau, M., Déverchère, J., Bracene, R., Belhai, D., Roure, F., Marok, F., Bouyahiaoui, B., Granjeon, D., Andriessen, P. and Sage, F. (2016). Tectonostratigraphic evolution of the eastern Algerian margin and basin from seismic data and onshore-offshore correlation. *Marine and Petroleum Geology*, 77, 1355-1375.

ArcGIS Help Library (2017). [online] [Consulted on September 9th, 2017] URL: *<http://resources.arcgis.com/en/help/main/10.1/>*

Argnani, A. and Bonazzi, C. (2005). Malta Escarpment fault zone offshore eastern Sicily: Pliocene-Quaternary tectonic evolution based on new multichannel seismic data. *Tectonics*, 24, doi: 10.1029/2004TC001656.

Astraldi, M., Balopoulos, S., Candela, J., Font, J., Gacic, M., Gasparini, G.P., Manca, B., Theocharis, A. and Tintoré, J. (1999). The role of straits and channels in understanding the characteristics of Mediterranean circulation. *Progress in Oceanography*, 44, 65-108.

Astraldi, M., Gasparini, G.P., Vetrano, A. and Vignudelli, S. (2002). Hydrographic characteristics and interannual variability of water masses in the central Mediterranean: A sensitivity test for long-term changes in the Mediterranean Sea. *Deep-Sea Research Part I: Oceanographic Research Papers*, 49, 661-680.

Auzende, J.M. (1971). La marge continentale Tunisienne: Resultats d'une etude par sismique reflexión: sa place dans le cadre tectonique de la Mediterranee occidentale. *Marine Geophysical Researches*, 1, 162-177.

Auzende, J.M., Olivet, J.L. and Bonnin, J. (1974). Le Detroit Sardano-Tunisien et la zone de fracture Nord-Tunisienne. *Tectonophysics*, 21, 357-374.

Auzende, J.M., Bonnin, J. and Olivet, J.L. (1975). La marge nord-africaine considérée comme marge active. *Bulletin de la Societe Geologique de France, 17, 4, 486-495.*

Azañón, J.M., Pérez-Peña, J.V., Giaconia, F., Booth-Rea, G., Martínez-Martínez, J.M. and Rodríguez-Peces, M.J. (2012). Active tectonics in the central and eastern Betic Cordillera through morphotectonic analysis: the case of Sierra Nevada and Sierra Alhamilla. *Journal of Iberian Geology*, 38, 225-238.

Azañón, J.M., Galve, J.P., Pérez-Peña, J.V., Giaconia, F., Carvajal, R., Booth-Rea, G., Janaloy, A., Vázquez, M., Azor, A. and Roldán, F.J. (2015). Relief and drainage evolution during the exhumation of the Sierra Nevada (SE Spain): Is denudation keeping pace with uplift?. *Tectonophysics*, 663, 19-32, doi: https://doi.org/10.1016/j.tecto.2015.06.015

Azor, A., Keller, E.A. and Yeats, R.S. (2002). Geomorphic indicators of active fold growth: South Mountain-Oak Ridge anticline, Ventura basin, southern California. *Geological Society of America Bulletin*, 114, 745-753.

Babault, J., Van Den Driessche, J. and Teixell, A. (2012). Longitudinal to transverse drainage network evolution in the High Atlas (Morocco): The role of tectonics. *Tectonics*, 31.

Babonneau, N., Cattaneo, A., Ratzov, G., Déverchère, J., Yelles-Chaouche, A., Lateb, T. and Bachir, R. S. (2017). Turbidite chronostratigraphy off Algiers, central Algerian margin: A key for reconstructing Holocene paleo-earthquake cycles. *Marine Geology*, 384, 63–80, doi: https://doi.org/10.1016/j.margeo.2016.10.017

Bahrouni, N., Bouaziz, S., Soumaya, A., Ben Ayed, Attafi, K., Houla, Y., El Ghali, A. and Rebai, N. (2014). Neotectonic and seismotectonic investigation of seismically active regions in Tunisia: a multidisciplinary approach. *Journal of Seismology*, 18, 235–256, doi: 10.1007/s10950-013-9395-y.

Bannour, H. and Bonvallot, J. (1988). Les dépôts quaternaires de la vallée de la Medjerda dans la "zone des diapirs", témoins de déformations quaternaires continues. *Méditerranée*, 7–12.

Beghoul, N., Chatelain, J. L., Boughacha, M. S., Benhallou, H., Dadou, R. and Mezioud-Saïch, A. (2009). Seismic empirical relations for the Tellian Atlas, North Africa, and their usefulness for seismic risk assessment. *Pure and Applied Geophysics*, 167(3), 277–321, doi: https://doi.org/10.1007/s00024-009-0018-z

Belayouni, H., Brunelli, D., Clocchiatti, R., Di Staso, A., El Amrani El Hassani, I-E., Guerrera, F., Kassaa, S., Laridhi Ouazaa, N., Martín Martín, M., Serrano, F. and Tramontana, M. (2010). La Galite Archipelago (Tunisia, North Africa): Stratigraphic and petrographic revision and insights for geodynamic evolution of the Maghrebian Chain. *Journal of African Earth Sciences*, 56, 15–28.

Belayouni, H., Guerrera, F., Martín Martín, M. and Serrano, F. (2012). Stratigraphic update of the Cenozoic Sub-Numidian formations of the Tunisian Tell (North Africa): Tectonic/sedimentary evolution and correlations along the Maghrebian Chain. *Journal of African Earth Sciences,* 64, 48–64, doi: 10.1016/j.jafrearsci.2011.11.010.

Belayouni, H., Guerrera, F., Martín-Martín, M. and Serrano F. (2013). Paleogeographic and geodynamic Miocene evolution of the Tunisian Tell (Numidian and Post-Numidian

Successions): bearing with the Maghrebian Chain. *International Journal of Earth Sciences*, 102(3), 831-855.

Belguith, Y., Geoffroy, L., Rigane, A., Gourmelen, C. and Ben Dhia, H. (2011). Neogene extensional deformation and related stress regimes in central Tunisia. *Tectonophysics*, 509, 198–207.

Belguith, Y., Geoffroy, L., Mourgues, R. and Rigane, A. (2013). Tectonophysics Analogue modelling of Late Miocene-Early Quaternary continental crustal extension in the Tunisia-Sicily Channel area Tunisia. *Tectonophysics*, 608, 576–585, doi: https://doi.org/10.1016/j.tecto.2013.08.023

Ben Ayed, N. (1993). Evolution Tectonique de l'Avant-pays de la Chaîne Alpine de Tunisie du Début du Mésozoïque à l'Actuel. *Annales des Mines et de la Géologie - Tunis*, 32, 286.

Benaouali-Mebarek, N., Frizon de Lamotte, D., Roca, E., Bracene, R., Faure, J. L., Sassi, W. and Roure, F. (2006). Post-Cretaceous kinematics of the Atlas and Tell systems in central Algeria: Early foreland folding and subduction-related deformation. *Comptes Rendus-Geoscience*, 338(1–2), 115–125, doi: https://doi.org/10.1016/j.crte.2005.11.005.

Ben Hassen, M., Deffontaines, B. and Turki, M.M. (2014). Semi-automatisation de l'extraction des anomalies de drainage. Application au centre de l'Atlas méridional de la Tunisie. *Géomorphologie: relief, processus, environnement*, 20 – 1, 3-14.

Bertoni, C. and Cartwright, J.A. (2005). 3D seismic analysis of circular evaporite dissolution structures, Eastern Mediterranean. *Journal of the Geological Society*, 162, 909–926.

Betzler, C., Lindhorst, S., Hübscher, C., Lüdmann, T., Fürstenau, J. and Reijmer, J. (2011). Giant pockmarks in a carbonate platform (Maldives, Indian Ocean). *Marine Geology*, 289, 1–16, doi: 10.1016/j.margeo.2011.09.004.

Bigot-Cormier, F., Sage, F., Sosson, M., Déverchère, J., Ferrandini, M., Guennoc, P., Popoff, M. and Stéphan, J.F. (2004). Déformations pliocènes de la marge nord-Ligure (France): Les conséquences d'un chevauchement crustal sud-alpin. *Bulletin de la Societe Geologique de France*, 175, 2, 197-211.

Billi, A., Presti, D., Faccenna, C., Neri, C. and Orecchio, B. (2007). Seismotectonics of the Nubia plate compressive margin in the south Tyrrhenian region, Italy: Clues for subduction inception. *Journal of Geophysical Research*, 112, doi: 10.1029/2006JB004837.

Billi, A., Faccenna, C., Bellier, O., Minelli, L., Neri, G., Piromallo, C., Presti, D., Scrocca, D. and Serpelloni, E. (2011). Recent tectonic reorganization of the Nubia-Eurasia convergent

boundary heading for the closure of the western Mediterranean. *Bulletin de la Société Géologique de France*, 182, 279-303.

Bloom, A. (1978). *Geomorphology, A systematic Analysis of Late Cenozoic Landforms*. Englewood Cliffs, NJ: Prentice-Hall, 510, ISBN: 0-13-353086-8.

Booth-Rea, G., Ranero, C., Martínez-Martínez, J.M. and Grevemeyer, I. (2007). Crustal types and Tertiary tectonic evolution of the Alboran sea, western Mediterranean. *G-Cubed*, 8(10), doi: 10010.11029/12007GC001661.

Booth-Rea, G., Gaidi, S., Melki, F., Marzougui, W., Azañón, J.M., Zargouni, F., Galvé, J.P. and Pérez-Peña, J.V. (2018). Late Miocene extensional collapse of northern Tunisia. *Tectonics*, 37, 1626–1647, doi: https://doi.org/10.1029/2017TC004846.

Bouaziz, S., Barrier, E., Soussi, M., Turki, M.M. and Zouari, H. (2002). Tectonic evolution of the northern African margin in Tunisia from paleostress data and sedimentary record. *Tectonophysics*, 357, 227–253.

Bouhadad, Y., Nour, A., Slimani, A., Laouami, N. Belhai, D. (2004). The Boumerdes (Algeria) earthquake of May 21, 2003 (Mw = 6.8): Ground deformation and intensity. *Journal of Seismology*, 8, 497-506.

Bouillin, J-P., Poupeau, G., Tricart, P., Bigot-Cormier, F., Mascle, G., Torelli, L., Compagnoni, R., Mascle, J., Pêcher, A., Peis, D., Rekhiss, F. and Rolfo, F. (1998). Premières données thermos-chronologiques sur les socles sarde et kabylo-péloritain submerges dans le canal de Sardaigne (Méditerranée occidentale). *Comptes Rendus de l'Académie des Sciences Paris*, 326, 561-566.

Bouyahiaoui, B., Sage, F., Abtout, A., Klingelhoefer, F., Yelles-Chaouche, K., Schnürle, P., Marok, A., Déverchère, L., Arab, M., Galve, A. and Collot, J.Y. (2015). Crustal structure of the eastern Algerian continental margin and adjacent deep basin: Implications for late Cenozoic geodynamic evolution of the western Mediterranean. *Geophysical Journal International*, 201(3), 1912–1938, doi: https://doi.org/10.1093/gji/ggv102

Bracène, R. and Frizon de Lamotte, D. (2002). The origin of intraplate deformation in the Atlas system of western and central Algeria: From Jurassic rifting to Cenozoic-Quaternary inversion. *Tectonophysics*, 357, 207 – 226.

Branellec, M., Callot, J. P., Nivière, B. and Ringenbach, J. C. (2015). The fracture network, a proxy for mesoscale deformation: Constraints on layer parallel shortening history from the

Malargüe fold and thrust belt, Argentina. *Tectonics*, 34, 623-647, doi: 10.1002/2014TC003738.

Braun, J. (2010). The many surface expressions of mantle dynamics, *Nature Geoscience*, 3, 825-833.

Braunmiller, J. and Bernardi, F. (2005). The 2003 Boumerdes, Algeria earthquake: Regional moment tensor analysis, *Geophysical Research Letters*, 32, doi: 10.1029/2004GL022038.

Brooke, S., Ross, S.W., Bane, J.M., Seim, H. and Young, C. (2013). Temperature tolerance of the deep-sea coral Lophelia pertusa from the southeastern United States, *Deep Sea Research Part II: Topical Studies in Oceanography*, 92, 240–248, doi: 10.1016/j.dsr2.2012.12.001.

Brookfield, M.E. (1998). The evolution of the great river systems of southern Asia during the Cenozoic India-Asia collision: rivers draining southwards. *Geomorphology*, 22, 285–312.

Bryant, E. (2014). *Tsunami: The Underrated Hazard*, Cambridge, UK: Cambridge University Press, doi: 10.1007/978-3-319-06133-7.

Budillon, F., Lirer, F., Iorio, M., Macrí, P., Sagnotti, L., Vallefuoco, M., Ferraro, L., Garziglia, S., Innangi, S., Sahabi, M. and Tonielli, R. (2009). Integrated stratigraphic reconstruction for the last 80kyr in a deep sector of the Sardinia Channel (Western Mediterranean). *Deep-Sea Research*, II 56, 725–737, doi:10.1016/j.dsr2.2008.07.026.

Bull, W.B. and McFadden, L., (1977). Tectonic geomorphology north and south of the Garlock Fault, California. In: Doering, D.O., (Ed.), *Geomorphology in Arid Regions*, Binghamton, NY: University of New York, 115-138.

Burbank, D., Meigs, A. and Brozovic, N. (1996). Interactions of growing folds and coeval depositional systems. *Basin Research*, 8, 199-223.

Calais, E., DeMets, C. and Nocquet, J. M. (2003). Evidence for a post-3.16-Ma change in Nubia-Eurasia-North America plate motions?. *Earth and Planetary Science Letters*, 216, 8–92.

Carminati, E., Lustrino, M., and Doglioni, C., (2012). Geodynamic evolution of the central and western Mediterranean: Tectonics vs. igneous petrology constraints. *Tectonophysics*, 579, 173–192, doi: 10.1016/j.tecto.2012.01.026.

Castany, G. (1954). L'accident Sud-tunisien, son âge et ses relations avec l'accident Sudatlasique d'Algérie. *Comptes Rendus de l'Académie des Sciences de Paris*, 238, 916–918.

Castillo, M., Bishop, P. and Jansen, J.D. (2013). Knickpoint retreat and transient bedrock channel morphology triggered by base-level fall in small bedrock river catchments: The case of the Isle of Jura, Scotland. *Geomorphology*, 180-181, 1-9, doi:10.1016/j.geomorph.2012.08.023.

Catalano, R., Franchino, A., Merlini, S. and Sulli, A. (2000). A Crustal section from the Eastern Algerian Basin to the Ionian Ocean (Central Mediterranean). *Mem. Soc. Geol. It.*, 55, 71-85, doi: 0.3997/2214-4609.201405983.

Cathles LM., Su, Z. and Chen, D. (2010). The physics of gas chimney and pockmark formation, with implications for assessment of seafloor hazards and gas sequestration. *Marine and Petroleum Geology*, 27, 82–91, doi:10.1016/j.marpetgeo.2009.09.010.

Chazot, G., Abbassene, F., Maury, R. C., Déverchère, J., Bellon, H., Ouabadi, A., and Bosch, D. (2017). An overview on the origin of post-collisional Miocene magmatism in the Kabylies (northern Algeria): Evidence for crustal stacking, delamination and slab detachment. *Journal of African Earth Sciences*, 125, 27–41, doi: https://doi.org/10.1016/j.jafrearsci.2016.10.005

Chertova, M.V., Spakman, W., Geenen, T., van den Berg, A.P. and van Hinsbergen, D.J.J. (2014). Underpinning tectonic reconstructions of the western Mediterranean region with dynamic slab evolution from 3-D numerical modeling. *Solid Earth*, 1–15, doi: 10.1002/2014JB011150.

Chiarabba, C. and Palano, M. (2017). Progressive migration of slab break-off along the southern Tyrrhenian plate boundary: Constraints for the present day kinematics. *Journal of Geodynamics*, 105, 51-61.

Chiba, T., Kaneta, S. and Suzuki, Y. (2008). Red relief image map: new visualization method for three dimensional data. *The International Archives of the Photogrammetry, Remote Sensing and Spatial Information Sciences*, 37, 1071-1076.

Chiba, T. and Hasi, B. (2016). Ground surface visualization using red relief image map for a variety of map scales. *The International Archives of the Photogrammetry, Remote Sensing and Spatial Information Sciences*, 41, 393-397.

Chiocci, F.L. and Orlando, L. (1996). Lowstand terraces on Tyrrhenian Sea steep continental slopes. *Marine Geology*, 134, 127-143

Compagnoni, R., Morlotti, E., and Torelli, L. (1989). Crystalline and sedimentary rocks from the scarps of the Sicily-Sardinia Trough and Cornaglia Terrace (southwestern Tyrrhenian Sea, Italy): Paleogeographic and geodynamic implications. *Chemical Geology*, 77(3–4), 375–

398, doi: https://doi.org/10.1016/0009-2541(89)90085-5.

Cox, A. and Hart, R.B. (1986). *Plate Tectonics: How it works,* Wiley-Blackwell.

Crosby, B.T. and Whipple, K.X. (2006). Knickpoint initiation and distribution within fluvial networks: 236 waterfalls in the Waipaoa River, North Island, New Zealand. *Geomorphology*, 82, 16-38.

D'agostino, N. and Selvaggi, G. (2004). Crustal motion along the Eurasia-Nubia plate boundary in the Calabrian Arc and Sicily and active extension in the Messina Straits from GPS measurements. *Journal of Geophysical Research*, 109, doi: 10.1029/2004JB002998.

DeCelles, P.G. and Giles, K.A. (1996). Foreland basin systems. *Basin Research*, 8, 105-123.

Decrée, S., Marignac, C., Liégeois, J.-P., Yans, J., Ben Abdallah, R. and Demaiffe, D. (2014). Miocene magmatic evolution in the Nefza district (Northern Tunisia) and its relationship with the genesis of polymetallic mineralizations. *Lithos*, 192–195, 240-258.

Delile, H., Abichou, A., Gadhoum, A., Goiran, J., Pleuger, E., Monchambert, J.-Y., Wilson, A., Fentress, E., Quinn, J., Jerbania, I. B. and Ghozzi, F. (2015). The Geoarchaeology of Utica, Tunisia: The Paleogeography of the Mejerda Delta and Hypotheses Concerning the Location of the Ancient Harbor. *Geoarchaeology: An International Journal*, 30, 291–306, doi: https://doi.org/10.1002/gea.21514

DeMets, C., Gordon, R.G., Argus, D.F. and Stein, S. (1994). Effect of recent revisions to the geomagnetic reversal time scale on estimates of current plate motions. *Geophysical Research Letters*, 21, 20, 2191–2194.

Demoulin, A. (1998). Testing the tectonic significance of some parameters of longitudinal river profiles: the case of the Ardenne (Belgium, NW Europe). *Geomorphology*, 24 (2-3), 189–208, doi: 10.1016/S0169-555X(98)00016-6

Déverchère, J., Yelles, K., Domzig, A., Mercier de Lépinay, B., Bouillin, J.P., Gaullier, V., Bracène, R., Calais, E., Savoye, E., Kherroubi, A., Le Roy, P., Pauc, H. and Dan, G. (2005). Active thrust faulting offshore Boumerdes, Algeria, and its relations to the 2003 Mw 6.9 earthquake. *Geophysical Research Letters*, 32, doi: 10.1029/2004GL021646.

Dewey, J.F., Helman, M.L., Knott, S.D., Turco, E. and Hutton, D.H.W. (1989). Kinematics of the western Mediterranean. In: Coward, M.P., Dietrich, D. and Park, R.G., (Eds.), *Alpine Tectonics*, Geological Society Special Publication, 45, 1, 265–283, doi: 10.1144/GSL.SP.1989.045.01.15.

Diez, S. and Gràcia, E. (2005). Submarine Mapping using Multibeam Bathymetry and Acoustic Backscatter: Illuminating the Seafloor*, Instrumentation Viewpoint*, 3, 10-14.

Dinarès-Turell, J., Sagnotti, L. and Roberts, A.P. (2002). Relative geomagnetic paleointensity from the Jaramillo Subchron to the Matuyama/Brunhes boundary as recorded in a Mediterranean piston core. *Earth and Planetary Science Letters*, 194, 327-341.

Dinarès-Turell, J., Hoogakker, B.A.A., Roberts, A.P., Rohling, E.J. and Sagnotti, L. (2003). Quaternary climatic control of biogenic magnetite production and eolian dust input in cores from the Mediterranean Sea. *Palaeogeography, Palaeoclimatology, Palaeoecology*, 195-209.

Domzig, A., Yelles, K., Le Roy, C., Déverchère, J., Bouillin, J.-P., Bracène, R., Mercier de Lépinay, B., Le Roy, P., Calais, E., Kherroubi, A., Gaullier, V., Savoye, B and Pauc, H. (2006). Searching for the Africa–Eurasia Miocene boundary offshore western Algeria (MARADJA'03 cruise). *Comptes Rendus Geoscience*, 338, 80-91.

Douarin, M., Sinclair, D.J., Elliot, M,. Henry, L.A., Long, D., Mitchison, F. and Roberts, J.M. (2009). Changes in fossil assemblage in sediment cores from Mingulay Reef Complex (NE Atlantic): Implications for coral reef build-up. *Deep Sea Research part II: Topical Studies in Oceanography,* 99, 286-296, doi: https://doi.org/10.1016/j.dsr2.2013.07.022.

Eichhubl P., Greene, H.G., Naehr, T. and Maher, N. (2000). Structural control of fluid flow: offshore fluid seepage in the Santa Barbara Basin, California. *Journal of Geochemical Exploration*, 69–70, 545–549.

ELAC Nautik (2011). Seabeam 1050/1055, Medium Water Multibeam Systems. *L-3 Communications ELAC Nautik GmbH*, Germany.

El Euchi, H., Saidi, M., Fourati, L. and El Maherssi, C. (2004). Northern Tunisia thrust belt: Deformation models and hydrocarbon systems. In: Swennen, R., Roure, F. and Granath, J.W., (Eds.), *Deformation, fluid flow, and reservoir appraisal in foreland fold and thrust belts*, AAPG Hedberg Series, 1, 371–390.

EMODnet (2018). [online] [Consulted on June 5th, 2018] URL: <*http://www.emodnet-bathymetry.eu/*>.

Encyclopaedia Britannica (2018). [online] [Consulted on July 20th, 2018] URL: <*https://www.britannica.com/science/continental-shelf*>

Essid, E. M., Kadri, A., Inoubli, M. H. and Zargouni, F. (2016). Identification of new NE-trending deep-seated faults and tectonic pattern updating in northern Tunisia (Mogodos–Bizerte region), insights from field and seismic reflection data. *Tectonophysics*, 682, 249–263, doi: https://doi.org/10.1016/j.tecto.2016.05.032.

Faccenna, C., Giardini, D., Davy, P. and Argentieri, A. (1999). Initiation of subduction at Atlantic-type margins: Insights from laboratory experiments. *Journal of Geophysical Research*, 104, 2749–2766.

Faccenna, C., Becker, T.W., Pio Lucente, F., Jolivet, L. and Rossetti, F. (2001). History of subduction and back-arc extension in the Central Mediterranean. *Geophysical Journal International*, 145, 809-820.

Faccenna, C., Piromallo, C., Crespo-Blanc, A., Jolivet, L and Rossetti, F. (2004). Lateral slab deformation and the origin of the western Mediterranean arcs. *Tectonics*, 23, doi:10.1029/2002TC001488.

Faccenna, C., Civetta, L., D'Antonio, M., Funiciello, F., Margheriti, L. and Piromallo, C. (2005). Constraints on mantle circulation around the deforming Calabrian slab. *Geophysical Research Letters*, 32, doi: 10.1029/2004GL021874.

Faccenna, C. and Becker, T.W. (2010). Shaping mobile belts by small-scale convection. *Nature*, 465, 602-605.

Faccenna, C., W. Becker, T., Auer, L., Billi, A., Boschi, L., Brun, J.P., A. Capitanio, F., Funiciello, F., Horvàth, F., Jolivet, L., Piromallo, C., Royden, L., Rossetti, F. and Serpelloni, E. (2014a). Mantle dynamics in the Mediterranean. *Reviews of Geophysics*, 52, 283-332, doi: 10.1002/ 2013RG000444.

Faccenna, C., Becker, T.W., Miller, M.S., Serpelloni, E. and Willett, S.D. (2014b). Isostasy, dynamic topography, and the elevation of the Apennines of Italy. *Earth and Planetary Science Letters*, 407, 163-174.

Farr, T.G., Rosen, P.A., Caro, E., Crippen, R., Duren, R., Hensley, S., Kobrick, M., Paller, M., Rodriguez, E., Roth, L., Seal, D., Shaffer, S., Shimada, K., Umland, J., Werner, M., Oskin, M., Burbank, D. and Alsdorf, D. (2007). The Shuttle Radar Topography Mission. *Reviews of Geophysics*, 45, doi: 10.1029/2005RG000183.

Faust, D., Zielhofer, C., Baena Escudero, R. and Diaz Del Olmo, F. (2004). High-resolution fluvial record of late Holocene geomorphic change in northern Tunisia: Climatic or human impact?,

Quaternary Science Reviews, 23 (16–17), 1757–1775, doi: https://doi.org/10.1016/j.quascirev.2004.02.007.

Ferrater, M., Booth-Rea, G., Pérez-Peña, J. V., Azañón, J.M., Giaconia, F. and Masana, E. (2015). From extension to transpression: Quaternary reorganization of an extensional-related drainage network by the Alhama de Murcia strike-slip fault (eastern Betics). *Tectonophysics*, 663, 33-47, doi: 10.1016/j.tecto.2015.06.011.

Fichtner, A. and Villaseñor, A. (2015). Crust and upper mantle of the western Mediterranean - Constraints from full-waveform inversion. *Earth and Planetary Science Letters*, 428, 52-62.

Fowler, C.M.R. (1990). *The Solid Earth, An Introduction to Global Geophysics*, Cambridge, UK: Cambridge University Press, 472.

Frizon de Lamotte, D., Raulin, C., Mouchot, N., Wrobel-Daveau, J.-C., Blanpied, C. and Ringenbach, J.-C. (2011). The southernmost margin of the Tethys realm during the Mesozoic and Cenozoic: Initial geometry and timing of the inversion processes. *Tectonics*, 30, TC3002, doi: 10.1029/2010TC002691.

Gelabert, B., Sàbat, F. and Rodríguez-Perea, A. (2002). A new proposal for the late Cenozoic geodynamic evolution of the western Mediterranean. *Terra Nova*, 14, 2, 93–100.

Gennesseaux, M.G. and Stanley, D.J. (1983). Neogene to Recent Displacement and Contact of Sardinian and Tunisian Margins, Central Mediterranean. *Smithsonian contributions to the marine sciences*, 23.

Giaconia, F., Booth-Rea, G., Martinez-Martinez, J.M., Azañón, J.M., Pérez-Peña, J.V. Pérez-Romero, J. and Villegas, I. (2012a). Geomorphic evidence of active tectonics in the Sierra Alhamilla (eastern Betics, SE Spain). *Geomorphology*, 145-146, 90-106, doi: 10.1016/j.geomorph.2011.12.043.

Giaconia, F., Booth-Rea, G., Martínez-Martínez, J.M., Azañón, J.M. and Pérez-Peña, J.V. (2012b). Geomorphic analysis of the Sierra Cabrera, an active pop-up in the constructional domain of conjugate strike-slip faults: The Palomares and Polopos fault zones (eastern Betics, SE Spain). *Tectonophysics*, 580, 27-42.

Giaconia, F., Booth-Rea, G., Ranero, C.R., Gracia, E., Bartolome, R., Calahorrano, A., Lo Iacono, C., Vendrell, M.G., Cameselle, A.L., Costa, S., de la Pena, L.G., Martinez-Loriente, S., Perea, H. and Vinas, M. (2015). Compressional tectonic inversion of the Algero-Balearic

basin: Latemost Miocene to present oblique convergence at the Palomares margin (Western Mediterranean). *Tectonics*, 34, 1516-1543.

Global CMT (2015). [online] [Consulted on November 24th, 2015] URL: <*http://www.globalcmt.org/*>.

Goes, S., Giardini, D., Jenny, S., Hollenstein, C., Kahle, H. G. and Geiger, A. (2004). A recent tectonic reorganization in the south-central Mediterranean. *Earth and Planetary Science Letters*, 226, 335-345.

Gogus, O.H. and Pysklywec, R.N. (2008). Mantle lithosphere delamination driving plateau uplift and synconvergent extension in eastern Anatolia. *Geology*, 36, 723-726.

Goren, L., Willett, S. D., Herman, F. and Braun, J. (2015). Coupled numerical-analytical approach to landscape evolution modeling. *Earth Surface Processes and Landforms*, 39, 522–545.

Govers, R. and Wortel, M.J.R. (2005). Lithosphere tearing at STEP faults: response to edges of subduction zones. *Earth and Planetary Science Letters*, 236, 505-523.

Gràcia, E. and Diez, S. (2005). Com s'explora el fons marí? Eines i aplicacions en Geociències Marines, *Mètode - Revista de Difusió de la Investigació*, Universitat de València Ed., 46, 80-88.

Gràcia, E., Pallàs, R., Soto, J.I., Comas, M., Moreno, X., Masana, E., Santanach, P., Diez, S., García, M. and Dañobeitia, J.J. (2006). Active faulting offshore SE Spain (Alboran Sea): Implications for earthquake hazard assessment in the Southern Iberian Margin. *Earth and Planetary Science Letters*, 241 (3-4), 734-749.

Gràcia, E., Vizcaino, A., Escutia, C., Asioli, A., Rodés, A., Pallàs, R., Garcia-Orellana, J., Lebreiro, S. and Goldfinger, C. (2010). Holocene earthquake record offshore Portugal (SW Iberia): Testing turbidite paleoseismology in a slow-convergence margin. *Quaternary Science Reviews*, 29, 1156–1172.

Gross, M.G. (1972). *Oceanography: A View of the Earth*. Englewood Cliffs, NJ: Prentice-Hall, 472, ISBN 978-0-13-629659-1.

Gueddiche, M., Ben Ayed, N., Mohammadioun, G., El Ghali, A., Chekhma, H., Diament, M. and Dubois, J. (1998). Etude sismotectonique de la Tunisie nord-orientale. *Bulletin de la Societe Geologique de France*, 169, 789-796.

Gueddiche, M., Harjono, H., Ben Ayed, N., Hfaiedh, M., Diament, M. and Dubois, J. (1992). Analyse de la séismicité et mise en évidence d'accidents actifs dans le nord de la Tunisie. *Bulletin de la Société Géologique de France*, 163(4), 415–425.

Gueguen, E., Doglioni, C and Fernandez, M. (1998). On the post-25 Ma geodynamic evolution of the western Mediterranean. *Tectonophysics*, 298, 1-3, 259-269, doi: 10.1016/S0040-1951(98)00189-9.

Guinan, J., Grehan, A.J., Dolan, M.F.J. and Brown, C. (2000). Quantifying relationships between video observations of cold-water coral cover and seafloor features in Rockall Trough, west of Ireland, *MEPS*, 375, 125-138.

Guzman, M. (2015). Understanding the Processes that Controlled Rifting of the Tyrrhenian Basin. *PhD. Thesis*, Universitat de Barcelona.

Hamblin, W.K. (1992). *Earth's dynamic systems*. Mcmillan publishing company.

Hampton, M.A., Lee, H.J. and Locat, J. (1996). Submarine Landslides. *Reviews of geophysics*, 34, 1, 33-59.

Hanks, T. C. and Kanamori, H. (1979). A Moment Magnitude Scale. *Journal of Geophysical Research*, 84(B5), 2348-2350.

Harris, P.T., MacMillan-Lawler, M., Rupp, J. and Baker, E.K. (2014). Geomorphology of the oceans. *Marine Geology,* 352, 4-24.

Harvey, A.M. and Wells, S.G. (1987). Response of Quaternary Fluvial Systems to Differential Epeirogenic Uplift - Aguas and Feos River Systems, Southeast Spain. *Geology*, 15, 689-693.

Hebbeln, D. and Samankassou, E. (2015). Where did ancient carbonate mounds grow - In bathyal depths or in shallow shelf waters?. *Earth-Science Reviews*, 145, 56–65.

Hergarten, S., Robl, J. and Stüwe, K. (2014). Extracting topographic swath profiles across curved geomorphic features. *Earth Surface Dynamics*, 2, 97-104, doi: 10.5194/esurf-2-97-2014.

Hess, H.H. (1962). History of Ocean Basins. In: Engel, A.E.J., James, H.L. and Leonard, B.F., (Eds.), *Petrologic Studies: A Volume to Honor A. F. Buddington*, Geological Society of America, Boulder, 599-620.

Hirst, J.P.P. and Nichols, G.J. (1986). Thrust tectonic controls on Miocene alluvial distribution patterns, Southern Pyrenees. In: Allen, P.A., Homewood P., (Eds.), *Foreland Basins,* Oxford, UK: Blackwell Publishing Ltd, 247-258, doi: 10.1002/9781444303810.ch13.

Hollenstein, Ch., Kahle, H.-G., Geiger, A., Jenny, S., Goes, S. and Giardini, D. (2003). New GPS constraints on the Africa-Eurasia plate boundary zone in southern Italy. *Geophysical Research Letters*, 30, 18, doi: 10.1029/2003GL017554.

Hovland, M. and Judd, A.G. (1988). *Seabed pockmarks and seepages - impact on geology, biology and the marine environment*. London, UK: Graham and Trotman Ltd., ISBN 0 86010 948 8.

Howard, A.D., Dietrich, W.E. and Seidl, M.A. (1994). Modeling fluvial erosion on regional to continental scales. *Journal of Geophysical Research*, 99, 13971–13986.

Howell, S. M., Ito, G., Behn, M.D., Martinez, F., Olive, J.-A. and Escartín, J. (2015). Magmatic and tectonic extension at the Chile Ridge: Evidence for mantle controls on ridge segmentation. *Geochemistry, Geophysics, Geosystems*, 17, 2354–2373, doi: 10.1002/ 2016GC006380.

Husson, L., Guillaume, B., Funiciello, F., Faccenna, C. and Royden, L.H. (2012). Unraveling topography around subduction zones from laboratory models. *Tectonophysics*, 526-529, 5-15.

Huvenne, V. A. I., Van Rooij, D., De Mol, B., Thierens, M., O'Donnell, R. and Foubert, A. (2009). Sediment dynamics and palaeo-environmental context at key stages in the Challenger cold-water coral mound formation: clues from sediment deposits at the mound base. *Deep Sea Research I*, 56, 2263-2280, doi: 10.1016/j.dsr.2009.08.003.

ICS (2018). [online] [Consulted on February 7th, 2018] URL: <*http://www.stratigraphy.org/index.php/ics-chart-timescale*>.

IHO (2008). *Standardization of Undersea Feature Names: Guidelines Proposal form Terminology.* Fourth Edition, Mónaco: International Hydrographic Organisation and Intergovernmental Oceanographic Commission, 32.

Innomar, (2018). [online] [Consulted on February 20th, 2018] URL: <*https://www.innomar.com/ses2000compact.php*>.

Isacks, B., Oliver, J. and Sykes, L.R. (1968). Seismology and the new global tectonics. *Journal of Geophysical Research*, 73, 18, 5855–5899, doi: 10.1029/JB073i018p05855.

ISC (2018). [online] [Consulted on June 15th, 2018] URL: <*http://www.isc.ac.uk/iscbulletin/*>.

ISC-GEM (2018). [online] [Consulted on June 15th, 2018] URL: <*http://www.isc.ac.uk/iscgem/*>.

Jenny, S., Goes, S., Giardini, D. and Khale, H.-G. (2006). Seismic potential of Southern Italy. *Tectonophysics*, 415, 81-101.

Jolivet, L., Faccenna, C. and Piromallo, C., (2009). From mantle to crust: Stretching the Mediterranean. *Earth and Planetary Science Letters*, 285, 1–2, 198–209, doi: 10.1016/j.epsl.2009.06.017.

Jones, S.J. (2004). Tectonic controls on drainage evolution and development of terminal alluvial fans, southern Pyrenees, Spain. *Terra Nova*, 16, 121-127.

Judd, A. and Hovland, M. (2007). *Seabed Fluid Flow: The Impact on Geology, Biology and the Marine Environment*. Cambridge, UK: Cambridge University Press.

Kanamori, H. (1977). The Energy Release in Great Earthquakes. *Journal of Geophysical Research*, 82(20), 2981-2987.

Kano, A., Ferdelman, T. G., Williams, T., Henriet, J. P., Ishikawa, T., Kawagoe, N., Takashima, C., Kakizaki, Y., Abe, K., Sakai, S., Browning, E. and Li, X. (2007). Age constraints on the origin and growth history of a deep-water coral mound in the northeast Atlantic drilled during Integrated Ocean Drilling Program Expedition 307. *Geology*, 35, 11, 1051-1054, doi: 10.1130/G23917A.1.

Kearey, P., Klepeis, K.A. and Vine, F.J. (2009). *Global tectonics*. Oxford, UK: Wiley-Blackwell Ed.

Keller, E.A. and Pinter, N. (2002). *Active Tectonics: Earthquakes, Uplift, and Landscape*. Second Edition, Upper Saddle River, NJ: Prentice-Hall.

Kennett J.P. (1982). *Marine Geology*. Englewood Cliffs, NJ: Prentice-Hall, 813.

Kharrat, S., Harbi, A., Meghraoui, M. and Bouaziz, S. (2018). The Tunisian Homogenized Macroseismic Database (Second Century–1981): First Investigations. *Seismological Research Letters*, doi: https://doi.org/10.1785/0220180237.

Kherroubi, A., Deverchere, J., Yelles, A., Mercier de Lepinay, B., Domzig, A., Cattaneo, A., Bracene, R., Gaullier, V. and Graindorge, D. (2009). Recent and active deformation pattern off the easternmost Algerian margin, Western Mediterranean Sea: New evidence for contractional tectonic reactivation. *Marine Geology*, 261(1-4), 17-32.

Khomsi, S., Soussi, M., Mahersi, C., Bédir, M., Fakhfakh-Ben Jemia, H., Riahi, S. and Bou Khalfa, K. (2009). New insights on the structural style of the subsurface of the Tell units in north-western Tunisia issued from seismic imaging: Geodynamic implications. *Comptes Rendus Geoscience*, 341, 347-356, doi:10.1016/j.crte.2009.01.002.

King, L.H. and MacLean, B. (1970). Pockmarks on the Scotian Shelf. *Geological Society of America Bulletin*, 81, 3141-3148.

Kirby, E. and Whipple, K.X. (2012). Expression of active tectonics in erosional landscapes. *Journal of Structural Geology*, 44, 54-75.

Kongsberg (2018a). [online] [Consulted on February 20th, 2018] URL: *<https://www.km.kongsberg.com/ks/web/nokbg0240.nsf/AllWeb/993132242751F5EDC1125FA300360548?OpenDocument>*.

Kongsberg (2018b). [online] [Consulted on February 20th, 2018] URL: *<https://www.km.kongsberg.com/ks/web/nokbg0240.nsf/AllWeb/750790F28DC4EE08C1125A690024C8CE?OpenDocument>*.

Ksentini, A. and Romhdane, N.B. (2011). On the seismic risk assessment of Tunis urban area: uncertainties investigation and treatment using logic tree approach. *6th International Conference of Seismology and Earthquake Engineering*, Tehran, Iran.

Ksentini, A. and Romhdane, N.B. (2014). Updated seismic hazard assessment of Tunisia. *Bulletin of Earthquake Engineering*, 12, 647–670.

Larroque, C., Béthoux, N., Calais, E., Courboulex, F., Deschamps, A., Déverchère, J., Stéphan, J.-F., Ritz, J.-F. and Gilli, E. (2001). Active and recent deformation at the Southern Alps – Ligurian basin junction. *Netherlands Journal of Geosciences / Geologie en Mijnbouw*, 80, 3-4, 255-272.

Lay, T. (2016). *Great Earthquakes on Plate Boundaries*. Oxford Research Encyclopedia of Natural Hazard Science, Online publication, doi: 10.1093/acrefore/9780199389407.013.32.

Le Pichon, X. (1968). Sea-floor spreading and continental drift. *Journal of Geophysical Research*, 73, 12, 3661-3697.

Leprêtre, R., Frizon de Lamotte, D., Combier, V., Gimeno-Vives, O., Mohn, G. and Eschard, R. (2018). The Tell-Rif orogenic system (Morocco, Algeria, Tunisia) and the structural heritage of the southern Tethys margin. *Earth Sciences Bulletin*, 189, 10, doi: https://doi.org/10.1051/bsgf/2018009.

Lobo, F.J., Maldonado, A., Hernández-Molina, F.J., Fernández-Salas, L.M., Ercilla, G. and Alonso, B. (2008). Growth patterns of a proximal terrigenous margin offshore the Guadalfeo River, northern Alboran Sea (SW Mediterranean Sea): Glacio-eustatic control and disturbing tectonic factors. *Marine Geophysical Researches*, 29, 195-216

Lofi, J., Berné, S., Tesson, M., Seranne, M. and Pezard, P. (2012). Giant solution-subsidence structure in the Western Mediterranean related to deep substratum dissolution. *Terra Nova*, 24, 181-188, doi: 10.1111/j.1365-3121.2011.01051.x.

Lo Iacono, C., Gràcia, E., R. Ranero, C., Emelianov, M., A.I. Huvenne, V., Bartolomé, R., Booth-Rea, G., Prades, J. and the MELCOR Cruise Party (2014). The West Melilla cold water coral mounds, Eastern Alboran Sea: Morphological characterization and environmental context. *Deep-Sea Research Part II, Topical Studies in Oceanography,* 99, 316-326, doi: http://dx.doi.org/10.1016/j.dsr2.2013.07.006

Lo Iacono, C., Savini, A. and Basso, D. (2018). Cold-water carbonate bioconstructions. In: Micallef, A., Krastel, S., Savini, A., (Eds.), *Submarine Geomorphology*, Springer International Publishing AG.

Lonergan, L. and White, N. (1997). Origin of the Betic-Rif mountain belt. *Tectonics*, 16, 3, 504–522.

Maldonado, A. and Stanley, D.J. (1976). Late Quaternary Sedimentation and Stratigraphy in the Strait of Sicily. *Smithsonian contributions to the earth sciences*, 16.

Malinverno, A. and Ryan, W.B.F. (1986). Extension in the Tyrrhenian Sea and shortening in the Apennines as result of arc migration driven by sinking of the lithosphere. *Tectonics*, 5, 2, 227-245.

Mancilla, F.D., Booth-Rea, G., Stich, D., Perez-Pena, J.V., Morales, J., Azanon, J.M., Martin, R. and Giaconia, F. (2015). Slab rupture and delamination under the Betics and Rif constrained from receiver functions. *Tectonophysics*, 663, 225-237.

Maouche, S., Meghraoui, M., Morhange, C., Belabbes, S., Bouhadad, Y. and Haddoum, H. (2011). Active coastal thrusting and folding, and uplift rate of the Sahel Anticline and Zemmouri earthquake area (Tell Atlas, Algeria). *Tectonophysics*, 509(1–2), 69–80, doi: https://doi.org/10.1016/j.tecto.2011.06.003.

Marlow, M.S., Gardner, J.V. and Normark, W.R. (2000). Using high-resolution multibeam bathymetry to identify seafloor surface rupture along the Palos Verdes fault complex in offshore southern California. *Geology*, 28, 7, 587-590.

Mart, Y., Aharonov, E., Mulugeta, G., Ryan, W., Tentler, T. and Goren, L. (2005). Analogue modelling of the initiation of subduction. *Journal of Geophysical Research*, 160, 1081-1091.

Martínez-García, P., Soto, J.I. and Comas, M. (2011). Recent structures in the Alboran Ridge and Yusuf fault zones based on swath bathymetry and sub-bottom profiling: evidence of active tectonics. *Geo-Marine Letters*, 31, 19-36, doi: 10.1007/s00367-010-0212-0

Mascle, J. and Rehault, J.P. (1990). A revised seismic stratigraphy of the Tyrrhenian Sea: implications for the basin evolution. In: Kastens, K.A., Mascle, J. et al., (Eds.), *Proceedings ODP Scientific Results*, 107, 617-636.

Mascle, G.H., Tricart, P., Torelli, L., Bouillin, J-P., Rolfo, F., Lapierre, H., Monié, P., Depardon, S., Mascle, J. and Peis, D. (2001). Evolution of the Sardinia Channel (Western Mediterranean): new constraints from a diving survey on Cornacya seamount off SE Sardinia. *Marine Geology*, 179, 179-202.

Mascle, G.H., Tricart, P., Torelli, L., Bouillin, J-P., Compagnoni, R., Depardon, S., Mascle, J., Pecher, A., Peis, D., Rekhiss, F., Rolfo, F., Bellon, H., Brocard, G., Lapierre, H., Monié, P. and Poupeau, G. (2004). Structure of the Sardinia Channel: crustal thinning and tardi-orogenic extension in the Apenninic-Maghrebian orogen; results of the Cyana submersible survey (SARCYA and SARTUCYA) in the western Mediterranean. *Bulletin de la Société Géologique de France*, 176 (6), 607-627.

Masrouhi, A., Bellier, O. and Koyi, H. (2014). Geometry and structural evolution of Lorbeus diapir, northwestern Tunisia: polyphase diapirism of the North African inverted passive margin. *International Journal of Earth Sciences*, 103, 881–900, doi: https://doi.org/10.1007/s00531-013-0992-3.

Matoš, B., Tomljenovic, B. and Trenc, N. (2014). Identification of tectonically active areas using DEM: a quantitative morphometric analysis of Mt. Medvednica, NW Croatia. *Geological Quarterly*, 58, 1.

Matoš, B., Pérez-Peña, J. V. and Tomljenović, B. (2016). Landscape response to recent tectonic deformation in the SW Pannonian Basin: Evidences from DEM-based morphometric

analysis of the Bilogora Mt. area, NE Croatia. *Geomorphology*, 263, 132-155, doi: 10.1016/j.geomorph.2016.03.020.

Mauffret, A. (2007). The Northwestern (Maghreb) boundary of the Nubia (Africa) Plate. *Tectonophysics*, 429(1–2), 21–44, doi: https://doi.org/10.1016/j.tecto.2006.09.007.

McClusky, S., Reilinger, R., Mahmoud, S., Ben Sari, D. and Tealeb, A. (2003). GPS constraints on Africa (Nubia) and Arabia plate motions. *Geophysical Journal International*, 155 (1), 126-138.

Meghraoui, D. and Doumaz, F. (1996). Earthquake-induced flooding and paleoseismicity of the El Asnam, Algeria, fault-related fold. *Journal of Geophysical Research*, 101, B8, 17617-17644.

Meghraoui, M., Morel, J.-L., Andrieux, J. and Dahmani, M. (1996b). Tectonique plio-quaternaire de la chaine tello-rifaine et de la mer d'Alboran: Une zone complexe de convergence continent-continent. *Bulletin de la Societé Géologique de France*, 167, 1, 141-157.

Meghraoui, D. and Pondrelli, S. (2012). Active faulting and transpression tectonics along the plate boundary in North Africa. *Annals of Geophysics*, 55, 5, doi: 10.4401/ag-4970.

Mejri, L., Regard, V., Carretier, S., Brusset, S. and Dlala, M. (2010). Evidence of Quaternary active folding near Utique (Northeast Tunisia) from tectonic observations and a seismic profile. *Comptes Rendus Geoscience*, 342(11), 864-872.

Melki, F., Zouaghi, T., Ben Chelbi, M., Bedir, M. and Zargouni, F. (2010). Tectono-sedimentary events and geodynamic evolution of the Mesozoic and Cenozoic basins of the Alpine Margin, Gulf of Tunis, north-eastern Tunisia offshore. *Comptes Rendus Geoscience*, 342(9), 741-753.

Melki, F., Zouaghi, T., Harrab, S., Sainz, A.C., Bedir, M. and Zargouni, F. (2011). Structuring and evolution of Neogene transcurrent basins in the Tellian foreland domain, north-eastern Tunisia. *Journal of Geodynamics*, 52(1), 57-69.

Melki, F., Zouaghi, T., Ben Chelbi, M., Bédir, M. and Zargouni, F. (2012). Role of the NE-SW Hercynian Master Fault Systems and Associated Lineaments on the Structuring and Evolution of the Mesozoic and Cenozoic Basins of the Alpine Margin, Northern Tunisia. In: Sharkov, E., (Ed.), *Tectonics: Recent Advances*, 131-168, doi: 10.5772/50145.

Mimouni, N., Van Den Driessche, J. and Bouaziz, S. (2016). L'espacement régulier des drains transversaux du front sud atlasique tunisien: implication morphotectonique. *Géomorphologie: relief, processus, environnement*, 22 (4), 377-388.

Missenard, Y., Zeyen, H., Frizon De Lamotte, D, Leturmy, P., Petit, C., Sebrier, M. and Saddiqi, O. (2006). Crustal versus asthenospheric origin of relief of the Atlas Mountains of Morocco. *Journal of Geophysical Research*, 111.

Molin, P., Pazzaglia, F.J. and Dramis, F. (2004). Geomorphic expression of active tectonics in a rapidly-deforming forear, Sila Massif, Calabria, southern Italy. *American Journal of Science*, 304, 559-589.

Monty, C.L.V. (1995). The rise and nature of carbonate mud-mounds: an introductory actualistic approach. In: Monty, C.L.V., Bosence, D.W.J., Bridges, P.H., and Pratt, B.R. (Eds.), *Carbonate Mud- Mounds: Their Origin and Evolution*, IAS Spec. Publ., 23, 11–48.

Morgan, W.J. (1968). Rises, trenches, great faults, and crustal blocks. *Journal of Geophysical Research*, 73, 6, 1959–1982.

Moss JL., Cartwright, J., Cartwright, A. and Moore, R. (2012). The spatial pattern and drainage cell characteristics of a pockmark field, Nile Deep Sea Fan. *Marine and Petroleum Geology,* 35, 321-336, doi:10.1016/j.marpetgeo.2012.02.019.

Naumann, M.S., Orejas, C. and Ferrier-Pagès, C. (2014). Species-specific physiological response by the cold-water corals Lophelia pertusa and Madrepora oculata to variations within their natural temperature range. *Deep-Sea Research II*, 99, 36-41.

NIWA (2018). [online] [Consulted on June 15th, 2018] URL: <*https://www.niwa.co.nz/*>.

Nocquet, J.M. (2012). Present-day kinematics of the Mediterranean: A comprehensive overview of GPS results. *Tectonophysics*, 579, 220–242, doi: 10.1016/j.tecto.2012.03.037.

O'Callaghan, J.F. and Mark, D.M. (1984). The extraction of drainage networks from digital elevation data. *Computer Vision, Graphics, and Image Processing*, 28, 323–344.

Ohmori, H. (1993). Changes in the hypsometric curve through mountain building resulting from concurrent tectonics and denudation. *Geomorphology*, 8, 263–277.

Oilfield Glossary (2017). [online] [Consulted on September 13th, 2017] URL: <*http://www.glossary.oilfield.slb.com/*>.

Onken, R. and Sellschopp, J. (2001). Water masses and circulation between the eastern Algerian Basin and the Strait of Sicily in October 1996. *Oceanologica Acta*, 24 (2), 151-166.

Ord, J. K. and A. Getis (1995). Local spatial autocorrelation statistics, Distributional issues and application. *Geographical Analysis*, 27, 286– 306.

Orejas, C., Gori, A., Lo Iacono, C., Puig, P. and Gili, J.M. (2009). Cold-water corals in the Cap de Creus canyon, northwestern Mediterranean: spatial distribution, density and anthropogenic impact. *Marine Ecology Progress Series*, 397, 37-51.

Ousadou, F., Dorbath, L., Ayadi, A., Dorbath, C. and Gharbi, S. (2014). Stress field variations along the Maghreb region derived from inversion of major seismic crisis fault plane solutions. *Tectonophysics*, 632, 261–280, doi: https://doi.org/10.1016/j.tecto.2014.06.017.

Ouyed, M., Meghraoui, M., Cisternas, A., Deschamps, A., Dorel, J., Frechet, L., Gaulon, R., Hatzfeld, D. and Philip, H. (1981). Seismotectonics of the El Asnam earthquake. *Nature*, 292, 26–31.

Palano, M., Ferranti, L., Monaco, C., Mattia, M., Aloisi, M., Bruno, V., Cannavò, F. and Siligato, G. (2012). GPS velocity and strain fields in Sicily and southern Calabria, Italy: Updated geodetic constraints on tectonic block interaction in the central Mediterranean. *Journal of Geophysical Research*, 117, B07401, doi: 10.1029/2012JB009254.

Papanikolau, I.D., Van Balen, R., Silva, P.G. and Reicheter, K. (2015). Geomorphology of active faulting and seismic hazard assessment: New tools and future challenges. *Geomorphology*, 237, 1-13.

Pedrera, A., Pérez-Peña, J.V., Galindo-Zaldivar, J., Azanon, J.M. and Azor, A. (2009). Testing the sensitivity of geomorphic indices in areas of low-rate active folding (eastern Betic Cordillera, Spain). *Geomorphology*, 105, 218-231.

Peirce, C. and Barton, P.J. (1992). Southern Segment of the European Geotraverse - A Wide-Angle Seismic Refraction Experiment in the Sardinia Channel. *Marine Geophysical Researches*, 14, 227-248.

Pepe, F., Sulli, A., Berotti, G. and Catalano, R. (2005). Structural highs formation and their relationship to sedimentary basins in the north Sicily continental margin (southern Tyrrhenian Sea): Implication for the Drepano Thrust Front. *Tectonophysics*, 409, 1-18.

Pérez-Peña, J. V., Azañón, J.M., Azor, A., Delgado, J. and González-Lodeiro, F. (2009a). Spatial analysis of stream power using GIS: SLk anomaly maps. *Earth Surface Processes and Landforms*, 34, 16–25, doi:10.1002/esp.1684.

Pérez-Peña, J.V., Azañón, J.M. and Azor, A. (2009b). CalHypso: An ArcGIS extension to calculate hypsometric curves and their statistical moments. Applications to drainage basin analysis in SE Spain. *Computers and Geosciences*, 35, 1214-1223.

Pérez-Peña, J.V., Azañón, J.M., Booth-Rea, G., Azor, A. and Delgado, J. (2009c). Differentiating geology and tectonics using a spatial autocorrelation technique for the hypsometric integral. *Journal of Geophysical Research*, 114, doi: 10.1029/2008JF001092.

Pérez-Peña, J.V., Azor, A., Azañón, J.M. and Keller, E.A. (2010). Active tectonics in the Sierra Nevada (Betic Cordillera, SE Spain): insights from geomorphic indexes and drainage pattern analysis. *Geomorphology*, 119, 74-87.

Perron, J.T. and Royden, L. (2013). An integral approach to bedrock river profile analysis. *Earth Surface Processes and Landforms*, 38, 570–576, doi:10.1002/esp.3302.

Petit, C., Le Pourhiet, L., Scalabrino, B., Corsini, M., Bonnin, M. and Romagny, A. (2015). Crustal structure and gravity anomalies beneath the Rif, northern Morocco: Implications for the current tectonics of the Alboran region. *Geophysical Journal International*, 202, 640-652.

Philip, H. and Meghraoui, M. (1983). Structural analysis and interpretation of the surface deformations of the Asnam earthquake of October 10, 1980. *Tectonics*, 2 (1), 17-49.

Pierdominici, S. and Heidbach, O. (2012). Stress field of Italy - Mean stress orientation at different depths and wave-length of the stress pattern. *Tectonophysics*, 532–535, 301–311, doi: https://doi.org/10.1016/j.tecto.2012.02.018.

Pike, R. J. and S. E. Wilson (1971). Elevation-relief ratio, hypsometric integral, and geomorphic area-altitude analysis. *Geological Society of America Bulletin*, 82, 1079–1084.

Pilcher R. and Argent J. (2007). Mega-pockmarks and linear pockmark trains on the West African continental margin. *Marine Geology*, 244, 15–32, doi:10.1016/j.margeo.2007.05.002.

Pinet, P.R. (2003). *Invitation to Oceanography*. Boston: Jones & Bartlett Learning, ISBN 978-0-7637-2136-7.

Piqué, A., Tricart, P., Guiraud, P., Laville, E., Bouaziz, S., Amrhar, M. and Ait Ouali, R. (2002). The Mesozoic-Cenozoic Atlas belt (North Africa): an overview. *Geodinamica Acta*, 15, 3, 185-208, doi: 10.1080/09853111.2002.10510752.

Piromallo, C. and Morelli, A. (2003). P wave tomography of the mantle under the Alpine-Mediterranean area. *Journal of Geophysical Research*, 108, doi: 2010.1029/2002JB001757.

Platt, J. P., Behr, W. M., Johanesen, K. and Williams, J. R. (2013). The Betic-Rif Arc and Its Orogenic Hinterland: A Review. *Annual Review of Earth and Planetary Sciences*, 41(1), 313–357, doi: https://doi.org/10.1146/annurev-earth-050212-123951.

Polonia, A., Cormier, M.-H., Çagatay, N., Bortoluzzi, G., Bonatti, E., Gasperini, L., Seeber, L., Gorur, N., Capotondi, L., McHugh, C., Ryan, W.B.F., Emre, Ö., Okay, N., Ligi, M., Tok, B., Blasi, A., Busetti, M., Eris, K., Fabretti, P., Fielfing, E.J., Imren, C., Kurt, H., Magagnoli, A., Marozzi, G., Imren, C., Penitenti, D., Serpi, G. and Sarikavak, K. (2002). Exploring submarine earthquake geology in the Marmara Sea, *Eos*, 83, 235-236.

Pondrelli, S., Piromallo, C. and Serpelloni, E. (2004). Convergence vs. retreat in Southern Tyrrhenian Sea: Insights from kinematics. *Geophysical Research Letters*, 31, doi: 10.1029/2003GL019223.

Pondrelli, S., Salimbeni, S., Ekström, G., Morelli, A., Gasperini, P. and Vannucci, G. (2006). The Italian CMT dataset from 1977 to the present. *Physics of the Earth and Planetary Interiors*, 159(3), 286–303.

Prada, M., Sallares, V., Ranero, C.R., Vendrell, M.G., Grevemeyer, I., Zitellini, N. and de Franco, R. (2014). Seismic structure of the Central Tyrrhenian basin: Geophysicalconstraints on the nature of the main crustal domains. *Journal of Geophysical Research: Solid Earth*, 119, 52-70, doi: 10.1002/2013JB010527.

Prada, M., Sallares, V., Ranero, C.R., Vendrell, M.G., Grevemeyer, I., Zitellini, N. and de Franco, R. (2016). Spatial variations of magmatic crustal accretion during the opening of the Tyrrhenian back-arc from wide-angle seismic velocity models and seismic reflection images. *Basin Research*, 30, 124–141, doi: 10.1111/bre.12211.

Presti, D., Billi, A., Orecchio, B., Totaro, C., Faccenna, C. and Neri, G. (2013). Earthquake focal mechanisms, seismogenic stress, and seismotectonics of the Calabrian Arc, Italy. *Tectonophysics*, 602, 153–175, doi: https://doi.org/10.1016/j.tecto.2013.01.030.

Rabaute, A. and Chamot-Rooke, N. (2015). Active tectonics of the Africa-Eurasia boundary from Algiers to Calabria (scale 1:500,000). Paris, FR, ISBN 978-2-9548197-0-9.

Rabii, F., Achour, H., Rebai, N. and Jallouli, C. (2016). Hypsometric integral for the identification of neotectonic and lithology differences in low tectonically active area (Utica-Mateur region, north-eastern Tunisia). *Geocarto International*, 1229-1242, doi: 10.1080/10106049.2016.1195890.

RCMT (2015). [online] [Consulted on November 24th, 2015] URL: <*http://rcmt2.bo.ingv.it/*>.

Rebesco, M., Hernández-Molina, F.J., Van Rooij, D. and Wåhlin, A. (2014). Contourites and associated sediments controlled by deep-water circulation processes: State-of-the-art and future considerations. *Marine Geology*, 352, 111–154, doi: https://doi.org/10.1016/j.margeo.2014.03.011.

Rehault, J.-P., Boillot, G., and Mauffret, A. (1984). The Western Mediterranean Basin geological evolution. *Marine Geology*, 55, 3–4, 447–477, doi: 10.1016/0025-3227(84)90081-1.

Reiter, L. (1991). *Earthquake Hazard Analysis, Issues and Insights*. Columbia University Press, 254.

Research Group for Lithospheric Structure in Tunisia (1992). The European Geotraverse, Part 8 The EGT'85 seismic experiment in Tunisia: a reconnaissance of the deep structures. *Tectonophysics*, 207, 245-267.

Riahi, S., Soussi, M. and Ben Ismail Lattrache, K. (2015). Age, internal stratigraphic architecture and structural style of the Oligocene–Miocene Numidian Formation of northern Tunisia. *Annales Societatis Geologorum Poloniae*, 85, 345–370.

Ribolout V., Cattaneo, A., Sultan, N., Garziglia, S., Ker, S., Imbert, P. and Voisset, M. (2013). Sea-level change and free gas occurrence influencing a submarine landslide and pockmark formation and distribution in deep water Nigeria. *Earth and Planetary Science Letters*, 375, 78-91, doi: https://doi.org/10.1016/j.epsl.2013.05.013.

Roberts, J. M., Wheeler, A., Freiwald, A. and Cairns, S. (2009). *Cold-Water Corals: The Biology and Geology of Deep-Sea Coral Habitats*. Cambridge University Press, ISBN: 9780521884853.

Roberts, D.G. and Bally, A.W. (2012). *Regional Geology and Tectonics: Principles of Geologic Analysis*. Elsevier, 900.

Rodriguez, M., Maleuvre, C., Jollivet-Castelot, M., d'Acremont, E., Rabaute, A., Lafosse, M., Ercilla, G., Vázquez, J.M., Alonso, B., Ammar, A. and Gorini, C. (2017). Tsunamigenic submarine landslides along the Xauen–Tof no banks in the Alboran Sea (Western Mediterranean Sea). *Geophysical Journal International*, 209, 266–281, doi: https://doi.org/10.1093/gji/ggx028

Rosenbaum, G., Lister, G.S. and Duboz, C. (2002). Reconstruction of the tectonic evolution of the western Mediterranean since the Oligocene. *Journal of the Virtual Explorer*, 8, 107-126.

Rosenbaum, G. and Lister, G. S. (2004). Neogene and Quaternary rollback evolution of the Tyrrhenian Sea, the Apennines, and the Sicilian Maghrebides. *Tectonics*, 23(1), 1–17, doi: https://doi.org/10.1029/2003TC001518.

Rothwell, R.G. (1995). Marion Dufresne Cruise 81, Cruise report, Mediterranean Giant Piston Coring Transect, MAST II PALAEOFLUX Programme, 17th January-9th February, 1995, Marseille, France – Limassol, Cyprus. Institute of Oceanographic Sciences, Brook Road, Wormley, Godalming, Surrey, GU8 5UB, UK.

Roure, F., Casero, P. and Addoum, B. (2012). Alpine inversion of the North African margin and delamination of its continental lithosphere. *Tectonics*, 31, doi: 10.1029/2011TC002989.

Rouvier, H. (1977). Géologie de l'Extrême-Nord tunisien: tectoniques et paléogéographies superposées à l'extrêmité orientale de la chaîne nord maghrébine. *PhD. Thesis*, Université Paris-VI, 898.

Royden, L. and Perron, J.T. (2013). Solutions of the stream power equation and application to the evolution of river longitudinal profiles. *Journal of Geophysical Research: Earth Surface*, 118, 497–518, doi: 10.1002/jgrf.20031.

Ruano, P. and Galindo-Zaldívar, J. (2004). Striated and pitted pebbles as paleostress markers: an example from the central transect of the Betic Cordillera (SE Spain). *Tectonophysics*, 379, 183–198.

Ruszkiczay-Rüdiger, Z., Fodor, L., Horváth, E. and Telbisz, T. (2009). Discrimination of fluvial, eolian and neotectonic features in a low hilly landscape: a DEM-based morphotectonic analysis in the Central Pannonian Basin, Hungary. *Geomorphology*, 104, 203-217.

Sadrette, S., Rebaï, N. and Mastere, M. (2016). Evaluation of Neotectonic Signature Using Morphometric Indicators: Case Study in Nefza, North-West of Tunisia. *Journal of Geographic Information System*, 8, 338-350, doi: 10.4236/jgis.2016.83029.

Sammari, C., Millot, C., Taupier-Letage, I., Stefani, A. and Brahim, M. (1999). Hydrological characteristics in the Tunisia-Sardinia-Sicily area during spring 1995. *Deep-Sea Research Part I: Oceanographic Research Papers*, 46, 1671-1703.

Sartori, R., Carrara, G., Torelli, L. and Zitellini, N. (2001). Neogene evolution of the southwestern Tyrrhenian sea (sardinia basin and western bathyal plain). *Marine Geology*, 175(1–4), 47–66, doi: https://doi.org/10.1016/S0025-3227(01)00116-5.

Savelli, C. (2002). Time-space distribution of magmatic activity in the western Mediterranean and peripheral orogens during the past 30 Ma (a stimulus to geodynamic considerations). *Journal of Geodynamics*, 34, 99-126.

Schembri, P., Dimech, M., Camilleri, M. and Page, R. (2007). Living deep-water Lophelia and Madrepora corals in Maltese waters (Strait of Sicily, Mediterranean Sea). *Cahiers de Biologie Marine*, 48(1), 77.

Schettino, A. and Turco, E. (2011). Tectonic history of the western Tethys since the Late Triassic. *GSA Bulletin*, 123, 1/2, 89-105, doi: 10.1130/B30064.1.

Scholz, C. (1988). The critical slip distance for seismic faulting. *Nature*, 336, 761-763, doi: https://doi.org/10.1038/336761a0.

Scholz, C.H. (2002). *The Mechanics of Earthquakes and Faulting*. Second Edition, Cambridge, UK: Cambridge University Press, doi: http://dx.doi.org/10.1017/cbo9780511818516.

Seidl, M.A. and Dietrich, W.E. (1992). The problem of channel erosion into bedrock. *Catena supplement*, 23, 101–124.

Sella, G.F., Dixon, T.H. and Mao, A. (2002). REVEL: a model for recent plate velocities from space geodesy. *Journal of Geophysical Research*, 107 (B4), 2081, doi: http://dx.doi.org/10.1029/2000JB000033.

Serpelloni, E., Vannucci, S., Pondrelli, S., Argnani, A., Casula, G., Anzidei, M., Baldi, P. and Gasperini, P. (2007). Kinematics of the Western Africa-Eurasia plate boundary from focal mechanisms and GPS data. *Geophysical Journal International*, 169, 1180–1200, doi: 10.1111/j.1365-246X.2007.03367.x.

Sibson, R.H. (1984). Roughness at the base of the seismogenic zone: contributing factors. *Journal of Geophysical Research*, 89, 5791-5799.

Slama, T., Deffontaines, B. and Moncef Turki., M. (2015). Morphotectonic and Morphodynamic investigations revealed by isobase surfaces analysis and derived differential mapping using GIS, Teboursouk area, northern Tunisia. *Earth Sciences Informatics*, 8, 759-773, doi: 10.1007/s12145-015-0208-4.

Soumaya, A., Ben Ayed, N., Delvaux, D. and Ghanmi, M. (2015). Spatial variation of present-day stress field and tectonic regime in Tunisia and surroundings from formal inversion of focal mechanisms: Geodynamic implications for central Mediterranean. *Tectonics*, 34, doi: 10.1002/ 2015TC003895.

Soumaya, A., Ben Ayed, N., Rajabi, M., Meghraoui, M., Delvaux, D., Kadri, A., Ziegler, M., Maouche, S. and Braham, A. (2018). Active faulting geometry and Stress pattern near complex strike-slip system along the Maghreb region: constraints on active convergence in the Western Mediterranean. *Tectonics*, 37, doi: https://doi.org/10.1029/2018TC004983.

Spakman, W. and Wortel, M.J.R. (2004). A tomographic view on Western Mediterranean Geodynamics. In: Cavazza, W., Roure, F., Spakman, W., Stampfli, G.M. and Ziegler, P., (Eds.), *The TRANSMED Atlas, The Mediterranean Region from Crust to Mantle*, 31-52.

Spakman, W., Chertova, M. V., van den Berg, A. and van Hinsbergen, D. J. J. (2018). Puzzling features of western Mediterranean tectonics explained by slab dragging. *Nature Geoscience*, 9, doi: https://doi.org/10.1038/s41561-018-0066-z.

Squires, D.F. (1964). Fossil coral thickets in Wairarapa, New Zealand. *Journal of Palaeontology*, 38, 904-915.

Stewart, S.A. (1999). Seismic interpretation of circular geological structures. *Petroleum Geoscience*, 5, 273–285.

Stich, D., Serpelloni, E., Mancilla, F.L. and Morales, J. (2006). Kinematics of the Iberia–Maghreb plate contact from seismic moment tensors and GPS observations. *Tectonophysics*, 426, 295-317, doi: 10.1016/j.tecto.2006.08.004.

Stirling, M., Goded, T., Berryman, K. and Litchfield, N. (2013). Selection of Earthquake Scaling Relationships for Seismic-Hazard Analysis. *Bulletin of the Seismological Society of America*, 103(6), 1-19, doi: 10.1785/0120130052.

Stock, J. and Dietrich, W.E. (2003). Valley incision by debris flows: evidence of a topographic signature. *Water Resources Research*, 39, 1089.

Stokes, M. (2008). Plio-Pleistocene drainage development in an inverted sedimentary basin: Vera basin, Betic Cordillera, SE Spain. *Geomorphology*, 100, 193-211.

Storchak, D.A., D. Di Giacomo, I. Bondár, E. R. Engdahl, J. Harris, W.H.K. Lee, A. Villaseñor and P. Bormann (2013). Public Release of the ISC-GEM Global Instrumental Earthquake Catalogue (1900-2009). *Seismological Research Letters*, 84, 5, 810-815, doi: 10.1785/0220130034.

Stow, D.A.V., Pudsey, C.J., Howe, J.A., Faugères, J.-C. and Viana, A.R. (2002). *Deep-water Contourite Systems: Modern Drifts and Ancient Series, Seismic and Sedimentary Characteristics*. London, UK: Geological Society of London, 22, 464.

Strahler, A.N. (1952). Hypsometric (area-altitude) analysis of erosional topography. *Geological Society of America Bulletin*, 63, 1117-1142, doi: 10.1130/0016-7606.

Strzerzynski, P., Déverchère, J., Cattaneo, A., Domzig, A., Yelles, K., Mercier de Lépinay, B., Babonneau, N. and Boudiaf, A. (2010). Tectonic inheritance and Pliocene-Pleistocene inversion of the Algerian margin around Algiers: Insights from multibeam and seismic reflection data. *Tectonics*, 29, doi:10.1029/2009TC002547.

Sulli, A. (2000). Structural framework and crustal characteristics of the Sardinia Channel Alpine transect in the central Mediterranean. *Tectonophysics*, 324(4), 321–336, doi: https://doi.org/10.1016/S0040-1951(00)00050-0.

Sultan, N., Marsset, B., Ker, S., Marsset, T., Voisset, M., Vernant, A.M., Bayon, G., Cauquil, E., Adamy, J., Colliat, J.L. and Drapeau, D. (2010). Hydrate dissolution as a potential mechanism for pockmark formation in the Niger delta. *Journal Geophysical Research*, 115, B08101, doi: 10.1029/2010JB007453.

Sultan, N., Bohrmann, G., Ruffine, L., Pape, T., Riboulot, V., Colliat, J.-L., De Rpunelé, A., Dennielou, B., Garziglia, S., Himmler, T., Marsset, T., Peters, C.A., Rabiu, A. and Wei, J. (2014). Pockmark formation and evolution in deep water Nigeria: Rapid hydrate growth versus slow hydrate dissolution. *Journal of Geophysical Research, Solid Earth*, 119, 2679–2694, doi: 10.1002/2013JB010546.

Taviani, M., Vertino, A., Correa, M. L., Savini, A., De Mol, B., Remia, A., DeMol, B., Remia, A., Montagna, P., Angeletti, A., Zibrowius, H., Alves, T., Salomidi, M. ,Ritt, B and Henry, P. (2011). Pleistocene to Recent scleractinian deep-water corals and coral facies in the Eastern Mediterranean. *Facies*, 57(4), 579-603.

Tondi, E., Zampieri, D., Giunta, G., Renda, P., Alessandroni, M., Unti, M., Giorgianni, A. and Cello, G. (2006). Active faults and inferred seismic sources in the San Vito lo Capo peninsula, northwestern Sicily, Italy. In: Moratti, G. and Chalouan, A., (Eds.), *Tectonics of the Western Mediterranean and North Africa*, Geological Society, London, Special Publications, 262, 365–377, doi: https://doi.org/10.1144/GSL.SP.2006.262.01.22.

Totaro, C., Orecchio, B., Presti, D., Scolaro, S. and Neri, G. (2016). Seismogenic stress field estimation in the Calabrian Arc region (south Italy) from a Bayesian approach. *Geophysical Research Letters*, 43, 8960–8969, doi: 10.1002/ 2016GL070107.

Tricart, P., Torelli, L., Zitellini, N., Bouhlel, H., Creuzot, G., De Santis, L., Morlotti, E., Ouali, J. and Peis, D. (1990). La tectonique d'inversion recente dans le Canal de Sardaigne: resultats de la campagne MATS 87. *Comptes rendus de l'Académie des Sciences - Paris II*, 310, 1083-1088.

Tricart, P., Torelli, L., Argnani, A., Rekhiss, F. and Zitellini, N. (1994). Extensional collapse related to compressional uplift in the Alpine Chain off northern Tunisia (Central Mediterranean). *Tectonophysics*, 238, 317-329.

Trincardi, F. and Zitellini, N. (1987). The rifting of the Tyrrhenian basin. *Geo-Marine Letters*, 7, 1-6.

Turcotte, D.L. and Schubert, G. (2002). *Geodynamics*. Second Edition, Cambridge, UK: Cambridge University Press, 456.

Urgeles, R. and Camerlenghi, A. (2013). Submarine landslides of the Mediterranean Sea: Trigger mechanisms, dynamics, and frequency-magnitude distribution. *Journal of Geophysical Research: Earth Surface*, 118, 2600-2618, doi: 10.1002/2013JF002720.

USGS (2018a). [online] [Consulted on February 6th, 2018] URL: <*https://pubs.usgs.gov/gip/dynamic/inside.html*>.

USGS (2018b). [online] [Consulted on February 6th, 2018] URL: <*https://earthquake.usgs.gov/static/lfs/learn/worldseis.pdf*>.

USGS (2018c). [online] [Consulted on May 29th, 2018] URL: <*https://pubs.usgs.gov/gip/dynamic/understanding.html*>.

van Hinsbergen, D.J.J., Vissers, R.L.M. and Spakman, W. (2014). Origin and consequences of western Mediterranean subduction, rollback, and slab segmentation. *Tectonics*, 33, 393-419.

Vertino, A., Savini, A., Rosso, A., Di Geronimo, I., Mastrototaro, F., Sanfilippo, R., Gay, G. and Etiope, G. (2010). Benthic habitat characterization and distribution from two representative sites of the deep-water SML Coral Province (Mediterranean). *Deep Sea Research Part II: Topical Studies in Oceanography*, 57(5), 380-396.

Villaseñor, A., Chevrot, S., Harnafi, M., Gallart, J., Pazos, A., Serrano, I., Córdoba, D., Pulgar, J.A., and Ibarra, P. (2015). Subduction and volcanism in the Iberia-North Africa collision zone from tomographic images of the upper mantle. *Tectonophysics*, 663, 238–249, doi: 10.1016/j.tecto.2015.08.042.

Vine, F.J. and Matthews, D.H. (1963). Magnetic Anomalies over Oceanic Ridges. *Nature*, 201, 4897, 947–949, doi: 10.1038/201591a0.

Vogt, J. (1993). Further research on the historical seismicity of Tunisia. *Terra Nova*, 5(5), 475–476, doi: https://doi.org/10.1111/j.1365-3121.1993.tb00287.x.

Wallace, R. E. (1986). *Active Tectonics*. National Academic Press, 266.

Wegener, A. (1915). *The origin of continents and oceans*. Courier Corporation.

Wells, D.L. and Coppersmith, J. (1994). New Empirical Relationships among Magnitude, Rupture Length, Rupture Width, Rupture Area, and Surface Displacement. *Bulletin of the Seismological Society of America*, 84, 4, 974-1002.

Vergés, J. and Fernàndez, M. (2012). Tethys-Atlantic interaction along the Iberia-Africa plate boundary: The Betic-Rif orogenic system. *Tectonophysics*, 579, 144–172, doi: https://doi.org/10.1016/j.tecto.2012.08.032.

Wesnousky, S.G. (2008). Displacement and Geometrical Characteristics of Earthquake Surface Ruptures: Issues and Implications for Seismic-Hazard Analysis and the Process of Earthquake Rupture. *Bulletin of the Seismological Society of America*, 98, 4, 1609-1632, doi: 10.1785/0120070111.

Wheeler, A.J., Beyer, A., Freiwald, A., de Haas, H., Huvenne, V.A.I., Kozachenko, M., Olu-Le Roy, K. and Opderbecke, J. (2007). Morphology and environment of cold-water coral carbonate mounds on the NW European margin. *International Journal of Earth Sciences*, 96, 37-56, doi: 10.1007/s00531-006-0130-6.

Whipple, K.X. and Tucker, G.E. (1999). Dynamics of the stream-power river incision model: Implications for height limits of mountain ranges, landscape response timescales, and research needs. *Journal of Geophysical Research*, 104, 661–674.

Whipple, K.X., (2004). Bedrock rivers and the geomorphology of active orogens. *Annual Review of Earth and Planetary Sciences*, 32, 151–185, doi: 10.1146/annurev.earth.32.101802.120356.

Whipple, K.X., DiBiase, R.A. and Crosby, B.T. (2013). Bedrocks Rivers. In: Shroder, J.F., (Ed.), *Treatise on Geomorphology*, Poland: Elsevier, 9, 550-573, doi:10.1016/B978-0-12-374739-6.00254-2.

Willett, S. D., McCoy, S. W., Perron, J. T., Goren, L. and Chen, C. Y. (2014). Dynamic reorganization of river basins. *Science*, 343, 6175, doi: 10.1126/science.1248765.

Wilson, J.B. (1979). 'Patch' development of the deep-water coral Lophelia pertusa (L.) on Rockall Bank. *Journal of the Marine Biological Association of the United Kingdom*, 59, 165–177.

Wisner, B., Blaikie, P., Cannon, T. and David, I. (2003). *At Risk, Natural hazards, people's vulnerability and disasters*. Abingdon, UK: Routledge Ed., ISBN: 0-415-25215-6.

Wood, N. (2011). Understanding risk and resilience to natural hazards. *U.S. Geological Survey Fact Sheet*, 2011-3008, 2.

Wortel, M.R.J. and Spakman, W. (2000). Subduction and Slab Detachment in the Mediterranean-Carpathian Region. *Science*, 290(5498), 1910-1917, doi: 10.1126/science.290.5498.1910.

Würtz, M. and Rovere, M. (2015). *Atlas of the Mediterranean Seamounts and Seamount-like Structures*. Gland, Switzerland and Málaga, Spain: IUCN, 276.

Yang, R., Willett, S. D. and Goren, L. (2015). In situ low-relief landscape formation as a result of river network disruption. *Nature*, 520, 526–529.

Yeats, R.S., Sieh, K. and Allen, C.R. (1997). *The geology of earthquakes*, New York, USA: Oxford University Press, ISBN: 0-19-507827-6.

Yelles, A., Domzig, A., Déverchère, J., Bracène, R., Mercier de Lépinay, B., Strzerzynski, P., Bertrand, G., Boudiaf, A., Winter, T., Kherroubi, A., Le Roy, P. and Djellit, H. (2009). Plio-Quaternary reactivation of the Neogene margin off NW Algiers, Algeria: The Khayr al Din bank. *Tectonophysics*, 475, 98-116, doi: 10.1016/j.tecto.2008.11.030.

Yelles-Chaouche, A., Kherroubi, A., and Beldjoudi, H. (2017). The large Algerian earthquakes (267 A.D.-2017). *Física de la Tierra*, 29, 159–182, doi: http://dx.doi.org/10.5209/FITE.57617.

Zalohar, J. (2009). *T-TECTO 3.0 Professional: integrated software for structural analysis of fault-slip data* (Software Tutorial), Ljubljana, SLO: Faculty of Natural Sciences and Engineering.

Zargouni, F. (1978). Analyse structurale de la chaîne de Lansarine (zone des diapirs, Atlas tunisien). *Bulletin de la Société des Sciences Naturelles de Tunisie*, 13, 97-104.

Zargouni, F. and Ruhland, M. (1981). Tectonic Features as Related to the Wrench Fault of Gafsa, and Chronology of the Tectonic Phases in Southern Atlas of Tunisia. *Comptes rendus de l'Académie des sciences*, 292, 913-915.

Zarroca, M., Linares, R., Roqué, C., Rosell, J. and Gutiérrez, F. (2013). Integrated geophysical and morphostratigraphic approach to investigate a coseismic (?) translational slide responsible for the destruction of the Montclús village (Spanish Pyrenees). *Landslides*, 11, 655-671, doi: 10.1007/s10346-013-0427-z.

Zielhofer, C. and Faust, D. (2008). Late Pleistocene and Holocene alluvial archives in the Southwestern Mediterranean: Changes in fluvial dynamics and past human response. *Quaternary International*, 181, 39–54, doi: https://doi.org/10.1016/j.quaint.2007.09.016.

Zouaghi, T., Bedir, M., Melki, F., Gabtni, H., Gharsalli, R., Bessioud, A. and Zargouni, F. (2011). Neogene sediment deformations and tectonic features of northeastern Tunisia: evidence for paleoseismicity. *Arabian Journal of Geosciences*, 4, 1301-1314.